THE 18302

F4

STRESS CORROSION CRACKING OF ROCK BOLTS

By

Erwin Gamboa

A thesis submitted to the University of Queensland

for the degree of Doctor of Philosophy

Division of Materials

November 2004

— A definition of madness is to continue to do things in the same way that we've always done them, but to expect a different outcome.

Anon

— A definition of research is to continue to perform experiments in the same way that we've always done them, but get a different outcome every time.

The Author

Produced in LaTeX 2_ε.

Except where acknowledged in the customary manner, the material presented in this thesis is, to the best of my knowledge, original and has not been submitted in whole or part for a degree in any university.

Erwin Gamboa

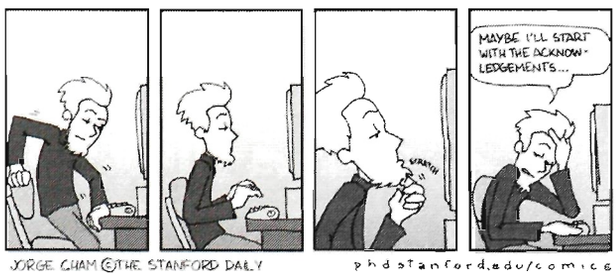

ACKNOWLEDGEMENTS

I would like to thank Dr. Andrej Atrens for providing me with this opportunity to undertake a PhD. His guidance, advice, teachings, patience, supervision and constant feedback has been priceless. Proofreading large manuscripts almost overnight has helped me to produce a higher quality of work.

A big thanks to Mr. Julio Aravena in the mechanical workshop. His expertise, knowledge and skill has allowed me to carry out all experimentation in a timely and effective manner, even when things were urgent. Producing high quality specimens overnight has helped beyond measure.

A huge thanks to Ms. Glenda Zemanek, Mr. Marc DeGlas and Mr. Steve Fick, who have helped me since day one and saved me countless headaches. Without your help I would still be looking for that elusive part or still leaving a trail of destruction in the labs. Your help and friendship will always be remembered.

Thank you to Dr. Rowan Truss and Dr. Graham Schaffer, for your support and advice. It has been a pleasure working in the Division. Thanks also to Dr. Jeff Gates for his invaluable advice on producing a better quality document with his feedback.

To the other dwellers of The Dungeon (room 109), a huge thanks for everything. To Dr. Wang, thanks for all the discussions and tips, and to Ms. Harjac for the coffee, atmosphere, discussions and great times. Without you, The Dungeon would have been just that.

To all the staff and students of the Division of Materials and Division of Mining and Minerals Process Engineering, a huge thanks for making my time here so enjoyable and enriching.

Thankful acknowledgement goes to Mr. Mietek Rataj, of Arnall Mining Products Division, for his support of the PhD and for supplying resources and samples. Grateful acknowledgement to the Australian Research Council for the provision of a SPIRT grant between 2000 and 2003. All cartoon strips have been used with permission from "Piled Higher and Deeper" by Jorge Cham, www.phdcomics.com (thanks Jorge!).

To Matthew Bilson, Jodie Hatfield and the rest of the postgrad gang, a huge thanks. Without your support, drive and enthusiasm I would have thrown in the towel a long time ago.

To Rowena Robins, you gave me strength, determination, friendship and love when I needed it most. I could not have made it without you.

To my parents, especially Mum, to whom this PhD is dedicated, thanks; your support has been invaluable. I can have a PhD, but I'll always be her little boy.

PUBLICATIONS

The following publications, published, submitted or in preparation, are based on the present dissertation:

- E Gamboa and A Atrens, **Environmental Influence on the Stress Corrosion Cracking of Rock Bolts**, *Engineering Failure Analysis* **10**(2003), pp 521-558.
- E Gamboa and A Atrens, **Stress Corrosion Cracking Fracture Mechanisms in Rock Bolts**, *Journal of Materials Science* **38**(2003) pp 3813-3829.
- E Gamboa and A Atrens, **Fractography of SCC Features for Rock Bolts**, 2nd International Conference on Environmental Degradation of Engineering Materials, Event No 264 European Federation of Corrosion, June 29 - July 3rd (2003) Bordeaux, France, ISBN 1-904350-07-0, paper SCC2-2-04b.
- E Gamboa and A Atrens, **Laboratory Testing of Rock Bolt Stress Corrosion Cracking**, COAL 2003, 4th Underground Coal Operators Conference, University of Wollongong, 12-14 February (2003) N Aziz and B Kinnimoth eds, publisher Aus IMM, pp 132-153.
- E Gamboa and A Atrens, **Analysis of a rock bolt failed in service**, Proceedings, 15th International Corrosion Congress, Granada (2002) paper 811, pp1-9.
- E Gamboa and A Atrens, **Relationship of Laboratory Tests of Rock Bolt SCC to Service Failures of Rock Bolts**, Proceedings, International Conference on Hydrogen Effects on Materials Behaviour and Corrosion Deformation Interactions, Jackson WY USA Sept 2002, ed R Jones, N Moody, A Thompson, T Magnin, R Ricker and G Was. TMS 2003, pp 647 641.
- E Gamboa and A Atrens **Material influence on the stress corrosion cracking of rock bolts**, *Engineering Failure Analysis*, accepted for publication 2 July 2004.
- E Gamboa, E Villalba and A Atrens **Stress Corrosion Cracking in Rock Bolts, Proceedings**, Structural Integrity and Fracture 2004, Brisbane 26-29 September (2004), ed A Atrens, J N Boland, R Clegg, J R Griffiths, pp 127-134.

ABSTRACT

The aim of this study was to understand Stress Corrosion Cracking (SCC) of rock bolts and to test possible countermeasures. Rock bolts have been failing in underground mines, causing the mine shaft to collapse and leading to loss of production.

The Linearly Increasing Stress Test (LIST) was used to undertake this study.

Service failures were examined and their fracture surfaces characterised. Typical features included a thumbnail shaped area (typically 1.2 mm deep) with a fast brittle failure overload. The topography of the thumbnail area was identified as Tearing Topography Surface (TTS), Corrugated Irregular Surface (CIS) and quasi Micro Void Coalescence (qMVC). Each region was identified as being related to decreasing amounts of hydrogen diffused into the material.

LIST testing in a sulphate solution with pH 2.1 at an applied stress rate of 0.019 MPa s^{-1} caused the steel samples to fail by SCC with the same morphology as the rock bolts studied. This confirmed LIST testing as a valid SCC test.

The LIST test was then used to understand the environmental conditions leading to rock bolt SCC. Various commercial metallurgies were tested at varying pH levels, solution concentrations and applied overpotentials. Conditions leading to SCC were found to be related to copious hydrogen being evolved (low pH values and / or negative overpotentials). A Pourbaix diagram was presented showing regions where each steel studied was susceptible to SCC.

The LIST test was also used to determine the threshold stress for each metallurgy. Threshold stresses were found to be close to the UTS of each material.

Rock bolt rib geometry was found to have no direct effect on SCC properties, but residual tensile stresses were found to reduce the SCC resistance of the rock bolt. Cold work was found to increase the SCC resistance of the material.

The fracture toughness of a rock bolt metallurgy was estimated to be about 50 MPa$\sqrt{m}$. Using that value with the estimated subcritical crack velocity of 2.5 x 10^{-8} m s^{-1} provided with an estimate of approximately 12 hours between crack initiation and final failure. Further increases of fracture toughness were found to be uneffective in solving the problem of rock bolt SCC, as the increase in lifetime would only extend the life of the component by a few days at most.

Galvanised steel samples were tested as a possible countermeasure, but their performance indicated that they were unsuitable. 304 stainless steel was also tested and also found to be unsuitable.

The conditions leading to SCC for each metallurgy were very specific. Some metallurgies are not susceptible to SCC at certain conditions that might cause SCC in other metallurgies. To solve the rock bolt SCC problem it is a matter of choosing an appropriate metallurgy if the previous metallurgy failed by SCC.

Contents

List of Figures

List of Tables

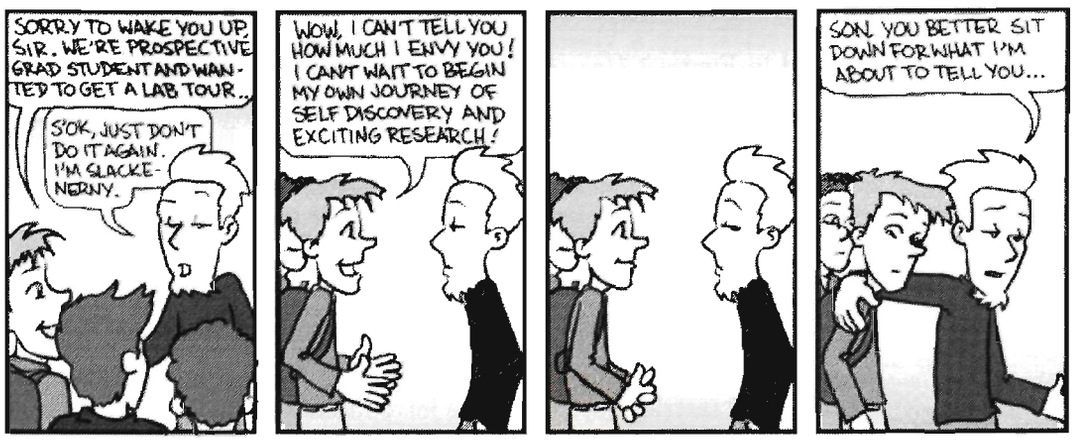

1

INTRODUCTION

1.1 STRESS CORROSION CRACKING

SCC may occur whenever a highly-stressed steel is in the presence of an aggressive environment. The stress corrosion cracks initiate and grow slowly. During this phase, which may last months or years, there may be no indication of any danger. Fast fracture occurs when the stress corrosion cracks reach a critical length, as determined by the applied stress and the fracture toughness of the steel. Reports indicate that the critical crack length can be of the order of only a few millimetres for rock bolts. The fast fracture is sudden and catastrophic.

A review of SCC [2] indicates that SCC is a complex multi-step process, involving the interaction of a stress, a susceptible material and a (fairly specific) environment. This means that SCC testing is not simple and must be done properly to ensure meaningful results. SCC propagates slowly. This necessitates that adequate time is required for testing. Furthermore, the absence of SCC in any test always raises the question of whether the testing time had been sufficiently long in that test. Field testing, particularly of possible SCC solutions, has the added complication that it may not be possible to guarantee that there were appropriate SCC conditions during the field exposure.

1.2 ROCK BOLTING

The principle of rock bolting is illustrated in Figure 1.1(a). Rock bolts provide reinforcement above mine openings such as roadways. The rock bolts are bonded into the rock strata keeping it together just like the steel in reinforced concrete. The rock bolts can be considered to provide a clamping action on the rock. For the strata to fail and collapse, the clamping action of the rockbolts has to be overcome. This requires considerably greater forces. The rock bolts thus maintain the load bearing capacity of the rock strata.

The chemical bolt is the most common rock bolt currently in use [6]. The modern system [6] provides a quick, easy and effective installation procedure, Figure 1.1(b). An appropriate hole is drilled (to the appropriate diameter and depth), the chemical cartridge(s) and bolt is introduced into the hole, the bolt is rotated and simultaneously pushed through the chemical cartridge(s) to mix together the resin and catalyst. After completion of the hold time (to allow curing of the chemical anchor) the bolt is tightened to the appropriate load. The load is distributed to the surrounding rock by means of the base plate, Figure 1.1(c). The chemical anchor fixes the bolt into the rock strata. Depending on amount of the chemicals used, the anchor can be at the end of the bolt as shown in Figure 1.1(c) or it can extend along the length of the bolt. The amount of load on the bolt can be measured using strain gauged test bolts. The amount of plastic deformation of the support plates indicates the load developed in the bottom (unencapsulated) part of the bolt only. Load within the encapsulated section will be different.

There are several rock bolts in the market, with varying strengths and varying rib design. Although bolts differ in metallurgy, reports from colleagues in the industry indicate every kind of bolt has been observed to have failed by SCC at some point.

1.3 INDUSTRIAL CONTEXT

The safety implications of Stress Corrosion Cracking (SCC) of rock bolts have been discussed within the industry for several years. SCC of rock bolts has been reported at a significant number of Australian mines since about 1994. Furthermore, there are reports from the USA of SCC of cable bolts, which is a related issue. SCC of rock bolts was reported to have caused the following sequence at one roadway at a particular colliery (ie coal mine):

- The roadway started to deteriorate in 1996 when it was observed that some broken bolts had fallen out. This corresponded to a period of the order of 3 months after the roadway was established.
- Subsequently, there were lots of broken bolts, and then
- there was a catastrophic collapse of the roof.

A back of the envelope evaluation estimated that the annual cost at that colliery was in excess of a hundred thousand dollars. This cost was that associated with the cost of lost production and the cost of

secondary support. In addition, there is the safety aspect of the consequences of roof falls.

Discussions have indicated that SCC is already a significant problem in a number of mines [7], [8]. Furthermore, it can be expected that the problems associated with SCC will become more severe as mines extend deeper and encounter more difficult conditions such as wet conditions combined with high rock stress. Furthermore, there are indications that the tendency to use rock bolts of higher strength could lead to a higher incidence of SCC [9]. However, at the start of this investigation the environment causing rock bolt SCC was unknown. Some possibilities were as follows.

Steels are expected to be susceptible to SCC in the region of the active-passive transition in carbonate/bicarbonate solutions. That is, at electrochemical potentials positive to their natural corrosion potential. Is electrical coupling to coal an issue? Characteristics of this sort of SCC include: high carbonate concentrations, "high" pH (8-9), low chlorides, intergranular cracking and crack propagation faster at higher temperatures.

Steels are expected to be susceptible to SCC at their corrosion potentials in sulphate/chloride solutions; more so at negative potentials in acid solutions. Note that if the solution is too acid, there will be fast general corrosion and no time for SCC. Characteristics of this type of SCC include "non-passive" macroscopic electrochemical behaviour and transgranular cracking associated with hydrogen embrittlement. Cracking susceptibility increases with (a) lower potential, (b) acid conditions, (c) temperatures approximately equal to 0°C and (d) the presence of H_2S.

SCC needs the conjoint presence of a stress and an appropriate environment. SCC is expected to be manifest as first a period of slow crack growth over an extended period of time (weeks or months) until the crack reaches a critical size, typically a half ellipse at the bolt edge with a crack depth of 2-3 mm. During the period of slow crack growth, there may be no indication of SCC, and the crack(s) may be hard to detect. On the crack reaching the critical length, there will be sudden (essentially instantaneous) fast fracture across the remaining section of the bolt.

Most SCC is reported to occur in the un-encapsulated part of rock bolt some distance into the roof. Cases are known of SCC in the resin-covered area. What drives these cases?

The presence of H_2S aggravates the hydrogen embrittlement type of SCC. Is there a link between SCC and lack of ventilation?

SCC susceptibility increases with steel strength. Cold work may increase SCC susceptibility.

Bacteria can influence the occurrence of SCC by their influence on the local environment production of H_2S and lowering the pH. Crevice conditions would likewise produce a local environment different to the bulk environment. Crevices may provide possible good conditions for the growth of bacteria.

1.4 FIGURES

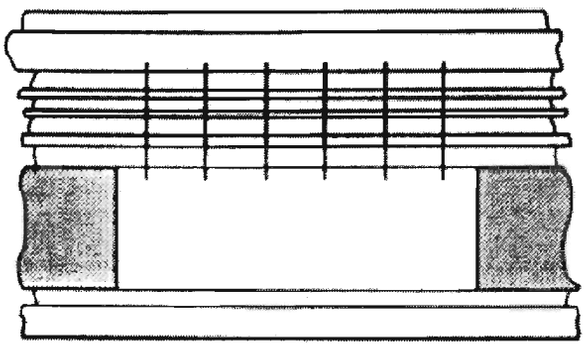

(a) Rock bolts provide reinforcement for rock strata above mine openings

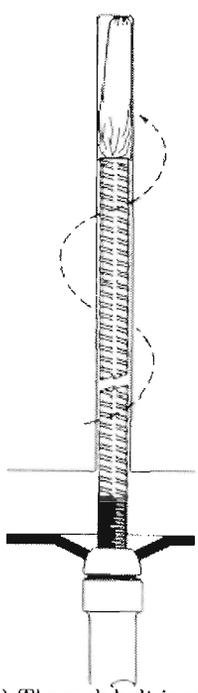

(b) The rock bolt is rotated, and at the same time pushed through the chemical cartridge mixing the resin components

FIGURE 1.1: Rock bolting

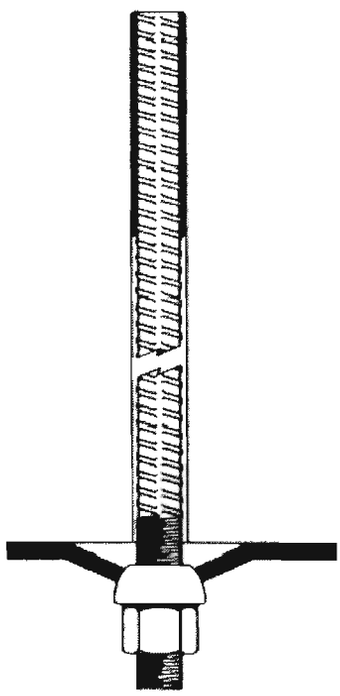

(c) A rock bolt after curing of the chemical fixative and tightening

FIGURE 1.1: Rock bolting

phd.stanford.edu/

2

LITERATURE REVIEW

2.1 INTRODUCTION

SCC describes a mode of failure of engineering materials. During SCC an environmentally induced crack slowly propagates through the material. The SCC crack velocity can range between $10^{-3}ms^{-1}$ and $10^{-10}ms^{-1}$ [5], depending on the material and the environment. When such a crack reaches a critical size, the remaining ligament is not able to withstand the imposed loading, and fails in a fast brittle manner. The fast brittle fracture occurs with little or no warning. SCC requires the interaction of (1) a susceptible material, (2) a specific environment, and (3) a tensile stress. These three requirements for the occurrence of SCC are often symbolised by the three intersecting circles of the following diagram.

SCC only occurs where the three circles intersect. SCC has two modes of propagation. In transgranular (TG) SCC the crack propagates through the grains, whereas propagation is along grain boundaries for intergranular (IG) SCC. SCC could be considered to develop in the following manner. Due to the geometry and small dimensions of the crack, the chemical and electrochemical conditions inside the crack can be different to conditions at a flat surface. This is known as an occluded cell. For SCC, these conditions inside the crack can be favourable to sustain the crack propagation mechanism. The tensile stress assists the crack propagation mechanism by opening up the crack, and by providing crack tip strain to fracture crack tip

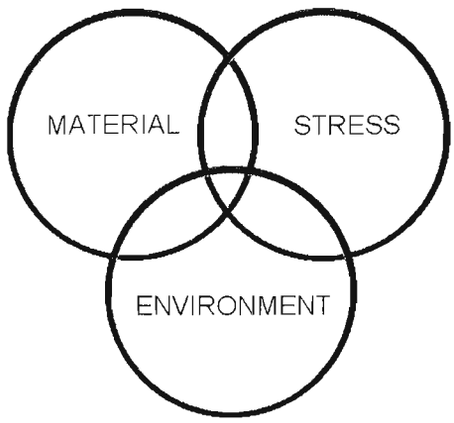

protective films. The result is that crack propagation is often perpendicular to the normal tensile stress. Figure 2.1 illustrates a typical IG failure. In IG SCC, the crack path tends to follow the grain boundaries.

Transgranular SCC can be considered in a similar manner. Inhomogeneities in the crystals cause a cell to be set up, allowing corrosion to be accelerated at that point. The crack is propagated through the crystal (rather than along the crystal boundaries). The tensile stress acting on the metal opens the crack up. This causes the crack to propagate perpendicular to the normal tensile stress, parting the crystal.

The first tests designed to study SCC were based on exposing deformed smooth samples to the environment of interest. Such specimens included the U-bend, the C-ring, the D-ring, the bent beam, direct tension and weldment specimens, as illustrated in Figures 2.2 to 2.5. Some of specimens included notches.

These tests were cheap to construct and to run, but they were time consuming, as the experimental time could be measured in weeks, if not months. Subsequently *dynamic tests* were developed which have the major advantage that they are generally much shorter [1] In a dynamic test, the sample is exposed to the environment whilst subjected to increasing loading until failure. The slow stress application and the long exposure to the electrolyte combine to induce SCC.

The two main dynamic tests are LIST (Linearly Increasing Stress Test) and CERT (Constant Extension Rate Test).

LIST and CERT are virtually the same test. Both slowly load a sample to be studied, while at the same time immersing the sample in an electrolyte. The core difference between the two tests is that the LIST is load controlled whereas the CERT is displacement controlled[10]. Both tests are similar up to crack initiation and for the early stages of crack propagation. However, the CERT test continues until the crack penetrates through the sample thickness. In contrast, the LIST test terminates in suddent brittle fracture when the crack reaches the critical crack size. Thus the LIST can be significantly shorter [10],[11].

2.2 SCC MECHANISMS

Many mechanisms have been proposed for SCC. These can be divided into models related to anodic dissolution, plasticity, film rupture and hydrogen embrittlement. Of these basic mechanisms, the most simple anodic mechanism is that of corrosion acting on the metal and slowly removing material (active dissolution) thereby causing crack advance.

Crack initiation sites could be surface scratches, grain boundaries, point defects, chemical inhomogeneities, inclusions, second phases and interphase boundaries [5]. Even in cases where particular care has been paid to the manufacturing of the material and surface finishing, normal corrosion processes can create surface defects. The most common of these defects (in materials that are susceptible to SCC) is pits caused by pitting corrosion. Figure 2.6 provides a particular schematic of SCC initiation by pitting. Since the material has a surface film providing some corrosion resistance, general corrosion does not occur, and the attack occurs only locally and does not spread out along the surface. The corrosion occurs at local points of breakdown of the protective surface film as pits. These pits develop an occluded cell within, which provides favourable conditions for further corrosion within the pit.

During crack initiation, the tensile stress may play a minor role, and in the extreme, it may not matter whether there was a tensile stress present. In contrast, during crack propagation the tensile stress can play a major role in the SCC process. One possibility is that the tensile stress fractures the surface film. The two main factors of importance during crack propagation could be considered to be the tensile stress (mechanical factor) and the corrosion reactions (dissolution factor) at the crack tip.

Mechanical fracture mechanisms can be divided into two different groups: ductile failure models and brittle failure models. The original mechanical model[5] assumed that the failure was caused when the stress concentration at the crack tip was sufficient to cause the material to fail. Later revisions on this original model incorporated the effects of dissolution and oxide films.

2.2.1 The Film Rupture Model

According to this dissolution model, the tensile stress opens the crack and ruptures the protective passive film at the crack tip, exposing fresh metal to the electrolyte. One school of thought is that this process is continuous, so that the rate of film rupture is greater than the rate of repassivation. On the other hand, an alternate view is that this process is discountinuous. The crack tip repassivates and then slip ruptures the film, allowing some crack advance. This model is not well accepted for transgranular SCC because fracture surfaces are flat, crystallography oriented, and opposing fracture surfaces match topographically, indicating little dissolution during crack advance (Jones [5] referencing Pugh [12]).

2.2.2 Active Path Model

Another dissolution model is the active path intergranular SCC model which suggests that SCC follows a preferential pre-existing reactive path. For example, chemical segregation at grain boundaries could cause preferential corrosion at the grain boundary, causing the crack to propagate along the grain boundary. The crack propagation is self sustaining, as an unstable electrochemical cell is formed at the tip (called an occluded corrosion cell). The tip of the crack is the anode, with the surrounding material acting as the cathode. In its drive to achieve stability, the crack propagates into the material following the path of least resistance, which is along the grain boundaries. This continuous process continues until the remaining cross sectional area of the material is unable to take the tensile load placed upon it, failing in a catastrophic manner.

2.2.3 The Corrosion Tunnel Model

This mechanism is summarised in Figure 2.8 and has been reported to cause TG SCC. Corrosion occurs as parallel corrosion tunnels in the direction of crack propagation, perpendicular to the applied tensile stress. These corrosion tunnels gradually increase in diameter until the material cannot bear the applied load, and the ligaments between the tunnels undergo a ductile tearing process. The crack hence grows, exposing a fresh surface for the pits to form (Jones [5] referencing Harwood [13]).

2.2.4 Adsorption Models

There are two different models that deal with adsorption of chemical species at the crack tip. Lynch's study of fracture surfaces has shown that the fracture surfaces in some cases of SCC, HE and liquid-metal embrittlement (LME) have similar features. Chemisorption was proposed to be common cause. This work into *adsorption enhanced plasticity* [14] led to the model that the fracture is caused by a mixture of cleavage fracture and the formation of voids ahead of the crack tip. Chemisorption was suggested to facilitate the nucleation of dislocations at the crack tip, as well as embrittling such area.

The other main model (Jones [5] referencing Uhlig [15]), *adsorption induced brittle model*, states that chemical species absorbed at the crack tip lower the interatomic bond strength. This means that the tensile stress and the dissolution reactions at the crack tip overcome the bonds, and advance the crack. This mechanism proposes that the crack velocity is dictated by the rate at which species are transported to the crack tip. This model is continuous by its nature and does not explain the discontinuous nature often observed of the crack propagation, nor how the crack can maintain a sharp tip in a ductile material. These two models are similar in that they rely on the adsorption of a chemical species, but the former model deals with the nucleation of voids, while the latter model concentrates on the weakening of the atomic bonds in the matrix.

2.2.5 The Tarnish Rupture Models

Models which can be described as oxide film rupture models deal with the formation of an oxide layer which cracks, propagating the crack forward and exposing a fresh surface to be oxidised.

The *tarnish rupture model* is different to the film rupture model (Section 2.2.1) in that this model is discontinuous, and explains intergranular and transgranular SCC (Jones [5] referencing Pugh [16]). In essence, this discontinuous process is divided into two phases; film formation and crack growth. A surface reacts with the electrolyte, forming an oxide film. The tensile stress then ruptures the film, allowing fresh metal to be exposed. The model of crack growth is illustrated in Figure 2.9.

In case a), the crack grows into the film. In case b), the crack grows through the slip planes but then the film grows along the grain boundary (intergranular SCC).

The other main oxide film rupture model (*film induced cleavage model*) explain the crack arrest markings, cleavage like facets and discontinuous crack propagation shown by many materials.

Similar to the tarnish rupture model, this mechanism postulates that a thin surface film is produced, which then cracks in a brittle manner. The difference with this model is that the crack does not stop at the film - material interface, if the crack is sharp and is propagating at a high velocity before it reaches the interface. This way, a brittle crack enters and propagates into the ductile material. Once in the ductile region, the crack is blunted, slows down and stops. The process then repeats (Jones [5] referencing Forty [17]).

2.2.6 Hydrogen Embrittlement

The work carried out by Mukhopadhyay et al [18], [19] suggests that when hydrogen enters a steel matrix it can reduce the strength between metal bonds,causing embrittlement. When the hydrogen concentration reaches a critical level, a crack can propagate through the embrittled region at a stress much lower than the material's yield strength. Such hydrogen embrittlement is believed to be a main mechanism of SCC.

During corrosion, the anodic partial reaction (sometimes known as a half cell) is metal dissolution,

$$Fe \rightarrow Fe^{2+} + 2e^{-} \tag{2.1}$$

In an acid solution, the cathodic partial reaction is hydrogen evolution. The hydrogen is discharged at the surface of the metal, with a high fugacity [20] and some of the hydrogen inevitably is dissolved into the metal.

When the hydrogen concentration reaches a critical level, crack propagation can occur through the embrittled region. As a consequence, if there is a critical amount of hydrogen within the metal, the metal can crack under a moderate stress.

Figure 2.10 illustrates an example of intergranular embrittlement of nickel at cathodic potentials. Hydrogen interacts with impurities at grain boundaries, leading to IG SCC.

During ductile fracture, crack formation and propagation only occurs under conditions of high stresses and strains, due to the link up of voids created by plasticity at such inhomogeneities as inclusions. In contrast, local subcritical crack advance can occur at a much lower stress if the material in front of the crack has a critical hydrogen concentration. This means that the speed of the crack propagation can be dictated by the speed with which hydrogen is transported to the region in front of the crack tip.

The question then arises of how the hydrogen gets to the region in front of the crack tip. The two main mechanisms that attempt to explain such transport of hydrogen transport are lattice diffusion and dislocation drag.

Hydrogen diffusion in steels is relatively fast because of the small effective size of the hydrogen atom in the steel lattice. The tendency is for hydrogen (or any species) to diffuse from a region of high concentration towards a region of lower concentration [21]. The entry of hydrogen into a metal, its transport to the region ahead of the crack tip and crack advance is illustrated in Figure 2.12.

Dislocation sweeping (or dislocation dragging) is postulated to occur in the plastic zone where dislocations drag hydrogen atoms that are bound to the dislocations. However, Toribio[19] has shown that the hydrogen affected area exceeded that of the region where dislocations could move. This suggests that although dislocation transport has been shown to be a hydrogen transport mechanism in a microscopic scale, it may not apply in a macroscopic scale and is dependent on the details of miroplasticity.

It is worth mentioning that hydrogen embrittlement tends to be most effective at a temperature around 300K. This temperature corresponds to the service temperature for rock bolts, so their service conditions makes them exposed to the maximum risk of hydrogen embrittlement, if other conditions are conducive to this mechanism being operative.

Hydrogen transport is hindered by the trapping of hydrogen at lattice imperfections such as point defects, precipitates, and grain boundaries. As a result, the speed at which the hydrogen concentration increases in the region ahead of the crack tip is dependent on the balance of hydrogen transport and hydrogen trapping.

2.2.7 Source of Hydrogen

The most obvious source of hydrogen is the cathodic partial reaction, which balances the anodic reaction of metal dissolution. In acid conditions, the cathodic reaction produces atomic hydrogen at the metal surface.

$$H^+ + e^- = H \tag{2.2}$$

$$H + H = H_2 \tag{2.3}$$

The atomic hydrogen can either enter the metal (and cause hydrogen embrittlement if there is sufficient hydrogen) or two hydrogen atoms can combine to form a hydrogen molecule which can then aggregate and form a hydrogen bubble that rises to the surface of the solution.

Another source of hydrogen is from microbial action. Micro-organisms(especially bacteria) can accelerate corrosion by several mechanisms, the simplest is by altering their immediate environment due to their metabolic by-products, such as organic and inorganic acids. For example, sulfuric acid is produced from sulfides (as present for example in coal seams) by sulfur oxidizing bacteria in aerobic conditions. Podesta, Estrella and Esteso [22] have shown that hydrogen embrittlement can be result from such bacterial action. Another common example is sulfate reducing bacteria (SRB). SRB often form colonies on the metal surface under anaerobic conditions because the presence of oxygen can be lethal to SRB. The anaerobic conditions are often formed under a biofilm which is usually formed by other (aerobic) microorganisms that can be commonly found close to SRB. SRB reduce sulfate to H_2S which can liberate hydrogen at the metal surface.

$$H_2S + Fe = FeS + H_2 \tag{2.4}$$

The H_2S can then cause hydrogen embrittlement [23], [24]. Section 7.2.2 further discusses the role of SRB in the SCC of rock bolts.

2.3 SCC OF STEELS

SCC is influenced by chemical composition, material properties, environment, stress, strain and temperature.

2.3.1 Effect of Environment

The nature of the environment is an important prerequisite for SCC. Although SCC has been observed to occur for a wide range of pH values and corrosion potentials, for any specific material, SCC occurs for a limited pH and potential range.

Table 2.1 summarises some of the known alloy and environment combinations that produce SCC.

Table 2.1: **Alloy and Environment Combinations that pProduceing SCC [5]**

Alloy	Environment
Carbon steel	Hot nitrate, hydroxide, and carbon/bicarbonate solutions
High strength steels	Aqueous electrolytes, particularly when containing H_2S
Austenitic stainless steels	Hot, concentrated chloride solutions; chloride contaminated steam
High nickel alloys	High purity steam
α brass	Ammoniacal solutions
Aluminium alloys	Aqueous Cl^-, Br^-, and I^- solutions
Titanium alloys	Aqueous Cl^-, Br^-, and I^- solutions, organic liquids, N_2O_4
Magnesium alloys	Aqueous Cl^- solutions
Zirconium alloys	Aqueous Cl^- solutions, organic liquids, I_2 at $350°C$

High strength steels [25], [26] are susceptible to SCC in aqueous environments, pure water, humid air

and humid air containing H_2S. In other words, in any environment where atomic hydrogen can be formed and enter the steel.

Kortovich [27] showed that hydrogen embrittled high strength steel had behaviour similar to steel tested under conditions where the hydrogen was continuously generated at the specimen surface and found that they were directly comparable. Hydrogen diffusivity measurements and insensitivity of the crack growth rate and incubation time to specimen thickness indicated that the stress corrosion process was dictated by the electrolyte-metal surface reactions. This indicated that the same embrittlement is caused, if the hydrogen is liberated continuously at the metal surface, or if the hydrogen was inside the steel at the start of the test.

2.3.2 Effect of Material Properties

An important material property is the yield strength. A rock bolt with a higher yield strength has a greater safety margin to resist rock movement. As a consequence, there has been a trend to use rock bolts with increased yield strength. However, the work of Speidel [28] has shown that higher yield strength means a lower resistance to SCC. Figure 2.13 and Figure 2.14 show that increasing yield strength correlates with increasing SCC growth rate for different steels, and the same conclusion is drawn from the stage II crack growth data of Figure 2.15 which shows the relationship between the stress intensity factor and stress corrosion crack growth rate of various high strength steels. Studies on high strength steels [29], [30] suggest that this increased susceptibility can be due to such microstructure features as grain boundaries or carbides facilitating the trapping of hydrogen. This agrees with the work of Magdowski and Speidel [3] who have shown that increasing carbon and sulphur contents increase the SCC growth rate of steels of similar yield strength as shown by Figures 2.16 and 2.17. This suggests that sulphur and carbon are hence likely to change the microstructure as to include more efficient hydrogen traps.

Another important material property is fracture toughness (K_{Ic}). K_{Ic} represents the ability of a material to withstand crack propagation. The fracture toughness of a material can depend on temperature and the loading rate. Ductile materials tend to be tough, requiring more energy to fracture than brittle materials. The rock bolts studied in this thesis fail in a ductile manner under tensile loading in air, but undergo brittle cleavage fracture in service when there is a SCC present, even at room temperature.

At low temperatures, the overload fracture surface of a material under tensile load can fail in a brittle manner. The temperature at which the overload surface would change appearance is called the ductile to brittle transition temperature. A fast loading rate (such as impact loading) increases the transition temperature of a material [31]. For this thesis, rock bolt steel samples have failed in a brittle manner after being struck immediately after immersing in liquid nitrogen (described in Section 4.1.3) or in the tests where there were SCC cracks.

One possible solution that has been suggested to solve the problem of premature rock bolt failure is to use steels with higher fracture toughness. Such a steel would have a larger critical crack size, so that the rock bolt would have a greater lifetime associated with the phase of slow growth of the subcritical crack

until the crack reached a critical crack size, hence increasing the rock bolt service lifetime. Section 8.1.3 in this thesis further discusses the implications of increased fracture toughness of rock bolts.

2.3.3 Effect of Strain and Stress

A tensile stress is another requirement for SCC, together with a susceptible material and a suitable environment.

The stress may pull apart the crack, so that the electrolyte can reach the crack tip. Hence the corrosive can reach the active surface and cause the corrosion process. Furthermore the tensile stress may cause a passive/protective layer to fracture and expose a fresh metal surface. Such an anodic dissolution mechanism is dependent on the balance between the rate of film rupture (by the applied plastic strain rate) and the passivation rate. Immediately following exposure of a fresh surface, passivation starts to occur. If the passivation rate is too fast, the crack cannot grow. Conversely, if the passivation rate is too slow, the crack is blunted.

For SCC, there is a range of stresses that allow SCC. If the stress is too large (above tensile stress), the material undergoes ductile failure. On the other hand, if the applied stress is too low, the material undergoes general corrosion. The stress at which SCC starts is the threshold stress. The threshold stress is probably related to the production of sufficient plasticity to expose sufficient fresh surface at the crack tip.

Previous studies have shown that pre–straining a sample before testing has increased SCC resistance. When the material has been cold worked, a greater stress is needed to produce sufficient plasticity. Similarly, pre-creep was found to increase the time to fracture and the threshold stress [32].

2.3.4 Effect of Temperature

The influence of temperature depends on the nature of the process at the SCC crack tip. A higher temperature may mean higher corrosion rates since there is more energy available to speed up any thermally activated process. Nelson and Williams have shown that this is also applicable to SCC [33]. This temperature acceleration often follows the Arrhenius equation:

$$k = Ae^{-E/RT} \tag{2.5}$$

where A is the frequency factor, E is the activation energy, R is the Universal Gas Constant and T is the absolute temperature [34].

Nelson and Williams showed that there was such an acceleration of the crack growth rate at a constant stress concentration for 4130 steels of different strengths in gaseous hydrogen, as shown in Figure 2.18 up to some maximum whereafter a further increase of temperature caused a decrease in crack growth rate. Clearly there was a change in mechanism at the temperature of maximum crack growth. It can be clearly seen from this Figure that beyond a certain temperature the crack growth decreases. Oehlert [32] referenced Magdowski

[9] by stating that this has been attributed to a rate controlling step of reactions at the metal/environment interface indicated by the higher activation energy.

Magdowski and Spiedel [3] have shown that low alloy steels also have a critical temperature above which temperature decreased the stress corrosion crack growth as shown in Figure 2.19. If the temperature was further increased, the crack growth rate increased once again, most likely due to the increased corrosion rates and implied increased hydrogen production. Magdowski references Gerberich [35] by suggesting that this negative temperature effect may be due to the "detrapping" of hydrogen. The increased temperature aids the hydrogen in escaping the hydrogen traps in the microstructure and diffuse out of the material.

2.4 SCC OF ROCK BOLTS AND MEDIUM STRENGTH PEARLITIC STEELS

The available literature tends to deal with SCC in pearlitic steels in the building industry, mostly in the form of prestressed reinforcement (rebar) bars in concrete. The environment around the rebars tends to be alkaline due to the concrete encasing the steel. Hence, most SCC testing of pearlitic steels has been carried out in alkaline solutions [36]. This thesis set out to study service SCC of rock bolts, which has occurred in a largely unknown environment. Section 7.2 presents these results.

Pearlitic steels have some resistance to stress corrosion crack propagation because of the irregular lamellar nature of the pearlite colonies [37]. If a crack encounters a pearlite colony, which is aligned perpendicular to the crack direction, the crack can continue to propagate in one of two ways. It can go around the pearlite colony or overcome the forces involved in entering and traversing alternating cementite and ferrite crystals.

Toribio and Ovejero [38] showed that for pearlitic steels in the hot rolled condition, or with a slight amount of cold drawing, the fracture micromechanism produced the Tearing Topography Surface (TTS). This fracture surface is discussed in Section 6.2.3. The micromechanisms in intermediately cold drawn steels have been studied by Miller and Smith [39] and by Gerberich [40]. Miller and Smith identified shear cracking of the cementite lamellae. Once the lamellae have fractured, hydrogen could penetrate into the pearlite through the newly opened path and also through the ferrite. Gerberich postulated hydrogen enhanced delamination or debonding (HEDE). In HEDE, hydrogen permeates into the ferrite phase of the pearlite, thereby causing embrittlement. When enough hydrogen has entered the ferrite, consecutive cementite phases delaminate as illustrated in Figure 2.20. Figure 2.21 shows the action of the two micromechanisms acting on a steel with an intermediate amount of cold drawing.

In heavily drawn steels, the importance of HEDE is greater because the pearlite lamellae are highly oriented, hydrogen diffuses much faster along a pearlite colony than across the lamellae, and stress corrosion crack propagation is faster along the colony.

Pearlitic steels can be subject to general corrosion in service, or less frequently can be subjected to SCC,

which is the more catastrophic of the two processes. Narayan [41] did not find a relation between the anodic polarisation behaviour of eutectoid steels and their susceptibility to SCC. He did find that quenched and tempered wires were more susceptible than annealed wires.

Toribio and Lancha found that a material, subjected to an overload prior to service, had improved SCC properties. Their interpretation was that the overload induced residual stresses that delayed hydrogen adsorption into the material (as well as delaying the metal dissolution). They concluded that the overload can increase the life of a component in harsh environments [42],[43]. They also concluded that residual compressive stresses can delay the entry of hydrogen into the metal, and that the local strain rate in the vicinity of the crack tip (not the externally applied displacement rate) is the variable which governs the SCC process [44].

In a separate study, Toribio and Lancha [45] investigated the influence of cold drawing a pearlitic steel on its resistance to environmental cracking. They concluded that cold drawing pearlitic steel increased resistance to Localised Anodic Dissolution (LAD) but increased susceptibility to Hydrogen Assisted Cracking (HAC). Cold drawing increased the fracture load in the anodic regime, but lowered the fracture load in an hydrogen environment. In contrast, a hot-rolled steel, with no cold drawing, had a similar resistance to LAD and to HAC. Toribio and Vasseur have studied the fractography of SCC in pearlitic steels and have identified the different fracture modes, namely Tearing Topography Surface (TTS) and quasi-Micro Void Coalescence (qMVC). These morphologies are discussed in Section 5.1.3 and Section 6.2.5.

2.5 HYDROGEN TRAPPING IN HIGH STRENGTH STEELS

The resistance of steel to hydrogen embrittlement is strongly influenced by the interaction of hydrogen with the material. Microstructural heterogeneities (such as dislocations and microstructural features like carbides) could act as effective hydrogen traps. Pound [29] has shown a correlation between the intrinsic susceptibility, yield strength and observed resistance to hydrogen embrittlement in high strength martensitic steels. The decrease in intrinsic susceptibility with decreasing yield strength indicated a decrease in the irreversible trapping capacity, consistent with a change in the principal type of irreversible trap from matrix boundaries at high yield strengths to increasingly coarse carbides at lower yield strengths.

2.6 FIGURES

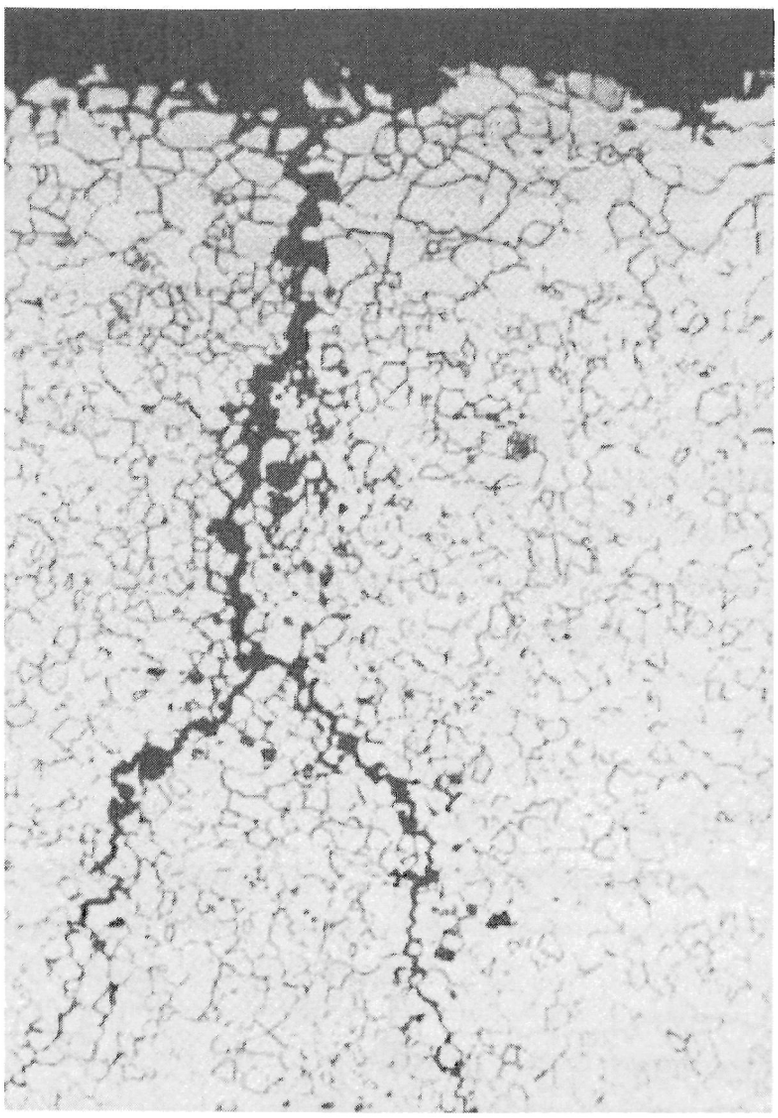

FIGURE 2.1: Intergranular SCC of a carbon steel that occurred in a concentrated ammonium nitrate solution (Nital etch 100x) [5].

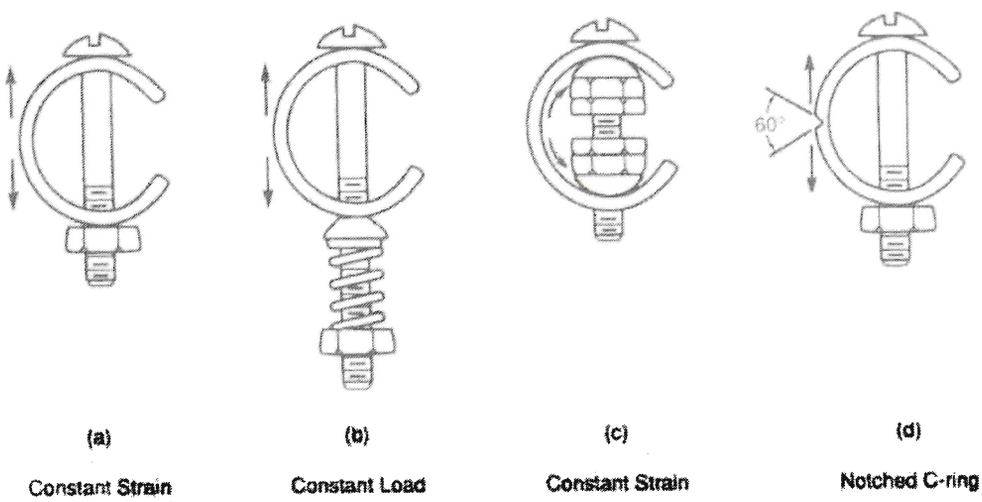

FIGURE 2.2: Methods of stressing C-rings [1].

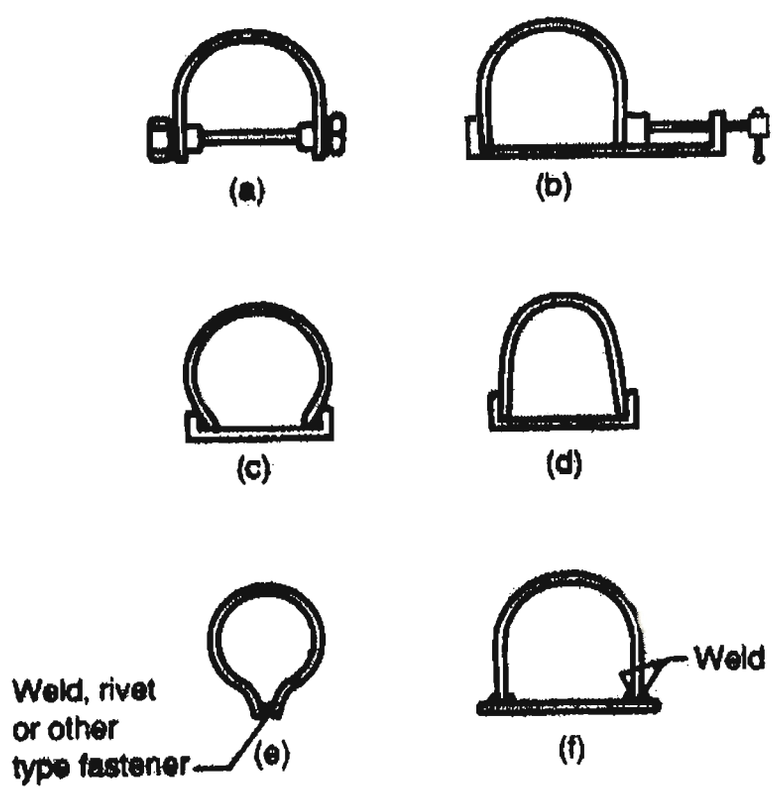

FIGURE 2.3: Methods of stressing D-rings [1].

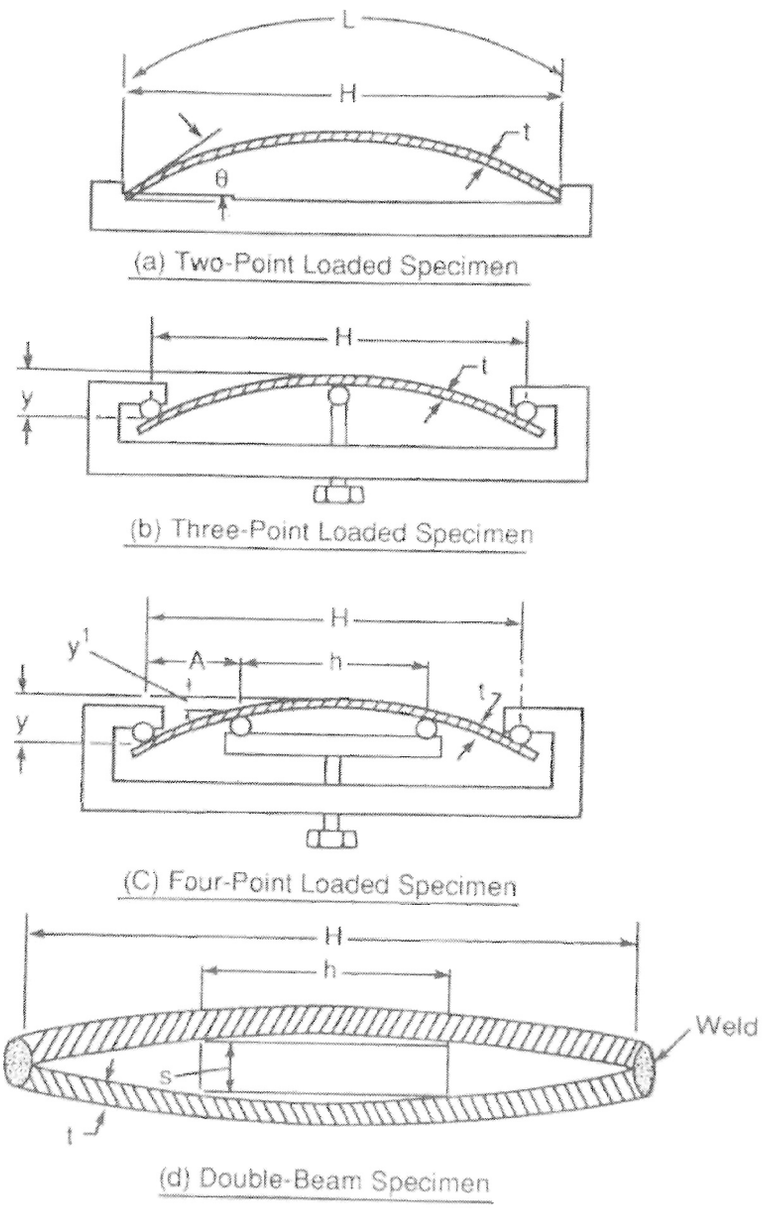

FIGURE 2.4: Methods of stressing bent beams [1].

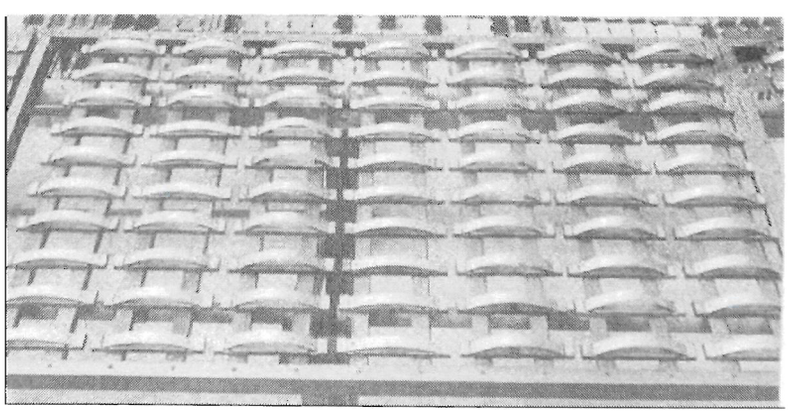

FIGURE 2.5: Bent beam specimens exposed to atmospheric conditions [1].

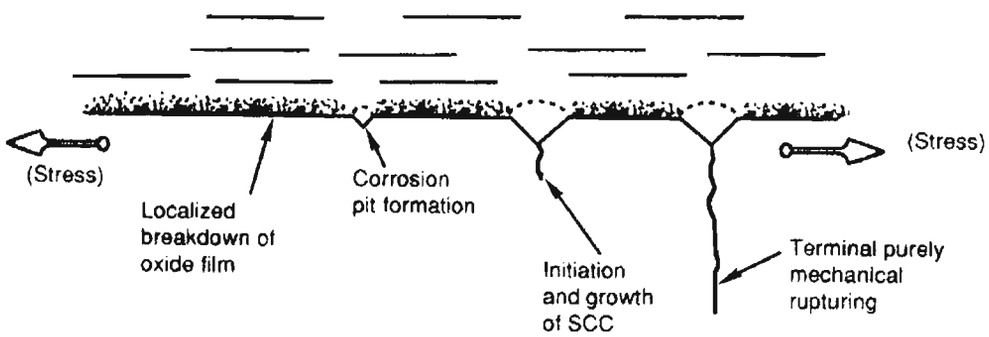

FIGURE 2.6: Sequence of events (left to right) in a stress corrosion test on an initially smooth specimen. For low alloy steels in sea water, the rate of growth of SCC is faster than it is for pitting by a factor of about 10^6, and fast fracture propagates at about 10^{10} times faster than SCC [1].

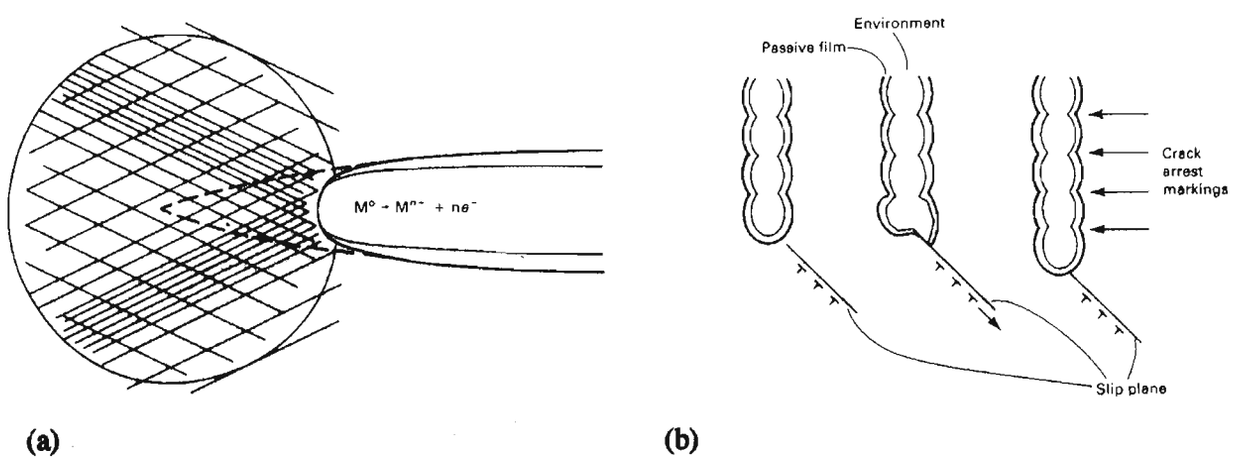

FIGURE 2.7: Schematic representation of crack propagation by the film rupture model. (a)Crack tip stays bare as a result of continuous deformation. (b)Crack tip passivates and is ruptured repeatedly (Jones [5] referencing Staehle [46], [47]).

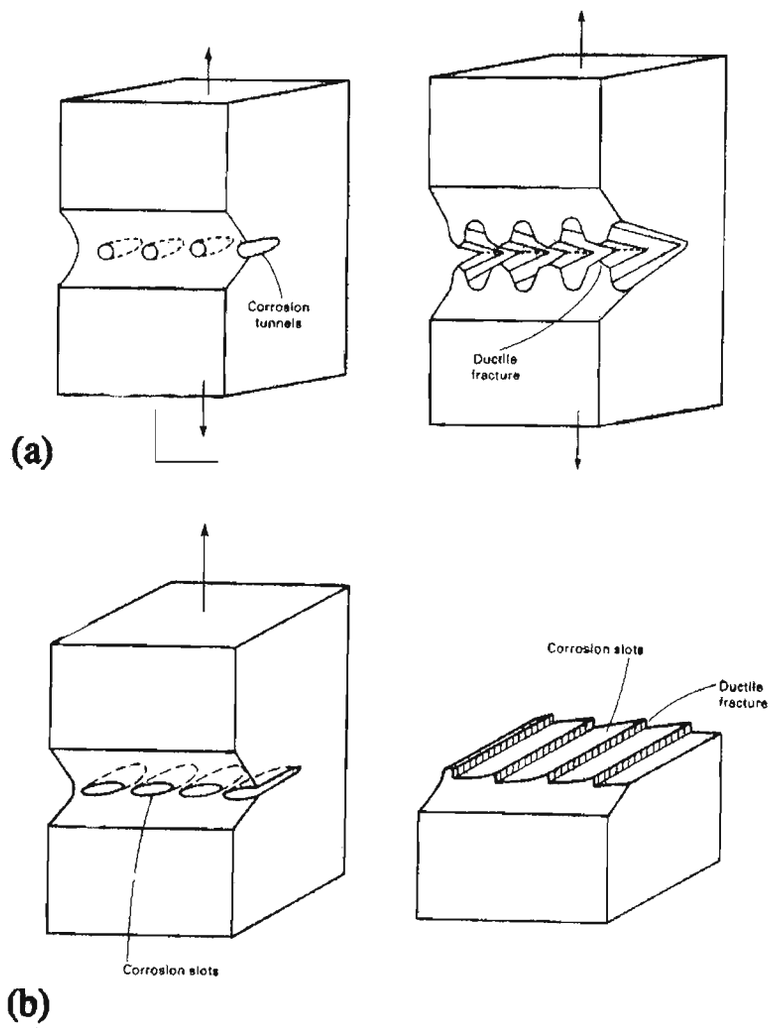

FIGURE 2.8: Corrosion tunnel models. (a) Schematic of tunnel showing the initiation of a crack by formation of corrosion tunnels at slip steps and ductile deformation and fracture of the remaining ligaments. (b) Schematic diagram of the tunnel mechanism of SCC and slot formation (Jones [5] referencing Silcock et al [48]).

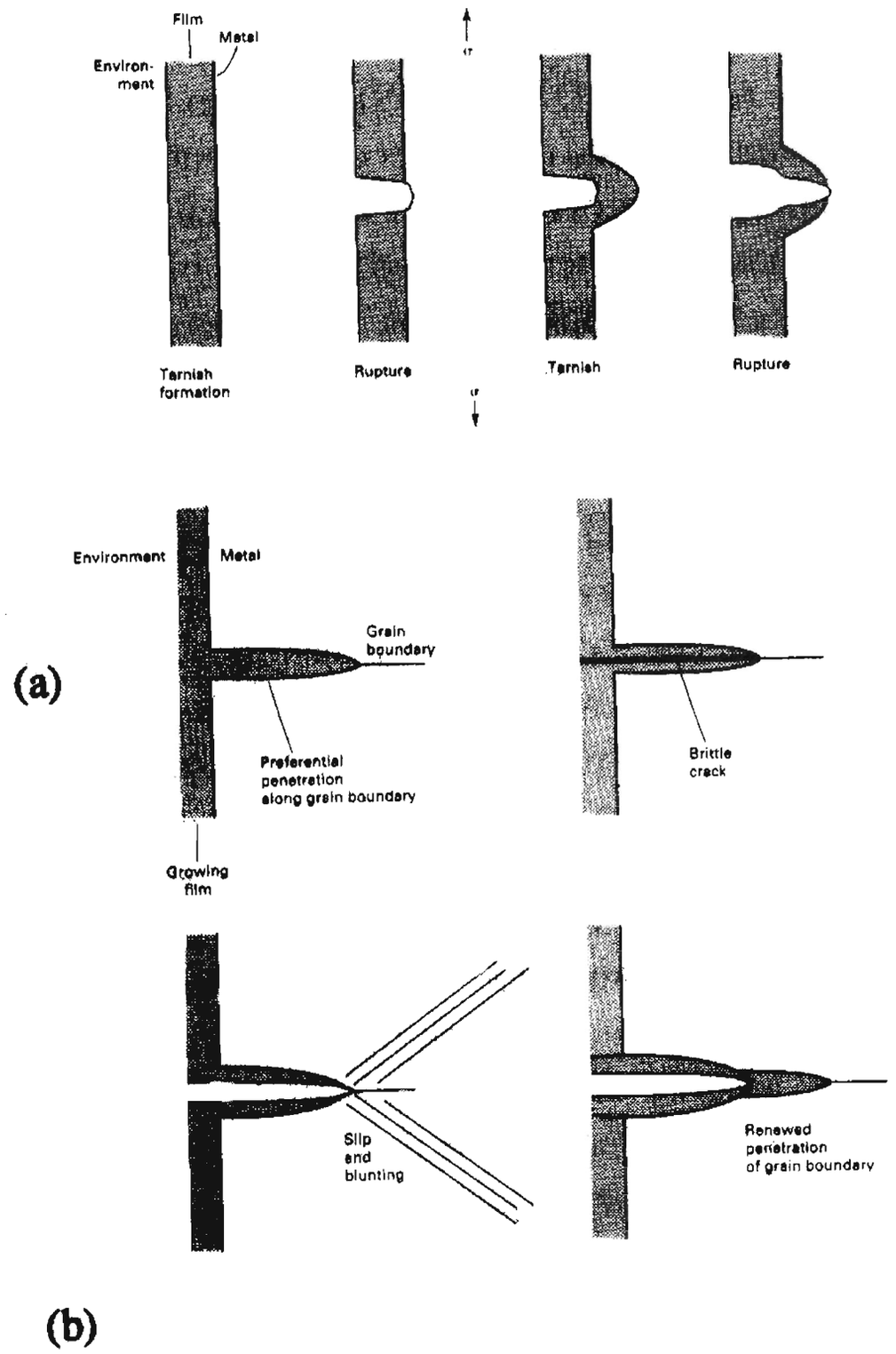

FIGURE 2.9: Tarnish rupture models. (a)Schematic of the tarnish rupture model for SCC. (b)Modified tarnish rupture model for SCC for systems with intergranular oxide film penetration (Jones [5]referencing Pugh [16]).

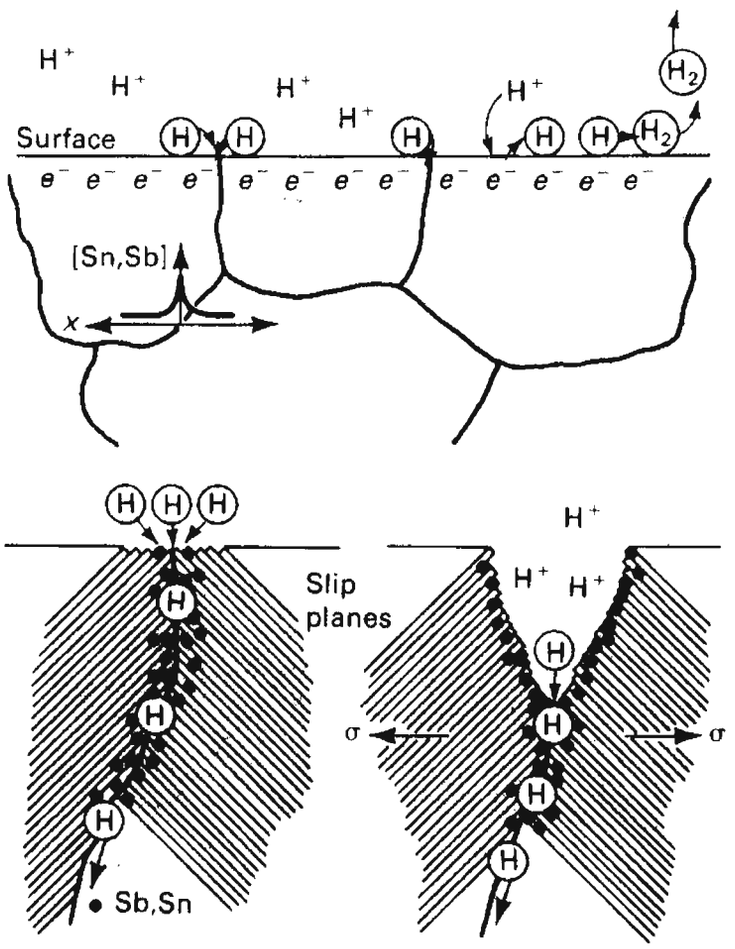

FIGURE 2.10: Schematic showing effect of some impurities on mechanism by which intergranular embrittlement of nickel is presumed to occur at cathodic potentials [5].

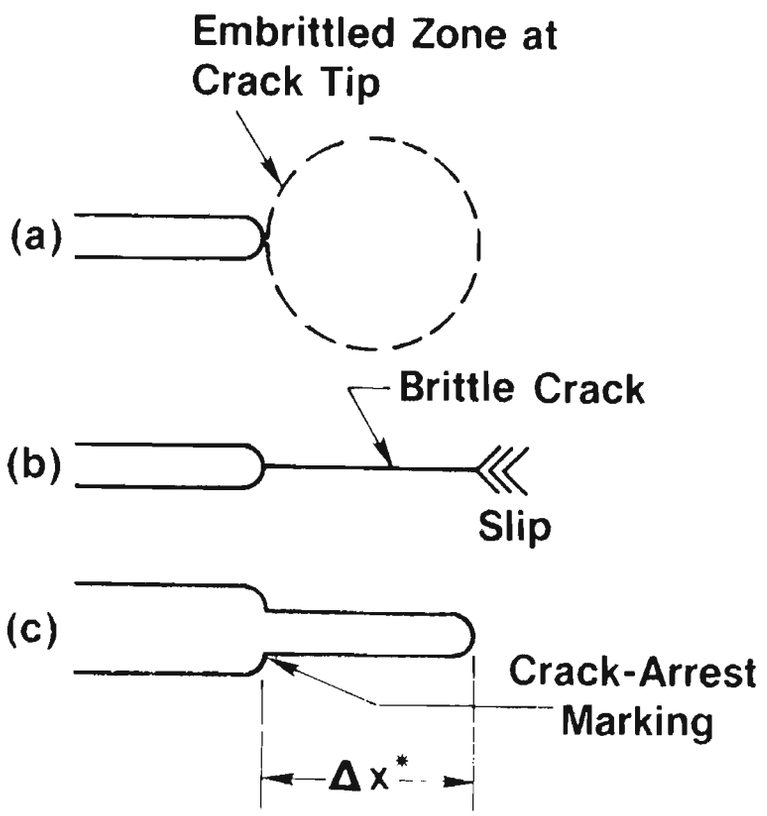

FIGURE 2.11: Schematic of the bulk embrittlement model for transgranular SCC. It is considered that the lattice ahead of the stationary crack front becomes embrittled by interaction with the solution, permitting the initiation of a cleavage crack. The latter is thought to be arrested by plastic deformation when it emerges from the embrittled region, producing a crack arrest marking on the fracture surface. The crack is thought to propagate discontinuously by repeated cycles of this process [21].

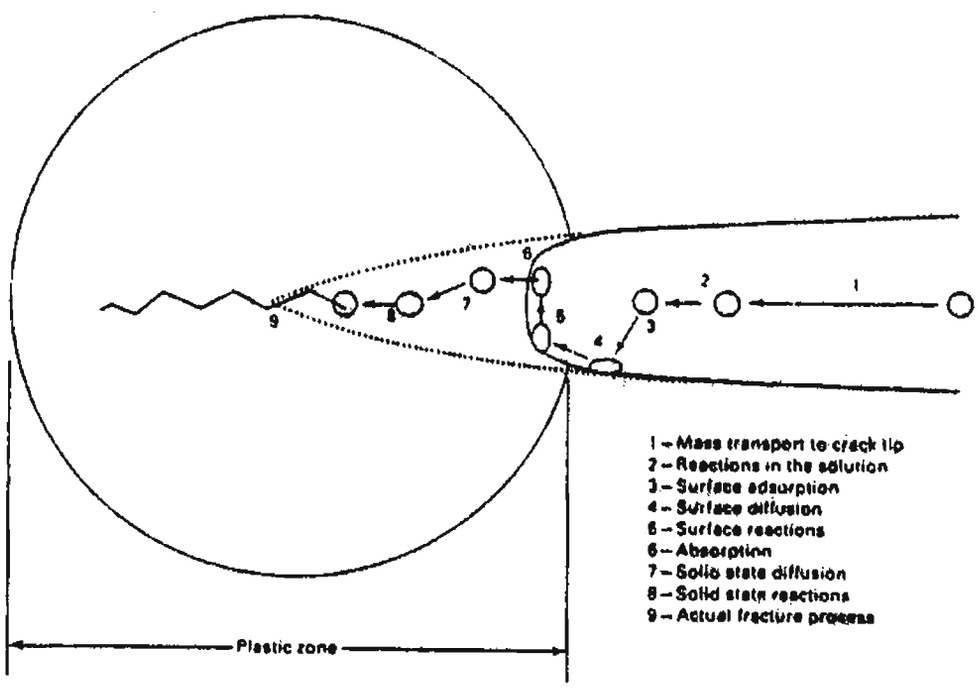

FIGURE 2.12: Schematic of crack tip processes that may be the rate determining step in environmentally assisted crack propagation. For this illustration, an internal hydrogen embrittlement mechanism is assumed [5].

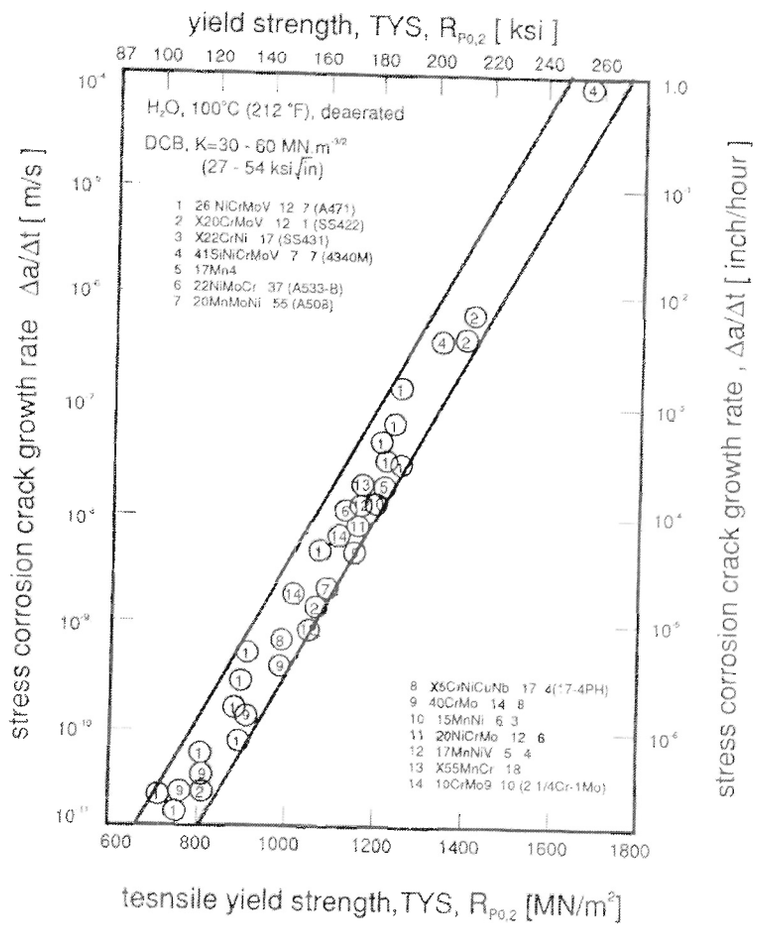

FIGURE 2.13: Increase of plateau stress corrosion crack velocity for high strength steels [2].

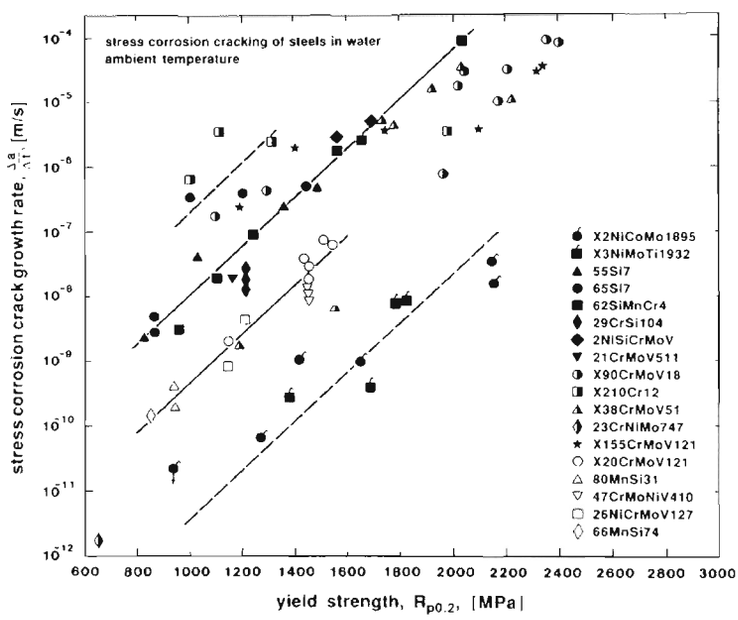

FIGURE 2.14: The effect of yield strength on the stress corrosion crack growth rates of various steels [3].

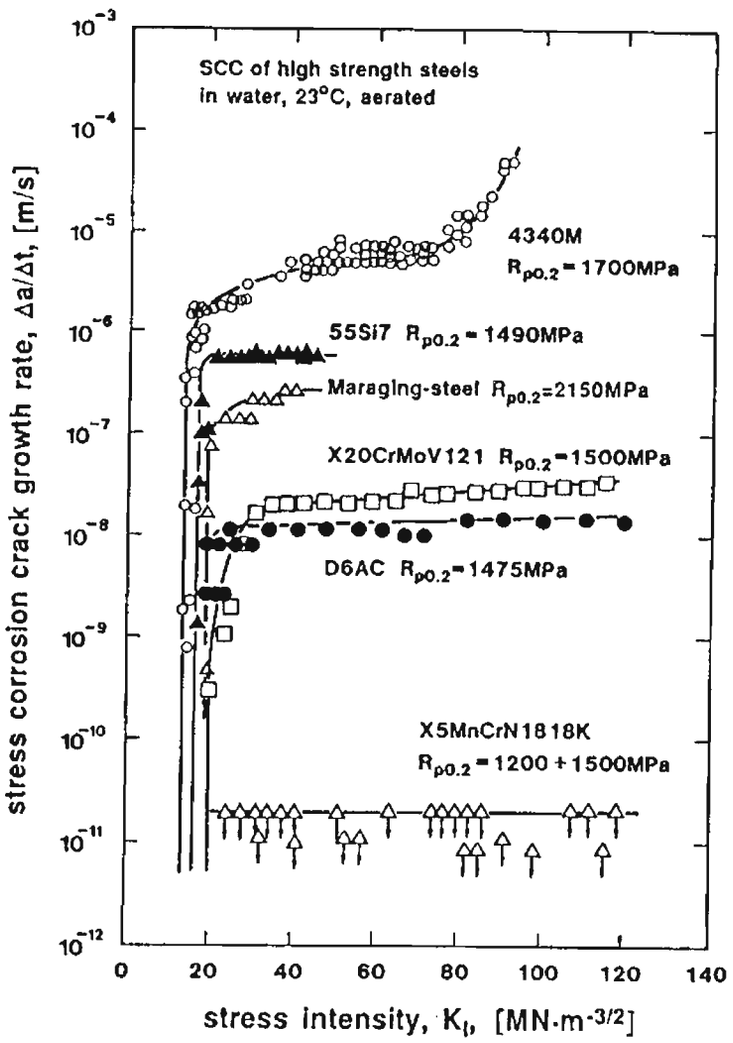

FIGURE 2.15: Stress corrosion crack growth curves of various high strength steels exposed to water at ambient temperature [3].

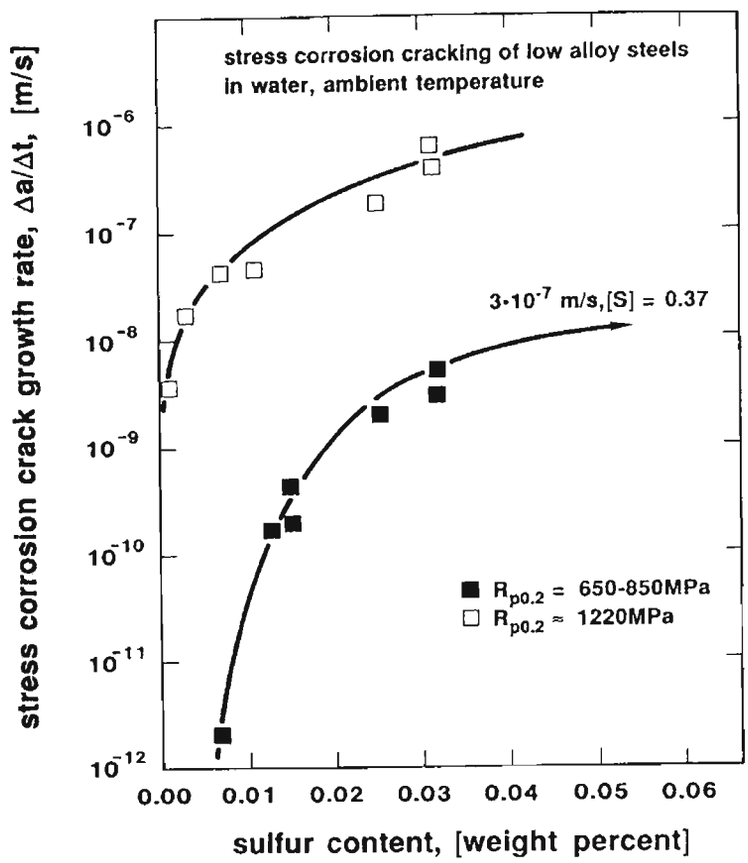

FIGURE 2.16: The effect of sulphur on the stress corrosion crack rates of low alloy steels in water at ambient temperature [3].

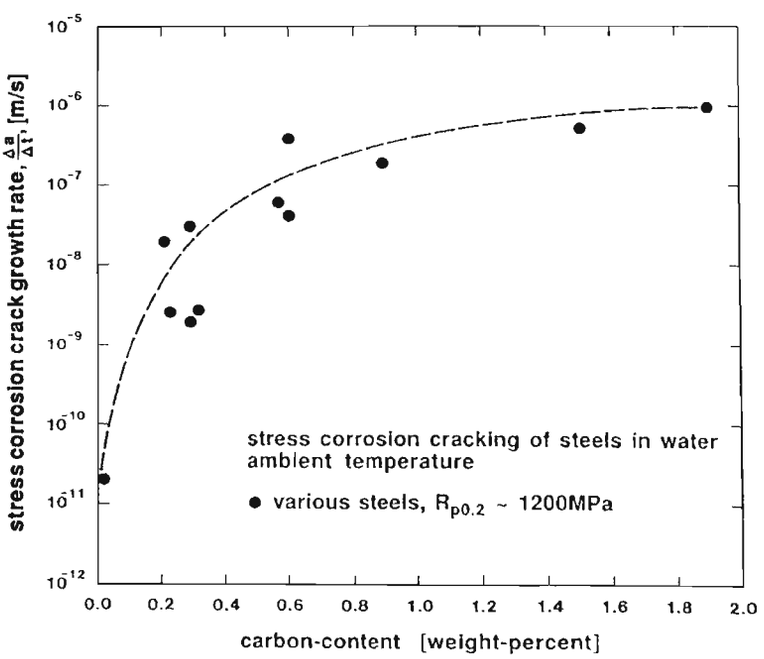

FIGURE 2.17: The effect of carbon on the stress corrosion crack rates of steels in water at ambient temperature [3].

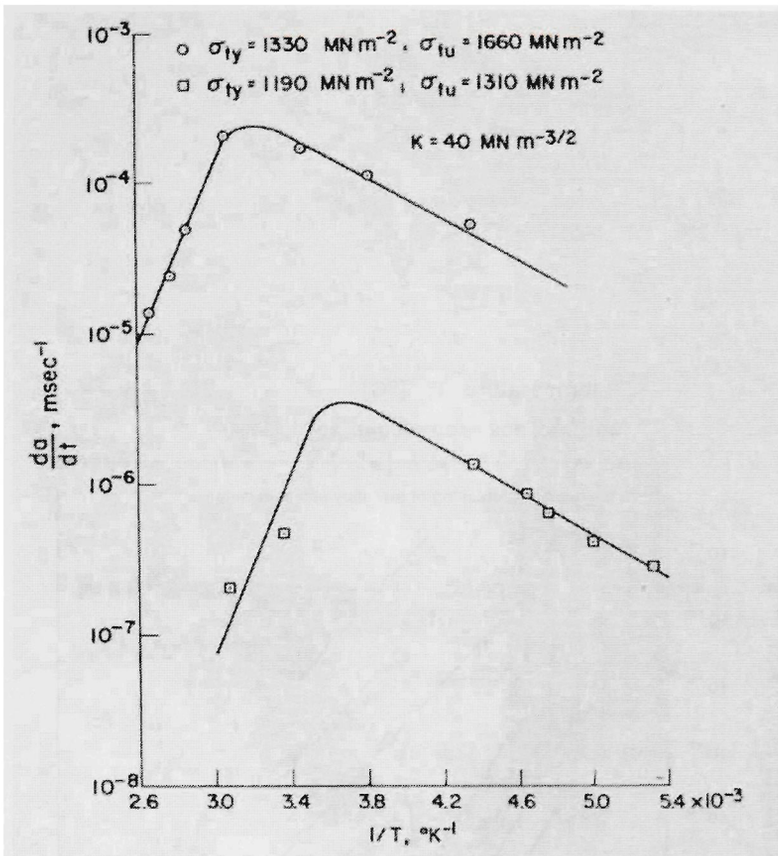

FIGURE 2.18: An Arrhenius plot of the temperature dependence of the crack growth rate at a constant stress intensity in 77.3 kNm^{-2} hydrogen for 4130 steel having yield strengths of 1330 and 1190 MNm^{-2} [33].

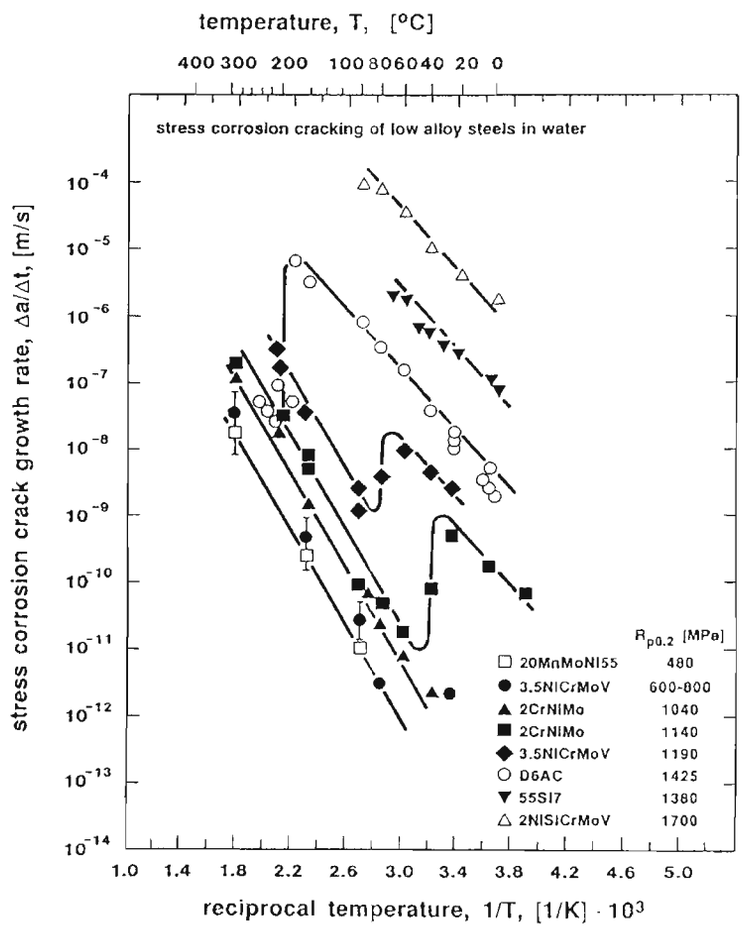

FIGURE 2.19: The effect of temperature on the stress corrosion crack growth rates of various quenched and tempered steels [3].

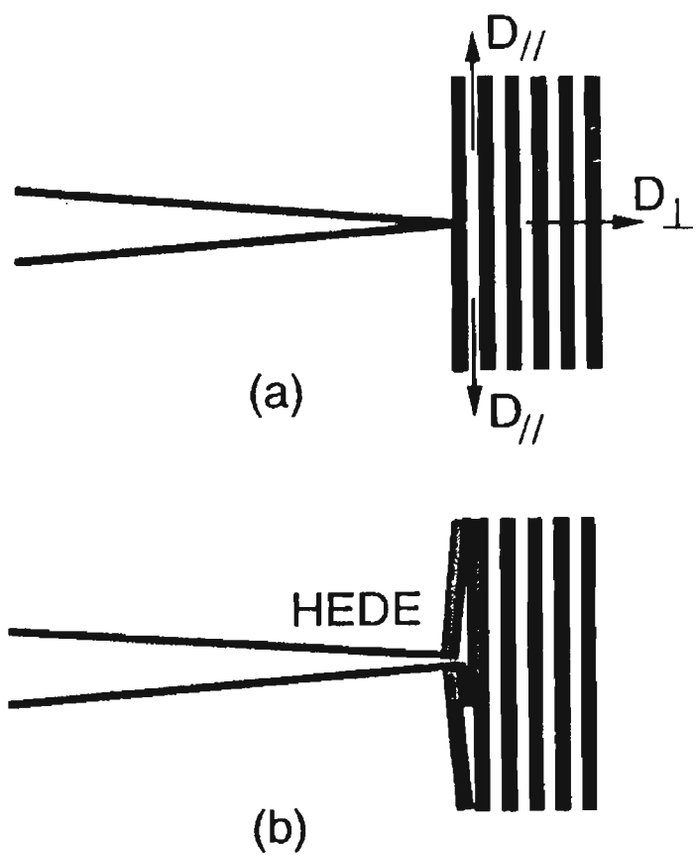

FIGURE 2.20: Micromechanical model of HAC in heavily drawn steels: (a) hydrogen diffusion in longitudinal and transverse directions; (b) fracture by hydrogen enhanced delamination or debonding (HEDE). The microstructure is assumed to be totally oriented in the cold drawing direction [38].

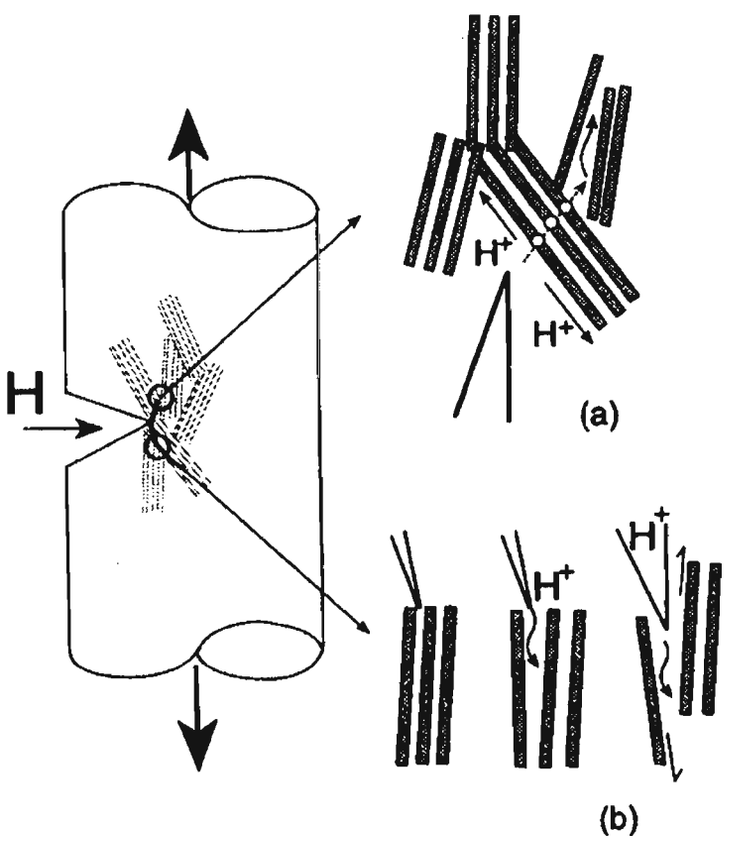

FIGURE 2.21: Micromechanical model of HAC in steels with an intermediate degree of drawing: (a) hydrogen diffusion in the pearlitic microstructure and penetration along the path opened by a Miller-Smith mechanism of shear cracking; (b) fracture by hydrogen enhanced delamination or debonding (HEDE) [38].

3

THESIS SCOPE

3.1 AIM/OBJECTIVE

Understand rock bolt stress corrosion cracking and test counter measures.

3.2 STRATEGY

A step in solving this service problem in the mining industry is to develop a laboratory SCC test to simulate service SCC in the laboratory, and then to use the laboratory SCC test to study the elements of the service problem. These are the aims of this project.

3.3 GOALS

1. Review state of the art and published literature.
2. Analyse bolt service failures.
3. Reproduce rock bolt SCC in the laboratory.

4. Study environmental conditions leading to rock bolt SCC:
    - pH values, corrosion potentials.
    - Chloride and sulphate ion concentration.
    - Applied stress.
5. Examine influence of rock bolt metallurgy.
6. Examine influence of rock bolt rib geometry.
7. Test countermeasures.

3.4 EXCLUSIONS

The scope of the thesis included mechanistic understanding to a sufficient level to be able to be confident that the failure mode in the laboratory SCC test did indeed simulate service SCC. This required testing to understand that the operative mechanism involved hydrogen. However, a study of the mechanism of hydrogen embrittlement was beyond the scope of research of this thesis.

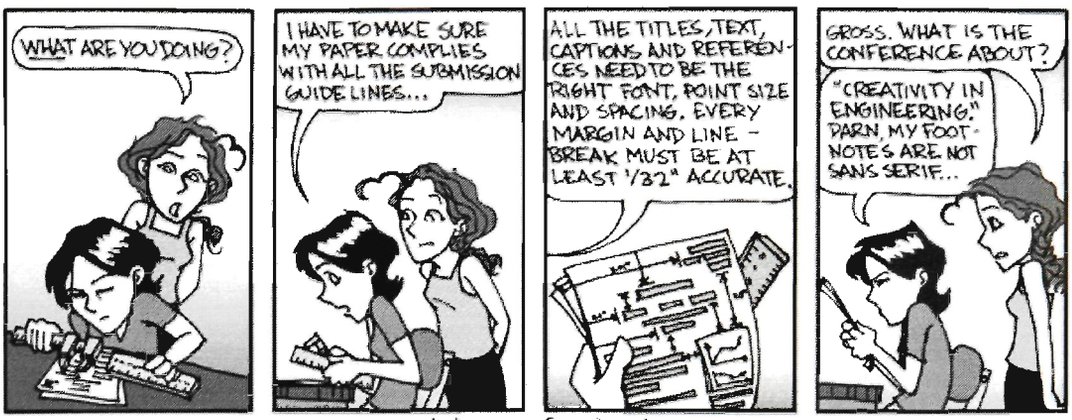

4

EXPERIMENTAL PROCEDURE

The research objectives were to develop a laboratory SCC test to simulate service SCC and to subsequently use the laboratory SCC test to evaluate: (1) the SCC tendency of rock bolt steels, (2) the contribution to SCC of the surface pattern and the surface state of the rock bolts as manufactured and installed, (3) the SCC tendency of different mine waters, and (4) countermeasures to rock bolt SCC.

The specification of a suitable laboratory SCC test includes the specification of all of the following:

- Specimen geometry, including crevices,
- stressing regime, including stress type and rate of stress application,
- environmental conditions including solution composition (both dissolved salts and dissolved gasses), pH and
- specimen electrochemical potential.

Moreover, it must be shown that the specimen failures produced by the laboratory test are equivalent to those produced in service.

This Chapter aims to provide details on the testing equipment, various methods used and the samples tested in this thesis.

4.1 LIST

The laboratory approach is based on the Linearly Increasing Stress Test (LIST) test [10]. The LIST test allows application of a linearly increasing engineering stress to a specimen exposed to the environment of interest as shown schematically in Figure 4.1.

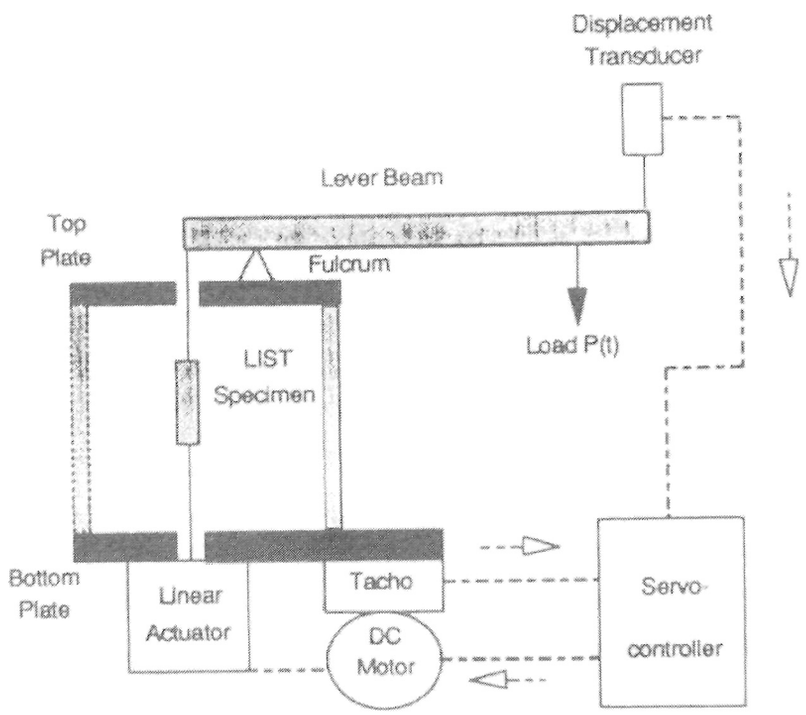

FIGURE 4.1: Schematic representation of the LIST apparatus

The load on the specimen is increased linearly by means of a lever principle and a moving load on the right hand side of the lever. The lever is maintained horizontal via a linear actuator and servo-controller by means of a displacement signal from the end of the lever arm. This testing method has been applied to high strength steels [49], copper [50] and pipeline steels [51]. The development of the SCC test involves the determination of the appropriate stress rate, the environmental composition, pH and electrochemical potential. To identify the environment causing the SCC requires a systematic evaluation of the alternatives starting with the most likely, and then carrying out a systematic search. The most likely environment can be approximated by the composition of mine waters at locations giving service SCC of rock bolts. Experience indicates that it is unwise to expect that the first test will reveal the right conditions. Rather, it is expected that several iterations will be required. However, until the correct conditions for SCC are identified, there is no possibility of being able to evaluate the relative SCC resistance.

4.1.1 Preferred Procedure

The apparatus is based on the principle of a lever beam. One side of the lever beam is connected to the specimen whilst the other side has a mass of 14 kg. Movement of the mass away from the fulcrum increases the load on the specimen. The applied engineering stress is calculated from the position of the mass at any time and the original cross section of the specimen.

The preferred LIST experimental procedure was as follows. A specimen was inserted into the environmental cell and connected to the loading arms. The environmental cell was filled with the desired electrolyte. The travelling mass was set in motion. Movement of the mass steadily transferred an increasing load onto the LIST sample. The mass was kept travelling until the sample fractured. All samples were loaded at 0.019 MPa s^{-1} (described in Chapter 6), indicated that the LIST test at this rate in the preferred sulphate solution reproduced in the laboratory the same type of SCC fracture as observed in service. After the LIST test, the fracture surfaces were examined by Scanning Electron Microscopy (SEM).

LIST samples were tensile samples with a gauge section of $\approx$ 20 mm x 3.5 mm x 2.5 mm. Figure 4.2 shows a dimensioned drawing of a LIST sample.

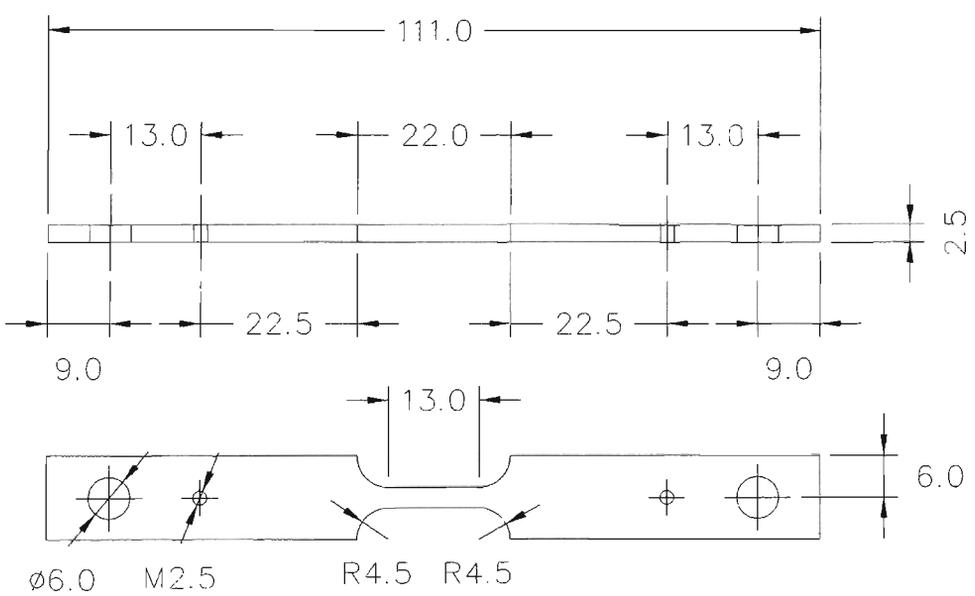

FIGURE 4.2: Technical dimensioned drawing of a LIST sample.

4.1.2 Metallurgies

LIST samples were machined from commercial rock bolts for five different steel metallurgies from actual rock bolt samples: 1355AX[1] steel, MAC steel, MA840B steel, 5152 steel[2] and 10M30 steel. Samples were

[1] 1355AX grade steel has the same chemical composition as 1355AXRC and 1355AXRO. 1355AX and 1355AXRC steels were obtained from the same manufacturer, whilst 1355AXRO was obtained from a different manufacturer.

[2] 5152 steel has the same chemical composition as 5152CW10D and 5152CW55 steels.

also machined from 304 stainless steel plate. Table 4.1 gives typical values of the chemical compositions of some of these steels. Table 4.2 gives typical values for ASTM grain size (D) and mechanical properties.

Table 4.1: **Rock Bolt Metallurgy (%)**

Grade	C	Si	Mn	P	S	Ni	Cr	Mo	Al	V
1355	0.54	0.26	1.63	0.017	0.027	0.09	0.08	0.03	0.004	0.003
5152CW10D	0.54	0.10	0.90	0.015	0.025	0.35	0.9	0.1	-	-
10M30	0.29	0.24	0.72	0.015	0.026	0.14	0.11	0.03	-	0.053
MA840B	0.37	1.05	1.46	0.013	0.009	0.01	0.02	0.01	0.004	0.043
MA810	0.36	1	1.4	0.021	0.013	0.01	0.02	0.01	0.005	0.04
MAC	0.25	0.36	1.32	0.016	0.027	0.07	0.05	0.01	0.005	0.21
304	0.044	0.41	1.24	0.023	0.005	8.11	18.21	0	-	-

Table 4.2: **Typical ASTM Grain Size (D) and Mechanical Properties of Rock Bolts**

Grade	D μm	YS (MPa)	UTS (MPa)	Elongation %	Reduction of Area %	YS/UTS	CVN
1355	75	622	954	18.0	37.9	0.65	6
5152CW10D	-	745	890	12.0	-	0.84	-
10M30	-	400	670	22	-	0.60	-
MA840B	65	635	873	22.2	50.3	0.73	18
MAC	43	689	838	21.4	52.2	0.82	29
304	-	337	667	48	-	0.51	-

The 1355AX steel is one of the higher carbon and manganese content steels studied (0.54% and 1.5% respectively) and has the highest UTS value (954MPa). The steel is made from scrap steel and Sullivan (1998) indicated that it contains residual elements such as Cr, Si, Ni, Cu and Mo. A computer program is used to modify the Mn content of the melt according to the contents of the Cr, Si, Ni, Cu and Mo residuals, so that the steel has a 650 MPa minimum Yield Strength with no heat treatment. The steel has a nearly fully eutectoid microstructure as shown in Figure 4.3.

The next strongest bolt (5152CW10D) has the same carbon content as the 1355AX, but its UTS is slightly lower (890 MPa). Trace element composition between these bolts is different. Strengthening of the 5152CW10D is produced by approximately 10% cold working the 5152 steel.

The MAC and the MA840B bolts were from microalloyed steel that have a lower carbon content (0.25 and 0.37 % respectively), a substantial microalloy content (V) which is used to control the fine austenite grain size during hot working, a lower UTS value (873MPa and 838 MPa) and a slightly higher Charpy V-notch impact energy (CVN values in Table 4.2).

304 stainless steel (σ_y = 337 MPa and UTS = 667 MPa) was the commercially available stainless steel.

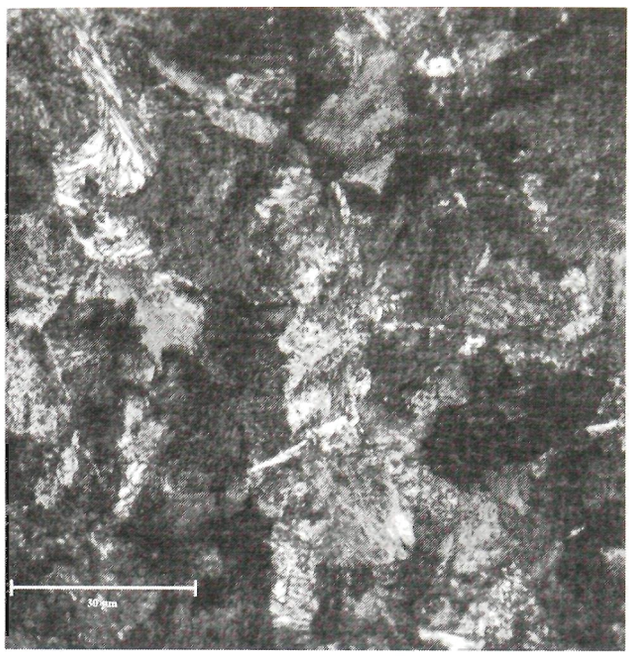

FIGURE 4.3: 1355AX microstructure

It was used to test this steel as a possible countermeasure.

10M30 steel grade AS1442/10M30 (σ_y = 375 MPa and UTS = 690 MPa) was manufactured from a special hot rolled deformed bar similar to the AX, MAC and MA840B bolts. Only the threading is cold rolled.

The SCC tendency of galvanised rock bolts was evaluated using LIST samples of 1355AX, that were hot dipped galvanised to have a 100 μm zinc layer. Galvanised specimens were subjected to a preferred LIST test in the sulphate pH 2.1 solution.

4.1.3 Constant Stress Test (Threshold Stress Determinations)

The threshold stress was determined using a modified LIST test. The mass was stopped at a predetermined position and the specimen was held at a constant stress for 3 days in the preferred sulphate pH 2.1 solution. If the sample did not fail by the end of the three day period, it was removed from the LIST apparatus, cooled to the temperature of liquid nitrogen at -197°C by immersion in liquid nitrogen, quickly withdrawn from the liquid nitrogen, clamped in a vice and struck with a hammer, breaking the sample into two pieces at the thinnest part of the test section. The liquid nitrogen was used to cool the sample so that it broke in a brittle manner. Breaking the sample at room temperature caused ductile tearing which distorted the fracture surface, masking subcritical cracks if any were present. The fracture surface was observed with SEM to determine the failure mode of the sample, and in particular whether a stress corrosion crack had formed. If no SCC crack was found, it indicated that the stress was below the threshold stress for SCC. For the interrupted experiments, the sulphate pH 2.1 solution was used in all cases.

4.1.4 Potential Drop Test

The potential drop technique used in the present investigation was the same as used in prior work [10], [49], [51] to measure the initiation stress in high strength steels and pipeline steels. However, in the present work, this technique did not prove to be reliable, and interrupted tests were carried out in the sulphate pH 2.1 solution in order to measure the initiation stress.

The electronic noise was comparable to that of the sample, hence the results became indistinguishable from the noise.

4.1.5 Potential Control

The LIST specimens had a free corrosion potential of -350 mV(SHE) in the preferred sulphate pH 2.1 solution. E_{corr} measurements of the samples was carried out using a Wenking model PGS 81 potentio-galvano-scanner. The electrode used was a silver / silver chloride (Ag/AgCl) electrode with a potential of +200 mV vs SHE. The potentio-galvano-scanner was also used to apply a desired potential on the system. The rest potential of the samples was taken after two hours' immersion in the sulphate solution. The pH of the solution was changed between the values of 1.4 and 12.5 in order to measure the corrosion potential at varying pH levels.

4.1.6 Electrolyte

All solutions were made using reagent grade chemicals and distilled water. Two preferred solutions were used: chloride based and sulphate based. These might be characteristic of two different chemistries that might be found in underground water samples at mine sites. The following provide the details of these two preferred solutions:

- *Sulphate pH 2.1 solution.* This contained 300 ppm sulphate, 100 ppm chloride and 100 ppm carbonate. This solution was made up as follows: 1.6543 g H_2SO_4, 0.3285 g NaCl and 0.5959 g Na_2CO_3 was dissolved in distilled water to make up 1000 mL of solution. The pH of this solution was measured to be 2.1. This solution is designated as "sulphate pH 2.1"

- *Chloride pH 1.8 solution.* This contained 1400 ppm chloride, 300 ppm sulphate and 100 ppm carbonate. This solution was made up as follows: 1.6543 g H_2SO_4, 4.6056 g NaCl and 0.5959 g Na_2CO_3 was dissolved in distilled water to make up 1000 mL of solution. The pH of this solution was measured to be 1.8. This solution is designated as "Chloride pH 1.8"

All tests were carried out at room temperature.

4.1.7 Modified Electrolyte

The modified environments used to study the effects of the environment on the SCC properties were as follows:

- CO_2 gas bubbled through the sulphate pH 2.1 solution for the duration of the experiment (to study the influence of deaeration)
- Air bubbled through the sulphate pH 2.1 solution for the duration of the experiment with carbon being coupled to the LIST sample (to study the effects of a more positive corrosion potential)
- Sulphate pH 2.1 solution with increased concentration, by concentrating the base solution by 10x, 100x and 1000x of the sulphate pH 2.1 solution
- Sulphate solution with the same concentration as the preferred solution, but with the modified pH values of 4.2, 6.3 and 9.4
- Sulphate pH 2.1 solution with applied electrochemical potential of E_{corr} + 100 mV, E_{corr} + 150 mV, E_{corr} 100 mV and E_{corr} 300 mV
- Sulphate pH 2.1 solutions concentrated to 100x, at the modified pH value of 6.16 and E_{corr}, pH 6.6 and E_{corr} 300 mV, pH 6.6 and E_{corr} 500 mV
- Sulphate pH 2.1 solution with modified pH and applied electrochemical potential as follows: (a) pH 6.2 E_{corr}, (b) pH 7.3 E_{corr} 300 mV, and (c) pH 7.5 E_{corr} - 570 mV
- CO_2 gas bubbled through the chloride pH 1.8 solution for the duration of the experiment
- Air bubbled through the chloride pH 1.8 solution for the duration of the experiment with carbon coupled to the LIST sample (to study the effects of a more positive corrosion potential)
- Chloride pH 1.8 concentrated by 100x with unmodified pH (1.8)
- Chloride pH 1.8 base solution with pH modified to 3.1, 7.7 and 10.7

The pH was modified when required by adding NaOH for a more basic solution or H_2SO_4 for a more acidic solution.

4.1.8 Preparation of Fracture Surfaces

Rock bolts were photographed at a macroscopic scale, to record the as received condition, any carbon deposits on the surface and any bending of the bolt due to shear forces. Subsequently, the rock bolts were cut 10 mm below the fracture surface. In order to remove surface oxide products and other surface contaminants, the samples were cleaned using a solution of 5% EDTA (Ethylenediaminetetra acetic acid disodium salt

solution). Cleaning in the EDTA solution for 15 minutes was necessary to remove all contaminants and surface oxides. In later samples, the cleaning time in EDTA was reduced to three minutes. Samples were then mounted on aluminium stubs for analysis using SEM, and were initially given a carbon coating to provide a more conductive surface, to prevent charging during SEM observation and consequently to provide better SEM observations.

LIST samples were prepared for fractographic analysis in a similar manner. Samples fractured in the LIST apparatus were cut 10 mm below the fracture surface and cleaned in EDTA, dried and mounted on the aluminium stubs.

Samples were stored after analysis in dehumidifiers to prevent surface corrosion.

All fracture surfaces (SCC and fast brittle areas) cleaned for 15 minutes in the 5% EDTA solution displayed small pits, distributed randomly throughout the surface. These pits were generated by the surface preparation process. A sample cleaned for 3 minutes in the EDTA solution did not have pits, but there were still remaining deposits of contaminants and surface oxides. The extent of these deposits were greatly reduced by the cleaning. Further work showed that an immersion time of one minute was enough to thoroughly clean the SCC region but not long enough to start causing pits on the fracture surface.

Carbon coating the samples was also discontinued since it was found that the samples tended to corrode after several weeks. Since the sample material itself was highly conductive, it was decided not to carbon coat the samples as it was better to preserve the samples. The consequence was the loss of some quality in the SEM micrographs.

4.2 GEOMETRY

In order to study the effects of bolt surface geometry, modified LIST samples were used in the preferred sulphate pH 2.1 solution. These samples were similar to the standard LIST sample, except the geometry samples were machined from the edge of the rock bolts such that one face was the free surface of the bolt, including the ribs. Due to the limited space available for mounting samples in the LIST apparatus, these geometry samples were thinner than their standard counterparts. The test gauge section was also made thinner to ensure that samples fractured in the test section rather than at the ends, where dowels connected the sample to the apparatus. The back of the geometry samples (the machined side) was coated so that only the free surface of the bolt was exposed to the electrolyte. Figure 4.4 compares a standard LIST sample (top) to a geometry sample (bottom). The recessed test section helping reduce the test section area can be seen in the geometry sample.

Geometry samples were machined out of two different regions within the same bolt; one region included the vertical rib running along the length of the bolt (placed in the middle of the geometry LIST sample), whereas the other had the plain ribs running in a helical form around the bolt. Figure 4.5 compares the various geometries. The top sample is the standard LIST sample. The middle sample shows the helical ribs,

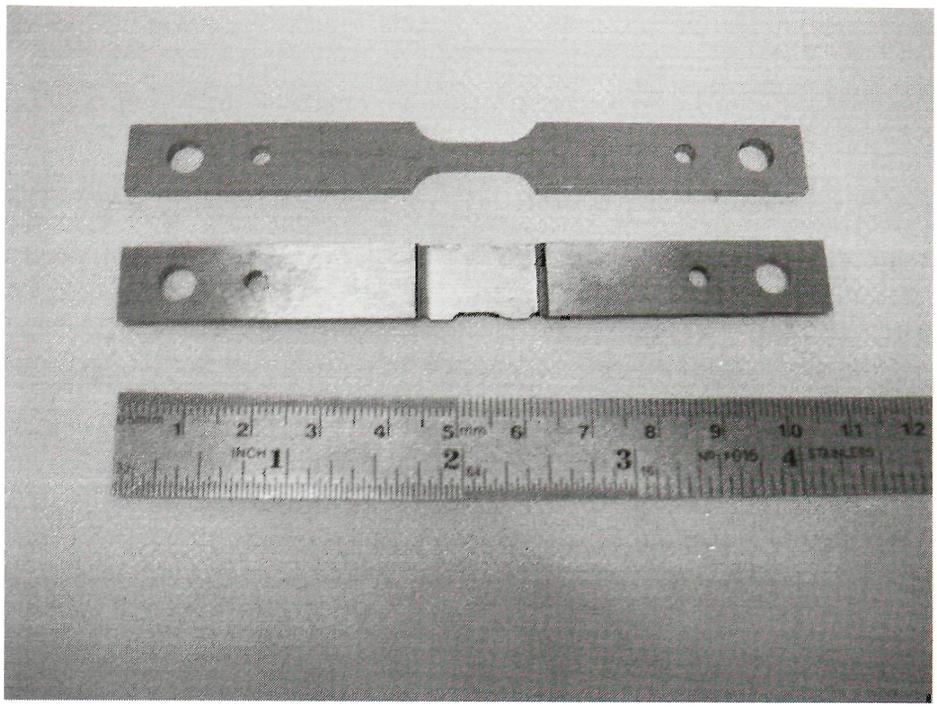

FIGURE 4.4: Comparison between standard and geometry LIST samples.

while the bottom sample shows the vertical rib running along the length of the bolt.

Rock bolt rib geometries were compared between 1355AXRC, 1355AXRO and 1355AX bolts. AXR bolts have a higher rib profile than AX bolts, although the profile of the AXR bolts vary between manufacturers. Bolt profiles are shown in Figure 4.6.

Samples were tested first by the preferred method (increasing the load linearly until failure). Together with tensile testing data, stresses were calculated for constant load tests. Tests were then performed at a constant stress as described in Section 4.1.3, except the holding time was increased to eight days rather than three.

4.3 FRACTURE TOUGHNESS

Fracture toughness samples were prepared in order to estimate the fracture toughness of the 1355AX bolts. Fracture toughness samples were machined out of rock bolts. The diameter of the rock bolts was the size limiting factor. Figure 4.7 shows the dimensions of a machined sample.

Section 7.1.3 from the Standard E399-90 provides a guideline for specimen size. Using $E = 190$ GPa and $\sigma_{ys} = 650$ MPa gives a minimum recommended thickness and crack length of 7.5 mm. Using a conservative estimate of $K_{Ic} = 30$ MPa$\sqrt{m}$, plane strain criteria (Equation 8.8) specifies that crack size is less than the

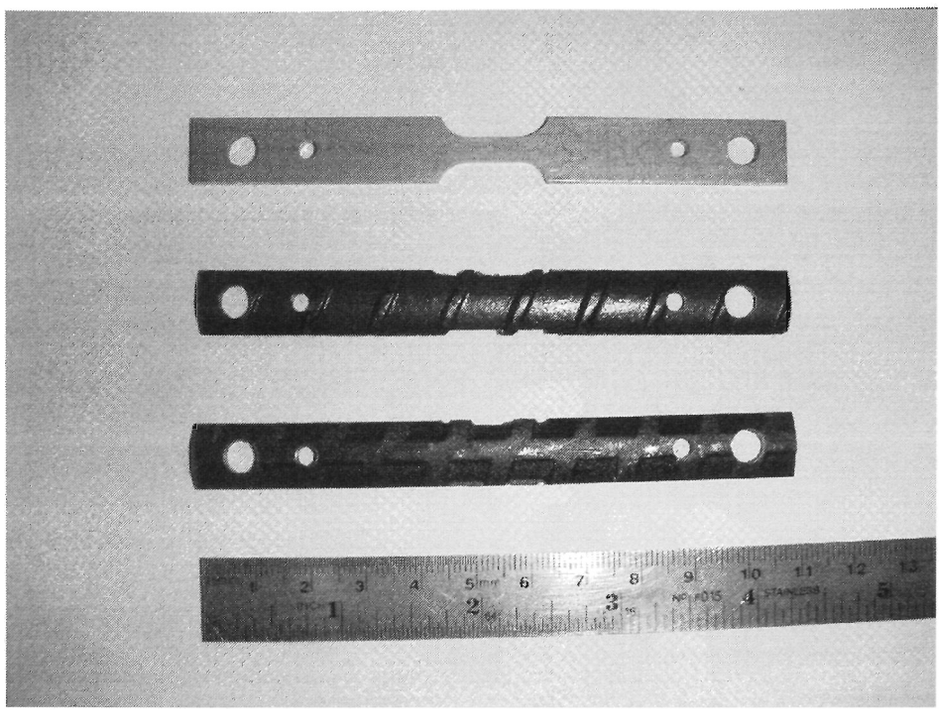

FIGURE 4.5: Varied geometry LIST samples. A- Standard LIST sample. B- Geometry sample without vertical side rib. C- Geometry sample with vertical side rib.

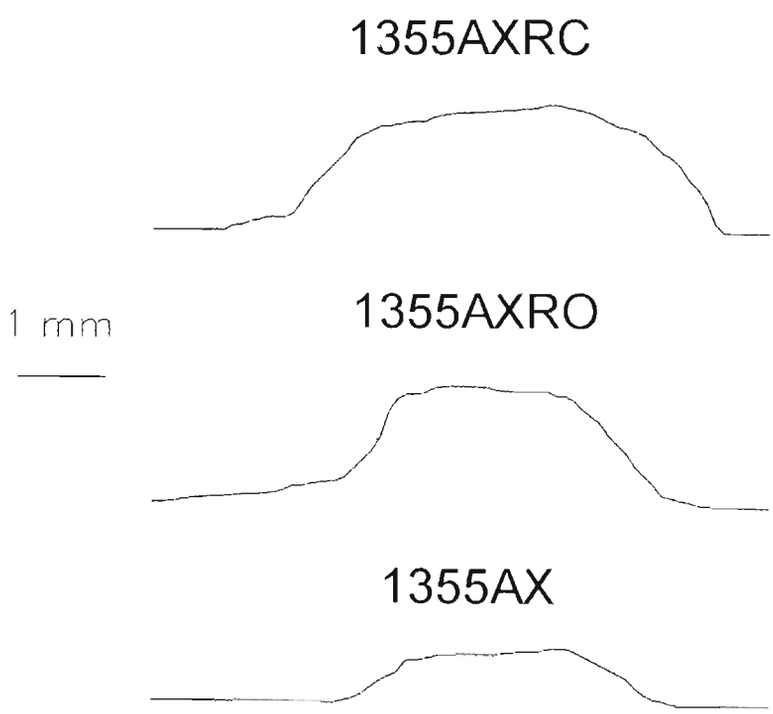

FIGURE 4.6: Rock bolt rib profiles

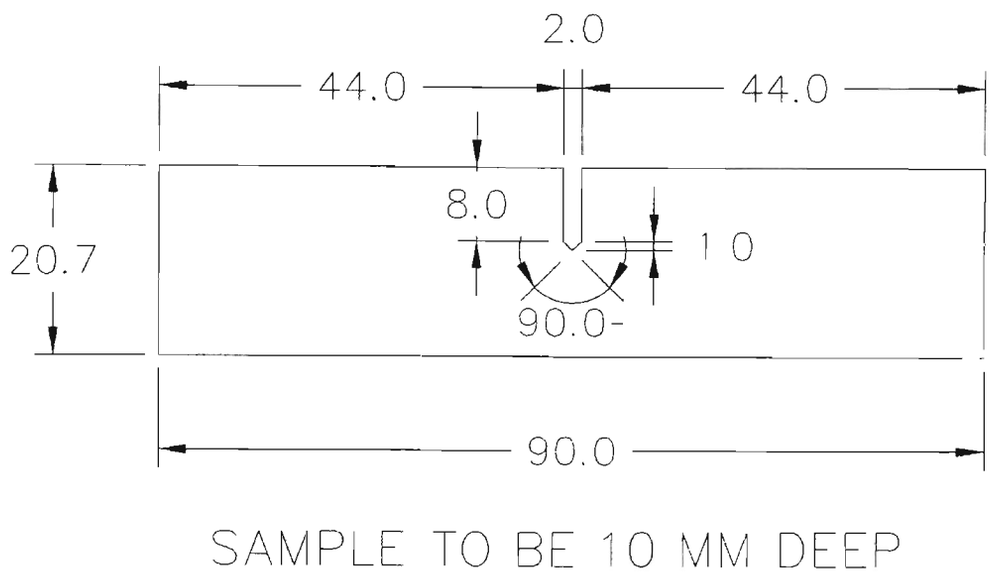

FIGURE 4.7: Fracture toughness sample dimensions

specimen size:

$$2.5 * \left(\frac{K_{Ic}}{\sigma_{ys}}\right)^2 = 0.0053m \tag{4.1}$$

The current specimen geometry is valid as 7.5 mm is less than the specimen size of 10 mm and less than the crack length of 10.3 mm.

K_{Ic} values for 1355AX were measured experimentally according to Standard E399-90, *"Standard Test Method for Plane Strain Fracture Toughness of Metallic Materials"* [4].

The Standard dictated that for a sample of those dimensions, a pre fatigue crack was needed to be 1.3 mm long. The required sharp crack was created by fatigue in the Instron Universal testing apparatus.

The samples were then loaded until failure, and calculations then performed as required from the Standard with values obtained from the stress-strain curve.

5

SERVICE FAILURES

This Chapter describes the fractographic investigation of rock bolts failed in service in various Australian mines. Sections 5.1 to 5.6 describe the analysis of each bolt received. These sections are in the order in which the bolts were analysed. This order reveals the development of understanding of these service failures. Two bolts were received from colliery W, two from colliery A, one from colliery C and one from colliery Q. In order to determine the responsible fracture mechanism, each bolt was examined using optical microscopy and Scanning Electron Microscopy (SEM).

Section 5.8 of this Chapter summarises the observed fracture topographies.

5.1 1355AXRC BOLT - COLLIERY W BOLT F

5.1.1 Information Supplied From Mine

The following information was supplied [52] concerning this bolt failure: *"The attached sample is one of four. The broken length of this bolt (AXR type) was 800 mm. The plate was slightly flattened suggesting about 10-15 tonnes of axial load in the bolt. As you can see the bolt is bent at the fractured end. The concerned area of the mine is dry. There is a claystone band in the roof which horizon appears to correspond with the length of the broken bolt. The hole in the roof was inspected visually. It was sheared but only a little."*

The plastic deformation of the base plate allowed the estimation of the service load on the rock bolt. A calculation based upon the suggested load (10-15 tonnes) indicated that the bolt stress was between 270 and 400 MPa. This load was significantly lower than the maximum permissible load.

5.1.2 Macroscopic Observations

Figure 5.1 presents a macroscopic view of the rock bolt. Figure 5.1 shows the curvature of the bolt caused by shear in the rock strata. The bolt was no longer straight and parallel to the straight edge also shown in the Figure. The fact that the bolt was in a bent condition indicates that there had been a bending moment on the bolt in service and that this bending moment had caused stresses on the bolt. Furthermore, these stresses exceeded the yield stress as was evident by the permanent (plastic) change of shape of the bolt. This bending was attributed to horizontal shear in the rock strata in which the bolt was operating. These shear stresses would add to the tensile stresses that were estimated from the plastic deformation of the support plate. The fracture surface was as the left end of the bolt segment. This fracture was macroscopically brittle. There was no evidence of any plasticity. This was unusual, because there was lots of plasticity if the bolt was caused to fail by increasing the stress until the stress exceeded the ultimate tensile stress. Under such conditions, there was lots of plasticity and the bolt necked down significantly. Such tensile testing has been carried out on such bolts failed in service and has produced normal ductile failure. Thus, Figure 5.1 presented a brittle failure of a bolt at a stress much lower than its ultimate tensile stress.

Figure 5.2 presented an overview of the fracture surface. The most striking feature was the dark thumbnail shaped area on the right of the bolt, near the rib. The rest of the fracture surface was quite shiny and irregular, speckled by dark areas. These dark areas were deposits of carbon/coal on the fracture surface. This combination of a dark thumbnail area together with the shiny surface, as well as lack of necking in the bolt, suggested that the bolt had failed by Stress Corrosion Cracking (SCC). The dark thumbnail area was where the stress corrosion crack initiated and grew slowly until the stress corrosion crack reached a critical size. Once this size was reached, the bolt failed instantaneously in a brittle manner, producing the shiny irregular surface. The diameter of the rock bolt was 21.5 mm, corresponding to an area of 363 mm^2 The thumbnail area was 6.6 mm long by 1.9 mm at its widest point, covering an area of approximately 7 mm^2 This corresponded to 1.9% of the total fracture area. Examination of the rock bolt indicated another phenomena that supported the theory that the bolt failed by SCC: secondary cracks. Due to the slow process of crack initiation and growth, it is not uncommon to find secondary cracks that did not grow to a size sufficient to initiate fast fracture. These secondary cracks were 7.5 mm from the crack initiation site, on the other side of the rib. Figure 5.3 shows a close up view of the secondary cracks. Another feature of these cracks was that they did not line up. They were all along the foot of the rib, but they were inclined at about 30° from the rib foot direction. If the rock bolt had failed along the plane of the secondary cracks, it would have looked like one of the bolts received from colliery A. Figure 5.4 shows the stepped fracture surface on the left of the picture, caused by the secondary cracks joining during fracture.

5.1.3 SEM Observations

Overview

Figure 5.5 shows an overview of the SCC region. This indicated a thumb nailed SCC region and a Fast Fracture Surface (FFS) as shown schematically.

Stress Corrosion Cracking

Figure 5.6 shows the fracture surface at the edge of the rock bolt at the crack initiation site. The main characteristic of this fracture surface was a porous network of branched channels. Such channels sometimes ran parallel, other times their direction appeared to be random. This fracture surface appeared to consist of minuscule shelves, which were porous. Such characteristic fracture surface has been seen in other samples obtained from service as well as laboratory samples.

SCC Fast Fracture Boundary

Figure 5.7 shows the boundary where the fracture mechanism changed from slow crack growth (bottom) to fast brittle fracture (top). A close examination revealed that the change of mechanism was sharp, indicating that there was no third mechanism involved during the fracture.

Figure 5.8 shows a metal grain where the fracture mechanism changed. On the lower section of this grain is the SCC surface.

Fast Fracture Surface

The fast fracture surface was typical of fast brittle fracture, and was similar to those of other rock bolts and of the laboratory samples. Figure 5.9 shows that the fast fracture surface was not smooth at this high magnification; there were ridges on the flat surfaces approximately 200 nm apart. These were attributed to the pearlite microstructure (alternating bands of ferrite and cementite).

5.1.4 Discussion

Service Conditions

Rock bolts [6] provide a cost efficient roof support system. Rock bolts have provided good service [6]. Rock bolts are made from ductile steel and do not usually fail in service in a brittle manner. However, Figures 5.1 and 5.2 indicate brittle failure for this particular rock bolt. Furthermore, the deformation of the support plate indicated that the service load was below the yield load. The local mine environment was described as "dry". This description of a dry local environment was consistent with the overall bolt appearance, Figure 5.1, which showed little corrosion. However, it was unlikely that there was no water at all in the mine. Coal mines are typically moist, and it is not uncommon to have significant water percolating through the rock

strata above the mine workings. It was expected that the "dry" description of the local conditions was to be interpreted in this context. There was probably little water pouring or dripping from the roof, but there probably was water in the rock strata, and the mine air was probably quite moist.

Macroscopic Fracture Appearance

Figures 5.1 and 5.2 indicated brittle fracture for this rock bolt at a stress much lower than the tensile stress. The appearance of Figure 5.2 was typical of SCC. There was a thumbnail shaped region, which was attributed to the slow crack growth region of SCC. SCC typically grows slowly. During this period of service there may be no obvious sign that there is damage occurring to the rock bolt. This period of service can in general take weeks or months. Nevertheless, during this period, the SCC is growing under the combined influence of the applied stress and the local environment. The introduction of the SCC changes the fracture mode. Without the SCC, fracture occurs at high tensile stresses and the overload failure is ductile. With the SCC, there was fast brittle fracture. This brittle fracture occured instantaneously when the SCC size exceeded the critical crack size.

Microscopic Fracture Appearance

The microscopic SEM examination of the fracture surface revealed three typical morphologies: CIS, TTS and FFS. The appearance of the first two fracture morphologies was consistent with SCC and the last fracture morphology was consistent with fast brittle fracture. All three fracture morphologies were different to the ductile microvoid coalescence dimple rupture fracture surface characteristic of ductile failure.

Figure 5.9 indicated that the spacing between the ridges for fast fracture was due to the regular microstructure of the steel. The steel microstructure was pearlite. It consisted of alternate plates of ferrite (essentially pure Fe) and cementite (iron carbide). The brittle fracture processes proceeded slightly differently in each of these two phases, with the result that the microstructure became revealed in the brittle fracture facets at high magnification. The ridges in the SCC area have a similar spacing to those in the fast fracture area, looking like preferential corrosion of one of the phases (either ferrite or the cementite).

The Tearing Topography Surface (TTS) occurred close to the free surface, within the dark thumbnail region. This topography has been described by Toribio and Vasseur [53] as a Tearing Topography Surface (TTS), a *"characteristic microscopic fracture mode with a kind of ductile tearing appearance, a certain degree of plasticity and a very closely spaced nucleation"* [53]. They pointed out that close to the surface of the specimen, the TTS has a kind of orientation in the direction of damage propagation. Such orientation was lost further into the sample. Figure 5.10 shows such orientation. Close to the surface the deep ridges tended to point towards the free surface, but as the distance from the free surface increased, the orientation became random. Toribio [53] suggested that this fracture surface was formed by hydrogen diffused into the metal and assisting fracture by embrittling the material. TTS occurred in this rock bolt as seen in Figure 5.11.

Identification of Environment

Full identification of the failure cause as SCC requires an identification of the causative factors. SCC requires three factors (a) a tensile stress, (b) a susceptible microstructure and (c) an environment. The tensile stress was caused by the service conditions. There was a tensile load due to the pre-stress on the bolt and the bending shear. The tensile pre-stress allowed the rock bolt to carry out its designed function, which was to reinforce the rock mass in which the rock bolt was secured. Identification of environment was not a straightforward exercise. The relevant mine area was described as "dry" That meant that it was difficult to extract a water sample from that location. Without a water sample, it was guesswork as to the actual environment that caused the SCC.

Laboratory Confirmation

This failure analysis has indicated that rock bolts can fail in service in a brittle manner with no prior warning at stresses much lower than their ultimate tensile strength. This represents a new failure mode for a critical mine component, that is critical for mine safety. There is no prior experience with this failure mode, and laboratory work is needed to understand the failure mechanisms. With understanding of the failure mechanism, it will be possible to devise counter-measures. Laboratory testing is also an effective way to determine the range of environmental conditions under which this failure mechanism operates. The alternative service testing often suffers from poor documentation of the actual local conditions.

5.1.5 Conclusions

Conclusions related to this rock bolt

- This rock bolt failed at a service stress lower than the tensile strength of the rock bolt.
- The failure was macroscopically brittle in a material that otherwise displays ductile overload fracture.
- The fracture surface revealed a thumbnail area approximately 1.9 mm in depth. This was interpreted as a stress corrosion crack that grew slowly, until it reached the critical crack size.
- The final fracture was by fast brittle fracture when the slow growing stress corrosion crack reached the critical crack size determined by the service load.
- The microscopic fracture surface observed using scanning electron microscopy was consistent with this interpretation.
- High magnification examination of the fast fracture facets revealed parallel ridges, which were attributed to the microstructure, which consisted of parallel platelets of ferrite and cementite.
- It has not been possible to identify the local environment causing this new failure mode because the local mine area was described as "dry"

- One way round this unknown causative environment was to carry out laboratory testing to reproduce this failure mode in the laboratory.

Implications for the use for rock bolts in strata support

- This failure analysis has indicated that rock bolts can fail in service in a brittle manner with no prior warning at stresses much lower than their ultimate tensile strength.
- This represents a new failure mode for a critical mine component, that is critical for mine safety. There was no prior experience with this failure mode, and laboratory work was needed to understand the failure mechanisms.
- With understanding of the failure mechanism, it will be possible to devise counter-measures.
- Laboratory testing is an effective way to determine the range of environmental conditions under which this failure mechanism operates.

5.2 1355AXRC BOLT - COLLIERY W BOLT G

This section describes a fractographic investigation of a rock bolt failed in service in an Australian colliery (colliery W). This was the second bolt received from this mine.

No information was supplied with the bolt regarding the conditions under which it was found. Visual inspection showed that the bolt was bent, due to shearing of the rock. The fracture surface was damaged and covered with various carbon deposits.

In order to document the fracture surface, macroscopic photographs were taken of the bolt and its fracture surface. After photography, the bolt was cut 10 mm below the fracture surface and prepared for observation with the Scanning Electron Microscope (SEM). A cleaning solution (EDTA) was used to remove surface oxides and carbon deposits in order to expose the fracture surface to SEM observation.

The regions examined using the SEM were the crack initiation site and the fast fracture area.

5.2.1 Macroscopic Observations

Figure 5.12 presents the rock bolt as seen from the side. The area just below the fracture was clearly bent, suggesting shearing in the rock strata.

Figure 5.13 shows the fracture surface of the rock bolt. The bolt was received with its fracture surface damaged in several areas. Although the macroscopic photograph shows much carbon deposits on the surface of the bolt, most could be washed away during preparation for SEM observation.

A higher magnification view is presented in Figure 5.14. There was extensive surface damage[1] as well

[1]Surface damage was attributed to plastic deformation altering the fracture surface. This was caused by these areas touching other surfaces under some load. This sample appeared to have fallen, landing on the SCC region.

as carbon deposits on the fracture surface. This rock bolt displayed features that indicated that SCC was responsible for the failure of this bolt. A thumbnail shaped SCC area was present, with fast fracture tear lines radiating from that area outwards. This thumbnail area was 1.27 mm deep and its half length was 1.59 mm long (half length as there was only half the SCC crack). From these measurements, the estimated total SCC area was approximately 4 mm^2 Compared to the bolt cross sectional area of approximately 363 mm^2, the thumbnail area barely covered 1.1% of the total bolt cross sectional area. This value was comparable to 1.9% of a previously analysed bolt.

Another similarity between this bolt and previously studied was that the SCC initiated at the foot of a rib. No bolt examined to date has shown an initiation site apart from at the foot of a rib.

On the other hand, one major difference between the SCC region of this bolt and those of other bolts was that this bolt did not have a full thumbnail shaped area. One corner of the SCC area seemed to have been cut away. The reason for this incomplete thumbnail area was attributed to the manner of interaction of the SCC crack and the final fast fracture. The final fracture of the bolt occurred at 90° to the bolt main axis intersecting the SCC crack which was parallel to the rib at 30° inclination to the axis. The fracture of the bolt divided the SCC area. This inclination of the SCC is shown in Figure 5.15, with the SCC running along the foot of the rib in the foreground.

5.2.2 SEM Observations

Overview

Figure 5.16 shows an overview of the SCC region. This showed a half thumb nailed SCC region and a fast fracture surface (FFS) region as shown schematically. As the bolt was cracking, the SCC region grew until it reached a critical size, after which the bolt failed by fast brittle failure. This almost instantaneous event produced the tear lines that radiate from the SCC area.

As mentioned previously, this bolt only displayed half the thumb nail shaped area since the difference between the SCC angle and the final fracture angle caused the SCC area to be divided. This was substantiated by the tear lines curving around the thumbnail in a tight radius.

There were carbon deposits present on the fracture. Although it had been endeavoured to remove these deposits, there were some remains firmly attached to the surface of the bolt. Total removal of these remains may have compromised the quality of the remaining fracture surface. Since there were no carbon deposits on the SCC area, these deposits were left as they did not interfere with the analysis in a significant manner.

Fast Fracture Surface

Figure 5.17 shows the typical brittle fracture surface in the overload region. The fracture resembled maple leaves, growing in the direction of the final crack propagation. The same fast fracture pattern had been found in other analysed rock bolts as well as LIST samples. This fracture surface covered about 99% of the

fracture surface.

For comparison, Figure 5.18 shows the overload region in another rock bolt at a higher magnification. The same maple leaf appearance were apparent in both pictures.

A minor but common feature in these Figures is the various small pits that are present throughout the surface.

Stress Corrosion Cracking

Figure 5.19 presents a detailed view of the thumbnail shaped area. Figure 5.20 is the key to Figures 5.17, 5.21, 5.22, 5.23 and 5.24. The darker areas on the top of the picture were the carbon deposits, whilst the smooth area on the bottom of the bolt was surface damage. The SCC region extended over the region that was at an angle to the viewer, starting from the bottom right towards the left of the picture. On the left, the SCC region ended abruptly, with tear lines following on. Figure 5.21 shows the SCC area division. On the right of the Figure is the SCC fractography whilst on the left there is fast brittle fracture.

Figures 5.22, 5.23 and 5.24 were from the regions that were not damaged within the SCC thumbnail. The surface displayed the network of branched porous channels typical of SCC in pearlitic steels. These corrugated surfaces were at different heights, joined by steep rough slopes. Similar features were seen in the SCC region of a different rock bolt, as Figure 5.6 demonstrates. Similar fracture surfaces were also found within the SCC region in LIST laboratory samples, as shown in Figures 5.25 and 5.26. Another feature was the numerous pits that appeared throughout the surface, both in the flat areas as well as the sloped regions.

5.2.3 Discussion

From the macroscopic observations, this rock bolt fracture was essentially similar to the previously examined bolts. It has the tell tale features of a small SCC region, surrounded by a fast brittle fracture region.

The SCC initiated in the foot of a rib. This suggested that it might be worthwhile to investigate the effects of increasing the radius of the bolt rib.

The SEM figures compare the SCC regions found in this rock bolt, in a previous rock bolt and in laboratory LIST samples. They all displayed the corrugated flat surfaces, joined by the steep rough slopes.

The figures also showed pitting on all surfaces. These pits were attributed to the surface preparation process for analysis in the SEM. During the surface preparation process the sample was immersed in a cleaning solution to remove the surface oxides. As well as removing the surface oxides, the fluid (an Ethylenediaminetetra acetic acid disodium salt solution (EDTA)) created those pits. This was demonstrated by immersing a sample in the EDTA solution for 3 minutes, rather than the usual 15 minutes. The thus prepared surface showed no pitting, on the fast fracture surface or on the SCC region.

5.2.4 Conclusions

The different fracture surfaces showed the same fractography as previously studied samples (rock bolts and LIST samples). This implied that the rock bolt failed due to SCC.

SCC tended to develop along the foot of the rib along the bolt. Although the crack developed along the angle of the rib, tensile stresses caused the final fast brittle failure to occur perpendicular to the bolt surface.

The current surface preparation methods followed to analyse the samples caused pits to developed on all surfaces. Further work was being carried out to find out if the preparation methods have any other effects on the fracture surfaces, but none were found.

By studying the various fracture surfaces and comparing them to other failed rock bolts and laboratory samples, the conclusion reached was that this rock bolt failed due to SCC.

5.3 5152CW10D - COLLIERY C BOLT H

5.3.1 Information Supplied From Mine

The following information was supplied with the rock bolt:

- *"The bolt was installed 2-3 months prior to failure.*
- *Bolt type 5152CW10D, σ_y = 745 MPa. This bolt was cold worked for strength. In contrast, the rock bolts previously examined were not cold worked.*
- *Installed in No. 5 heading between 21 and 22 cut through on right hand side.*
- *Total sample length 305 mm, bolt tail below nut 58 mm.*
- *Roof plate supplied with the broken bolt shows very little deformation, therefore the axial load would not be greater than 5-10 tonnes (145 MPa) [54]".*

Visual inspection of rock bolt did not show any deformation due to shear. The fracture surface had very little oxides or carbon deposits and no obvious surface damage.

In order to document the fracture surface, macroscopic photographs were taken of the bolt and its fracture surface. After photography, the bolt was cut 10 mm below the fracture surface and prepared for observation with the Scanning Electron Microscope (SEM). A cleaning solution (EDTA) was used to remove surface oxides and carbon deposits in order to expose the fracture surface to SEM observation.

The regions examined using the SEM were the crack initiation site, the fast fracture area and the interface between these two regions.

5.3.2 Macroscopic Observations

Figure 5.27 presents a side view of the bolt. The bolt was straight, not showing any obvious signs of shear.

Figures 5.28 and 5.29 show the fracture surface of the rock bolt. The darker areas were dirt and carbon deposits. This rock bolt displayed features that indicated that SCC was responsible for the failure of this bolt. A thumbnail shaped SCC area was present, with fast fracture tear lines radiating from that area outwards. This thumbnail area was 3.11 mm deep and its length was 6.44 mm long. From these measurements, the estimated total SCC area in the bolt was approximately 15 mm^2. Compared to the bolt area of approximately 370 mm^2, the thumbnail area barely covered 4.06% of the total bolt area. This value was larger than the 1.9% and 1.1% of previously analysed bolts. This larger value was attributed to the different metallurgy of this bolt as well as the manufacturing process this bolt underwent (cold rolling). LIST tests have been carried out to characterise the SCC characteristics of this bolt.

Another similarity between this bolt and previous ones studied was that the SCC initiated at the foot of a rib. No bolt examined to date has shown an initiation site apart from at the foot of a rib. Figure 5.30 shows where the SCC initiated, and Figure 5.31 shows a diagram of where the SCC initiated on the bolt shaft.

5.3.3 SEM Observations

Overview

Figure 5.32 shows an overview of the SCC region. This showed a half thumb nailed SCC region and a fast fracture surface (FFS) region as shown schematically. As the bolt was cracking, the SCC region grew until it reached a critical size, after which the bolt failed by fast brittle failure. This almost instantaneous event produced the tear lines that radiate from the SCC area.

Towards the inner edge of the SCC area there was a small region that is FFS. That FFS region was completely enclosed within the SCC region.

Fast Fracture Surface

Figures 5.34 and 5.35 show the typical brittle fracture found in the overload region. The surface tearing resembled maple leaves, growing in the direction of the final crack propagation. The same fast fracture pattern has been found in other analysed rock bolts as well as LIST samples.

For comparison, Figure 5.18 shows the overload region in another rock bolt at a higher magnification. The same maple leaf appearance can be seen in Figures 5.34 to 5.18.

Stress Corrosion Cracking

Figure 5.36 presents a detailed view of the thumbnail shaped area.

The crack appears to have initiated in the pit at the top left of the picture, just to the left of the two dark spots on the border of the sample. There were channels that radiate from these two dark spots outwards through the SCC region. With increasing distance from the crack initiation site, the channel orientation became less prominent. Figures 5.37 and 5.38 illustrates the channels close to the crack initiation site.

Further away from the crack initiation site and closer to the SCC - FFS interface, the SCC region tended to lose channel orientation, giving way to corrugated surfaces joined by rough slopes. Figure 5.39 and 5.40 depict such a region. The channel orientation was still visible in this region. At the magnification of x3076 it was possible to see the pearlite colonies that make up the metal structure in the from of small ridges and a furry appearance.

Figures 5.41, 5.42 and 5.43 show various aspects of the SCC topography. Figures 5.44, 5.45 and 5.46 show another series from a different location, within the SCC region. Both these locations showed some amount of macroscopic orientation of the channels, as well as some pits randomly distributed throughout the surface. Some areas also displayed a degree of micro void coalescence (MVC) scattered around the channels. The porous channels, together with the quasi MVC, pits, the corrugated surfaces and the rough slopes were typical of SCC in pearlitic steels. Similar features could be seen in the SCC region of a different rock bolt, as Figure 5.6 demonstrates. Similar fracture surfaces were also found within the SCC region in LIST laboratory samples, as seen in Figures 5.25 and 5.26. This surface has been named Corrugated Irregular Surface (CIS).

SCC-FFS Interface

Figures 5.47 and 5.48 show the interface between the SCC region and the FFS region. The interface line can be traced easily, as the contrast between the maple leaf flat appearance of the FFS was quite different to the quasi MVC, rough slopes and corrugated channels (CIS). To gain a better understanding of the fracture mechanics, high magnification views were taken of the interface. Figure 5.49 shows one such interfaces region, with Figures 5.50 and 5.51 being details within the centre of Figure 5.49. From these Figures it can be seen that the pearlite colony orientation was random; sometimes it was aligned in the direction of the crack propagation (bottom to top), other times it was perpendicular to the crack path. In Figure 5.50 it can be seen that the mechanism changed from SCC to FFS in the middle of a pearlite colony aligned along the crack growth direction.

5.3.4 Discussion

From the macroscopic observations, this rock bolt fracture was essentially similar to the previously examined bolts. It had the tell tale features of a small SCC region, surrounded by a fast brittle fracture region.

The SCC initiated as the foot of a rib along the shaft of the bolt. This was consistent with other bolts, as SCC seemed to initiate on curves of small radius on the surface.

The SEM figures compare the SCC regions found in this rock bolt, in a previous rock bolt and in

laboratory LIST samples. They all displayed the corrugated flat surfaces, joined by the steep rough slopes. This suggested that this bolt also failed by SCC, same as previously studied rock bolts. The only difference between this bolt and previously studied ones was the presence of channels radiating from the crack initiation site towards the SCC-FFS interface. This was thought to be due to the manufacturing process by which the bolt was formed (cold working) and the slightly different metallurgy of the bolt.

Analysis of the crack interface fractography suggested that pearlite colony orientation had no effect on crack propagation direction nor on determining when SCC changed to FFS. This in turn suggested that hydrogen diffused into the steel in a linear manner, with the microstructure playing no part in the transport mechanism of hydrogen ahead of the crack tip.

This bolt was prepared with a shorter immersion time in EDTA (3 minutes rather than 20 minutes). The result was a high quality surface, without pitting damage displayed by longer immersion times.

5.3.5 Conclusions

The different fracture surfaces show the same fractography as previously studied samples (rock bolts and LIST samples). This implied that the rock bolt failed due to SCC.

SCC tended to develop along the foot of the rib along the bolt. Tensile stresses caused the final fast brittle failure to occur perpendicular to the bolt surface.

Bolt microstructure seemed to play no part in hydrogen diffusion mechanisms.

By studying the various fracture surfaces and comparing them to other failed rock bolts and laboratory samples, the conclusion reached was that this rock bolt failed due to SCC.

5.4 MA840B BOLT - COLLIERY A BOLT I

5.4.1 Introduction

The fracture surface of this bolt was too corroded to be able to accurately determine the mechanism of failure. The characteristics of the fracture surface and application of this rock bolt suggested that the bolt failed due to either fatigue or corrosion fatigue.

The following information was supplied with the rock bolt:

"Bolt was one of four used, fan was in position 1 or 2 weeks, but bolts installed were 4 weeks old. An estimate of the load was between 250 kgs and 1 tonne on the one bolt [55]"

After the fracture surface was documented, the bolt was cut 10 mm below the fracture surface and prepared for observation with the Scanning Electron Microscope (SEM). A cleaning solution (EDTA) was used to remove surface oxides and carbon deposits in order to expose the fracture surface to SEM observation. The regions examined using the SEM were the crack initiation site, the fast fracture area and the interface between these two regions.

5.4.2 Macroscopic Observations

Visual inspection of the bolt indicated that the bolt was straight and did not show signs of shear. The fracture occurred at the root of the threaded section of the bolt. The fracture surface had several oxides but not much physical damage.

Figures 5.52 and 5.53 show the fracture surface of the rock bolt. A thumbnail shaped area was present, with fast fracture tear lines radiating from that area outwards. This area was interpreted as being the subcritical crack growth region and can be seen at the bottom of the Figures. The thumbnail area was 5.5 mm deep and its length was 14 mm. From these measurements, the estimated total subcritical crack area in the bolt was approximately 51.3 mm^2 Compared to the bolt area of approximately 370 mm^2, the thumbnail area covered 15% of the total bolt area. This value is larger than the 1.9% and 1.1% of previously analysed bolts.

5.4.3 SEM Observations

Fast Fracture Surface (FFS)

Figure 5.54 shows typical brittle fracture in the overload region. The surface is made up of many facets which resemble maple leaves, growing in the direction of the final crack propagation. This fast fracture pattern was essentially the same as that found in the fast fracture region of the fracture surfaces of other rock bolts and laboratory LIST samples.

Subcritical Crack Growth

Figures 5.55 and 5.56 present an overview of the thumbnail shaped fracture area. They show a region that has sustained corrosion damage, erasing features within this region that could have provided clues as to the source of fracture mode.

Figure 5.57 is a higher magnification view of the thumbnail area. The surface showed corrosion damage, but also some remnants of the original fracture topography. The topography was rough and could be interpreted as heavily damaged transgranular SCC. The remaining topography did not resemble corroded FFS. Because the surface was corrugated, it was difficult to tell whether the corroded surface was originally MVC, hydrogen embrittled MVC, beach marks from fatigue, Tearing Topography Surface (TTS) or Corrugated Irregular Surface (CIS). If the bolt had failed by fatigue, it would be expected that there would be macroscopic beach marks on the surface visible on SEM examination. Due to the bolt's exposure and subsequent corrosion, the beach marks could have been wiped away. If the bolt failed by corrosion fatigue, the electolyte would have helped erase the beach marks and fatigue striations even before the bolt failed.

SCC-FFS Interface

Figure 5.58 shows the interface between the subcritical crack growth region and the FFS region. The interface line could be traced easily, as the contrast between the maple leaf flat appearance of the FFS was quite marked compared to the heavily corroded area.

5.4.4 Discussion

The subcritical crack growth region in this bolt was too damaged to be able to confidently determine the cause of failure. The thumbnail area was more than 10 times larger than the previously studied rock bolts, suggesting that this bolt suffered failure by a mechanism different to that causing the failures of the bolts previously examined.

This bolt was used to support a heavy ventilation fan. This together with the fact that the bolt failed at the threaded section (region of greatest stress concentration) suggested that this bolt failed by fatigue or by fatigue corrosion. The FFS did not seem to be heavily corroded, whilst the thumbnail region was damaged by corrosion. This, together with the fact that no tell tale beach marks were found, suggests that the bolt failed by fatigue corrosion, as the beach marks would have been erased while the subcritical crack propagated through the bolt.

Back of the envelope calculation indicated that the thread root stress at the failure site was about 81 MPa static loading (when the fan was off). For this given material, an infinite fatigue life ($>10^6$cycles) is achieved at a stress lower than 114 MPa. This only leaves a safety margin of 33 MPa for static loading. Such a small margin can be exceeded if the fan was not properly balanced. As an initial calculation (due to lack of data of the actual fan), a 4 tonne fan could have an imbalance of 1 kg at 0.5 m away from the shaft. Such an unbalanced fan running at 1500 rpm would exceed the 114 MPa limit. In such a case, 10^6 cycles would be exceeded within 12 hours. In actuality, fans run at higher speeds than 1500 rpm, allowing a smaller imbalance to exceed the 114 MPa limit.

5.4.5 Conclusions

This rock bolt showed fracture characteristics different to previously studied rock bolts. The bolt had a subcritical crack growth region that had been too heavily damaged to accurately obtain conclusions. This region was more than 10 times the area of previously studied rock bolts.

The fact that the bolt would be experiencing an alternating load due to a ventilation fan, the subcritical crack growth region was heavily corroded and that the FFS region was not heavily corroded points to the fact that the bolt failed due to fatigue corrosion.

An initial calculation suggested that the bolt was loaded to a stress close to the infinite fatigue life limit of that material. A relatively low imbalance of the fan would have caused a fatigue crack to initiate and to grow in the bolt. The heavy corrosion on the thumbnail area suggested that the environment helped the

crack to propagate to some degree.

5.5 MA810 BOLT - COLLIERY A BOLT J

5.5.1 Introduction

This section describes a fractographic investigation of the second rock bolt received that had failed in service in colliery A.

No information was supplied with the bolt regarding the conditions under which it was found. Visual inspection showed that the bolt was slightly bent near the thread, away from the fracture surface, attributed to be due to shearing of the rock. The fracture surface was damaged and covered with various corrosion products.

A sliver 10 mm thick was cut from the bolt and sent for spectrometer analysis. The results showed the chemical composition to be 0.36% C, 1.4% Mn, 1% Si, 0.013% S, 0.021% P, 0.01% Ni, 0.02% Cr, 0.01% Mo, 0.01% Cu, 0.04% V, 0.01% Nb, 0.01% Ti, 0.005% Al and 0.0006% B. This chemical analysis confirmed the rock bolt to be of grade MA810, a variant of the MA840B bolt studied previously.

In order to document the fracture surface, macroscopic photographs were taken of the fracture surface. After photography, the bolt was cut 10 mm below the fracture surface and prepared for observation with the Scanning Electron Microscope (SEM). A cleaning solution (EDTA) was used to remove surface oxides and carbon deposits in order to expose the fracture surface to SEM observation. The bolt was immersed in the EDTA solution for 3 minutes. Longer exposure times damage the remaining fracture surface without a significant gain in information.

The regions examined using the SEM were the crack initiation site and the fast fracture area.

5.5.2 Macroscopic Observations

Figure 5.59 shows the fracture surface of the rock bolt. The bolt was received with its fracture surface damaged in several areas. Most damage occurred in the subcritical crack growth region, the thumbnail shaped area. The fast brittle fracture region was relatively intact, with little corrosion products on its surface.

A higher magnification view is presented in Figure 5.60. This rock bolt displayed features that indicated that SCC was responsible for the failure of this bolt. A thumbnail shaped SCC area was present, with fast fracture tear lines radiating from that area outwards. This thumbnail area was 8 mm deep and its length was 15 mm long. From these measurements, the estimated total SCC area in the bolt was approximately 60 mm^2. Compared to the bolt area of approximately 363 mm^2, the thumbnail area covered 16.7% of the total bolt area. This value was much larger than previous values measured from other bolts of approximately 1.9%.

Another similarity between this bolt and previous ones studied others was that the SCC initiated at the foot of a rib. No bolt examined to date has shown an initiation site apart from at the foot of a rib.

On the other hand, one major difference between the SCC region of this bolt and those of other bolts was that this bolt seemed to have two regions of subcritical crack growth. The region closest to the surface was more damaged, with corrosion products covering the fracture surface completely. Further into the bolt there was a region that was not as damaged as the first region. The difference in damage was attributed to outside factors between the bolt fracturing and falling out of the rock and the bolt arriving to the laboratory for analysis.

5.5.3 SEM Observations

Overview

Figure 5.61 shows an overview of the SCC region. This shows a thumb nailed SCC region and a fast fracture surface (FFS) region as shown schematically. As the bolt was cracking, the SCC region grew until it reached a critical size, after which the bolt failed by fast brittle failure. This almost instantaneous event produced the tear lines that radiate from the SCC area.

As mentioned previously, this bolt displayed heavy corrosion damage in the thumbnail area. Even though the details might have been corroded away, enough information remained to extract meaningful data.

The outermost edge seen in the Figure is the rib of the bolt. The fracture surface commenced 1.1 millimeters further in, where the shaft of the bolt began. At this inner lip the crack grew into the bolt at different heights, as shown by the appearance of small steps running along the edge, following the bolt rib.

Fast Fracture Surface (FFS)

Figure 5.62 shows the typical brittle fracture surface in the overload region. The surface tearing resembled maple leaves, growing in the direction of the final crack propagation. The same fast fracture pattern has been found in other analysed rock bolts as well as LIST samples. This fracture surface covered about 83% of the fracture surface.

For comparison, Figure 5.18 shows the overload region in another rock bolt at a higher magnification. The same maple leaf appearance can be seen in both pictures.

Stress Corrosion Cracking

Figures 5.63 - 5.65 were taken from within the thumbnail shaped area close to the FFS. All useful microscopic information in the darker region close to the free surface had been erased by the general corrosion. The three Figures show traces of Corrugated Irregular Surfaces (CIS) which have been found in other rock bolts failed by SCC. Figure 5.22 shows a typical CIS surface in a different rock bolt. By comparing these Figures it can be seen that both bolts show irregular surfaces. Both display the typical features of CIS (a network

of branched porous channels on flat corrugated regions joined by steep corrugated slopes). The features of the bolt under consideration were not as marked as those of the comparison bolt, as the general corrosion process had erased many features and blunted the sharpness of others.

One difference between the two bolts was that the previously studied bolt displayed a number of pits throughout the surface. This was due to prolonged immersion in the EDTA solution. Shorter immersion times have been found to clean the surface satisfactorily without introduction of the pits.

Similar fracture surfaces were also found within the SCC region in LIST laboratory samples, as seen in Figures 5.25 and 5.26.

Figure 5.66 shows the slow crack growth region on the left and the FFS on the right. Both regions were separated by a marked line. Both the slow crack growth region and the interface between the different fracture regions were covered in corrosion products (the closely packed spheres). The interface between these fracture surfaces was quite small and marked, consistent with previously studied bolts.

5.5.4 Discussion

From the macroscopic observations, this rock bolt fracture was essentially similar to the previously examined bolts. It had the tell tale features of a thumb nailed SCC region, surrounded by a fast brittle fracture region.

The large SCC region of this bolt was unusual, but not enough fine detail remained on this bolt to refine the measurements. No information had been gathered on the service conditions, so it was difficult to estimate the reasons for the enlarged SCC region.

The SCC initiated in the foot of a rib. This suggested that it might be worthwhile to investigate the effects of increasing the radius of the bolt rib. This investigation is detailed in Chapter 9.

The SEM figures compared the SCC regions found in this rock bolt, in a previous rock bolt and in laboratory LIST samples. They all displayed the corrugated flat surfaces, joined by the steep rough slopes, although the surfaces on this bolt were damaged.

5.5.5 Conclusions

The different fracture surfaces showed the same fractography as previously studied samples (rock bolts and LIST samples). This implied that the rock bolt failed due to SCC.

SCC tended to develop along the foot of the rib along the bolt. Although the crack developed along the angle of the rib, tensile stresses caused the final fast brittle failure to occur perpendicular to the bolt surface.

By studying the various fracture surfaces and comparing them to other failed rock bolts and laboratory samples, the conclusion reached was that this rock bolt failed due to SCC.

5.6 1355AXRC BOLT - COLLIERY Q BOLT K

5.6.1 Introduction

This section describes a fractographic investigation of a rock bolt failed in service in colliery Q.

No information was supplied with the bolt regarding the conditions under which it was found. Visual inspection showed that the bolt was slightly bent near the fracture surface, due to shearing of the rock. The fracture surface was mostly shiny, with little damage done to the original fracture surface.

A sliver 10 mm thick was cut from the bolt and sent for spectrometer analysis. The results showed the chemical composition to be 0.57% C, 1.5% Mn, 0.22% Si, 0.024% S, 0.025% P, 0.12% Ni, 0.11% Cr, 0.03% Mo, 0.26% Cu, 0.01% V. 0.01% Nb, 0.01% Ti, 0.005% Al and 0.0005% B. This chemical analysis confirmed the rock bolt to be a 1355AX bolt.

In order to document the fracture surface, macroscopic photographs were taken of the fracture surface. After photography, the bolt was cut 10 mm below the fracture surface and prepared for observation with the Scanning Electron Microscope (SEM). A cleaning solution (EDTA) was used to remove surface oxides and carbon deposits in order to expose the fracture surface to SEM observation. The bolt was immersed in the EDTA solution for 3 minutes.

The regions examined using the SEM were the crack initiation site and the fast fracture area.

5.6.2 Macroscopic Observations

Figure 5.67 presents the rock bolt from the side. The area just below the fracture was clearly bent, suggesting shearing in the rock strata.

Figure 5.68 shows the fracture surface. The fracture surface was relatively intact, with little corrosion products on its surface. Away from the thumbnail region, on the opposite side of the bolt, there was a depression. This depression was caused by the path that the fast brittle crack followed. This crack path has been observed in previous bolts. The fracture surface of this region was the was as found in the Fast Fracture Surface (FFS).

This rock bolt displayed features that indicated that SCC was responsible for the failure of this bolt. A thumbnail shaped SCC area was present, with fast fracture tear lines radiating from that area outwards. This thumbnail area was 1.07 mm deep and its length was 4.94 mm long. From these measurements, the estimated total SCC area in the bolt was approximately 3.27 mm^2 Compared to the bolt area of approximately 363 mm^2, the thumbnail area barely covered 0.9% of the total bolt area. This value was slightly smaller but comparable to previous values measured from other bolts of approximately 1.9%.

Another similarity between this bolt and ones previously studied was that the SCC initiated at the foot of a rib. No bolt examined to date had shown an initiation site apart from at the foot of a rib. Figure 5.69 shows the dark thumbnail region originating on the bolt rib.

One difference between the SCC region of this bolt and those of most bolts was that this bolt did not have a full thumbnail shaped area. One corner of the SCC area seemed to be cut away. This incomplete thumbnail area has been observed occasionally in other bolts. The reason for this incomplete thumbnail area was attributed to the manner of interaction of the SCC crack and the final fast fracture. The final fracture of the bolt occurred at 90° to the bolt main axis intersection the SCC crack which was parallel to the rib at a 30° inclination to the axis. The fracture of the bolt divided the SCC area.

5.6.3 SEM Observations

Overview

Figure 5.70 shows an overview of the SCC region. This shows a thumb nailed SCC region and a fast fracture surface (FFS) region as shown schematically. As the bolt was cracking, the SCC region grew until it reached a critical size, after which the bolt failed by fast brittle failure. This almost instantaneous event produced the tear lines that radiate from the SCC area.

The outermost edge in the Figure was the rib of the bolt. The fracture surface commenced 1.1 millimeters further in, where the shaft of the bolt began. At this inner lip the crack grew into the bolt, following the bolt rib. The crack followed the rib, even though the final fracture occurred in the observed manner.

Fast Fracture Surface (FFS)

The brittle fracture surface was found in the overload region. The surface tearing resembled maple leaves, growing in the direction of the final crack propagation. The same fast fracture pattern had been found in other analysed rock bolts as well as LIST samples. This fracture surface covered about 99% of the fracture surface.

For comparison, Figure 5.18 shows the overload region in another rock bolt at a higher magnification. The same maple leaf appearance was observed in both bolts.

Stress Corrosion Cracking

Figure 5.71 was taken from within the thumbnail shaped area close to the FFS. The Figure shows a typical Corrugated Irregular Surface (CIS) similar to other such surfaces which have been found in other rock bolts failed by SCC. Figure 5.22 shows a typical CIS surface in a different rock bolt. By comparing these Figures it can be seen that both bolts showed irregular surfaces. Both display the typical features of CIS (a network of branched porous channels on flat corrugated regions joined by steep corrugated slopes).

One difference between the two bolts was that the previously studied bolt displays a number of pits throughout the surface. This was due to prolonged immersion in the EDTA solution. Shorter immersion times have been found to clean the surface satisfactorily without introduction of the pits.

Similar fracture surfaces were also found within the SCC region in LIST laboratory samples, as seen in Figures 5.25 and 5.26.

Figure 5.72 shows the slow crack growth region on the top and the FFS on the bottom. Both regions were separated by patches of quasi Micro Void Coalescence (qMVC). It is suggested that qMVC was formed when hydrogen had penetrated ahead of the crack tip. If hydrogen was not present in the material, the fracture of the interface at that point would resemble that of Micro Void Coalescence (MVC) observed in pure ductile failures, but with the presence of hydrogen there was qMVC. It is worthy to note that the overload region was brittle cleavage, as the crack was larger than the critical crack size of the fracture criterion. The appearance of the interface region between the CIS region of the subcritical crack growth and the overload was interpreted as being influenced by the amount of hydrogen diffused ahead of the crack tip. Typical features of qMVC was the porous surface and small microvoids in relatively flat regions, extending "fingers" into the FFS.

It is possible that the topography of qMVC could be explained in the terms of the local (triaxial) stress state and the micro-mechanics of fracture, such that no hydrogen is required to produce such a fracture surface. That is, that there could be ductile tearing of ligaments between CIS regions of SCC by MVC. However, such ductile tearing of ligaments between CIS regions is contrary to the work carried out by Toribio et al [56], [57], [53] who indicated as follows.

"The MVC area cannot appear after the TTS since the latter can be analysed in fracture mechanics terms as a macroscopic crack (produced by hydrogen assisted micro-damage) prolonging the original notch and greatly increasing the triaxiality level as a consequence of its sharp border."

Toribio et al [57] demonstrated that for *"fracture in air of the same pearlitic steel that there is a triaxiality level below which fracture is MVC and above which it is cleavage like, and therefore the appearance of MVC topography does not seem to be possible in high-triaxiality areas not sufficiently hydrogenated [53]."*

This research indicates that cleavage would occur in air (i.e. in the absence of hydrogen) in the areas between CIS and the FFS where qMVC was observed on the fracture surfaces. This indicates that the qMVC areas were produced by a local enhancement of ductility by hydrogen. Moreover, there were differences in appearance between MVC as observed for samples fractured in air (in the absence of hydrogen) and the qMVC as observed in fracture surfaces in the transition regions just adjacent to FFS. Whilst this difference must in part be due to differences in local stress state, it would also be expected that there could be a contribution due to the micro-mechanism of hydrogen-induced plasticity.

The work carried out in this thesis is consistent with the prior work. Samples failing in air showed MVC ductile failure, whilst the qMVC associated with SCC was different in appearance, and occurred under local stress conditions where brittle cleavage would be expected in the absence of hydrogen.

Figures 5.73 - 5.75 show the crack running along the bolt rib. The secondary cracks grew on the rib and the fracture surface of these cracks (CIS) was the same as that seen on the main fracture surface. Figure 5.75 shows the fracture surface at a higher magnification.

5.6.4 Discussion

From the macroscopic observations, this rock bolt fracture was essentially similar to that of the previously examined bolts. It has the tell tale features of a thumb nailed SCC region, surrounded by a fast brittle fracture region.

The SCC initiated at the foot of a rib. The SEM figures compared the SCC regions of this rock bolt, in a previous rock bolt and in laboratory LIST samples. They all displayed the corrugated flat surfaces, joined by the steep rough slopes.

5.6.5 Conclusions

The different fracture surfaces showed the same fractography as for previously studied samples (rock bolts and LIST samples). This implied that the rock bolt failed due to SCC.

SCC tended to develop along the foot of the rib along the bolt. Although the crack developed along the angle of the rib, tensile stresses caused the final fast brittle failure to occur perpendicular to the bolt surface.

By studying the various fracture surfaces and comparing them to other failed rock bolts and laboratory samples, the conclusion reached was that this rock bolt failed due to SCC.

5.7 SUMMARY OF SERVICE FAILURES

All of the received bolts displayed environmental damage. Only one bolt (colliery A bolt I) was suspected to have failed by a mechanism other than SCC. Bolt I was suspected to have failed by either fatigue or fatigue corrosion.

Some bolts showed plastic deformation near the fracture surface. In some cases, examination of the bolt hole showed shearing of the rock strata. It is this shearing of the rock strata that was the reason attributed to the permanent deformation of the bolts.

All bolts displayed a subcritical crack growth region surrounded by a fast brittle fracture region. The area covered by the subcritical crack growth region in the 1355AX bolts was approximately 2%, with 4% in the 5152CW10D bolt and 17% for the MA810 bolt.

SCC was found to have initiated at the foot of the rib in all bolts. Secondary cracks have been found along the foot of the rib.

Little information is known about the service environments in which the bolts were installed. All bolts have been found in "dry" mine conditions (no water dripping from the roof nor running along the mine shaft).

These studies have characterised the failure mode, in particular the fractography associated with the SCC. These studies are consistent with the recent ACARP report on Project No C8008 of Crosky et al [7]. In this study, fractography has been studied to greater detail than included in the ACARP report.

5.8 SUMMARY OF FRACTURE TOPOGRAPHIES

The fracture topographies found in the analysed rock bolts were Tearing Topography Surface (TTS), Corrugated Irregular Surface (CIS), quasi Micro Void Coalescence (qMVC) and Fast Fracture Surface (FFS).

Tearing Topography Surface has been described as a *"characteristic microscopic fracture mode with a kind of ductile tearing appearance, a certain degree of plasticity and a very closely spaced nucleation"* [53]. Close to the free surface of the specimen, the TTS had a kind of orientation in the direction of damage propagation. Such orientation was lost further into the sample.

Corrugated Irregular Surface was described as a network of branched porous channels on flat corrugated regions joined by steep corrugated slopes. This surface made up the bulk of the dark thumbnail region in the rock bolt fracture surface.

quasi - Micro Void Coalescence was formed when hydrogen had penetrated ahead of the crack tip, enough to change the fracture micromechanism to qMVC but insufficient to allow the crack to grow as CIS. Typical features of qMVC were the porous surface and small microvoids in relatively flat regions, extending "fingers" into the FFS. qMVC was usually found between CIS and FFS. qMVC has been previously shown to occur in pearlitic steels under conditions where there is a local hydrogen concentration together with local triaxiality, whilst no qMVC has been observed in pearlitic steels tested in air. Moreover tests in air would produce brittle cleavage fracture under the triaxial stress state corresponding to that producing qMVC [56], [57], [53]. Work presented in this thesis is consistent with those observations.

Fast Fracture Surface was made up of cleavage like fracture. The surface was made up of many facets which resembled maple leaves, growing in the direction of the final crack propagation. This surface was produced by the brittle catastrophic failure of the bolt.

5.9 FIGURES

FIGURE 5.1: Macroscopic view of colliery A rock bolt. The fracture was at the left end of the bolt segment

FIGURE 5.2: Overview of fracture surface

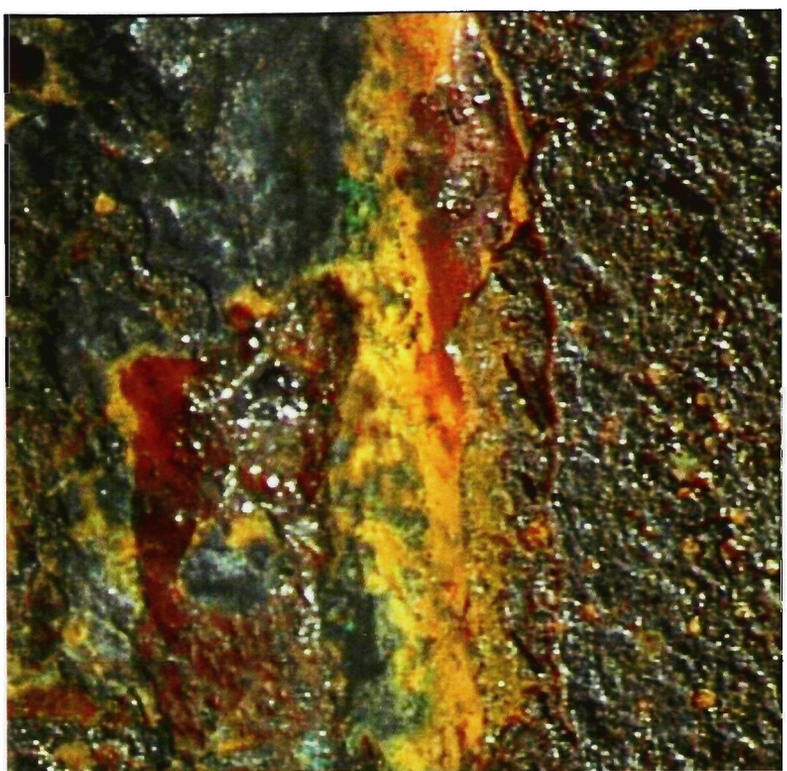

(a) View of secondary cracks

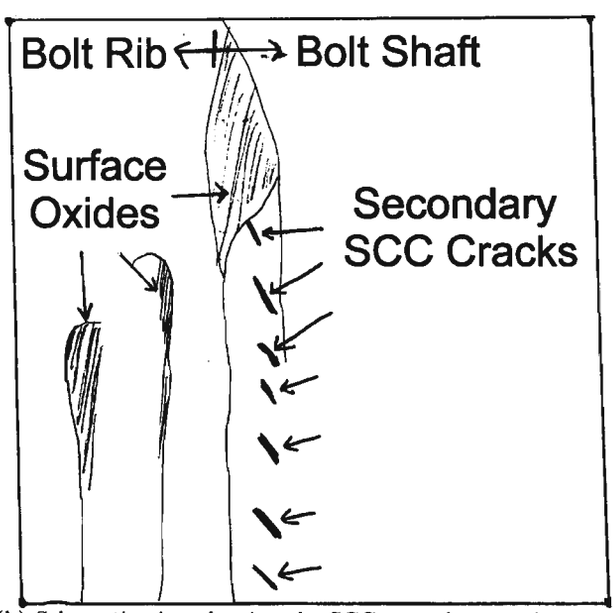

(b) Schematic view showing the SCC secondary cracks along the foot of the rib. The tensile direction was the horizontal plane (sideways)

FIGURE 5.3: SCC secondary cracks

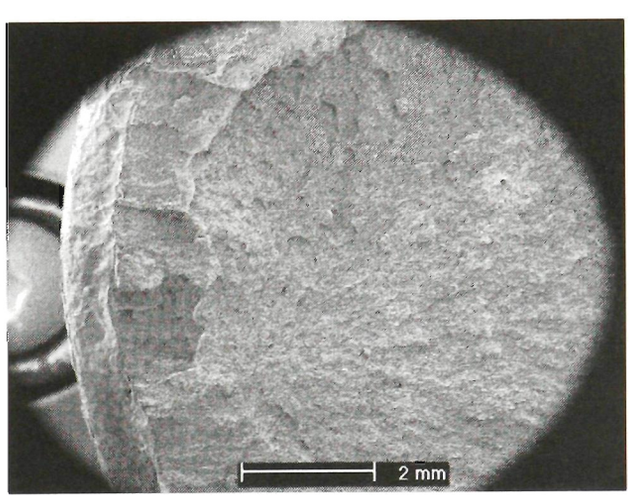

FIGURE 5.4: Stepped fracture surface of rock bolt from colliery A.

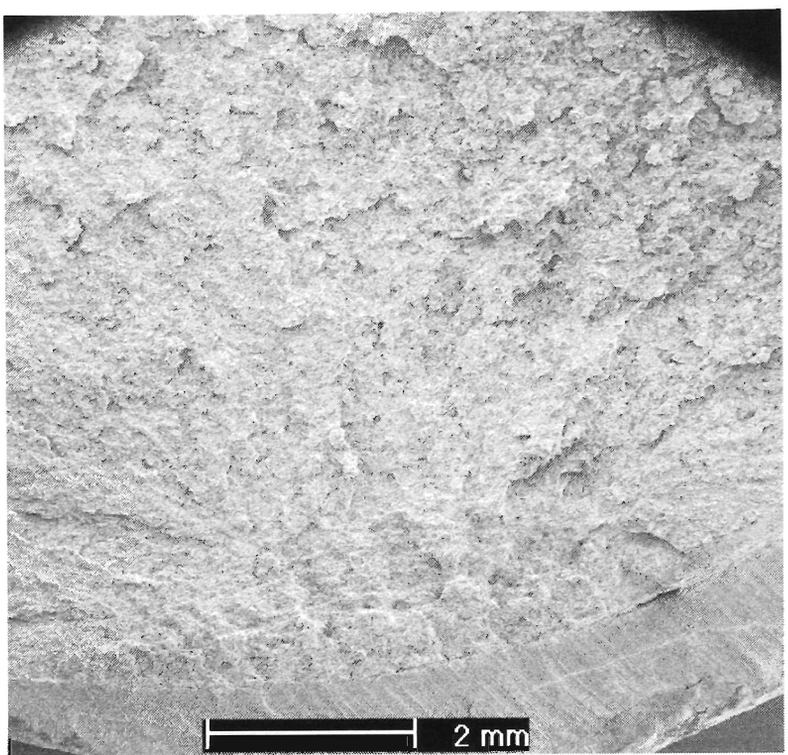

(a) SCC region overview

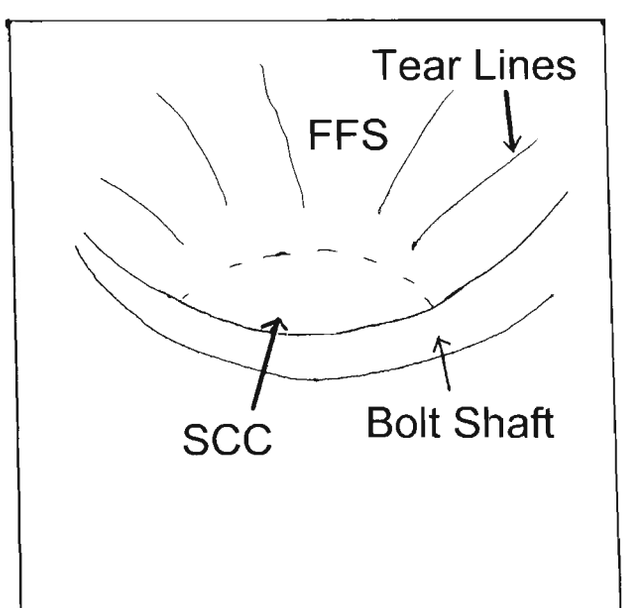

(b) Schematic view showing different fracture regions (FFS = Fast Fracture Surface)

FIGURE 5.5: SCC region overview

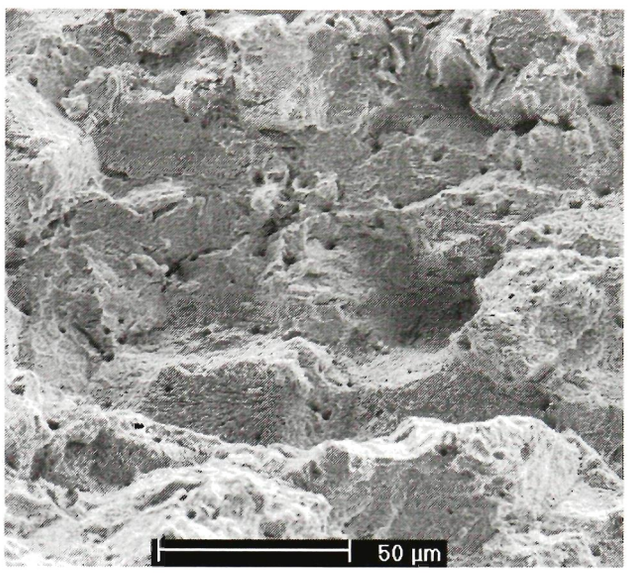

FIGURE 5.6: SCC region detail

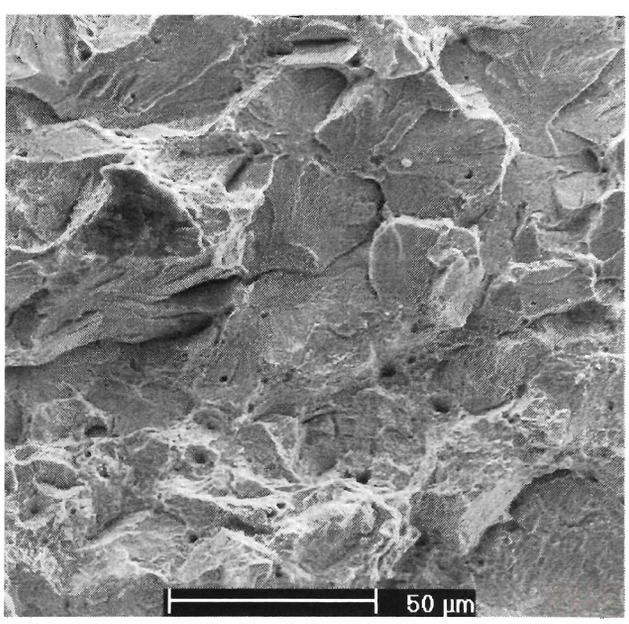

FIGURE 5.7: SCC - fast fracture interface

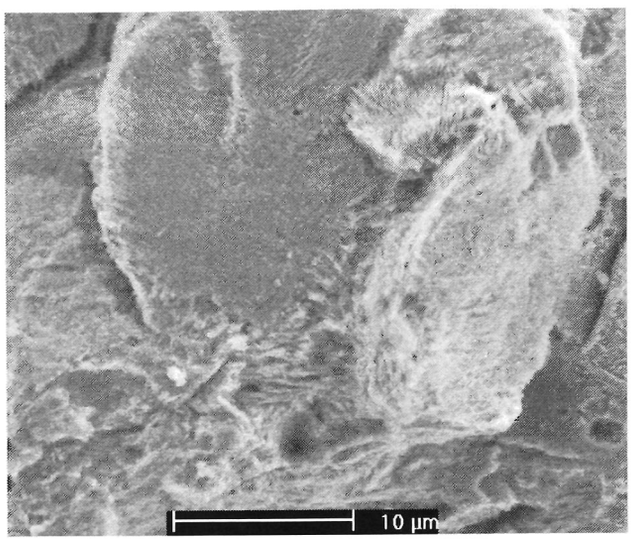

FIGURE 5.8: Detail of Figure 5.7

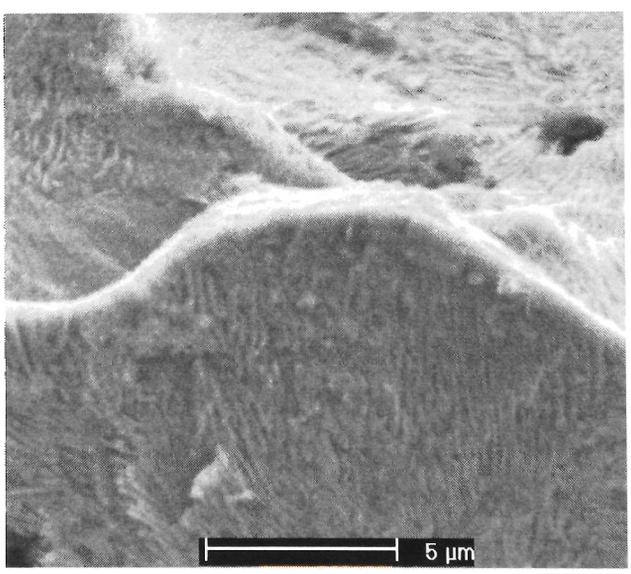

FIGURE 5.9: Very high magnification view of fast fracture surface

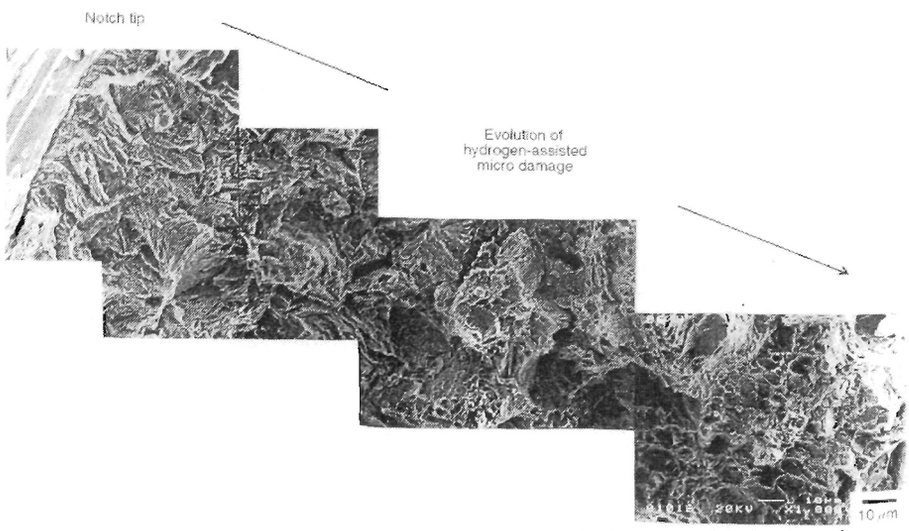

(a) Picture taken by Toribio and Vasseur of evolution of hydrogen assisted micro damage. [53]

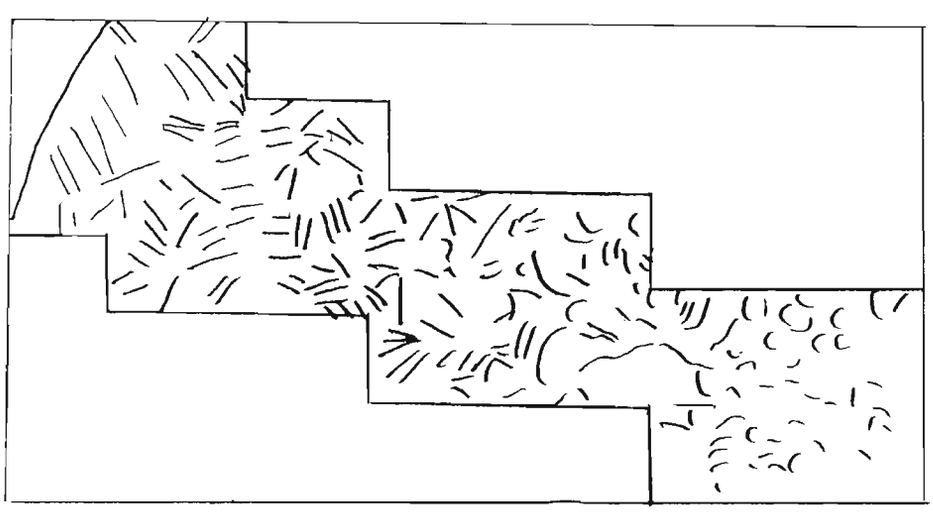

(b) Schematic view showing TTS ridge orientation

FIGURE 5.10: TTS region overview

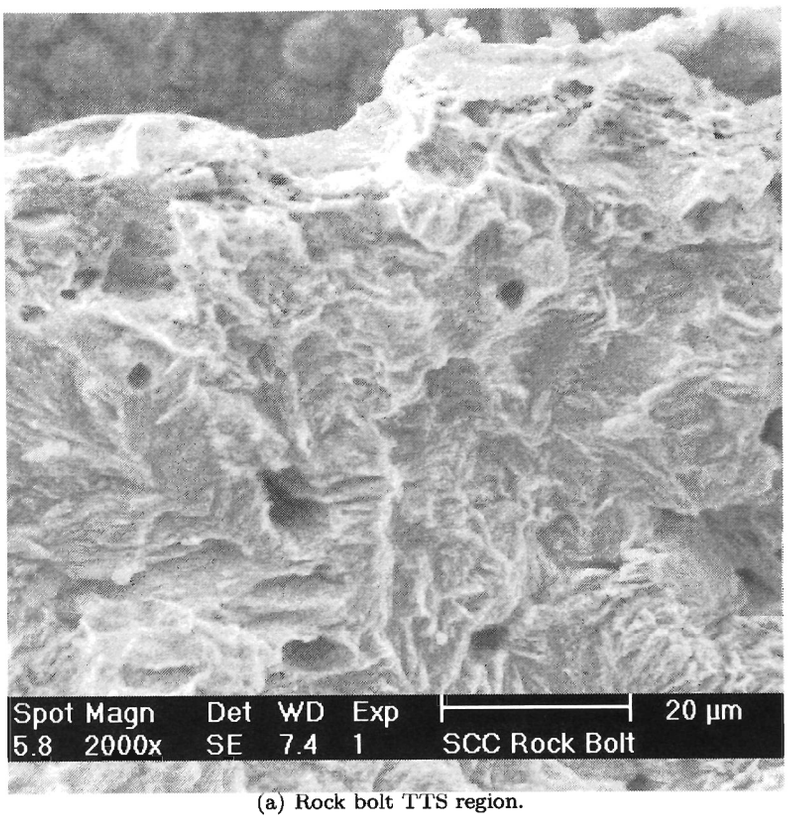

(a) Rock bolt TTS region.

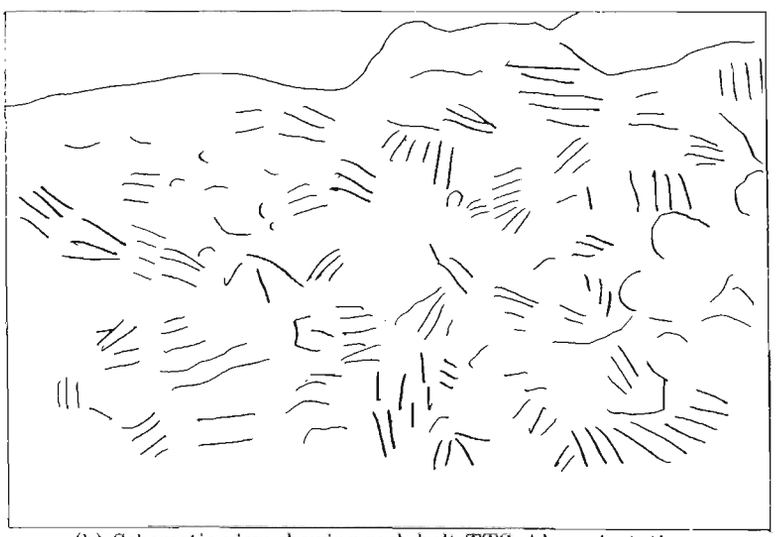

(b) Schematic view showing rock bolt TTS ridge orientation

FIGURE 5.11: Rock bolt TTS region

FIGURE 5.12: Macroscopic view of colliery W rock bolt. The fracture was at the right end of the bolt segment.

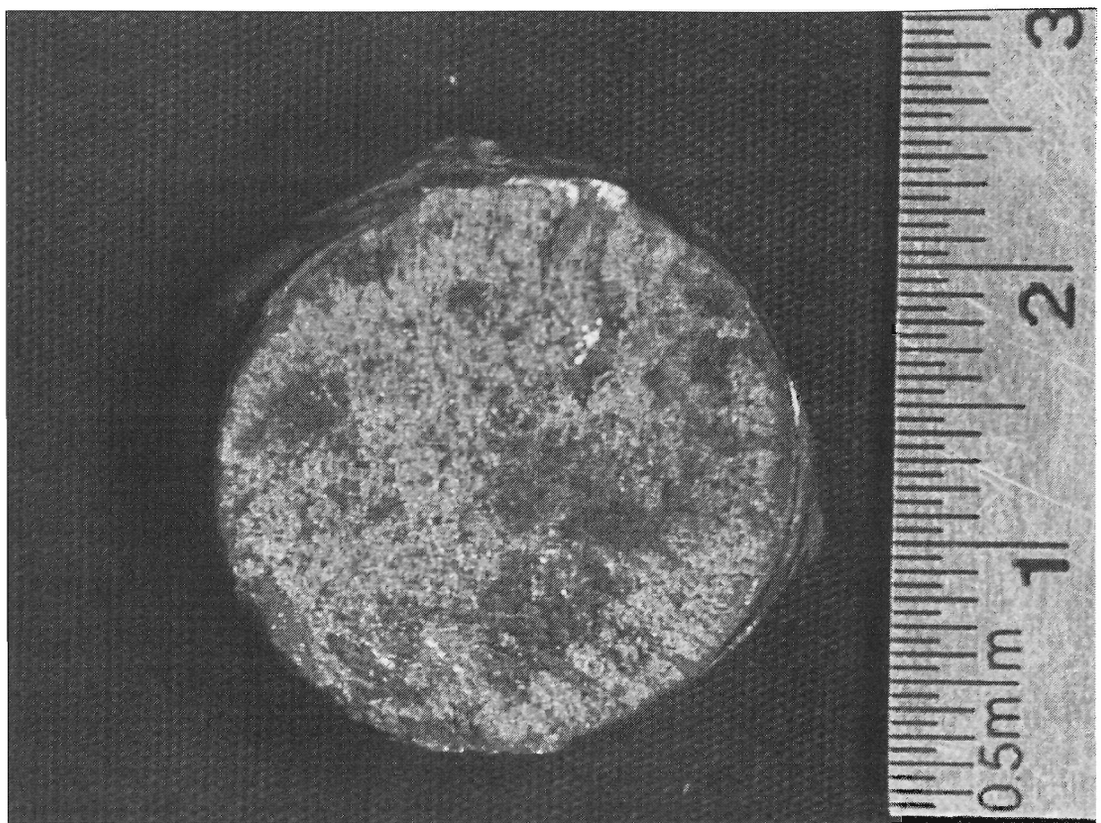

(a) Macroscopic view of the bolt's fracture surface

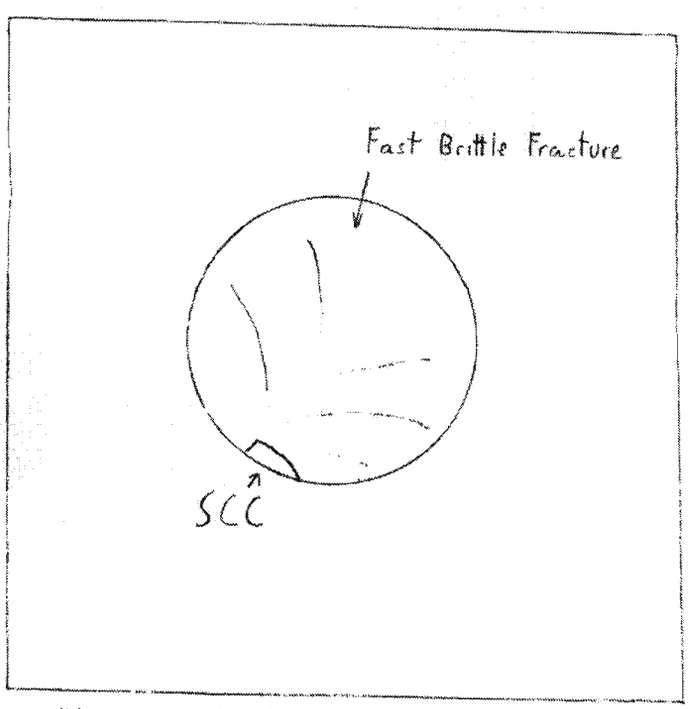

(b) Schematic view showing SCC and fast fracture areas

FIGURE 5.13: Rock Bolt fracture surface

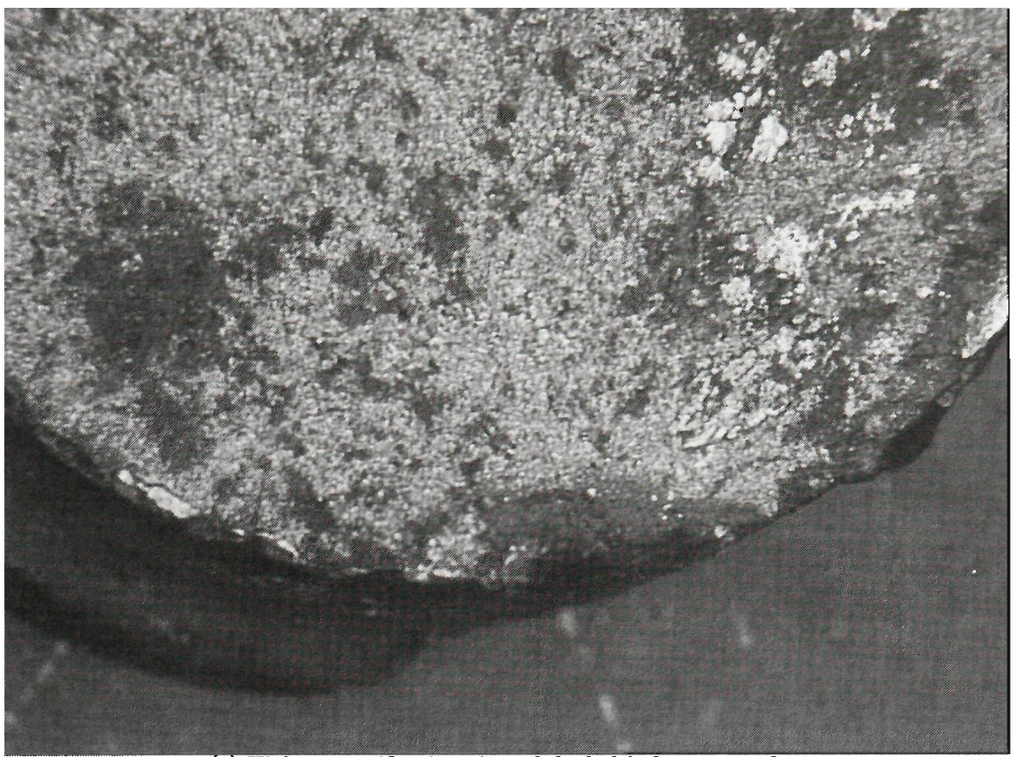

(a) Higher magnification view of the bolt's fracture surface

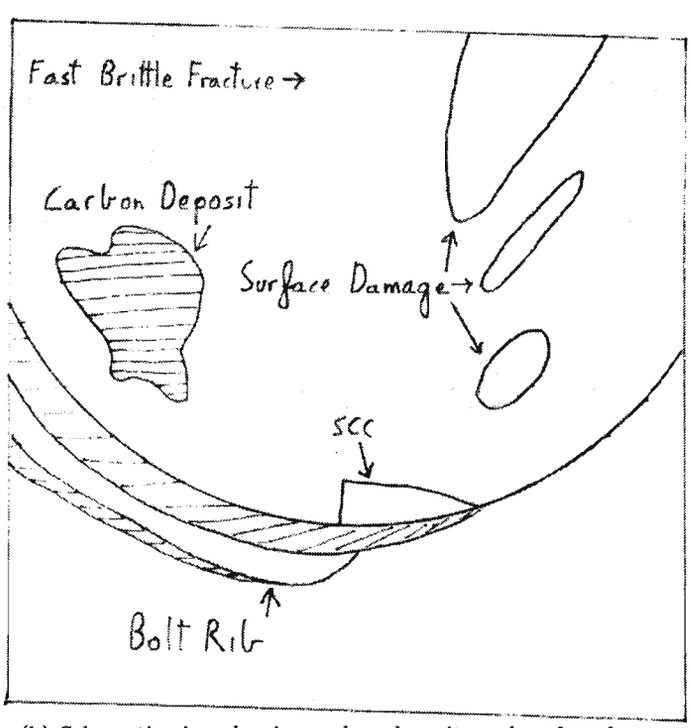

(b) Schematic view showing carbon deposits and surface damage

FIGURE 5.14: Rock Bolt fracture surface

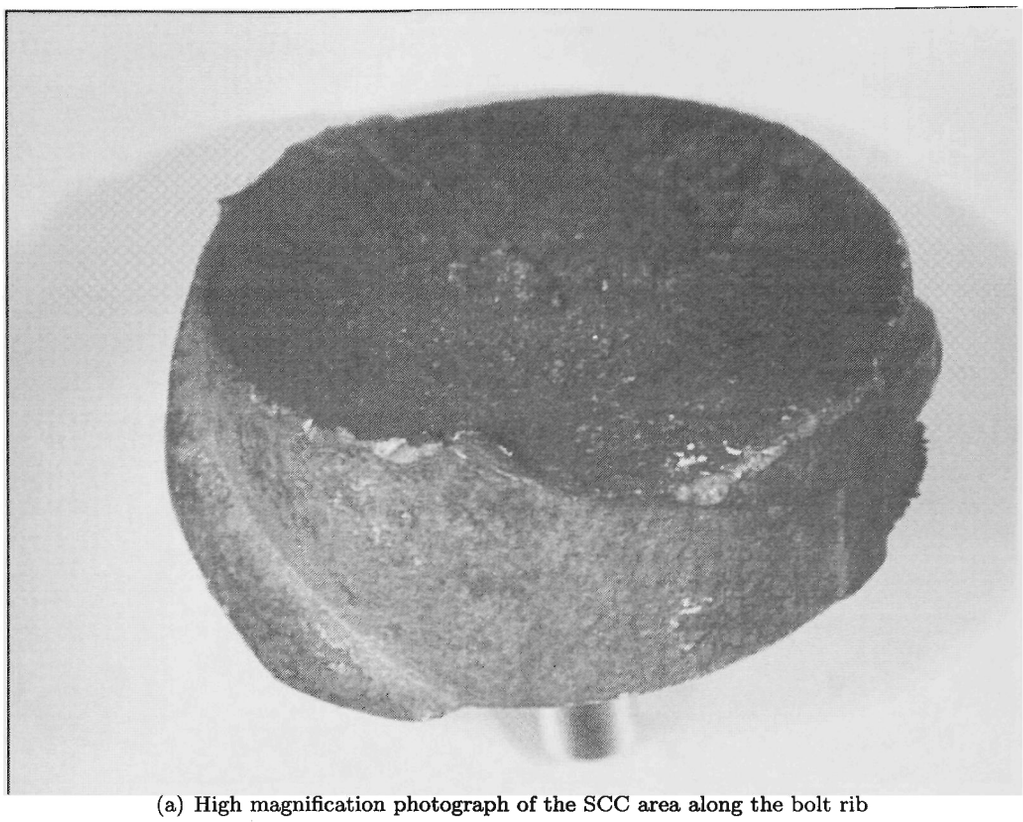

(a) High magnification photograph of the SCC area along the bolt rib

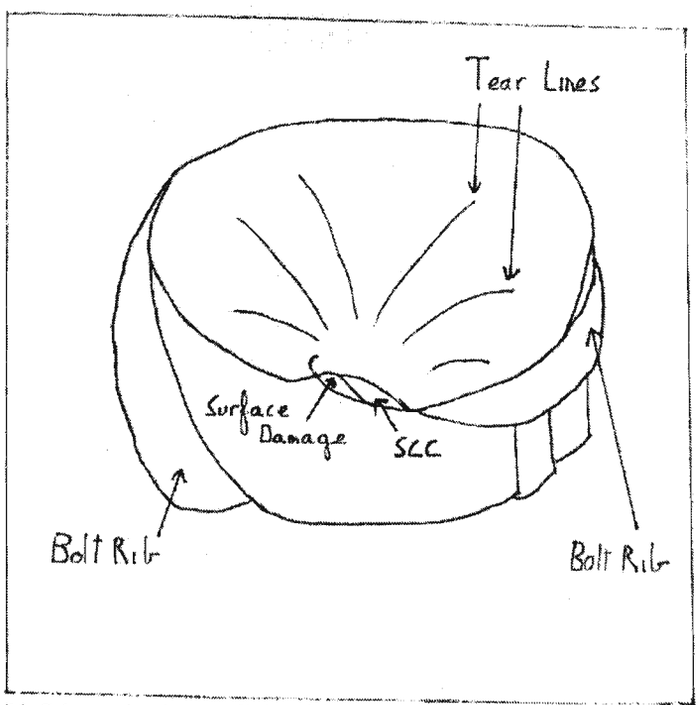

(b) Schematic view outlining SCC area, carbon deposits and surface damage

FIGURE 5.15: SCC along the foot of the bolt rib

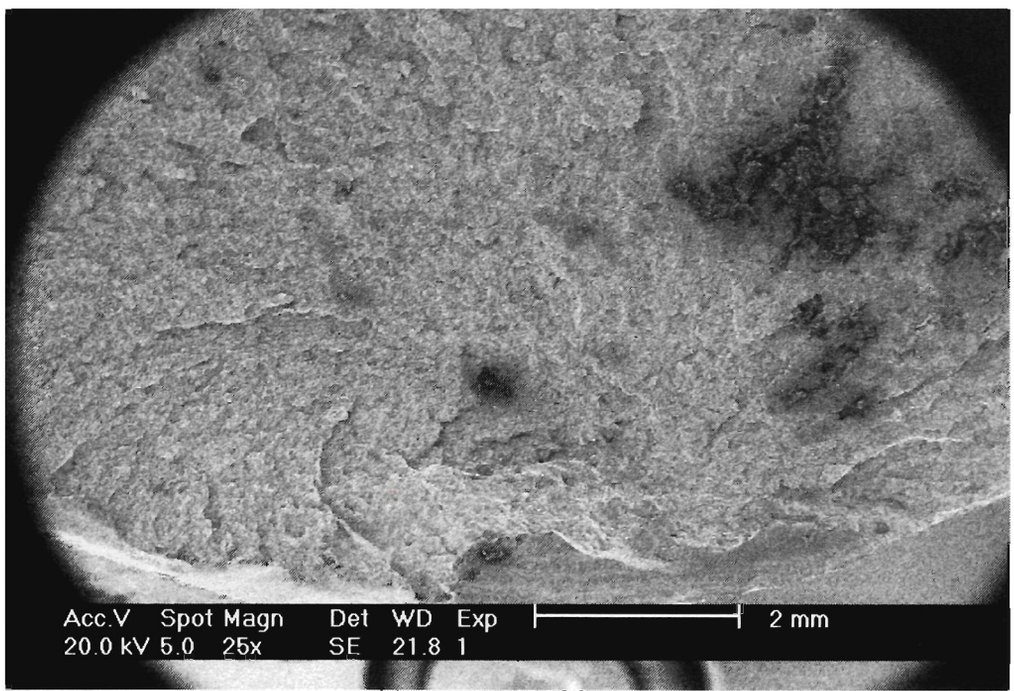

(a) Overview of SCC area

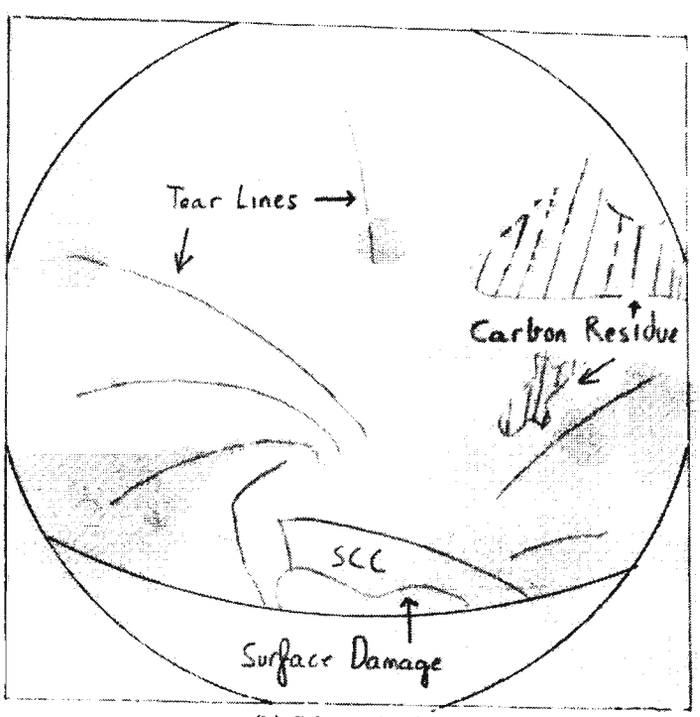

(b) Schematic view

FIGURE 5.16: SCC overview

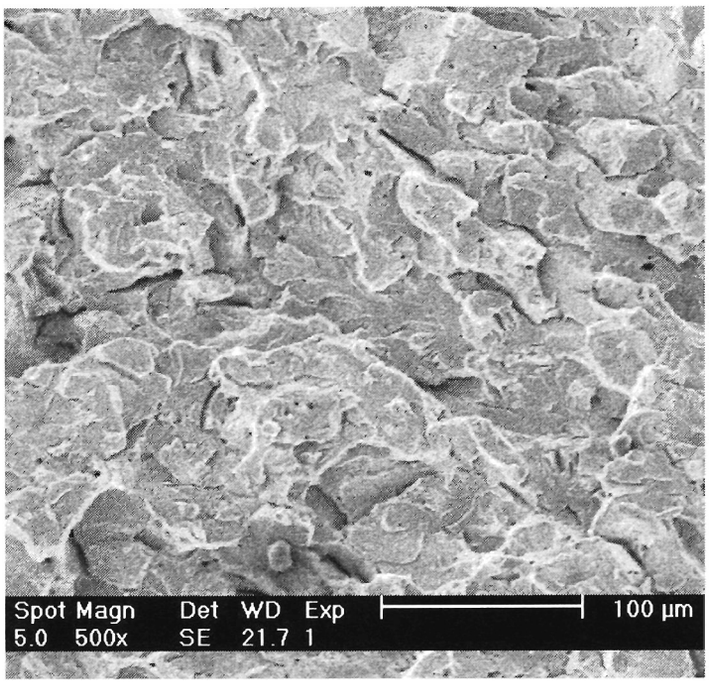

FIGURE 5.17: Typical Fast Fracture surface.

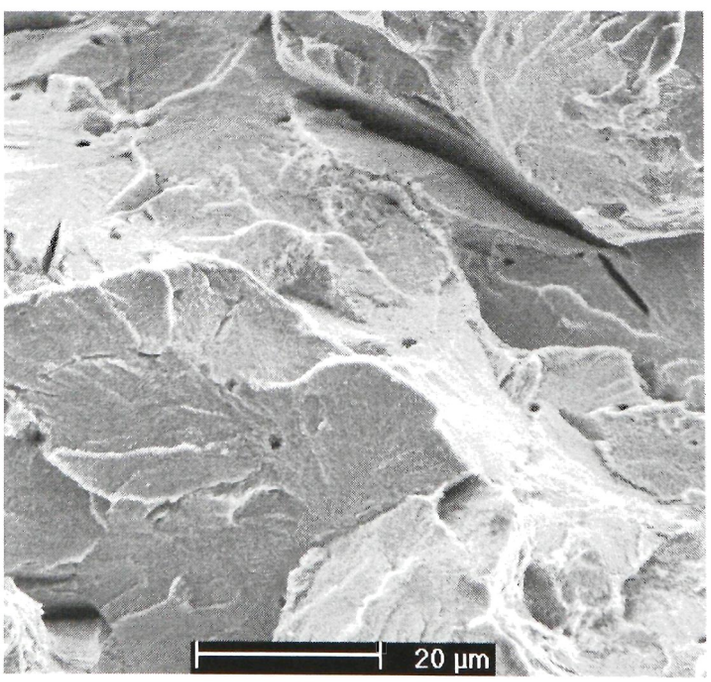

FIGURE 5.18: Higher magnification of fast fracture in a different bolt.

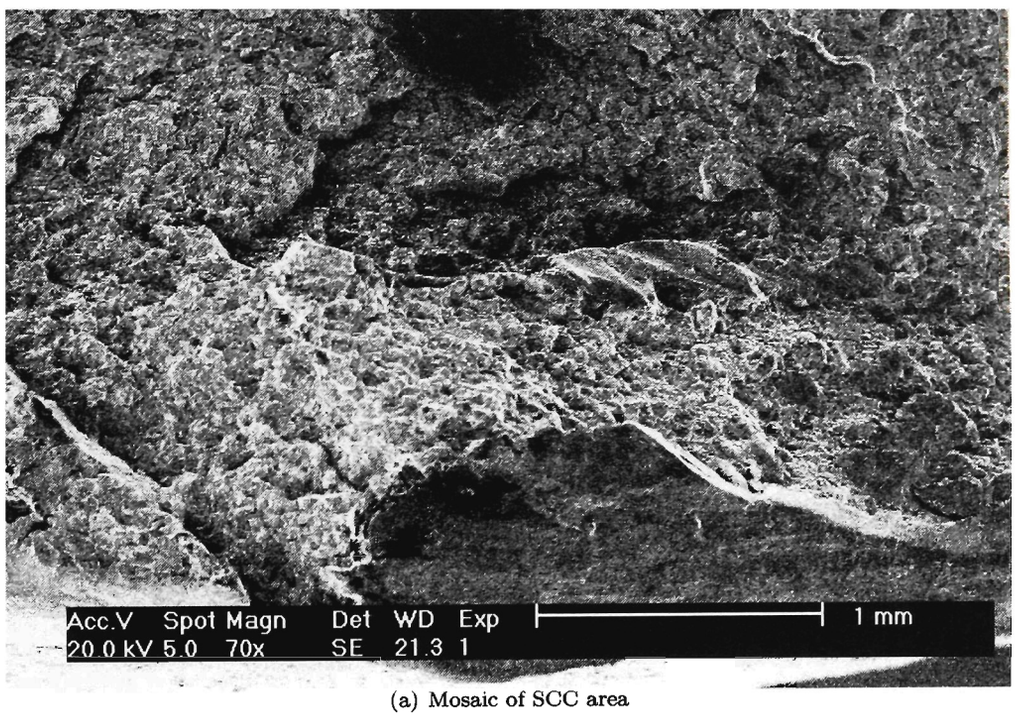

(a) Mosaic of SCC area

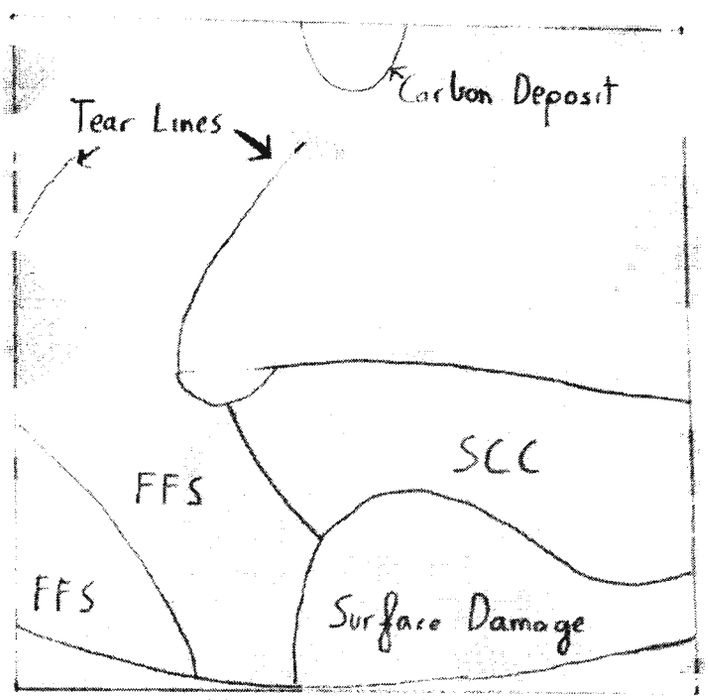

(b) Schematic view of mosaic

FIGURE 5.19: SCC overview

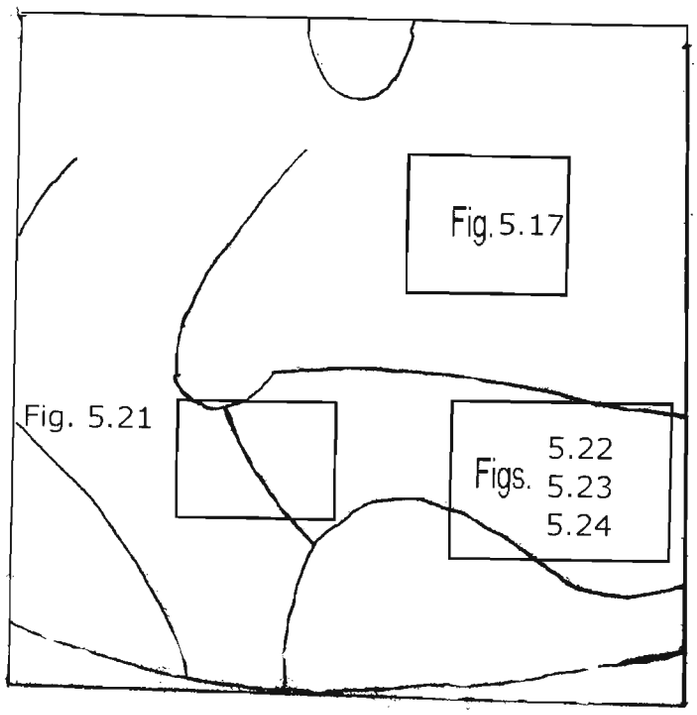

FIGURE 5.20: Key to Figures 5.17, 5.21, 5.22, 5.23 and 5.24

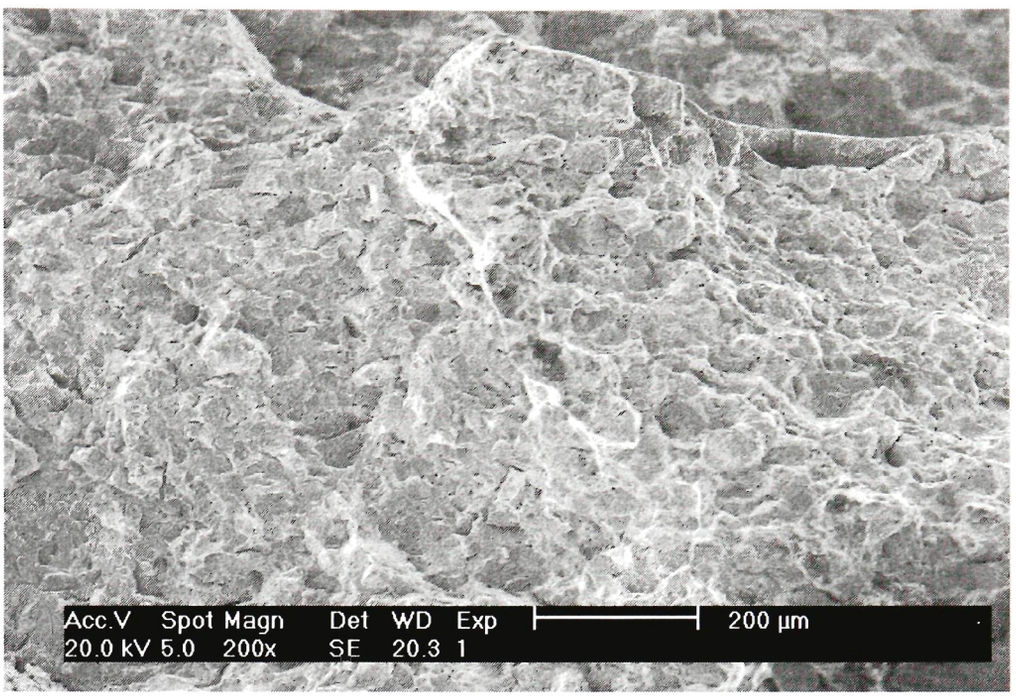

FIGURE 5.21: Fast brittle fracture interface with SCC.

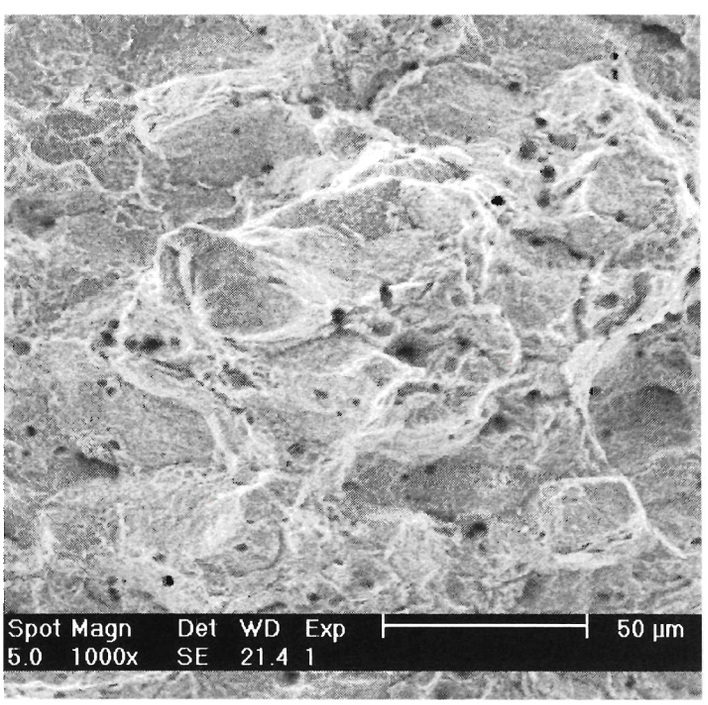

FIGURE 5.22: Typical SCC topography.

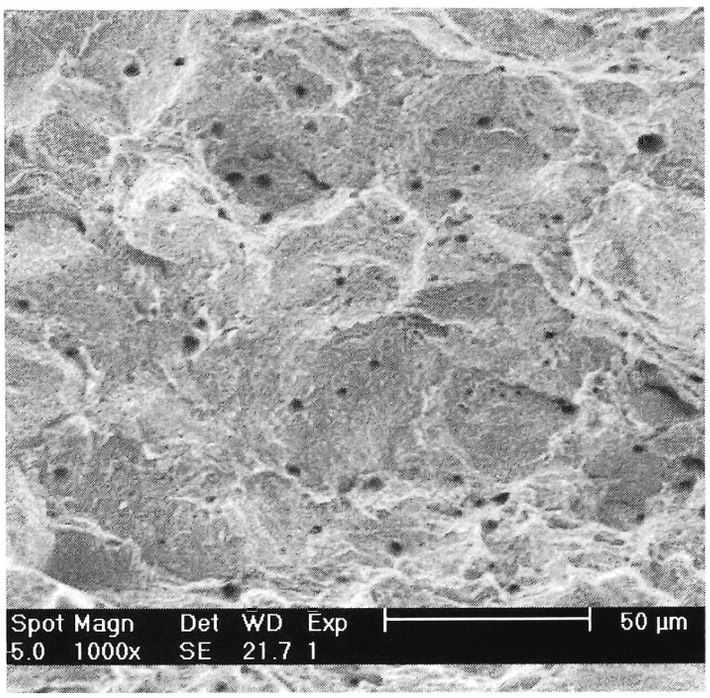

FIGURE 5.23: Typical SCC topography.

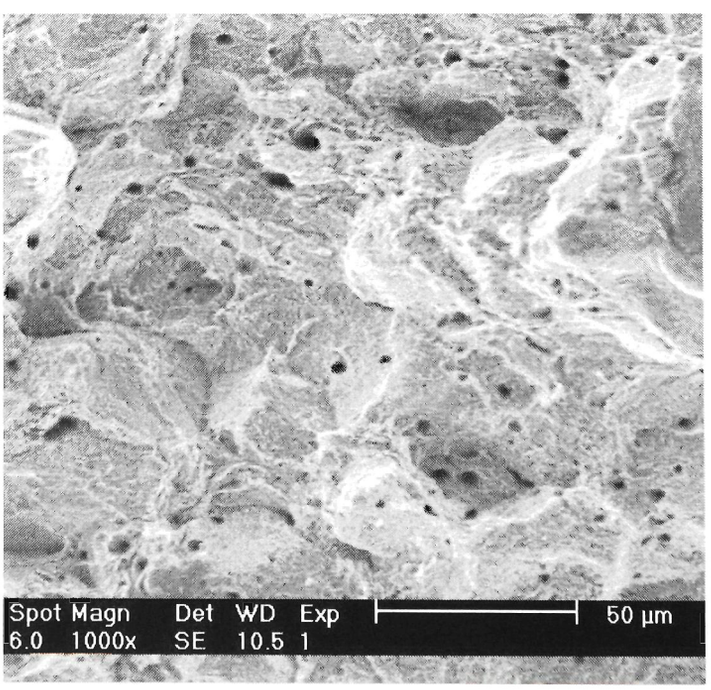

FIGURE 5.24: Typical SCC topography.

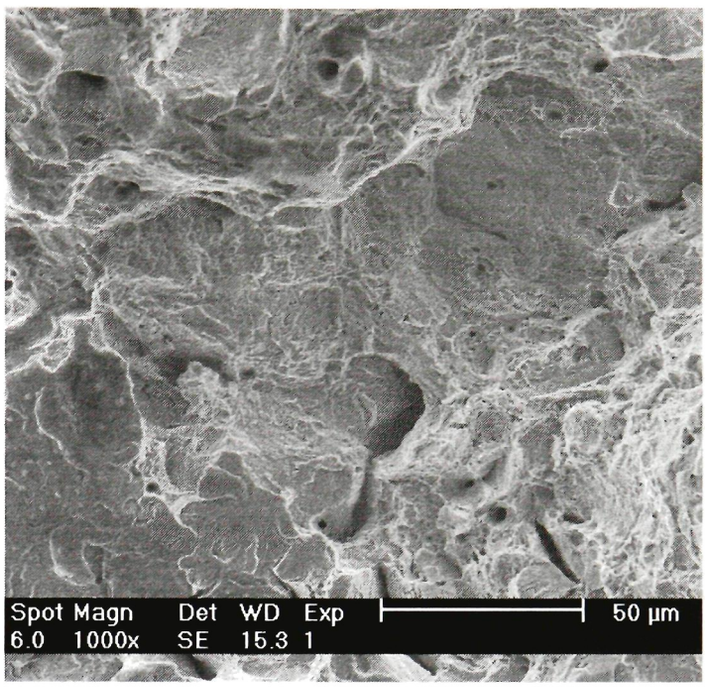

FIGURE 5.25: SCC from sample LIST08. Fast Fracture region is on lower left, whilst SCC is on the upper right.

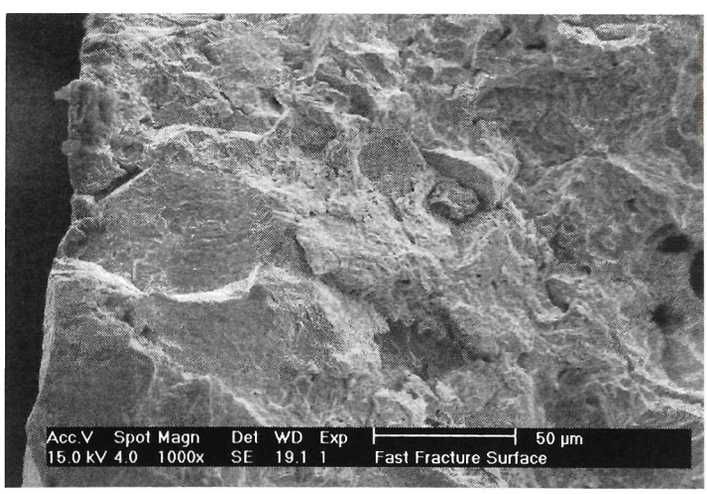

FIGURE 5.26: SCC region from sample LIST01

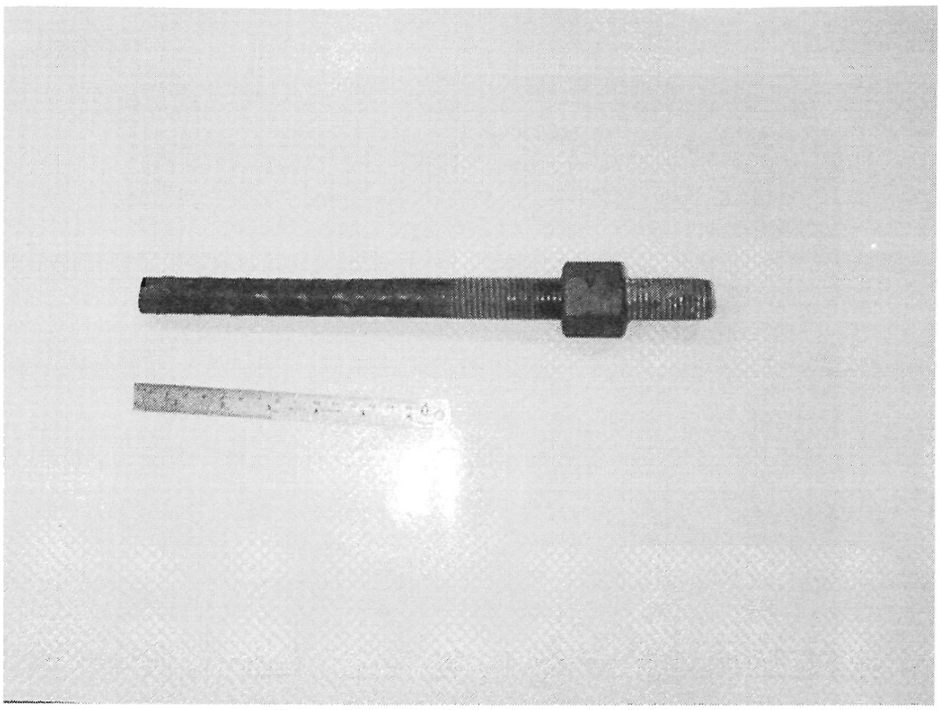

FIGURE 5.27: Overview of failed rock bolt

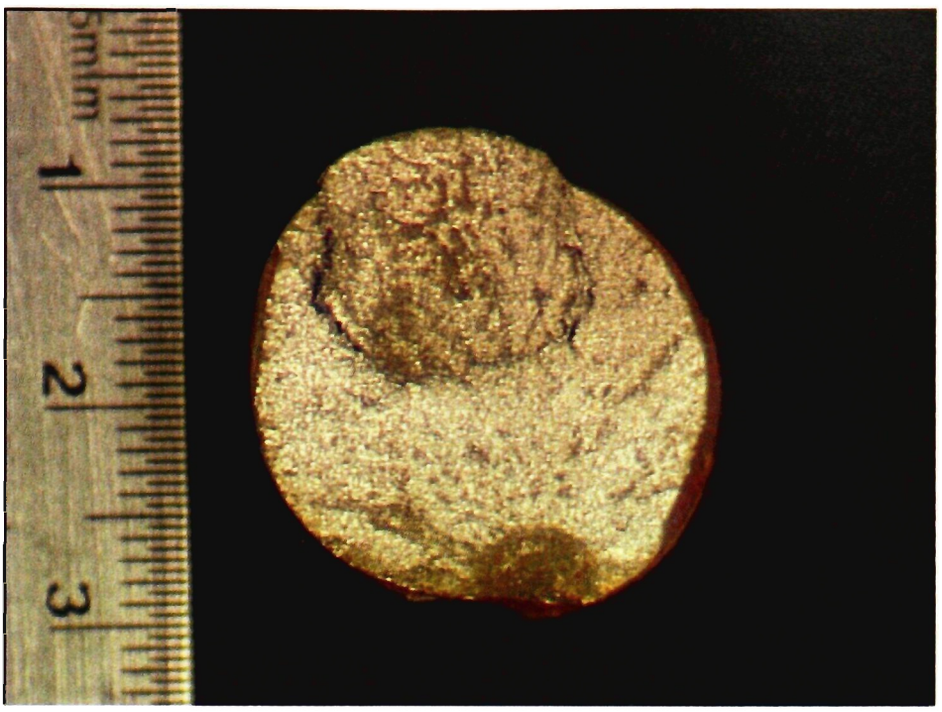

FIGURE 5.28: Macroscopic view of rock bolt's fracture surface

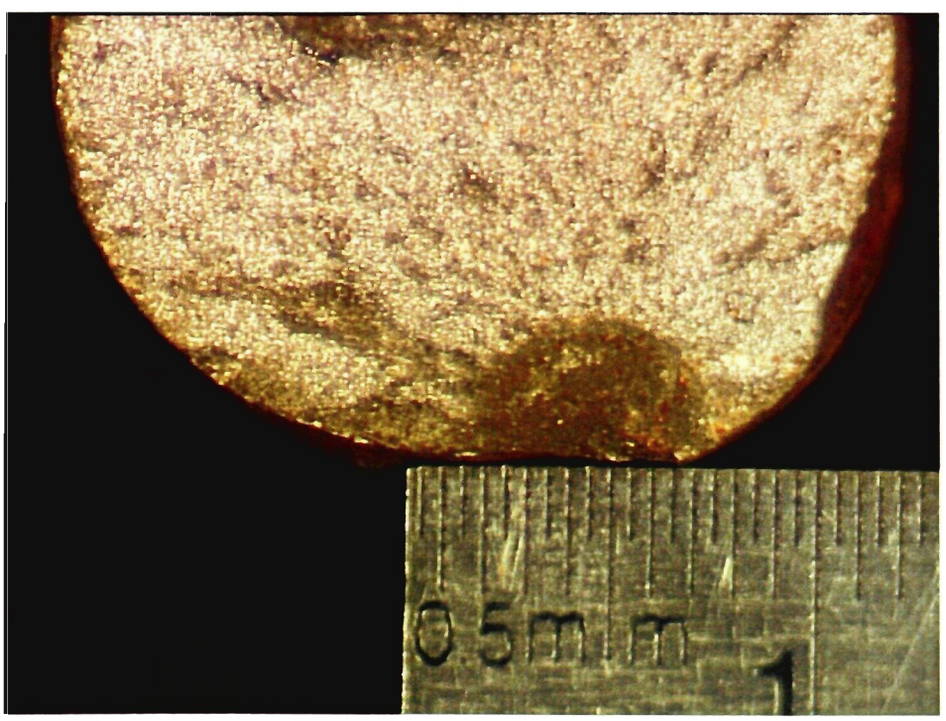

FIGURE 5.29: Macroscopic view of rock bolt's fracture surface at higher magnification

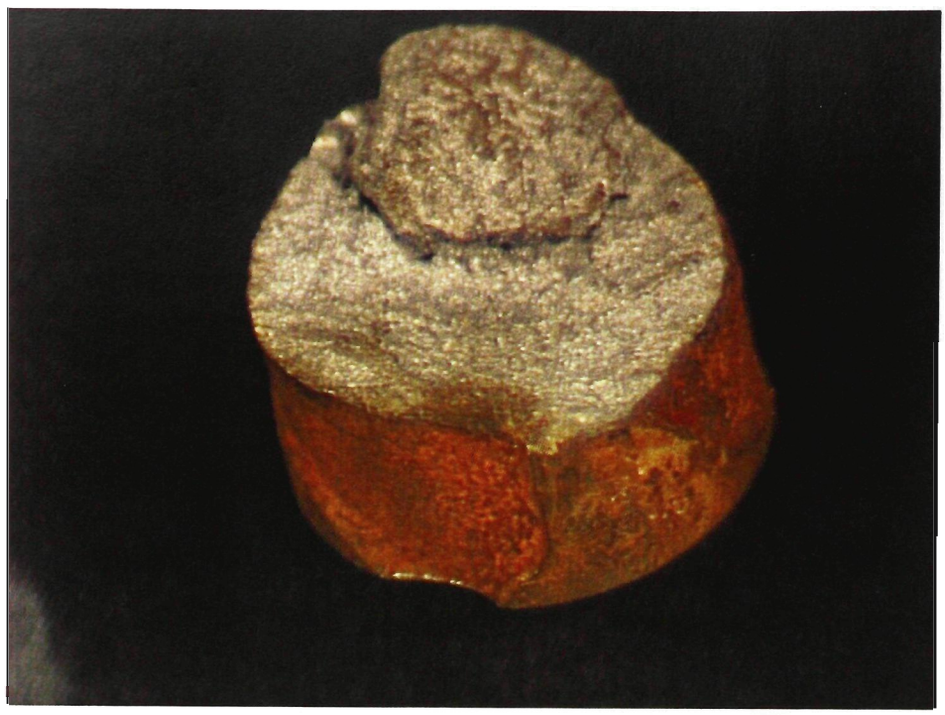

FIGURE 5.30: Side view of rock bolt displaying rib pattern

FIGURE 5.31: Diagram displaying SCC initiation site on the bolt rib pattern

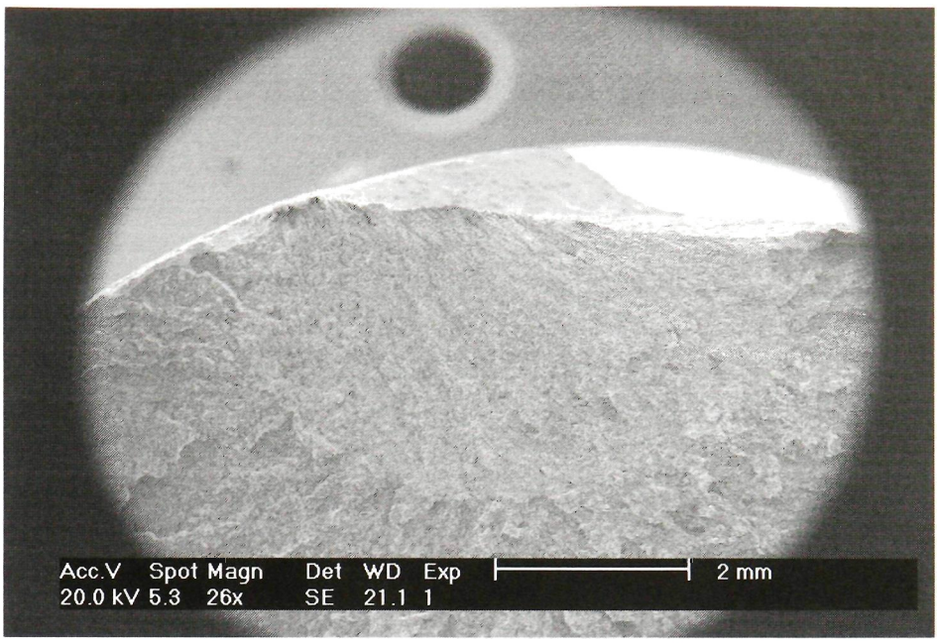

FIGURE 5.32: Overview of SCC region

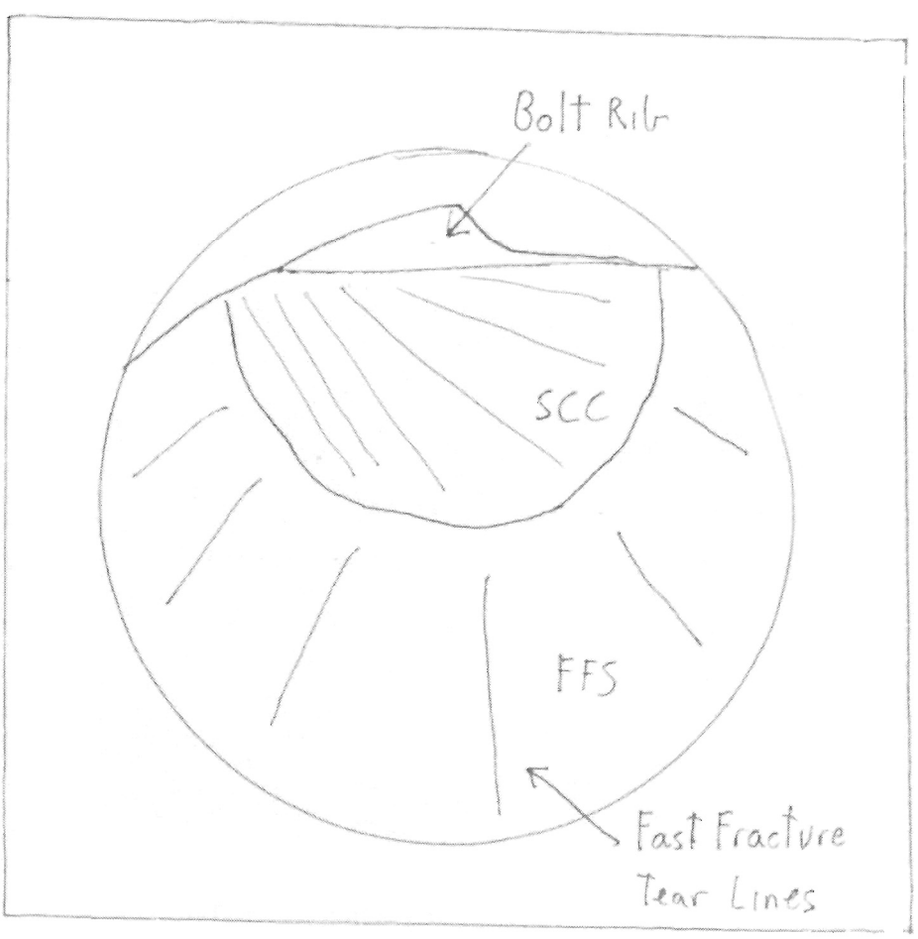

FIGURE 5.33: Diagram displaying overview of SCC region

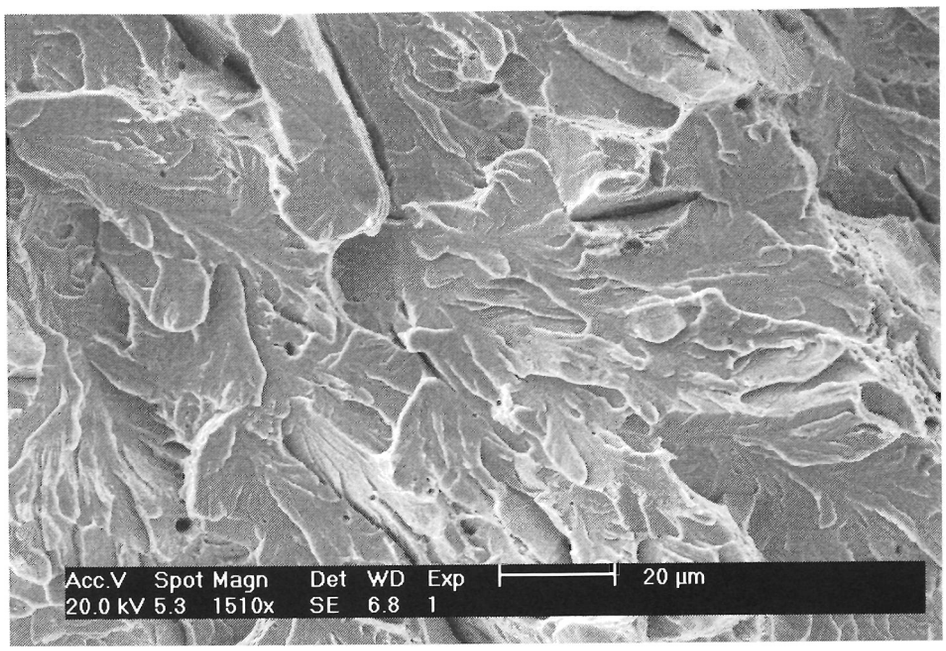

FIGURE 5.34: Fast fracture surface at x1510

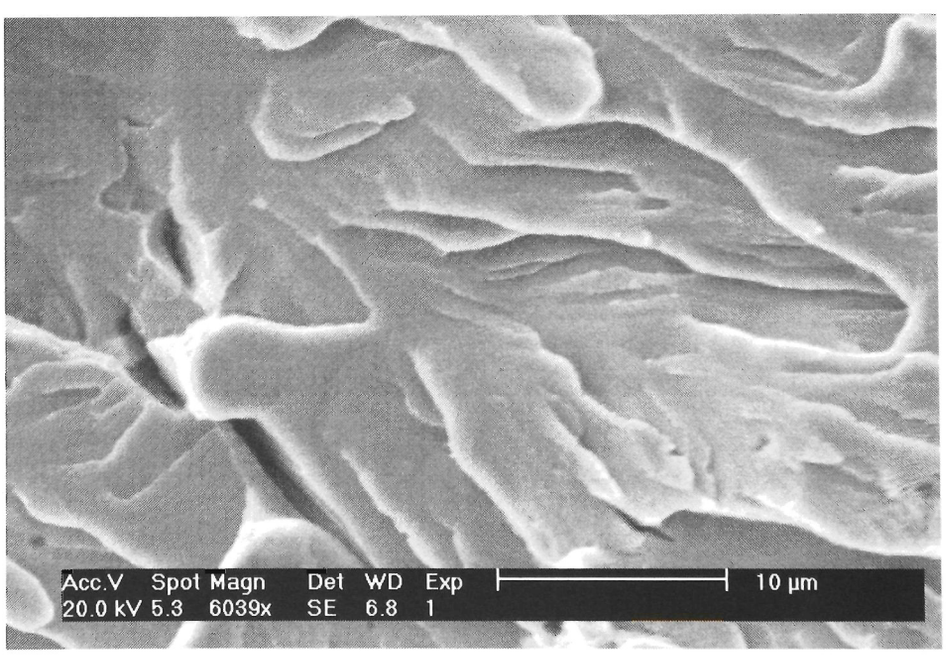

FIGURE 5.35: Fast fracture surface at x6039

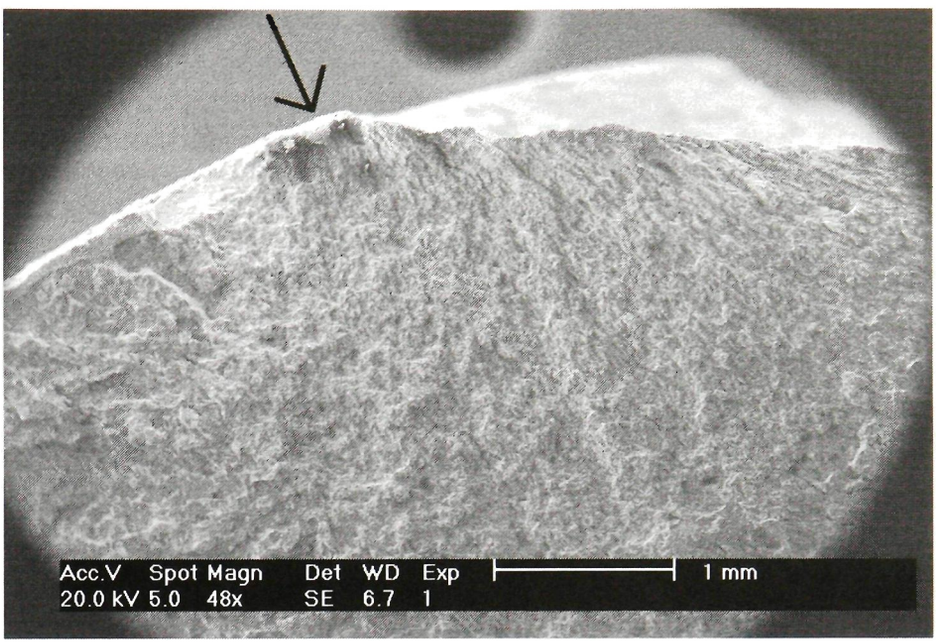

FIGURE 5.36: SCC overview. Arrow points to crack initiation site.

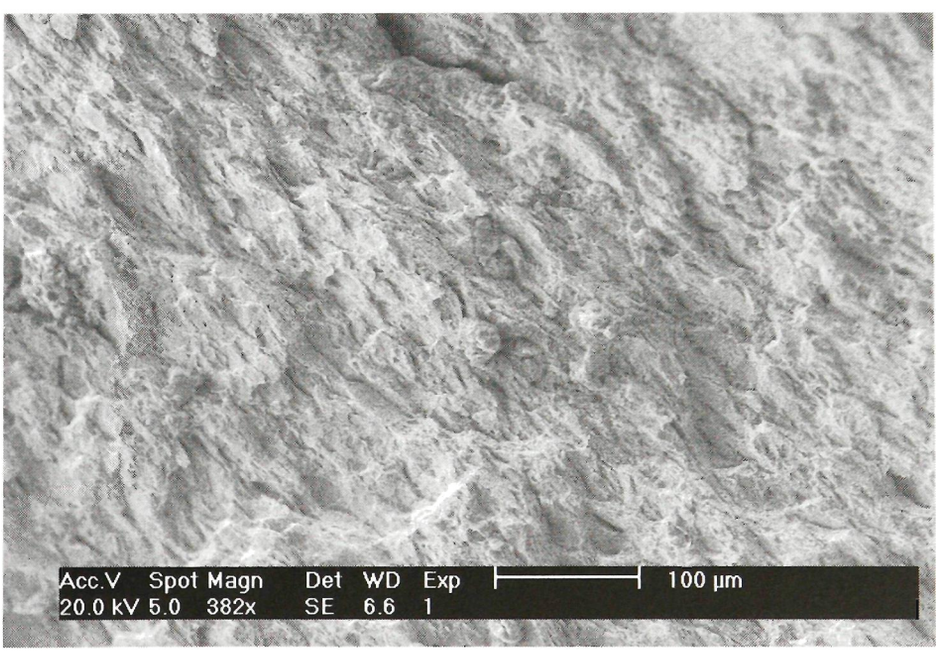

FIGURE 5.37: Detailed view of channels

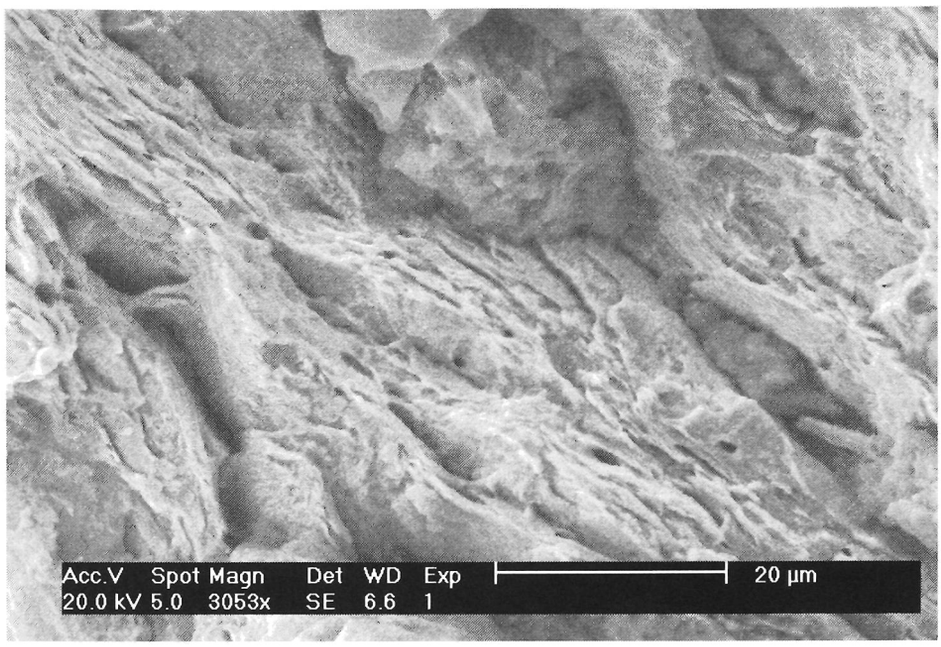

FIGURE 5.38: Detailed view of channels

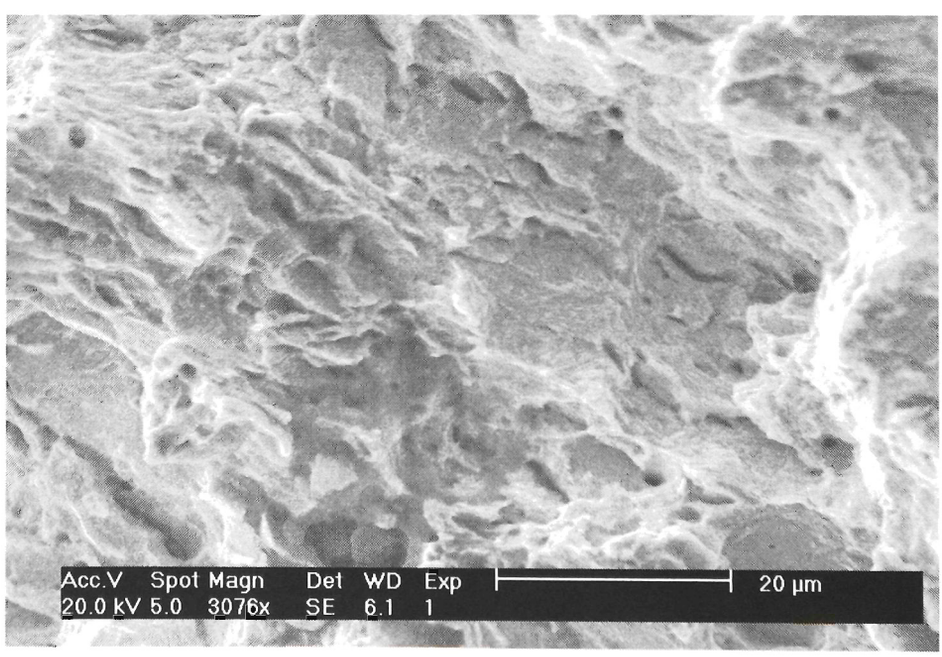

FIGURE 5.39: Non oriented SCC

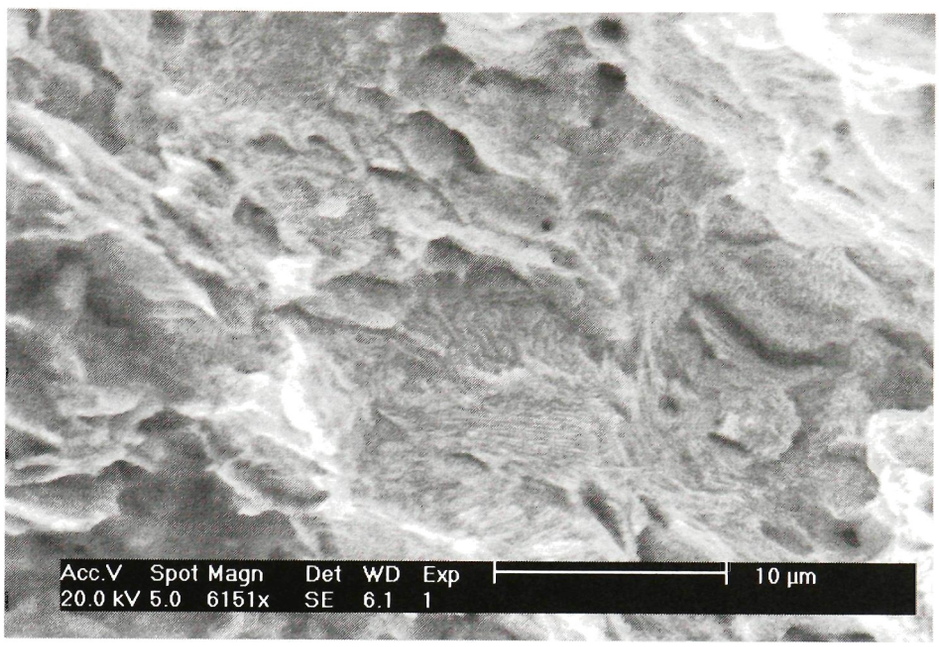

FIGURE 5.40: Higher magnification shot of Figure 5.39

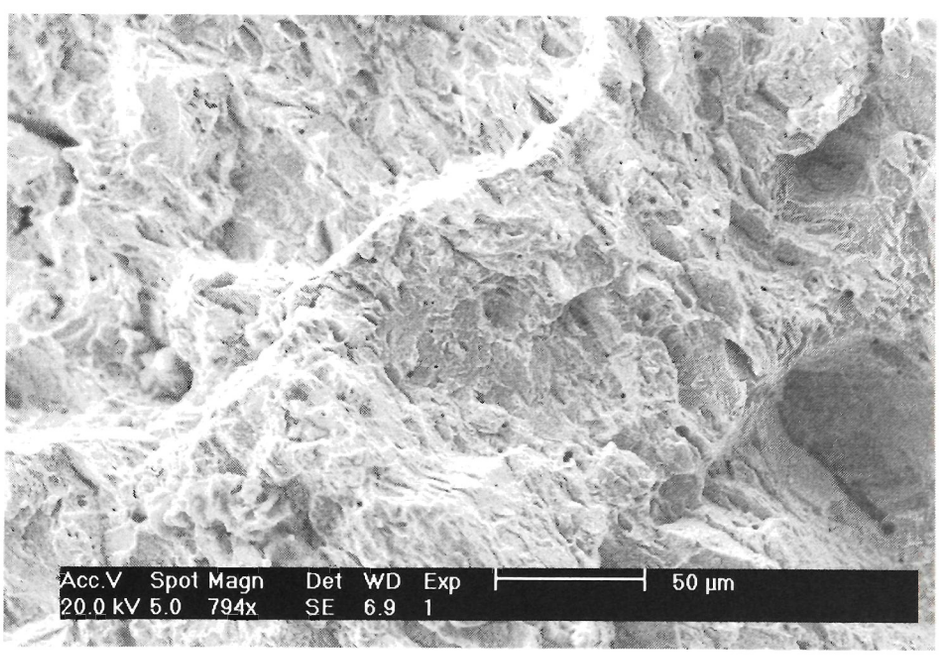

FIGURE 5.41: SCC region x794

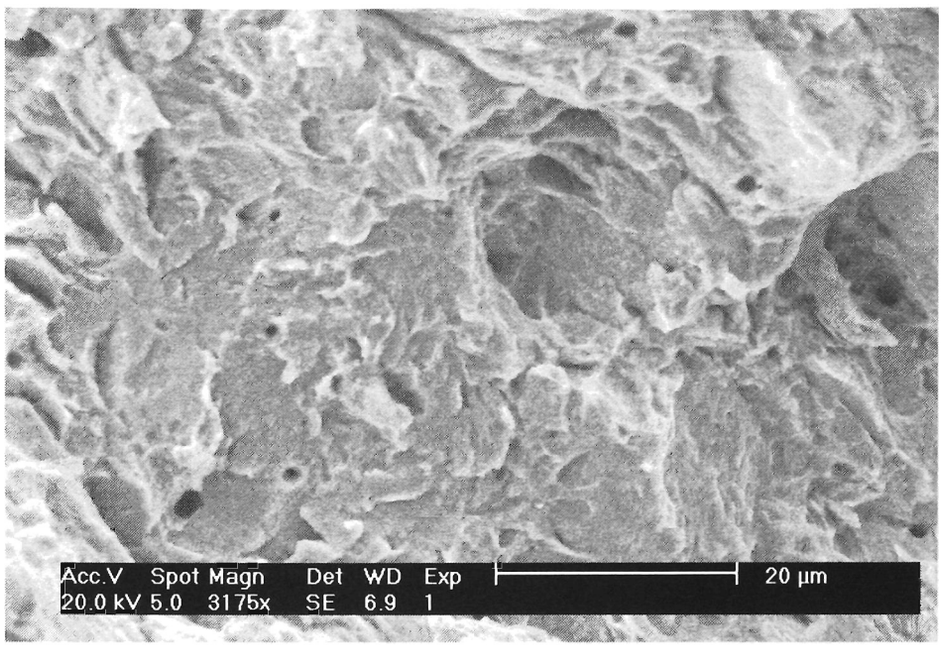

FIGURE 5.42: Detail of Figure 5.41 x3175

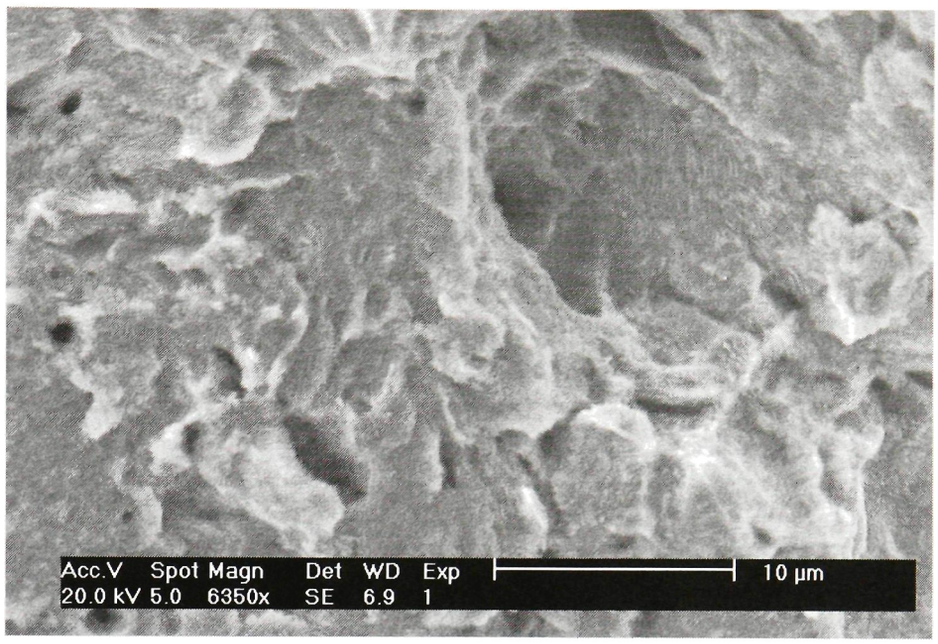

FIGURE 5.43: Detail of Figure 5.41 x6350

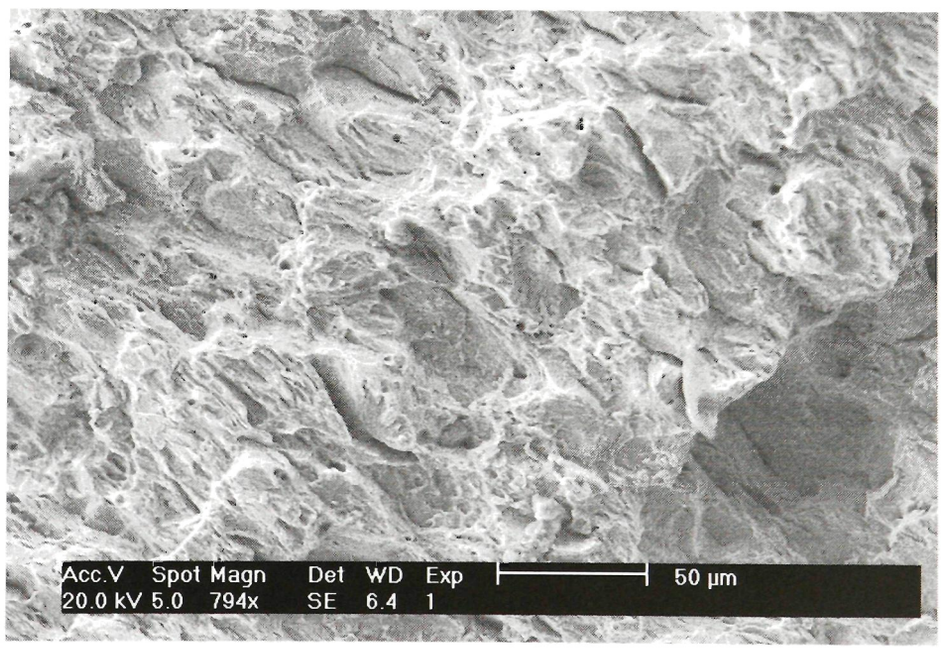

FIGURE 5.44: SCC region x794

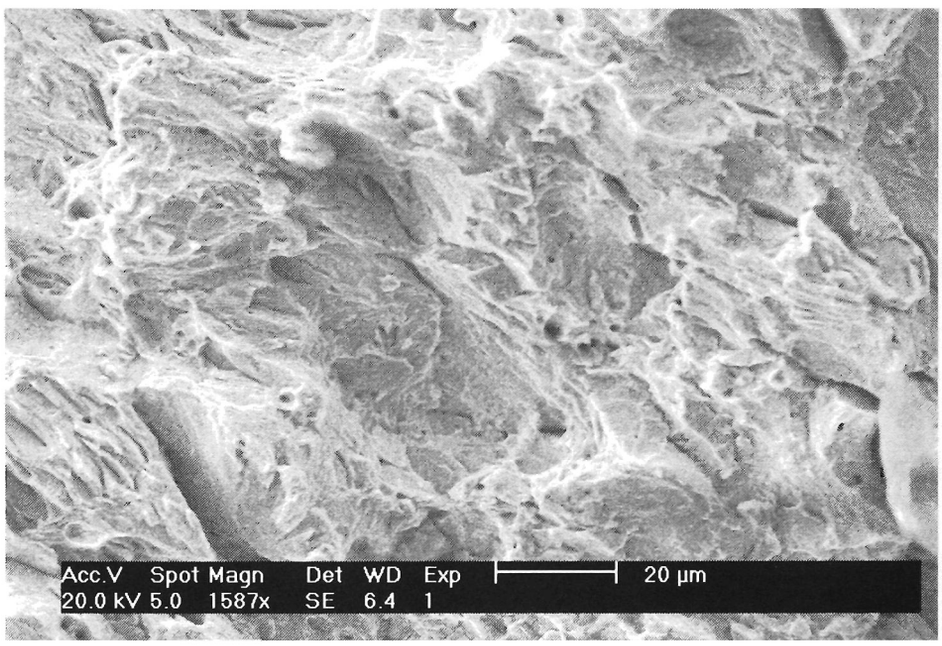

FIGURE 5.45: Detail of Figure 5.44 x1587

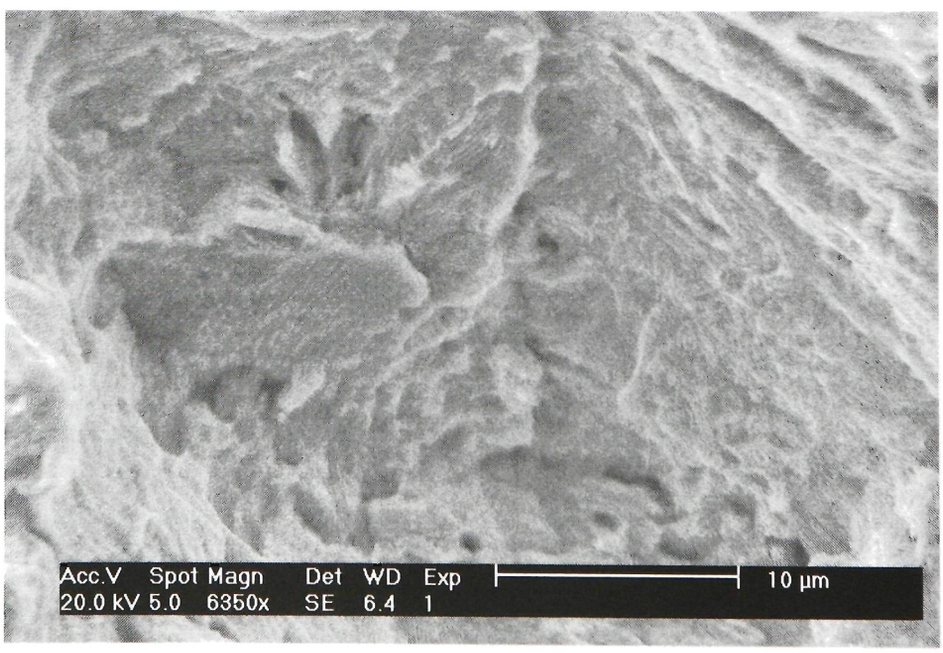

FIGURE 5.46: Detail of Figure 5.44 x6350

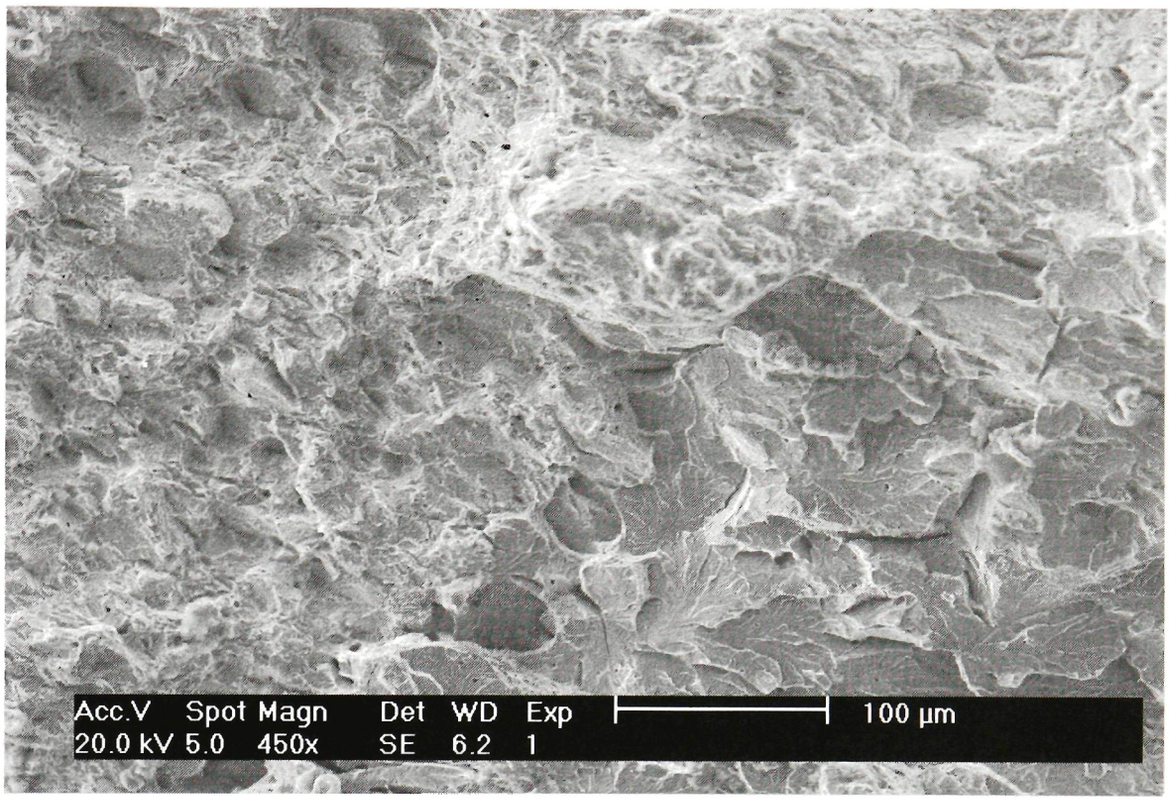

FIGURE 5.47: SCC-FFS interface x450

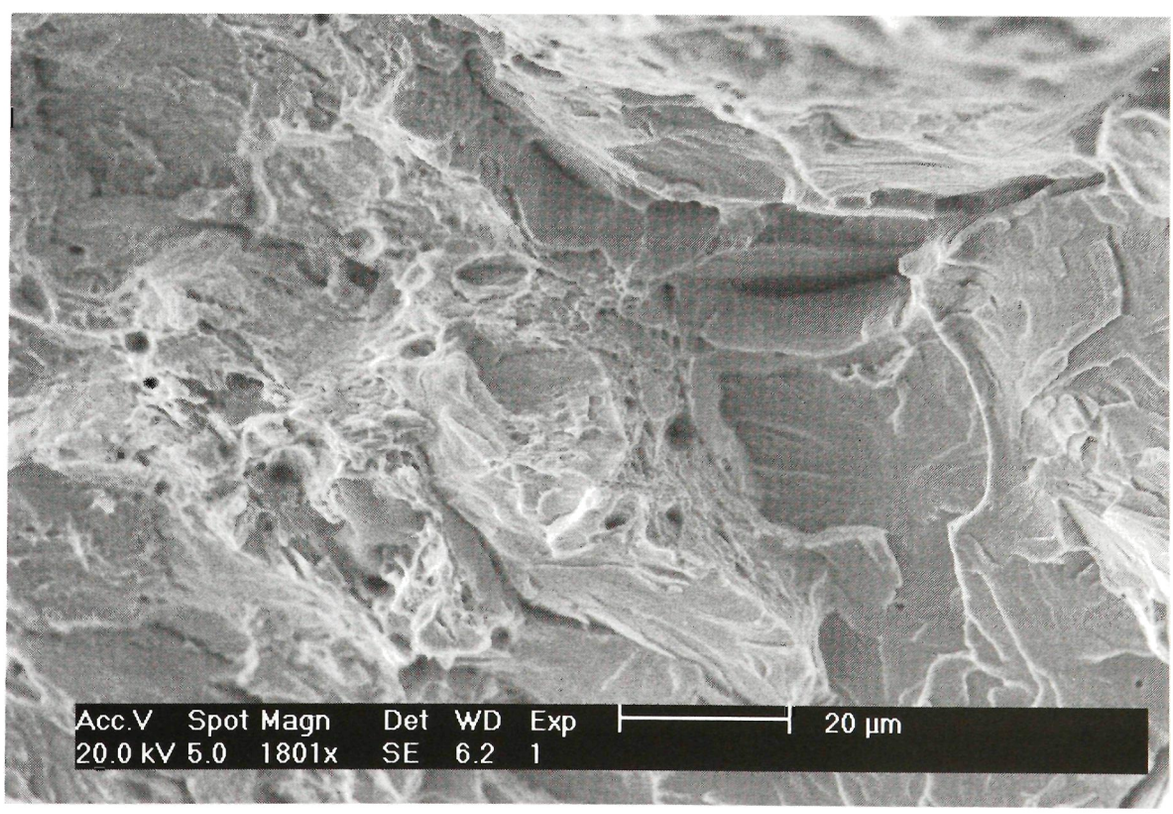

FIGURE 5.48: SCC-FFS interface x1801

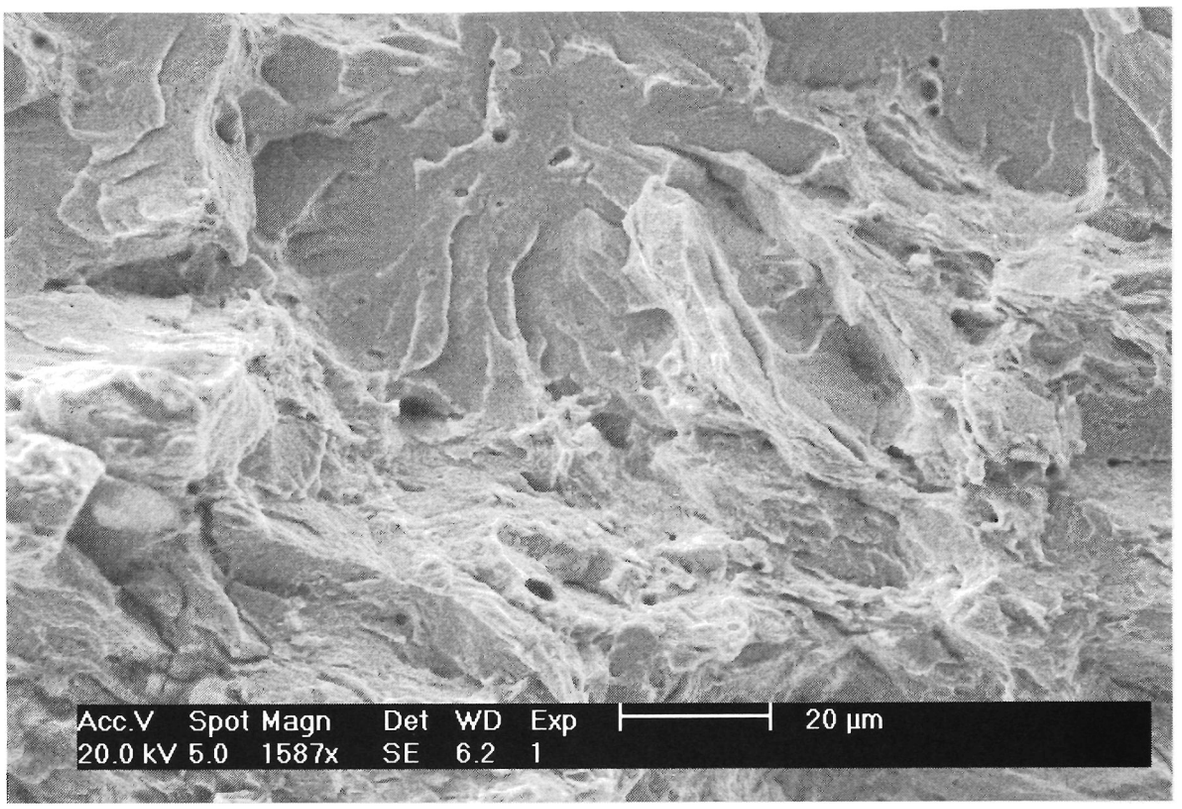

FIGURE 5.49: SCC-FFS interface x1587

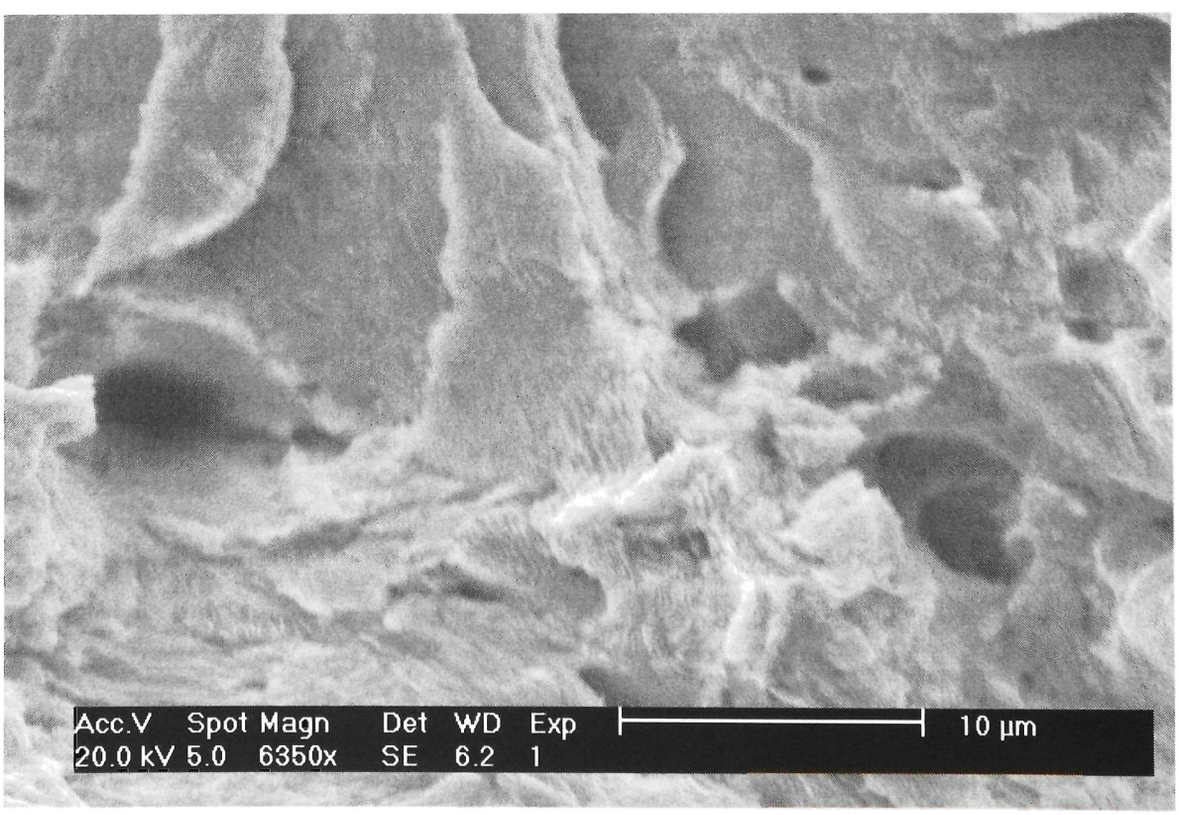

FIGURE 5.50: SCC-FFS interface x6350

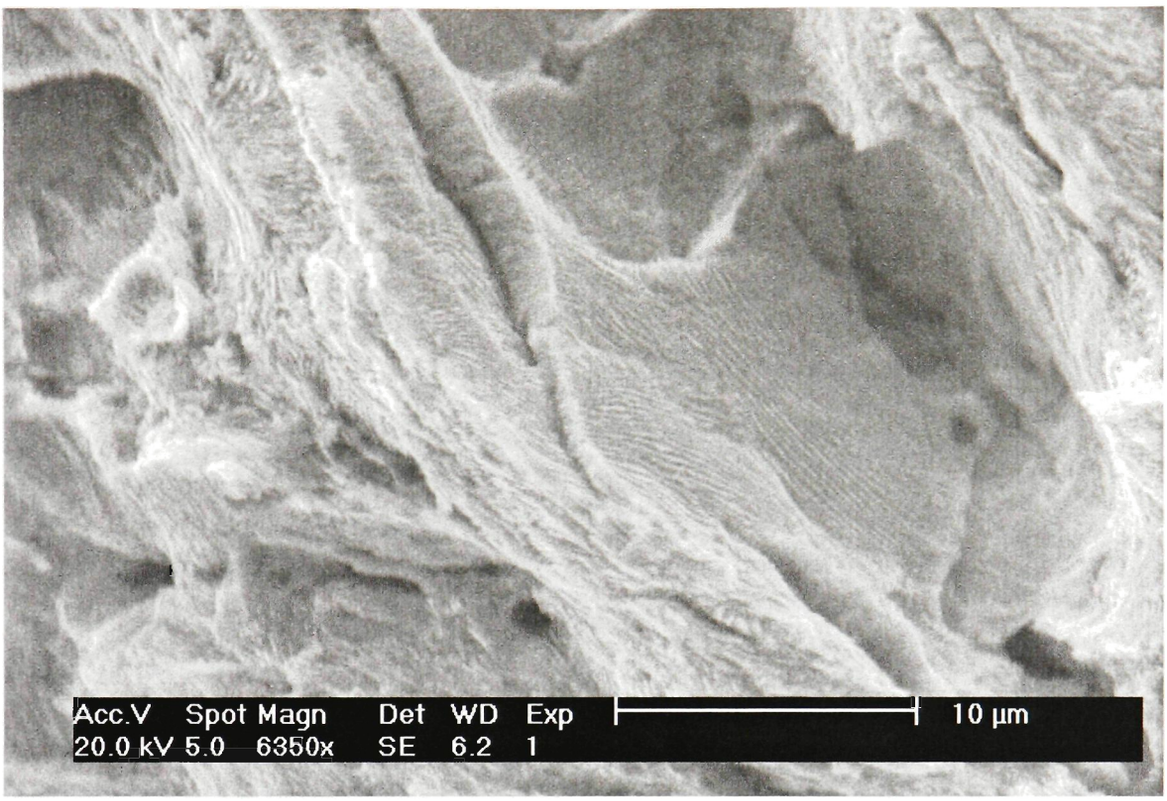

FIGURE 5.51: SCC-FFS interface x6350

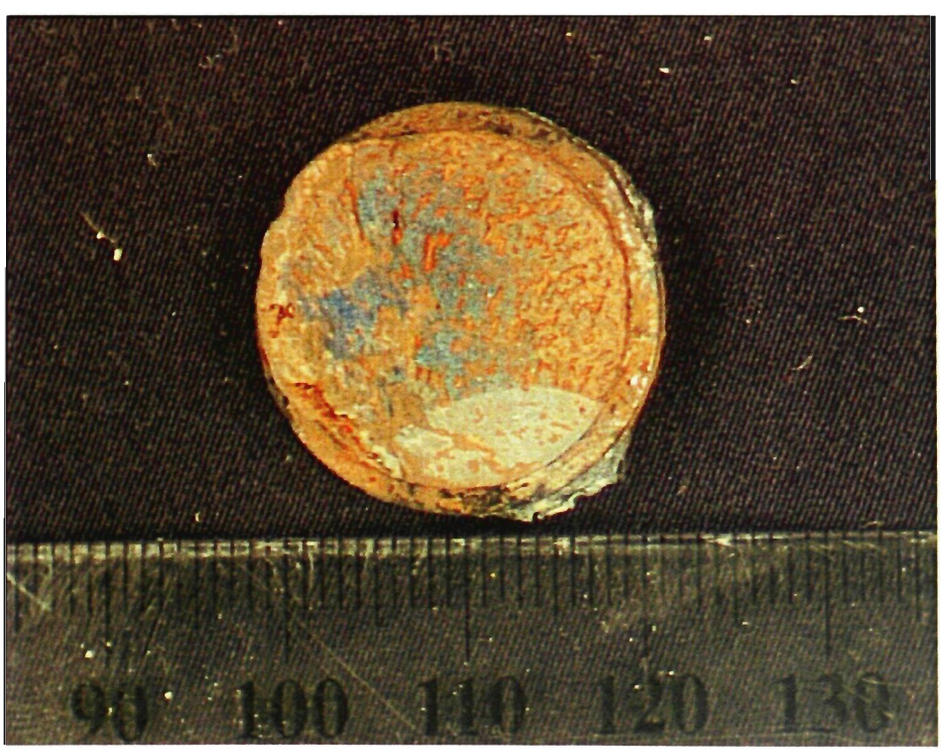

FIGURE 5.52: Rock bolt fracture surface overview

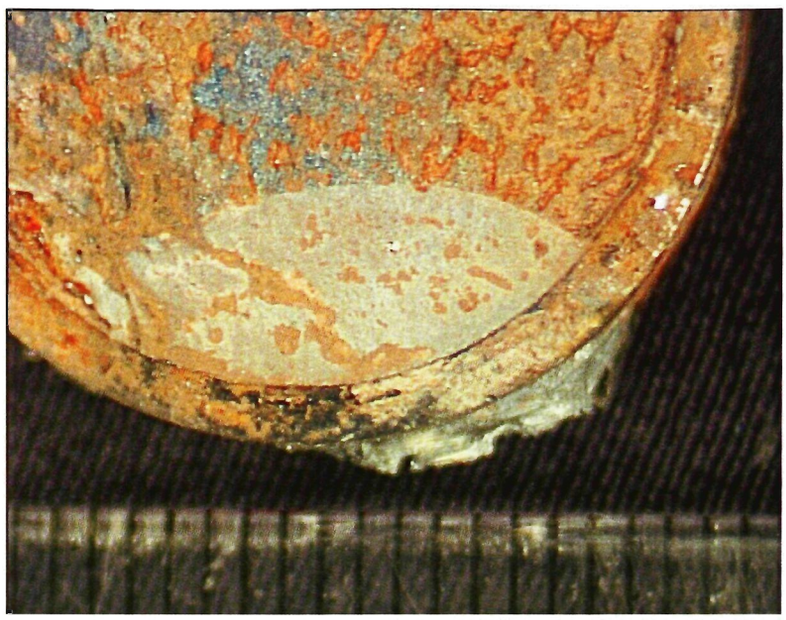

FIGURE 5.53: Rock bolt thumbnail area overview

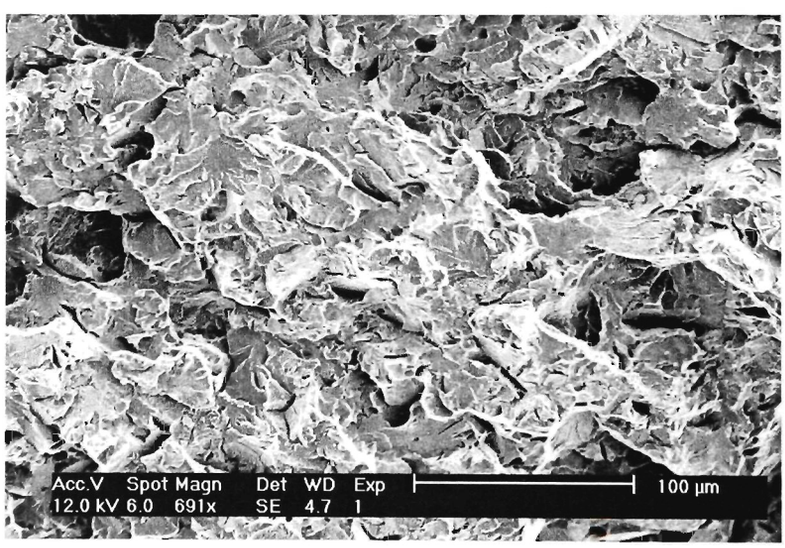

FIGURE 5.54: Rock bolt Fast Fracture Surface

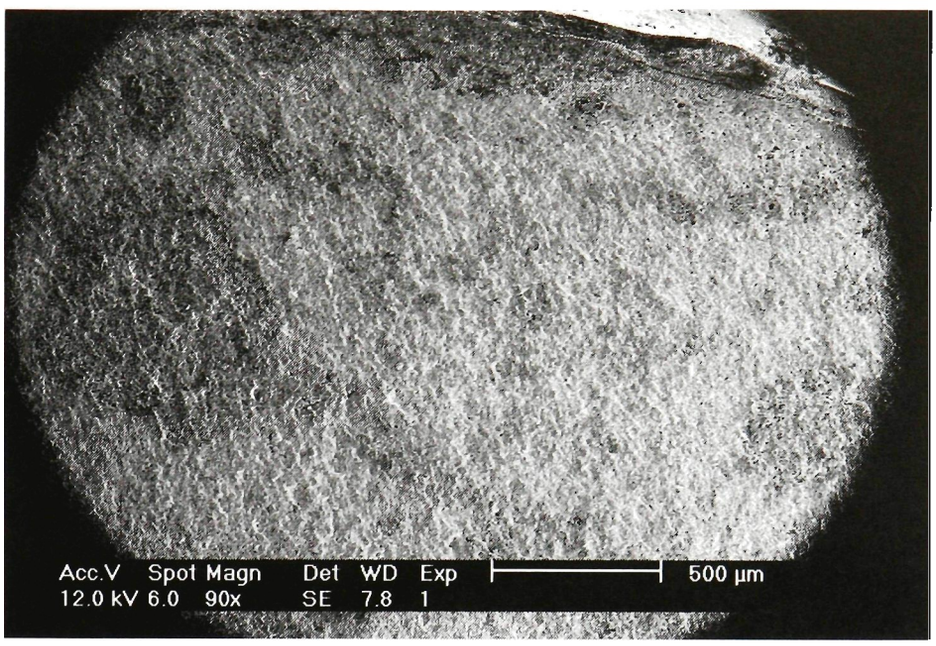

FIGURE 5.55: Overview of thumbnail region

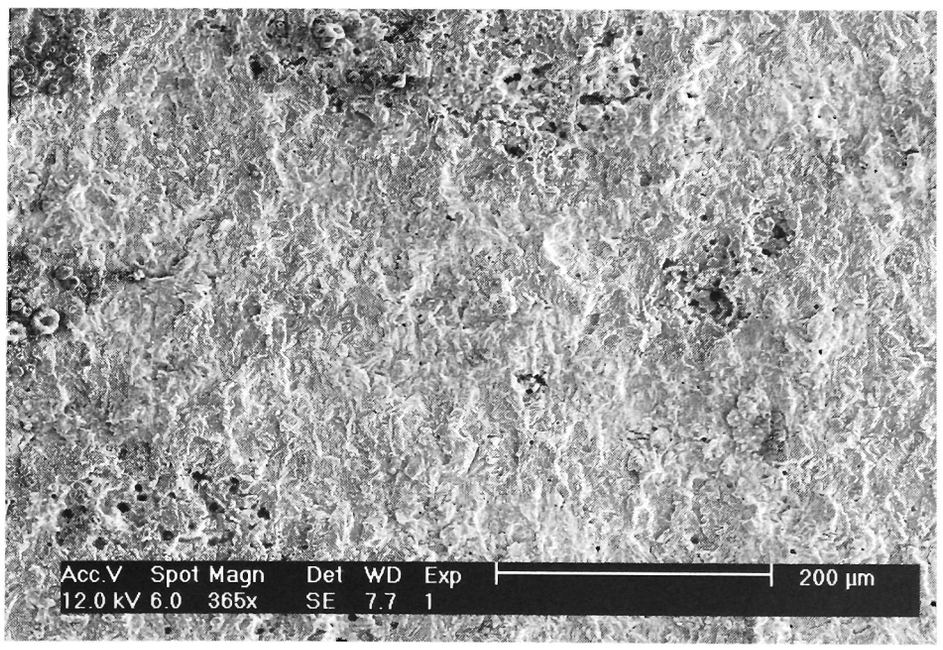

FIGURE 5.56: Subcritical crack growth region

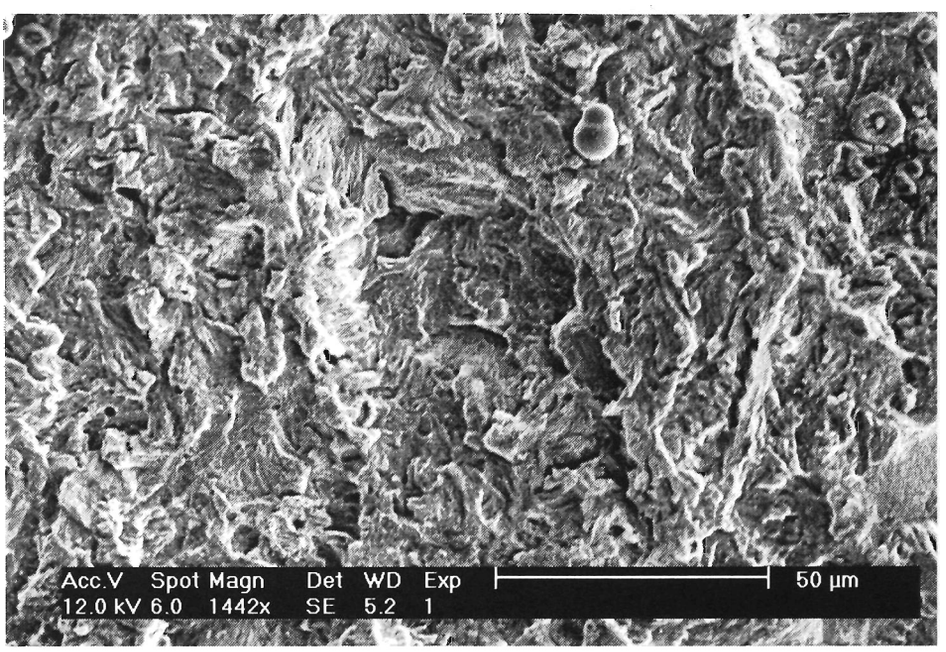

FIGURE 5.57: High magnitude view of subcritical crack growth region

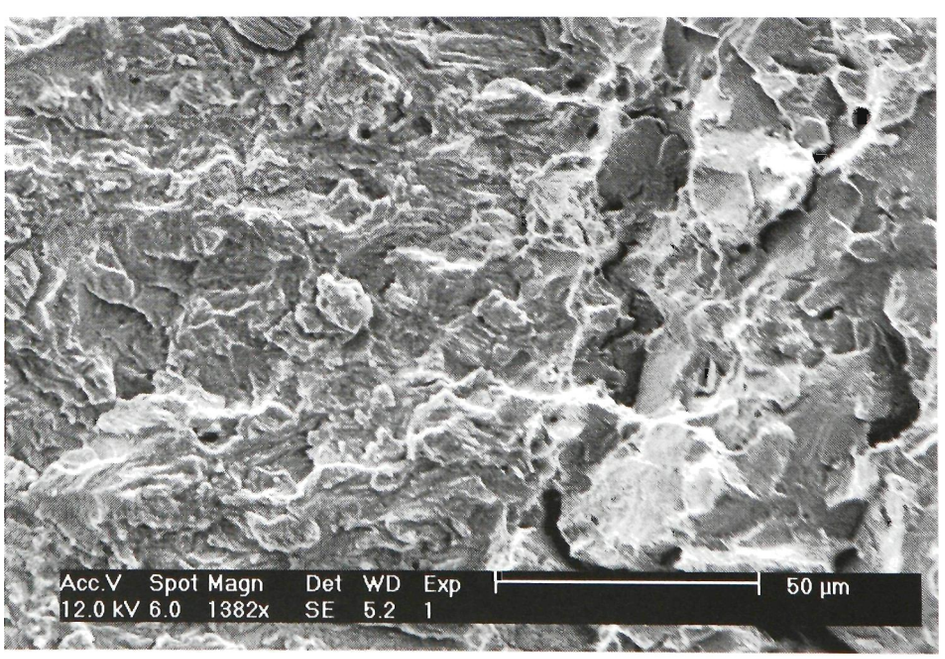

FIGURE 5.58: Interface between subcritical crack growth and FFS

(a) Macroscopic view of the bolt's fracture surface

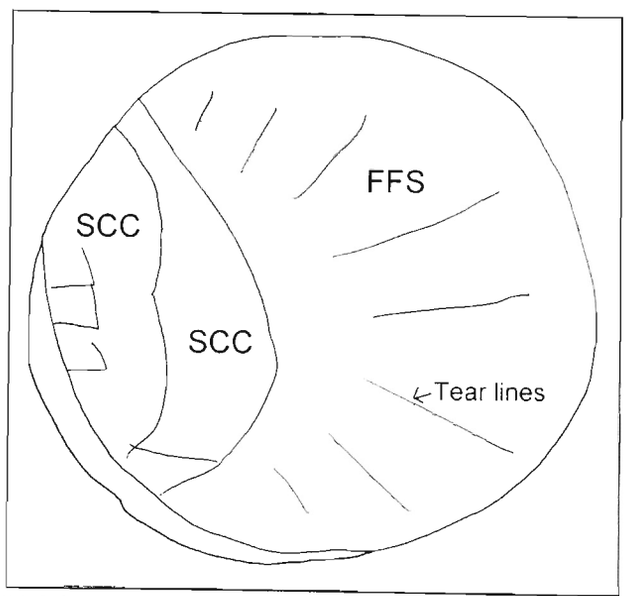

(b) Schematic view showing SCC, tear lines and fast fracture areas

FIGURE 5.59: Rock Bolt fracture surface

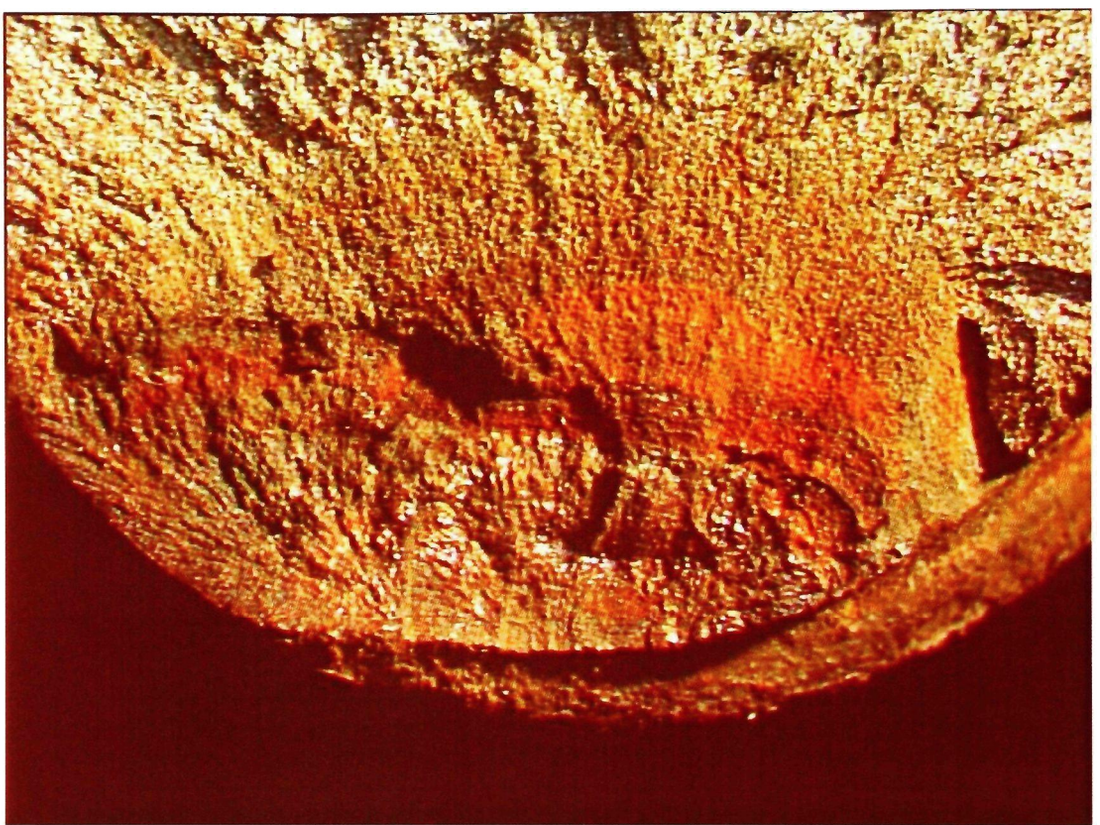

(a) Macroscopic view of the bolt's SCC surface

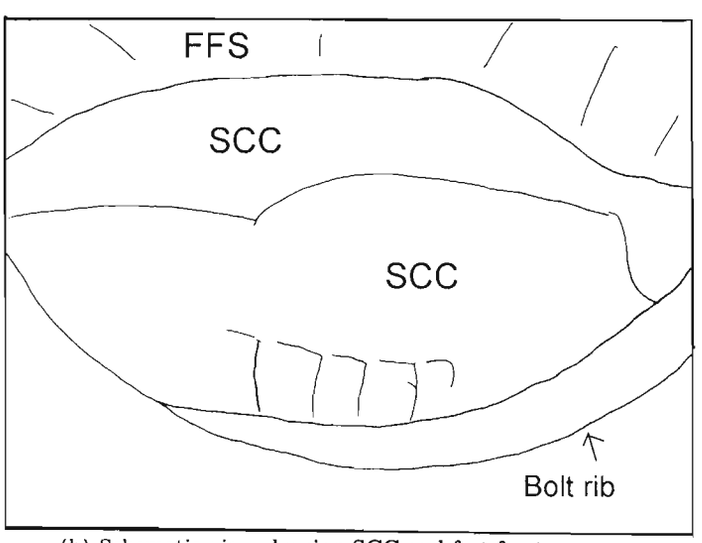

(b) Schematic view showing SCC and fast fracture areas

FIGURE 5.60: Rock bolt SCC overview

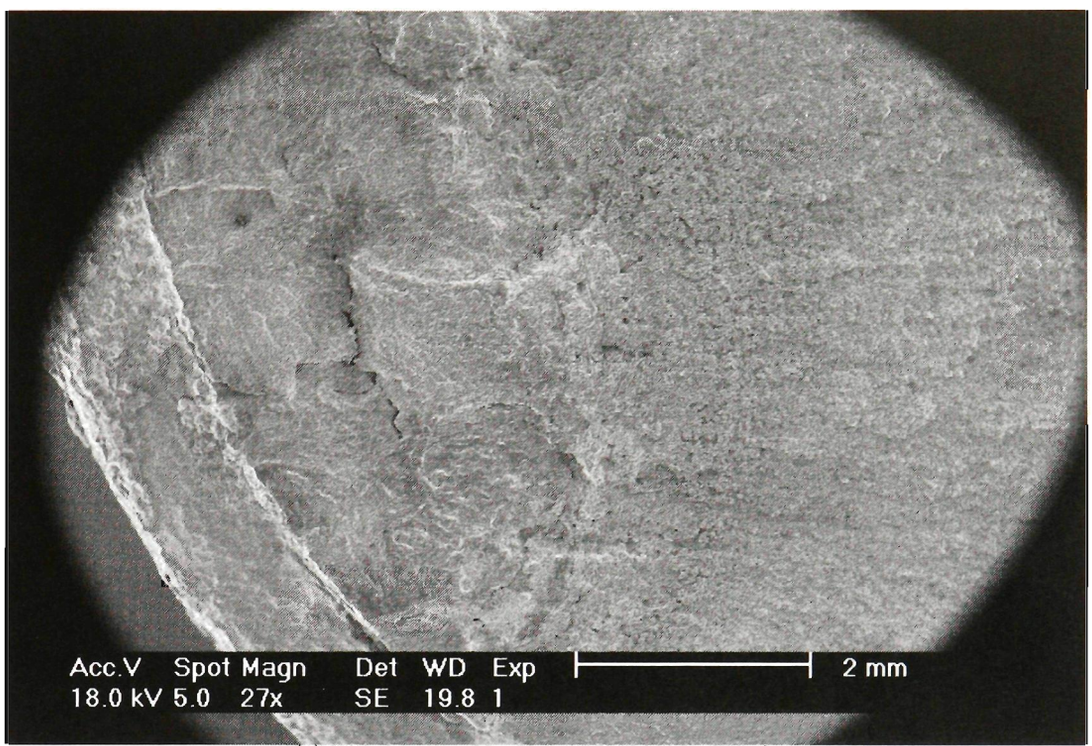

(a) Microscopic view of the bolt's fracture surface

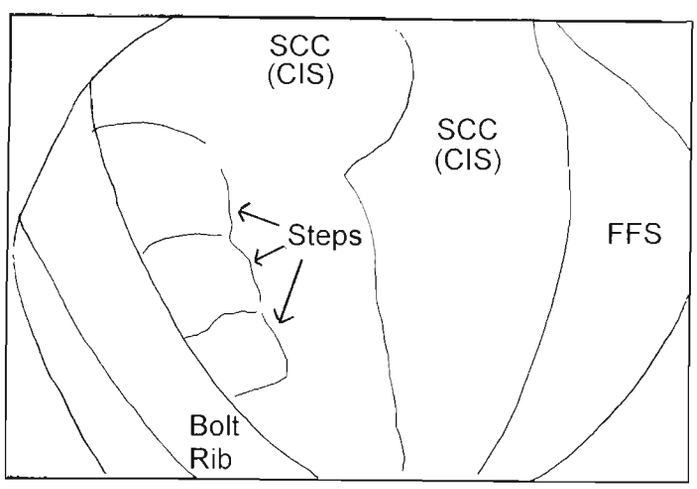

(b) Schematic view showing bolt rib, SCC and fast fracture areas

FIGURE 5.61: Rock Bolt SCC overview

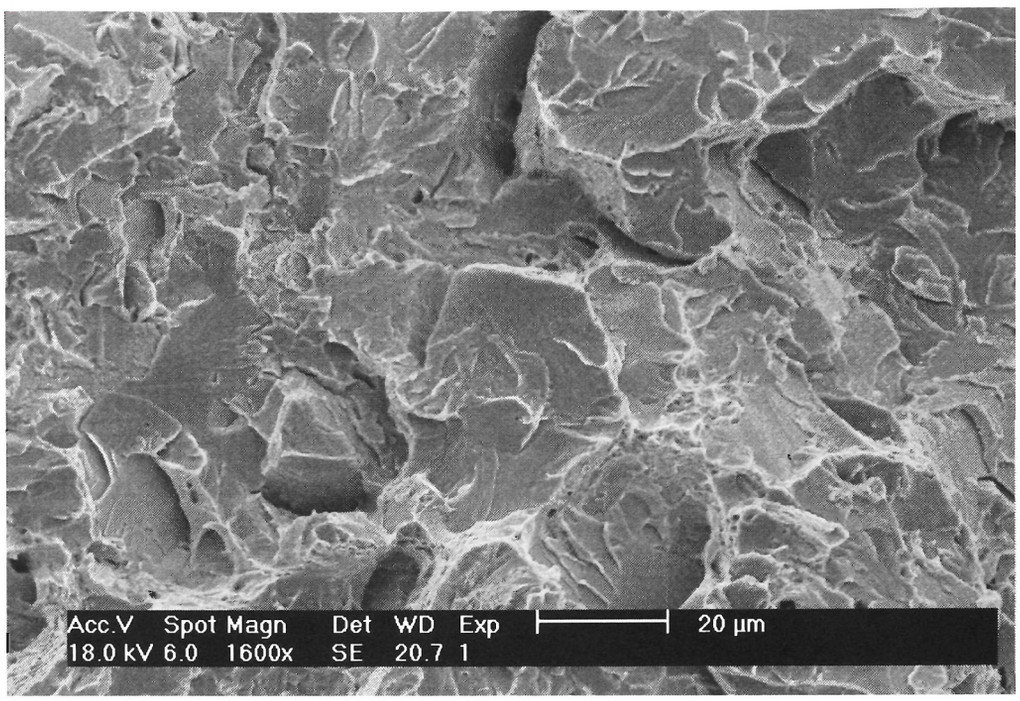

FIGURE 5.62: Typical Fast Fracture Surface (FFS)

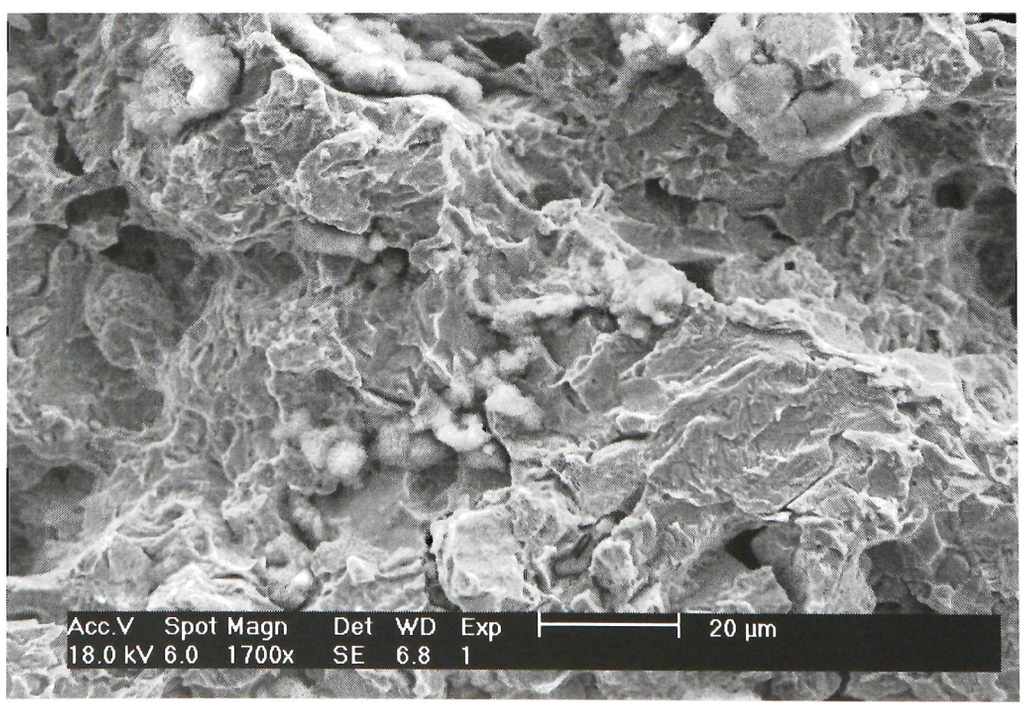

FIGURE 5.63: Typical SCC topography (damaged)

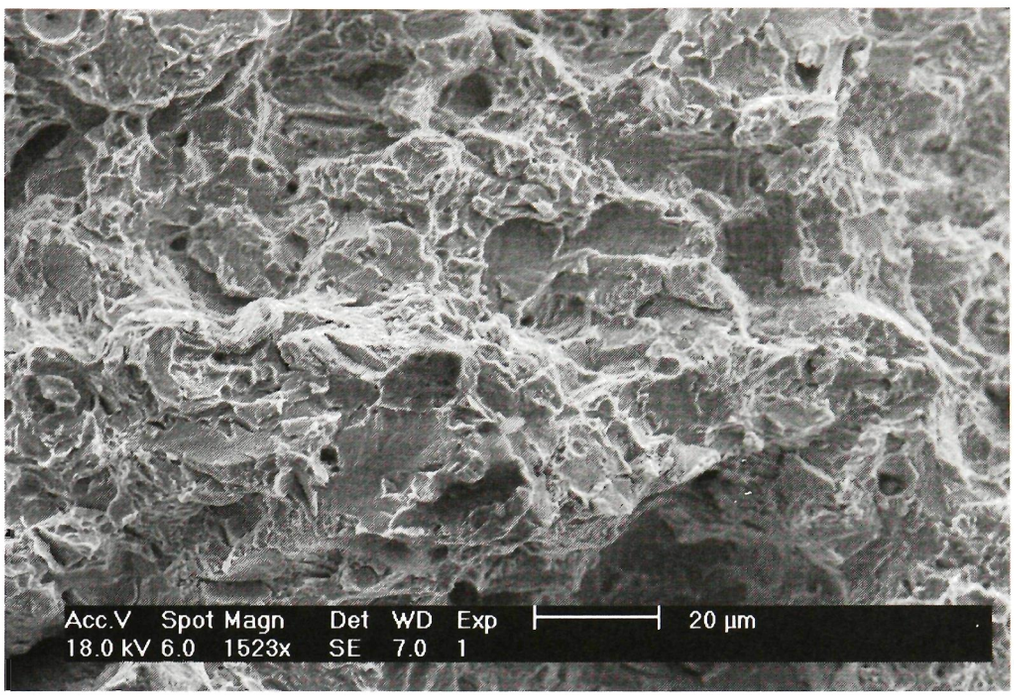

FIGURE 5.64: Typical SCC topography (damaged)

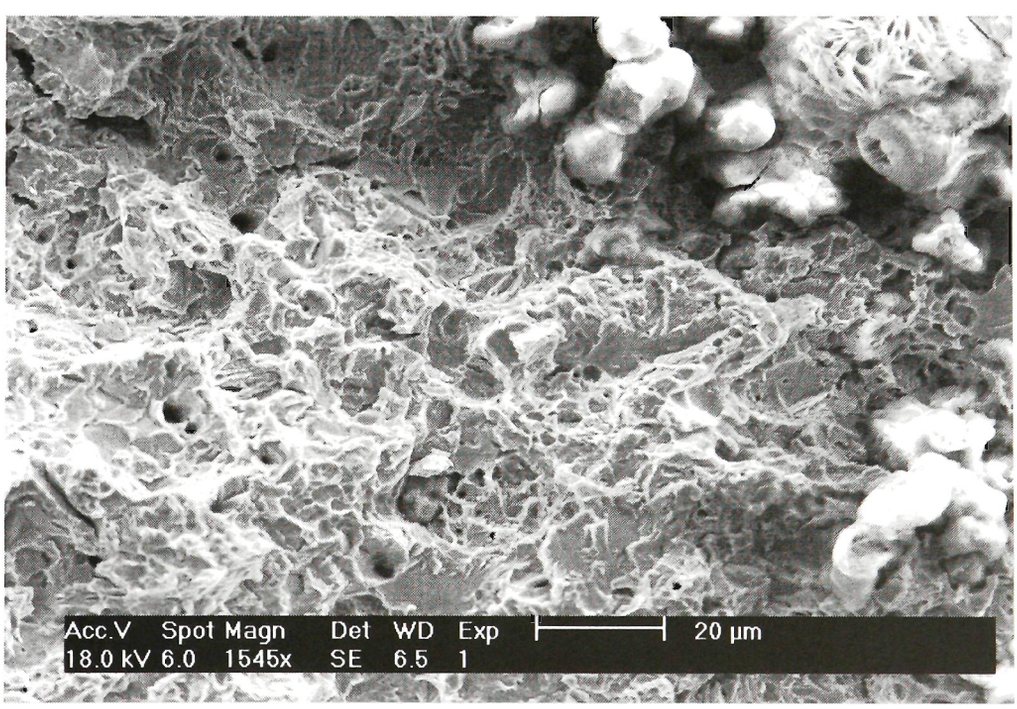

FIGURE 5.65: Typical SCC topography (damaged)

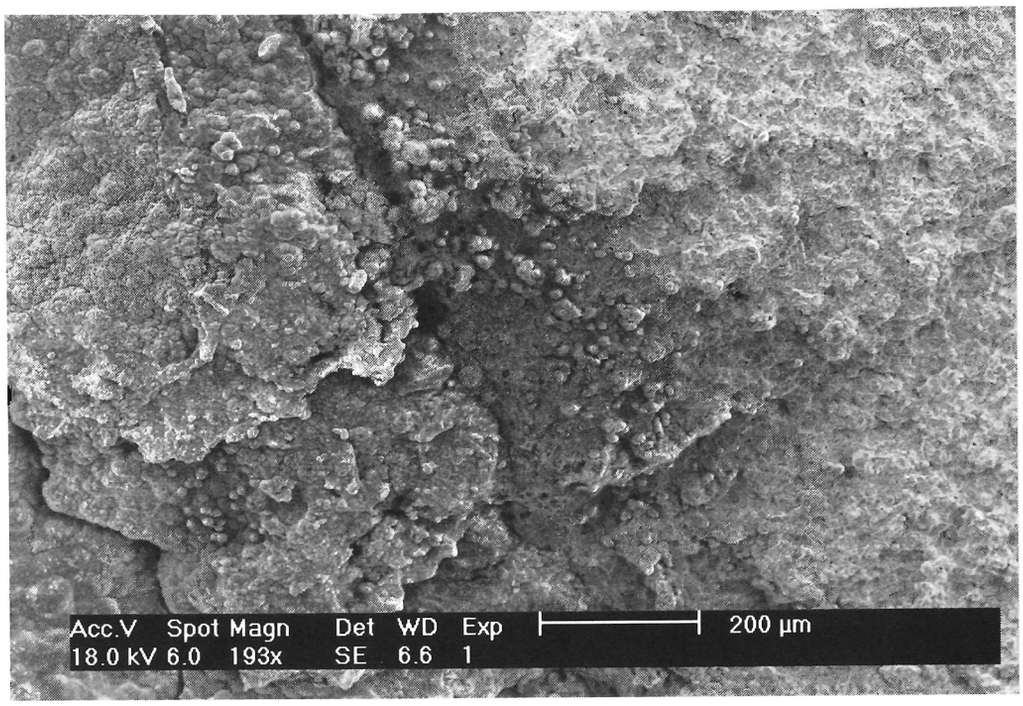

FIGURE 5.66: Damaged CIS - FFS interface

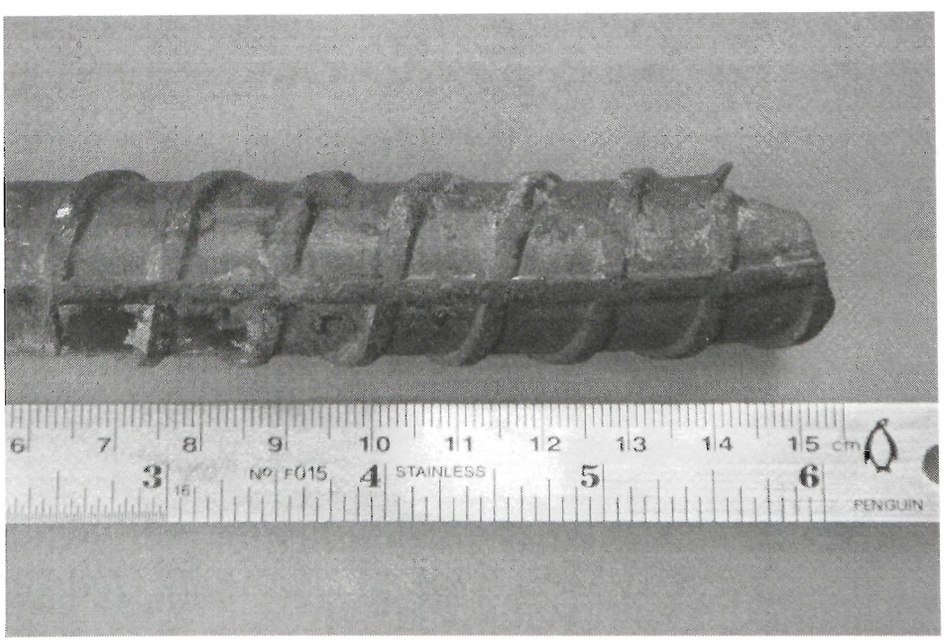

FIGURE 5.67: Macroscopic view of colliery Q rock bolt. The fracture was at the right end of the bolt segment.

(a) Macroscopic view of the bolt's fracture surface

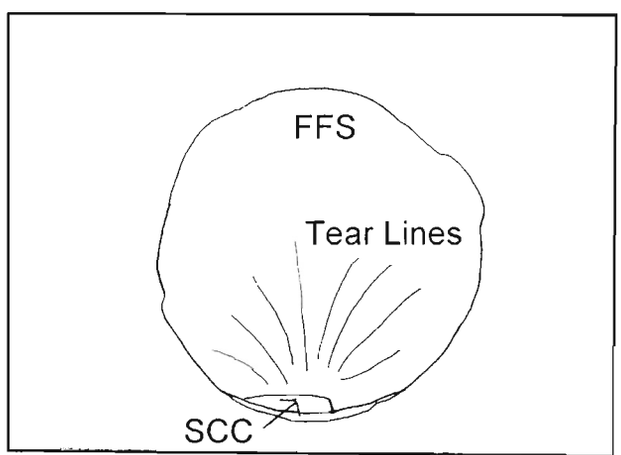

(b) Schematic view showing SCC, tear lines and fast fracture areas

FIGURE 5.68: Rock Bolt fracture surface

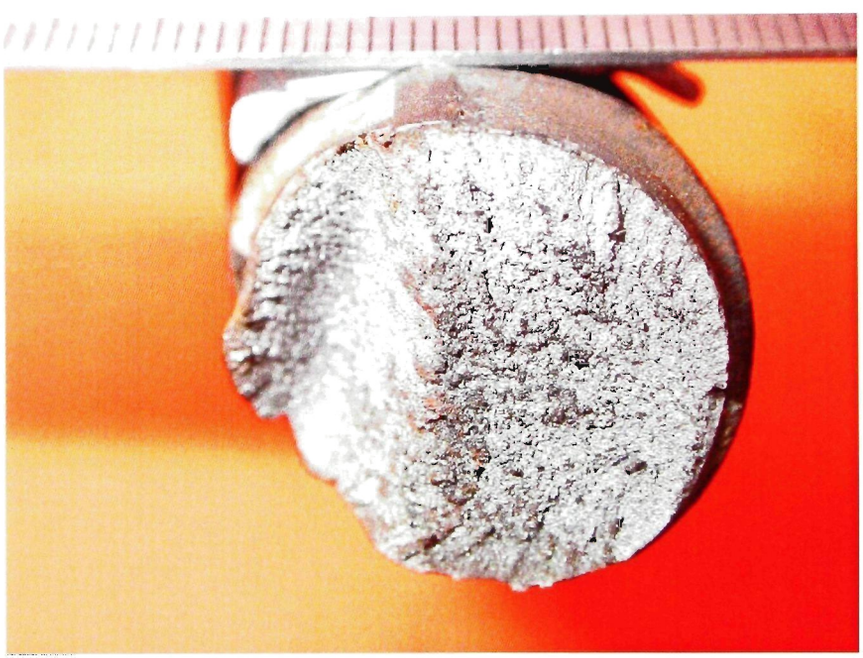

FIGURE 5.69: Macroscopic view of colliery Q rock bolt. The SCC initiation site was at the foot of the bolt rib.

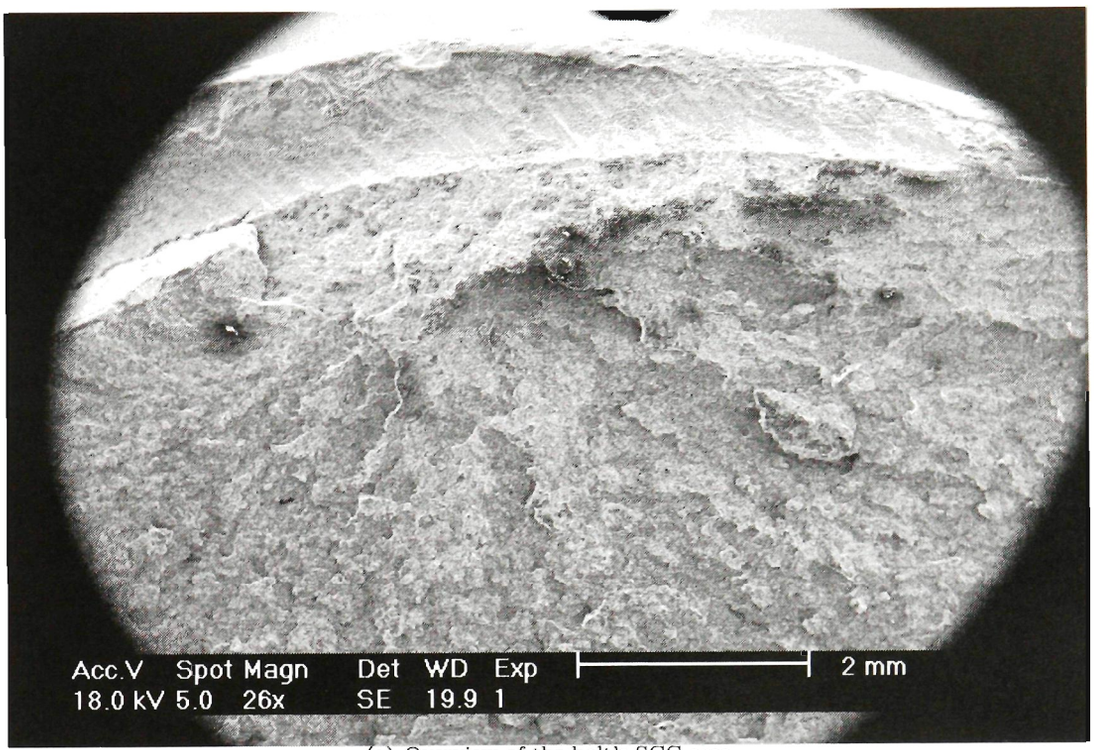

(a) Overview of the bolt's SCC area

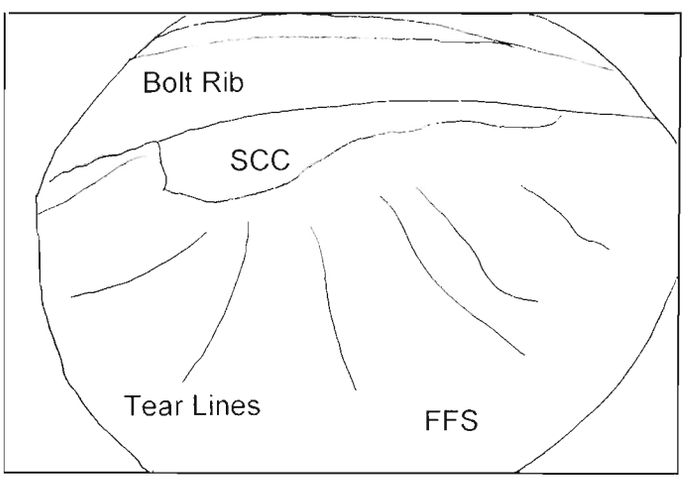

(b) Schematic view showing SCC, tear lines and fast fracture areas

FIGURE 5.70: Rock bolt SCC overview

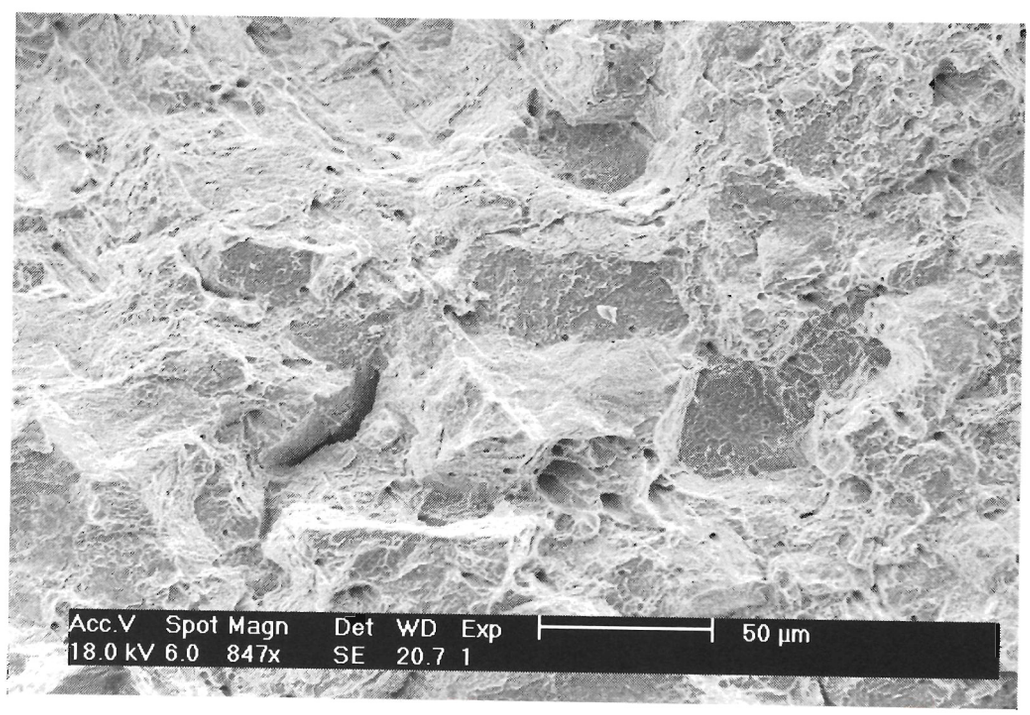

FIGURE 5.71: Typical SCC (CIS) topography

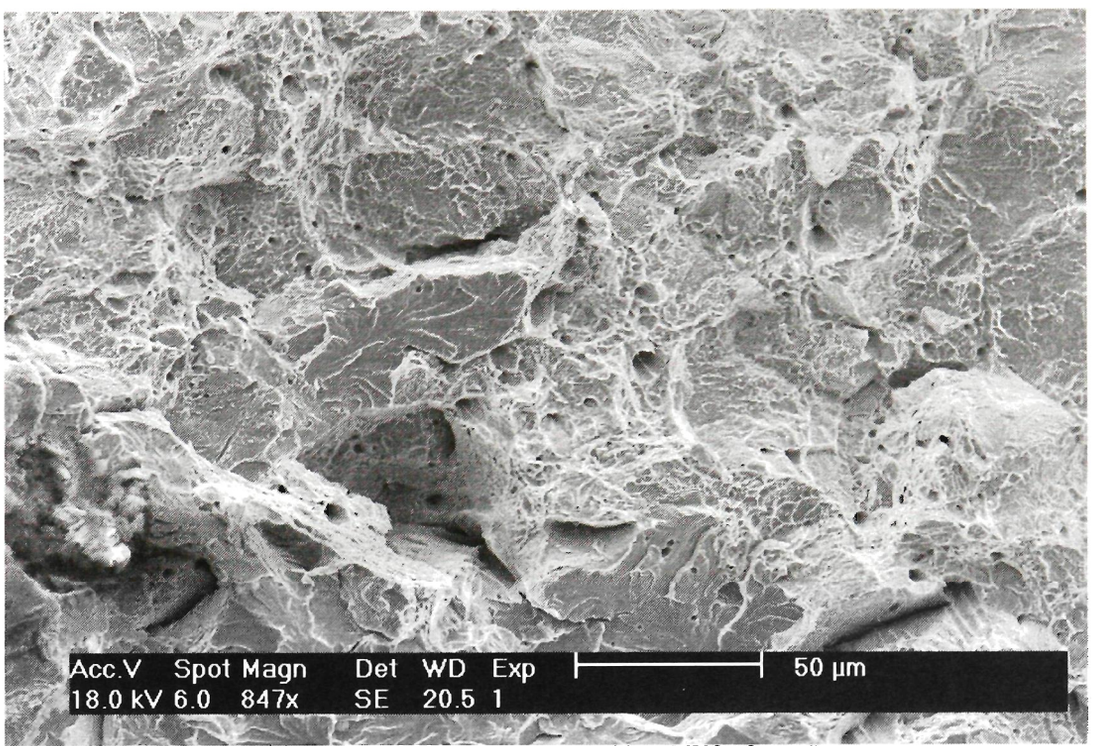

(a) CIS and FFS regions separated by qMVC "fingers"

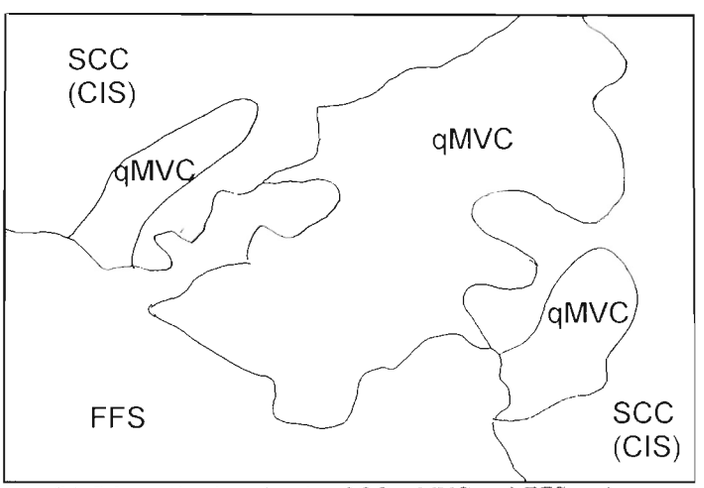

(b) Schematic view showing SCC, qMVC and FFS regions

FIGURE 5.72: SCC (CIS) - FFS interface

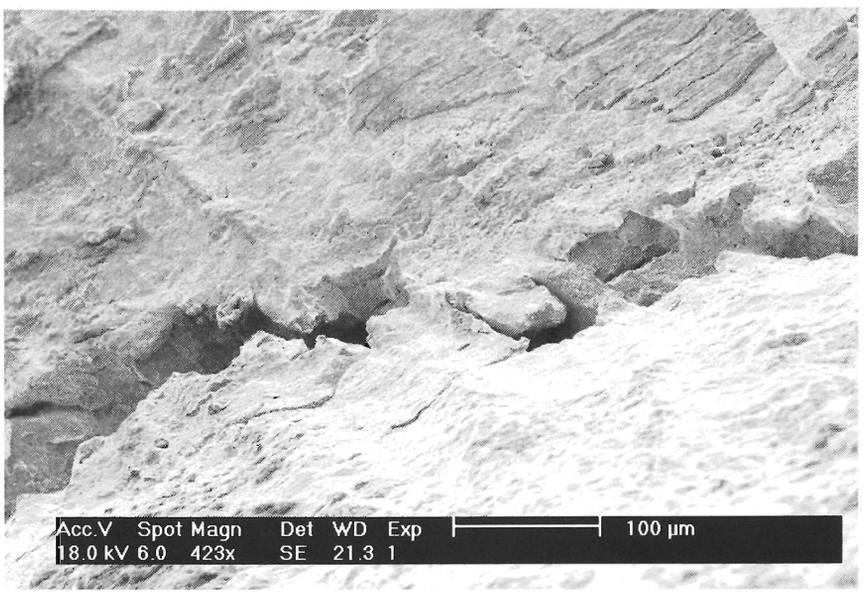

FIGURE 5.73: SCC crack running along the bolt rib

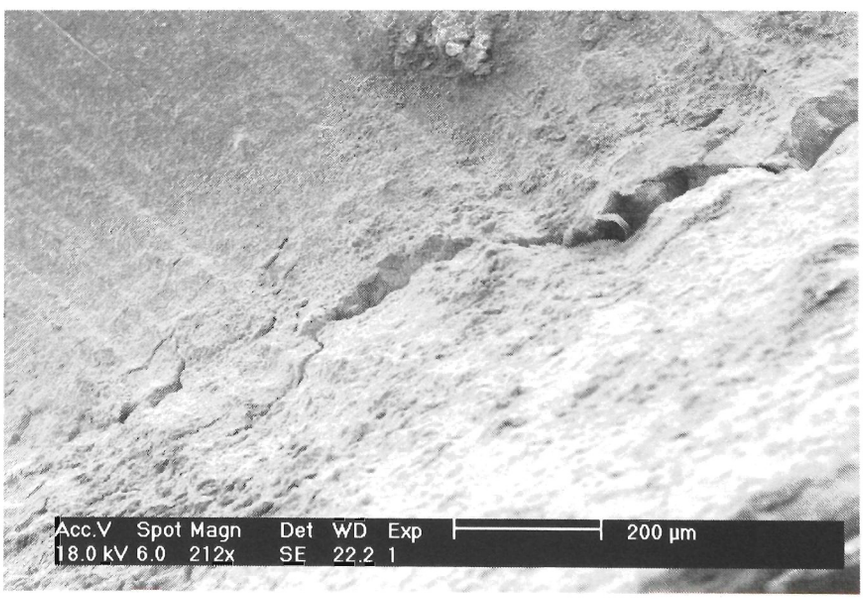

FIGURE 5.74: Beginning of SCC crack running along the bolt rib

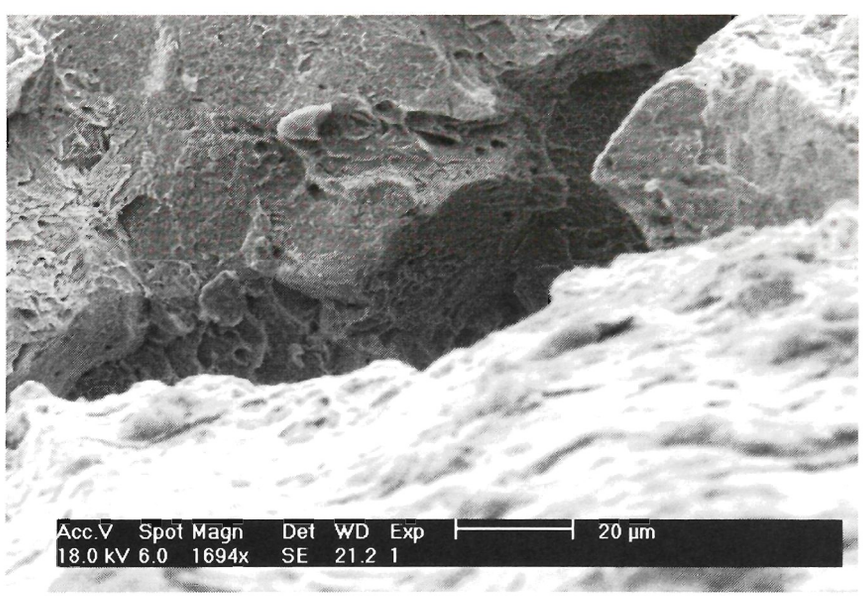

FIGURE 5.75: CIS topography running inside the SCC crack along the bolt rib

6

FRACTOGRAPHY

This Chapter presents the fractography of the rock bolts studied, as well as the fractography of LIST samples produced in the laboratory. A comparison was made between the service and laboratory surfaces. Both surfaces were shown to be similar, establishing the Linearly Increasing Stress Test as a valid laboratory test for SCC.

Rock bolts have failed by Stress Corrosion Cracking (SCC). The SCC fracture surfaces, studied using Scanning Electron Microscopy (SEM), contained the following different surfaces: Tearing Topography Surface (TTS), Corrugated Irregular Surface (CIS) and quasi Micro Void Coalescence (qMVC). TTS was characterised by a ridge pattern independent of the pearlite microstructure, but having a spacing only slightly coarser than the pearlite spacing. CIS was characterised as porous irregular corrugated surfaces joined by rough slopes. The qMVC found in the studied rock bolts was different to that in samples failed in a pure ductile manner. The qMVC observed in rock bolts was more flat and regular than the pure MVC, being attributed to hydrogen embrittling the ductile material near the crack tip. This different qMVC has been termed quasi Micro Void Coalescence (qMVC).

The interface between the different fracture surfaces revealed no evidence of any additional mechanisms involved in the transition between the fracture mechanisms.

The microstructure had no effect on the diffusion of hydrogen nor on the fracture mechanisms.

A hypothesis was put forward that explains the fracture surfaces in both rock bolts and LIST samples.

The following SCC mechanism was consistent with the fracture surfaces. Hydrogen diffused into the material, reaching a critical concentration level. The thus embrittled material allowed a crack to propagate through the brittle region. The crack was arrested once it propagated outside the brittle region. Corrosion reactions produced hydrogen that diffused into the material and allowed the process to continue.

LIST testing has shown to be a reliable method of simulating field SCC in the laboratory.

6.1 INTRODUCTION

Rock bolts failed during service by Stress Corrosion Cracking (SCC) have been described previously (Chapter 5). Rock bolt microstructure was fine pearlitic steel.

Subsequent work, which is described in this thesis in Chapter 7 has shown that service failures can be duplicated in the laboratory using the Linearly Increasing Stress Test (LIST) apparatus [10]. LIST testing using a sulphate pH 2.1 solution at a rate of 0.019 MPa s^{-1} was found to provide a good foundation for a test to mimic service SCC. The resulting fractography of LIST samples were similar to those from service SCC.

The purpose of this Chapter was to examine, in detail, the fracture surfaces in order to understand the fracture processes and to relate the fracture processes to the material microstructure. Furthermore, the fracture surfaces examined were those from service failures and from LIST laboratory tests. A particular point of study was to compare these two types of fracture surfaces. The fracture surfaces were related to the work carried out by Toribio [53], in which the Tearing Topography Surface (TTS) has been documented. This paper compared the TTS documented by Toribio [53] to that found in rock bolts. A hypothesis was advanced regarding the crack propagation mechanism.

6.2 ROCK BOLT FRACTURE SURFACES

A convention used in the Figures in this Chapter is that solid lines represent topographical features and dashed lines represent changes of fracture mechanism. Dot-dashed lines represent pearlite colony boundaries.

Figure 4.3 showed the microscopic structure of the 1355AXRC rock bolt. It showed a fine pearlitic microstructure.

6.2.1 Overview

Figure 5.5 illustrated a typical fracture surface of a bolt failed by SCC. The typical features were the thumb-nail shaped slow crack growth region (SCC), surrounded by the fast brittle fracture region (Fast Fracture Surface (FFS) displaying cleavage fracture) marked by tear lines radiating out from the subcritical crack growth region. Crack branching was not evident on the slow crack growth region. On closer examination,

SCC consisted of three distinct fracture morphologies: Tearing Topography Surface (TTS), Corrugated Irregular surface (CIS) and quasi Micro Void Coalescence (qMVC). TTS occurred close to the free surface whereas qMVC was located mainly at the SCC-FFS transition. Most of the SCC region consisted of CIS.

Figure 5.2 shows a typical fracture surface for a different rock bolt failed in service by SCC. The most prominent feature was the small thumbnail shaped area on the right side of the fracture. The rest of the bolt showed a shiny irregular surface. Within the shiny irregular region there were tear lines that radiated away from the thumbnail area. The darker thumbnail shaped area is shown in more detail in Figure 6.1. This was the region where the Stress Corrosion Crack grew until it reached a critical size. Note that the SCC initiation was associated with a rib. This was a common observation.

6.2.2 Fast Brittle Fracture

Figure 6.6 was an overview of the SCC region. This shows tear lines on the FFS pointing towards the thumbnail shaped area on the bottom of the Figure. The brittle fracture region typically covered 98% of the total rock bolt surface area.

Typical surface topograpy of the fast fracture region (the shiny irregular surface) at magnifications of x10000, x500, x2500 and x1000 are shown in Figures 5.9, 5.17, 5.18 and 6.2 respectively. The main feature found in this surface were the flat areas marked by tear lines. These tear lines gave the appearance of maple leaves. These "leaves" were at slightly different heights, but the leaves and the tear lines on them pointed towards the origin of the fast brittle crack. The different height leaves were joined by flat, rough, featureless slopes that were inclined almost vertically. Figure 5.9 showed that the flat areas were made up of fine regularly spaced ridges spaced approximately 200 nanometers apart.

Another common obvious feature was the chasm formed when two leaves (metal grains) were separated. Figure 6.3 points to one such feature. Just beside this chasm the surface was not smooth, but had a ductile tearing appearance.

6.2.3 Tearing Topography Surface (TTS)

The Tearing Topography Surface (TTS) occured close to the free surface. This topography has been described by Toribio and Vasseur [53] as a Tearing Topography Surface (TTS), a *"characteristic microscopic fracture mode with a kind of ductile tearing appearance, a certain degree of plasticity and a very closely spaced nucleation"* [53]. They point out that close to the surface of the specimen, the TTS had a kind of orientation in the direction of damage propagation. Such orientation was lost further into the sample. Figure 5.10 showed such orientation. Close to the surface the deep ridges tended to point towards the free surface, but as the distance from the free surface increased, the orientation became random. Toribio [53] suggested that this fracture surface was formed by hydrogen diffusing into the metal and assisting fracture by embrittling the material.

TTS occurred in rock bolt samples as shown in Figures 5.11 and 6.4 6.5. TTS in the rock bolts had a lower degree of orientation. Figures 5.11 and 6.4 illustrate the range of appearance for TTS. These Figures show the main features of TTS that were observed in rock bolts. These features were the flat ridged areas and the secondary cracks. The ridges sometimes seemed to radiate from one point within a flat area. At other places the ridges were parallel to each other. The flat regions within TTS did not correspond to a single pearlite grain as shown in Figure 6.5. Figure 6.5 shows also that the TTS ridged structure did not follow pearlite colony orientation nor pearlite colony boundaries, as pearlite colonies were aligned differently to the ridges. The flat region shown by the figure was made up by at least 3 different pearlite colonies of different orientations (the dot-dash lines show the pearlite colony boundaries). The top colony had an orientation similar to that of the ridges, whereas the bottom colony was aligned perpendicularly to the ridge direction. The ridges of the top part of the figure had a spacing similar to the pearlite lamella, but the deep ridges apparent throughout the surface were not dependent on pearlite colony orientation; sometimes the pearlite colony lay perpendicular to these deep ridges. The perpendicular orientation of the ridges to the pearlite colony suggested that the fracture mechanism was independent of the pearlite. TTS had been found in rock bolt samples, as shown in Figures 6.11, 6.12 and 6.13.

6.2.4 Corrugated Irregular Surface (CIS)

Figures 5.6, 5.22, 5.23 and 5.24 each showed typical examples of the fracture surface within the SCC region that has been named the "Corrugated Irregular Surface" (CIS). It can be described as a network of corrugated surfaces, joined by rough slopes. The corrugated surfaces displayed a network of branched channels. In places these slopes were quite steep, and their surface typically appeared to have fine ridges (Figure 6.7). The flat areas also displayed ridges, as shown by Figures 6.8 and 6.9. The spacing between these ridges was approximately 200 nm. The flat regions were perpendicular to the longitudinal axis of the rock bolt. Although there was a high quantity of slopes, there was overall a small change in depth in the fracture topography (of the order of a few hundred microns). Figures 6.14 6.15 show different aspects of CIS. Surfaces could appear rough without displaying the ridges. CIS was typically found between the TTS and the quasi Micro Void Coalescence (qMVC) regions. In some cases, CIS was found at the edge of specimens instead of a TTS region.

Figure 6.14 showed typical CIS regions. Figure 6.14 also contained a diagram identifying the characteristic plateaus, slopes and isolated regions of qMVC. The holes in the surfaces of this Figure was due to the cleaning process. This surface was cleaned with the EDTA solution for 15 minutes, before it was discovered that such a long immersion time introduced holes in the fracture surfaces although it produced no other discernible change. Subsequent surfaces have been cleaned for 3 minutes.

Figure 6.15 illustrates a plateau and the irregular corrugated slopes. In the foreground there was a plateau, with slopes leading down from the mesa in an irregular fashion. The mean change in depth between flat regions was of the order of 30 microns. Figure 6.15 also shows the plateau at high magnification revealing

the pearlite colonies and their orientation. The mean depth of features on these plateaus was of the order of a micron. The diagram depicts the different fracture regions, as well as the pearlite colony orientation.

The flat plateau regions within CIS were not individual pearlite grains. Figure 6.15 shows that there were several pearlite colonies in each flat area, and that the boundary of such regions did not follow the orientation or the boundary of pearlite colonies.

6.2.5 quasi Micro Void Coalescence (qMVC)

Superficially, qMVC found in samples failed by SCC appeared similar to that found in samples that had failed by ductile overload. On closer examination, SCC related qMVC had subtle differences. Although dimple size could be similar, topographic height variations was different. In pure ductile overload samples, the fracture surface depth could vary of the order of 2 mm, whereas in SCC samples the depth change was of the order of 50 microns. Another difference was that SCC qMVC could occur over relatively large flat regions with little change in height (of the order of 5 microns as seen on the top of Figure 6.15).

An important point was that the bulk of the sample failure surface was cleavage (FFS), not MVC as in ductile overload samples. The regions that resembled MVC were small, and were found in the interface between the subcritical crack growth regions and the FFS. Even though these regions looked like MVC, they displayed the small differences mentioned previously. These small differences suggested that the MVC region had been embrittled in some manner, suspectedly due to hydrogen. It is believed that SCC qMVC occurred when the slow crack had achieved a critical size and the sample failed suddenly. Areas that had a significant concentration of hydrogen ahead of the crack tip did not fail by cleaving producing a FFS, but failed in an embrittled form of MVC. Toribio [53] mentions that *"With regard to the quasi-MVC topography, it appears only when the penetration path for the hydrogen is long compared with the dimensions of the sample ... This seems to demonstrate that the MVC area is a "future" TTS zone which does not reach such a condition because of an insufficient level of hydrogenation."* Toribio observed that the quasi-MVC region was found near the SCC-FFS transition. Similarly, qMVC in this study was located mainly near the SCC (CIS) FFS transition, although there were also pockets of qMVC within the CIS regions.

It is possible that the topography of qMVC could be explained in terms of local stress state and micromechanics of fracture, such that no hydrogen is required to produce a similar fracture surface. That is, that there could be ductile tearing of ligaments between CIS regions of SCC by MVC. However, this view is not consistent with existing literature concerning the fracture modes of pearlitic steels. Toribio et al [57], [56] showed that there is a triaxiality stress level below which fracture is MVC, hence MVC topography does not seem to be possible in high triaxiality areas not sufficiently hydrogenated. This research indicates that cleavage would occur in air (i.e. in the absence of hydrogen) in the areas between CIS and the FFS where qMVC was observed on the fracture surfaces. This indicates that the qMVC areas were produced by a local enhancement of ductility by hydrogen.

The work carried out in this thesis is consistent with the prior work. Samples failing in air showed MVC

ductile failure, whilst the qMVC associated with SCC was different in appearance, and occurred under local stress conditions where brittle cleavage would be expected in the absence of hydrogen.

6.3 FRACTURE SURFACE INTERFACES

6.3.1 Interface TTS-CIS

The TTS - CIS interface was difficult to identify since both surfaces were similar in appearance. Both surfaces have small irregular, broken features. Usually both showed a flat area with ridges upon its surface, while the surface did not show great topographical depth variance. Small pits could be found in either surface. The main differences between TTS and CIS was (1) the TTS surface was not as corrugated as the Corrugated Irregular Surface (CIS), and (2) the ridges tended to be more clearly defined in TTS. Slopes joining TTS flat regions were smaller, shorter and less common than in CIS regions. The typical case was TTS areas surrounded by CIS slopes. As the TTS had little orientation, the transition from one to the other fracture surface was difficult to pinpoint.

6.3.2 Interface TTS-qMVC, TTS-FFS

No cases have been found of a TTS region bordered with a qMVC region, nor of TTS bordered with FFS. This indicated that TTS was associated with a high level of hydrogen, whereas qMVC was associated with a low level. For the same reason it would be even less likely to find a pure TTS-FFS interface, as the TTS region is formed by a high concentration of hydrogen. If enough hydrogen diffused into the material to form TTS, enough would have propagated ahead of the crack tip to form qMVC between TTS and FFS before the crack started growing in a catastrophic manner (FFS).

6.3.3 Interface CIS-qMVC

The CIS-qMVC interface was common. Figure 6.16 shows one such interface. The qMVC region was nestled between CIS and FFS. The topographical height difference between CIS and qMVC could vary. At times qMVC continued at the same height as CIS, with the interface line being difficult to identify. The sudden abundance of small microvoids was one way of identifying the change in these cases. This was the case in Figure 6.16. The region in the qMVC finger and a horizontal band in the centre of the Figure (within the qMVC region) shows several small holes which were not readily found in the upper right portion (in the CIS region) of the Figure. Figure 6.17 shows one such hole in greater detail (just beside the interface line to the right of the Figure).

At other times, the CIS-qMVC interface was clear as a steep CIS slope separated two fracture surfaces, one of which was a CIS plateau, while the other was the dimpled perforated qMVC.

6.3.4 Interface CIS-FFS

On the left side of Figure 6.16 was a typical CIS-FFS interface. The two surfaces were separated by a difference in height, joined by a steep corrugated slope. Cases have also been found where the fracture mechanism changed in the middle of a flat region. Figures 5.7 and 5.8 illustrated the boundary between the fast fracture (FF) region and the SCC region in the middle of a flat region. The grain in the centre of the picture illustrated that the topography changed markedly from the smooth ridged FF surface to an irregular SCC surface with the ridges being more prominent. There was very little qMVC between the SCC region and the FF region.

Figures 6.18 - 6.20 show another case of the CIS-FFS interface. Figure 6.18 shows CIS on the bottom part of the figure, with a slope leading down to the FFS region. The actual interface line was distinctive and has been indicated in the diagram. On one side of the line the surface was corrugated and irregular, whilst on the other side of the line the surface was flat and smooth. An interesting feature of this CIS - FFS interface illustrated in Figure 6.18 were the "fingers" of CIS pointing inside the FFS. These CIS fingers were similar to the qMVC fingers and are attributed to a similar mechanism.

Figure 6.19 shows the pearlite colony orientation across the interface line. The diagram shows that the pearlite colony in the centre of the Figure was aligned with the direction of the crack propagation. There was a clear imaginary line separating the coarse ridged area of the CIS and the smoother FFS. The pearlite colony lamella appeared coarser (grooves were more marked) in the CIS region, with the lamella of the same colony appearing smoother in the FFS region. This indicated that the fracture mechanism changed from CIS to cleavage in the middle of a pearlite colony in an abrupt manner, indicating no third mechanism. At first sight it appeared that this coarser appearance of the lamella within the CIS region was due to preferential corrosion of one of the phases. This hypothesis was discarded as lamella near the free fracture surface would then be more markedly ridged as they would have been exposed to the electrolyte for longer periods of time, but this was not the case. The similarity of ridge depth at the interface and the free surface suggested that the coarseness was due to the fracture mechanism itself.

Figure 6.20 shows the opposite. The diagram indicated that the pearlite colony direction towards the top of the figure was perpendicular to the crack propagation direction. Towards the bottom of the figure the pearlite colony direction was not quite perpendicular to the crack propagation direction, but nevertheless it was at a high angle. The fracture mechanism changed from CIS to cleavage while the crack propagated perpendicular (or close to perpendicular) to pearlite lamella direction. Again a smooth transition suggested that there was no third fracture mechanism involved in the change over. Moreover, there was a change from CIS to FFS in the middle of a pearlite colony.

6.3.5 Interface qMVC-FFS

The qMVC-FFS interface was the most common one. Figure 6.16 shows one typical interface. In the figure, the dimples were common near the interface, and holes are mostly restricted to the qMVC side. The diagram shows that the interface line could waver. This suggested that the crack front grew in an irregular front rather than a straight uniform front. As the irregular crack front propagated, hydrogen propagated in front of the crack in a similar irregular manner giving rise to the irregular shape of the qMVC region. The overall front could be macroscopically described as a straight line, as the average difference of penetration of the front into the FFS region was typically 50 microns.

Figure 6.16 shows a qMVC region that has grown as a "finger" into the FFS region, whilst the rest of the qMVC-FFS interface was a relatively straight line. These fingers could extend into the FFS region by a much greater amount than the 50 microns mentioned previously. Fingers have been detected of up to 350 microns in length, but tended to be a maximum of 100 microns across. These fingers were attributed to hydrogen finding a path that allowed easier diffusion into the material.

Figures 6.17 and 6.21 6.22 show high magnification views of the qMVC-FFS interface.

Figure 6.21 shows the pearlite colony orientation across the interface. Figure 6.21 also shows that the pearlite lamella was oriented parallel to the crack propagation direction and the interface was at an angle θ to that direction. The transition of qMVC to FFS was smooth without a third mechanism. Figure 6.17 shows an interface where the qMVC side showed shallow dimples on a flat surface. There were several different pearlite colonies within this flat region, with different orientations. Figure 6.22 shows another interface. This time pearlite colonies were aligned perpendicular to the crack direction, and the fracture mechanism changed within these perpendicular colonies. The change over was again smooth. Another point of note was that fast fracture tear lines were in close proximity to the interface line (as in Figure 6.22). At times, these tear lines occurred within the same pearlite colony that displayed a change in fracture mechanism. Hence, the same colony with a single lamellar orientation could display a mechanism change as well as tear lines regardless of the pearlite orientation.

These Figures suggest that the pearlite colony orientation did not influence the crack front direction nor the fracture mechanism initiation. In other words, pearlite orientation did not affect hydrogen diffusion through the material.

6.4 ROCK BOLT DISCUSSION

6.4.1 FFS Region

On a macroscopic level, the tear lines displayed on the FFS region were formed by the material failing in a brittle rapid manner, initiating at the SCC region and propagating outwards.

The orientation of the maples leaves in the FFS tended to fan away from the crack initiation site. This

was due to the crack propagating quickly away from the subcritical growth area.

Chasms sometimes occurred between the maple leaves. This separation was thought to be caused by the material ahead of the fast crack tip yielding plastically, pulling open the grain boundary by a small amount before the brittle crack reached around this plastic region and severed the plastic yielding tendril. This was supported by the dimpled rupture region in Figure 6.3, where just below the chasm there was a dimpled rupture region bounded by the flat featureless surface of the fast fracture region.

6.4.2 SCC Region

The features in the SCC region of rock bolts were several and varied. The most striking feature was the network of corrugated surfaces, joined by rough slopes. These corrugated surfaces displayed a network of branched channels, initially believed to be formed by the preferential corrosion of one of the components of a pearlite colony. The spacing between these channels was 200 nm. Further study showed that these spacings were independent of pearlite lamellar orientation and were not caused by preferential corrosion. This spacing was the same as that found in the maple leaves, being the spacing between the ferrite and pearlite in the pearlite colony. In these cases, the crack tip had been travelling perpendicularly to the main pearlite colony axis. Figure 6.8 shows one such surface.

In the TTS region it had been noted that the orientation of the TTS diminished with distance away from the free surface. This loss of orientation was attributed to the increase of triaxiality associated with crack growth or to the decrease of hydrogen concentration at larger distances from the boundary. Evidence has been put forward supporting the idea that TTS occurred due to hydrogen embrittlement [56], [58].

6.4.3 Macroscopic Propagation

The random distribution of pearlite colony orientation within each fracture region (SCC (CIS), SCC (TTS) and FFS) suggested that the mechanism by which SCC propagated was not influenced at all by pearlite colony orientation. Furthermore, pearlite colony structure did not seem to influence the point at which the crack changed mechanism from slow subcritical crack growth to fast brittle propagation. Only the fracture toughness of the material dictated the maximum crack size allowed before brittle failure.

The interface between SCC and FFS was created by the edges of the maple leaves appearing to be the transition line. The straightness of such a line suggested that the crack propagated as a front. Once the crack reached a critical size, the fast brittle failure occurred along the front at the same time. In many of those places, the crack propagated outward producing the maple leaf pattern. This resulted in the edges of the maple leaves creating a distinctive line along the crack front. The line could easily be identified as the FFS side was quite smooth and flat, while the SCC side could be rough and dimply. In some cases, the separation between CIS and qMVC was not so clear, as the transition region resembled a flat irregular dimpled surface (as in Figure 6.17). This irregular dimpled surface was where hydrogen has had some time to

diffuse ahead of the crack tip during the subcritical growth phase, enough to slightly embrittle the material. The resulting topography was similar to Micro Void Coalescence (MVC) found in ductile tearing. Hence the small region was neither pure ductile tearing nor brittle fracture.

6.4.4 Fracture Mechanism

The following describes the proposed mechanisms that were responsible for the fractographies studied.

The chronology of SCC fracture can be divided into three parts: crack initiation, crack propagation and fast brittle fracture. This needs to be stated as different mechanisms may act for each phase.

Crack initiation was the first step that needed to occur in order for a stress corrosion crack to develop. Once a crack had initiated, other mechanisms could take over and the crack propagation phase could begin. In most cases, it is difficult to predict where a crack will initiate. Crack initiation sites could be surface scratches, grain boundaries, point defects, chemical inhomogeneities, inclusions, second phases and interphase boundaries. Even in cases where particular care has been paid to the manufacturing of the material and surface finishing, normal corrosion processes can create surface defects. The most common of these defects (in materials that are susceptible to SCC) is pitting corrosion. These pits, once formed, are further maintained by chemical reactions that have different (more favourable) dynamics in crevices than on a flat surface.

Once a crack has been initiated several factors come into play in order to propel the crack along the material. The two main factors could be considered to be the tensile stress (mechanical factor) and the corrosion reactions (dissolution factor) at the crack tip.

The results suggested that as the corrosion reaction takes place during subcritical crack growth, released hydrogen at the crack tip diffused into the material irrespective of the metal microstructure. This was due to the size of hydrogen being several times smaller than other species of atoms, allowing the atoms to diffuse into the metal without difficulty. Hence due to triaxial stresses being higher perpendicular to the free surface of the material, hydrogen tended to diffuse ahead of the crack in greater concentration than parallel to the free surface.

The resulting region of critical hydrogen concentration resembled the shape of a flame, as illustrated in Figure 6.23. This shape was the result of two effects. The first effect was the diffusion of hydrogen into the material, driven by the concentration gradient and the triaxial stress at the crack tip. The region of hydrogen concentration due to the concentration gradient was a sphere around the crack tip, as shown in A. The second effect was due to the tensile stress present. The tensile stress (lower than the yield stress) caused the atomic bonds to stretch. Due to the stress concentration caused by the crack, the local stress at the crack tip was higher than inside the material, hence the atomic bonds at the crack tip were stretched elastically more than those further into the material. This is illustrated in B. As the bonds were stretched, the hydrogen atoms found an easier passage into the metal matrix than through the unstretched material. The resulting hydrogen concentration envelope is illustrated in C. By adding these two effects, the envelope of total hydrogen concentration is represented by D. Outside that envelope there still was hydrogen diffused

into the material, but not to critical levels.

Once brittle, the crack propagated in a discrete step through the brittle region until it reached the hydrogen free ductile region, and the crack was arrested. The path the crack took was random. Due to the high concentration of hydrogen just in front of the crack tip, the initial growth could occur in almost any direction. Due to the triaxial stresses there was a greater hydrogen concentration directly into the material, hence the crack grew directly into the material.

It is proposed that the slow crack growth mechanism can occur in two phases. The first phase consists of the crack growing in a random direction away from the free surface of the material. The crack could grow directly into the material, in a direction perpendicular to the applied stress. Overall, the SCC did indeed grow perpendicular to the applied stress. However, at the microscopic level, the crack could grow in any direction within the region of high hydrogen concentration. There were indeed many more possible directions at an angle to the perpendicular compared with the single possibility for crack growth directly ahead of the crack tip in a direction perpendicular to the applied stress.

A crack that did grow in a direction at a high angle to the perpendicular, eventually reached the region where the hydrogen concentration was insufficient to allow further propagation. At this point, it is suggested that there occurred the second phase of crack propagation.

The second phase consisted of the crack turning towards the perpendicular and growing into the material and growing in a direction where there was sufficient hydrogen concentration to support hydrogen assisted fracture. Hydrogen assisted fracture continued until the crack reached the ductile region in the material, where it was arrested. The corrosion process continued, with hydrogen entering the metal matrix and diffusing again ahead of the crack tip.

Figure 6.24 presents the suggested mechanism for crack propagation within the embrittled region:

a. The volume with the solid line stretching out from the crack was a region that had reached the critical concentration of hydrogen; that region was now brittle. The volume between the dotted line and the solid line was a region that has some hydrogen but the hydrogen content had not yet reached a critical level.

b. The crack propagated in a random direction with the tendency of staying within the brittle region. Crack propagation at a high angle away from the perpendicular corresponded to a CIS slope on the fracture surface. Overall the fracture surface was perpendicular to the applied stress. The CIS slopes made significant angles to this overall direction. This was because fracture surfaces were observed perpendicular to the fracture surface.

c. The crack turned and grew directly into the material due to the tensile stress, aided by the larger embrittled region directly in front of the crack. The crack was arrested when it extended beyond the brittle region. This phase corresponded to a long flat region, hence a plateau. Due to the nature of

the SEM it was difficult to determine the angle the plateau made to the perpendicular, hence most long flat areas appeared as plateaus.

d. During the crack growth stages described in (b) and (c), the crack became wider as it became longer. By the end of the stage (c), the width was as illustrated in (d).

e. Corrosion processes produced hydrogen that diffused into the material, causing a new brittle region ahead of the crack.

Figure 6.25 relates the fractography to the proposed mechanism. Point A corresponds to prior crack arrest. The hydrogen brittle envelope was developed around point A. Once the hydrogen concentration became critical, the crack grew from point A to point B at a random angle, producing a CIS slope. Subsequent crack propagation was across a region of high hydrogen concentration towards point C in a straight line. As the crack travelled it cut across pearlite colonies indiscriminately, following the region of highest hydrogen concentration. At point C the hydrogen concentration fell below the critical level. As the crack propagated beyond point C it started to be arrested, coming to a stop at point D. The resulting fractography from point B to D was the flat plateau (mildly corrugated due to the pearlite colonies) from B to C, and the shallow dimpled qMVC region between points C and D.

6.5 FRACTURE MECHANISM CONCLUSION

The microstructure of the metal did not affect hydrogen diffusion, crack propagation nor the fracture mechanism transition (slow subcritical crack growth to fast brittle failure). This was seen by the crack growing across grain boundaries irrespective of their orientation.

The crack propagated as a front outwardly from the crack initiation site, perpendicular to the free surface of the material. Hydrogen formed due to corrosion reactions diffused into the metal along the direction of the greatest triaxial stress; directly into the material perpendicular to the applied axial stress. Subcritical crack growth propagated once the material ahead of the crack tip had reached a critical hydrogen concentration. Once a critical crack size had been reached, the rest of the material failed by fast brittle failure.

Subcritical crack growth was thought to occur in two stages:

- In the first stage, the crack grew in a random manner within the hydrogen saturated area ahead of the crack tip.

- The second stage saw the crack turn and propagate directly into the material, following the path of greater hydrogen concentration. The crack continued until it hit the ductile region. Then the corrosion process continued, producing more hydrogen that diffused into the metal matrix.

All this evidence suggested that the crack growth rate was dictated by the rate of hydrogen evolution at the crack tip and its rate of diffusion ahead of the crack tip.

6.6 EXPERIMENTAL FRACTURES

6.6.1 Tensile Test EG01 In Air and Distilled Water

Figures 6.26, 6.27 and 6.28 characterise a ductile fracture for LIST sample EG01, which was subject to a tensile test in air in the Instron tensile testing apparatus.

These pictures show the typical cup-and-cone fracture surface. The dimple rupture was clear in all three pictures, shown as the porous uneven surface with large variations in depth. The dark region to the right of the centerline of Figure 6.26 is caused by a piece of lint that landed on the sample prior to insertion into the microscope. The unconductive lint charged up and deflected the electron beam from the region.

Tensile tests in air in the Instron testing machine gave values of mechanical parameters within specifications. Similarly, tests in the LIST machine in air gave comparable values, as did a LIST test in distilled water. In all these cases there was a ductile overload fracture, and the overload fractography was typical Micro-Void Coalescence.

6.6.2 Applied Stress Rate

No SCC and ductile overload fracture occurred for the LIST test in the "sulphate pH 2.1" solution for the relatively fast stress rate of 0.19 MPa s^{-1}. In contrast, SCC occurred at the slower applied stress rates 0.019 and 0.0019 MPa s^{-1} in the "sulphate pH 2.1" solution. Figures 6.29 and 6.30 present fracture surfaces typical of those observed in the sulphate pH 2.1 solution. These fracture surfaces were similar to the fracture surfaces of the rock bolts failed in service by SCC.

6.7 LIST SAMPLE FRACTURE SURFACE

Figures 6.31 and 6.32 present an overview of the fracture surface of one LIST sample whilst Figures 6.33 and 6.34 show the overview of another LIST sample. Figure 6.34(a) shows several pits on the free surface, with the subcritical growth spreading from them towards the centre of the sample. Figure 6.34(b) provides a map of Figure 6.34(a) identifying the fracture regions as FFS, qMVC and SCC (CIS).

In both samples the SCC region was an elliptical region in the corner of the sample. The rest of the surface was covered in a different coarser topography (FFS). Within the FFS there were tear lines that radiated away from the subcritical crack growth region.

6.7.1 Fast Fracture Features

The FFS region typically covered 80-85% of the total surface area of the LIST samples.

Figures 6.35, 6.36 and 6.37 show the fracture topography from the FFS at x500, x1000 and x2000 magnification respectively. These figures show the maple leaf features typical of fast brittle fracture.

There were chasms between maple leaves in the LIST samples. Figure 6.38 depicts such a chasm, immediately surrounded by ductile tearing topography, with maple leaf features framing the chasm.

6.7.2 SCC Features

Features identified on LIST SCC fracture surfaces were CIS, TTS and quasi Microvoid Coalescence (qMVC).

Figures 5.25, 6.39 and 6.40 show the regions where the slow subcritical crack achieved critical dimensions, and the fracture changed from slow crack growth to fast brittle failure. The change was abrupt. There was no additional fracture mechanism. The demarkation between SCC and FFS however was not a straight line but was quite tortuous.

Figures 6.41, 6.42, 6.43, 6.44, 6.45 and 6.46 show typical fracture surfaces within the SCC region in LIST samples. These Figures show the CIS SCC morphology, although flat areas perpendicular to the field of vision were not common, particularly in Figure 6.41.

No dimpling was found on FF regions, very little was found on CIS, but all qMVC displayed these dimple like features. Consequently these dimple like features in the qMVC were attributed to the dimple rupture process.

Figures 6.47, 6.48 and 6.49 show areas close to the free surface of the samples, where the fracture was typical of TTS. There were no large pits present, and the surfaces had a relief that tended to have an orientation that pointed towards the free surface of the sample.

6.8 LIST SAMPLE DISCUSSION

6.8.1 FFS Region

On a macroscopic level, the tear lines displayed on the FFS region were formed by the material failing in a brittle rapid manner, initiating at the SCC region and propagating outwards.

The orientation of the maples leaves in the FFS tended to fan away from the crack initiation site. This was due to the crack propagating quickly away from the subcritical growth area.

Chasms sometimes occurred between the maple leaves. This separation was attributed to the material ahead of the fast crack tip yielding plastically, pulling open the chasm by a small amount before the brittle crack reached around this plastic region and severed the plastic yielding tendril. This was supported by the dimpled rupture region in Figure 6.38, where just below the chasm there was a dimpled rupture region bounded by the flat featureless surface of the fast fracture region.

The maple leaf features in the LIST samples showed the expected orientation as they pointed towards the region of subcritical crack growth.

The high magnification view of a typical chasm showed that the chasm was not very deep. The borders of the chasm showed the ductile failure dimples, while the surrounding features showed that the overall the

fracture was brittle.

6.8.2 SCC Region

Figure 6.34(b) provides a map of Figure 6.34(a) identifying the regions as FFS, quasi Micro Void Coalescence (qMVC) and SCC. qMVC surfaces were identified by the amount of small pits and almost ductile fracture appearance. qMVC tended to appear away from the sample surface where hydrogen had not had as much time to diffuse throughout the material. It has been suggested that this qMVC region would fail as a TTS if enough hydrogen diffused into the area [53]. This suggestion was supported by the fact that qMVC regions appeared at the fringes of the SCC regions, penetrating into the FFS region in finger like protuberances. This in turn suggests that the SCC crack slowly advances into the material, with hydrogen slowly diffusing ahead of the crack tip. When the crack reached a critical size, the crack then propagated throughout the material in a fast brittle manner. The region immediately in front of the crack tip had received an amount of hydrogen that was not enough to allow the SCC to grow into that region, but enough to weaken the material to allow it to fail in a quasi ductile manner as it failed in a fast manner.

The change in fractography from SCC to FFS was abrupt indicating that there was no third mechanism involved during the fracture.

In many samples, in the CIS region the amount of flat surfaces could be scarce, with the slopes being the most common feature. An estimate places the percentage of flat surfaces to sloped surfaces within the SCC region at 10%. At times, flat surfaces have been found that do not have the clear channels, but have a rough appearance with irregular relief. This difference in appearance was attributed to whether the crack travelled across a pearlite colony (rougher surface) or along a colony. The amount of hydrogen diffused into the material also played a part, as the more hydrogen is diffused into the material, the more brittle it behaved, leaving a smoother surface behind.

This is attributed to the crack tip advancing along the main pearlite colony axis as one of the components of the pearlite is preferentially corroded away.

Two different kinds of slopes were identified. One was a corrugated, relatively even slope (as shown by the rectangles in Figure 6.50). The other kind was a dimpled surface, irregular and suggests ductile tearing (as shown by the rectangles in Figure 6.51). It is postulated that the first of these slopes was produced by the crack tip advancing at an angle through the pearlite colony. The smoother these surfaces appear, the closer the angle of crack growth along the pearlite grain's main axis.

6.9 FRACTOGRAPHY COMPARISONS

A detailed comparison was carried out between LIST tests of 1355AXRC samples exposed to the sulphate pH 2.1 solution and 1355AXRC rock bolts failed in service. There were the same fracture modes in both the service and laboratory samples that were also similar to the reported literature. The fractures involved

a small SCC region followed by a large fast fracture (FF) region. Figure 5.2 provides a typical overview for a service fracture. The SCC region was easily identified by its darker colour due to the presence of corrosion products on the metal surface in the SCC region. This was due to the fact that the stress corrosion cracks grew slowly, allowing a period of time for corrosion to occur. In contrast, the overload region occurred essentially instantaneously, so that the surface was bight and shiny as an un-oxidized steel surface. The tear lines radiated away from the fracture origin. These tear lines facilitated the identification of the SCC feature that initiated the final fast fracture event. It was particularly noteworthy that the service stress corrosion cracks often initiated in association with the ribs on the surface of the rock bolt as illustrated in Figure 6.1.

A direct comparison of a service fracture and a LIST fracture is provided in Figure 6.52. Again, there was the SCC region and the brittle fast fracture (FF) of the overload region. These regions are identified in the schematics of Figures 6.52(b) and 6.52(d). It is worth noting that the fracture surfaces are macroscopically brittle with little indications of any macroscopic ductility.

Within the SCC region there were three different and distinct fracture morphologies: Tearing Topography Surface (TTS), Corrugated Irregular Slopes (CIS), and Micro Void Coalescence (MVC). These are illustrated in Figures 6.53-6.55. Figure 6.34(a) provides an overview of the SCC region of a LIST fracture surface, with the schematic of Figure 6.34(b) identifying the various fracture micro-mechanisms.

Typical TTS morphologies for rock bolts are presented in Figures 6.53(a) and 6.53(b) to allow comparison of typical TTS morphologies from LIST samples in Figures 6.53(c) and 6.53(d). The tearing topography surface was characterised by a flat convoluted surface with tiny ridges apparently oriented randomly. TTS typically occurred close to the free surface and consequently was associated with the early stages of SCC.

Typical CIS morphologies for rock bolts are presented in Figures 6.54(a) and 6.54(b) to allow comparison of typical morphologies from LIST samples in Figures 6.54(c) and 6.54(d). The CIS surface was characterised by flat plateaus separated by corrugated slopes.

Typical morphologies for the qMVC-FF transition for rock bolts are presented in Figures 6.55(a) and 6.55(b) to allow comparison of typical morphologies from LIST samples in Figure 6.55(c) and 6.55(d). The qMVC within the SCC region was significantly flatter that the dimple rupture observed in the overload region of tensile samples without SCC.

Typical brittle fast fracture (FF) morphologies for rock bolts are presented in Figures 6.56(a) and 6.56(b) to allow comparison of typical FF morphologies from LIST samples in Figures 6.56(c) and 6.56(d). The FF morphology was typical of cleavage fracture.

6.10 FRACTOGRAPHY DISCUSSION

The fractography indicated that the service failures and the LIST tests were associated with slow crack growth by a SCC mechanism, until the critical crack size was reached. When the critical crack size was reached, there was sudden fast fracture by a brittle cleavage mechanism. Within the SCC region, there were

three distinct fracture morphologies: Tearing Topography Surface (TTS), Corrugated Irregular Slopes (CIS), and quasi Micro Void Coalescence (qMVC). TTS was found close to the specimen surface, Figure 6.53, which was interpreted as indicating that TTS occurred during the early stages of SCC, and its occurrence may be associated with higher availability of hydrogen. CIS occurred subsequently, and made up the majority of the SCC fracture region. At the SCC FF interface, there was often qMVC. This qMVC may be part of the slow SCC process or may represent material where some hydrogen had diffused and consequently could fail in a qMVC mode during the fast fracture event.

6.11 CONCLUSIONS

The conclusions that are naturally drawn from the fractography also involve details of the testing methodology which logically fits into Chapter 7 of this thesis. Thus the conclusions drawn in this Section are based on material presented in this Chapter as well as material presented in Chapter 7.

Tensile testing of the rock bolt steel in air using the Instron tensile testing machine and LIST testing in air and in distilled water produced ductile micro-void coalescence overload fracture. In all these tests, the measured mechanical properties (σ_y, UTS) were all within specification.

The sulphate pH 2.1 solution produced SCC in the LIST test at an applied stress rate of 0.019 MPa s^{-1} The fractures were macroscopically brittle in contrast to the ductile overload fracture measured in air and also in the distilled water. Detailed SEM examination of the LIST samples tested in the sulphate pH 2.1 solution indicated a fractography similar to that of the service failures. On a macroscopic scale, the samples subjected to the preferred LIST test (in the sulphate pH 2.1 solution) displayed the same characteristics as those displayed by the rock bolts failed in service by SCC: a small dark thumbnail shaped area surrounded by a shiny irregular surface.

The sulphate pH 2.1 solution at the fast applied stress rate of 0.19 MPa s^{-1} produced a ductile overload failure with no SCC. This is typical of SCC. In the faster test, there was insufficient time for SCC, and consequently, there was a ductile overload failure. In contrast, LIST testing at a much slower rate of 0.0019 MPa s^{-1} produced a result similar to the LIST tests at 0.019 MPa s^{-1}.

Thus it can be concluded that LIST testing at 0.019 MPa s^{-1} in the sulphate pH 2.1 solution produced SCC comparable to that of the service SCC.

The LIST test in the sulphate pH 2.1 provided a good foundation for a test to mimic service SCC, to be used to study the influences of rock bolt metallurgy and to explore countermeasures to service SCC.

The transgranular nature of the SCC fracture, and the fact that SCC occurred at room temperature in the sulphate pH 2.1 solution point to the likelihood that the SCC mechanism probably involved hydrogen.

Rock bolts failed in service had macroscopic surfaces that were similar to the LIST fractures produced by LIST testing at 0.019 MPa s^{-1} in preferred sulphate solution of pH 2.1.

These features were a SCC region typically 1-1.2 mm in depth followed by a brittle fast fracture region.

There was an abrupt change between SCC region and FFS, although the demarkation was not straight but tortuous.

The SCC region had three typical fracture morphologies: TTS, CIS, and qMVC.

CIS had the following features: a network of corrugated surfaces, joined by rough slopes. The corrugated surfaces usually displayed ridges formed by the different phases within pearlite colonies. CIS can display minor pitting on its surface. The main fracture mechanism was thought to be the slow advance of the crack tip through the material. Sometimes the crack advanced across a pearlite colony (giving a ridged surface), while other times it travelled through it (preferentially eating away one of the phases within the pearlite *after* the crack propagated through). The degree of roughness depended on the angle that the crack travelled through the grain.

qMVC was found between CIS and FFS. It was typified by the rough dimpled look with pits scattered along its surface. qMVC regions were areas where hydrogen had diffused into them, but in not enough concentration to cause SCC, but enough to allow the material to fail in a different manner to the typical ductile tearing (cup and cone) failure.

TTS had been described as a *"characteristic microscopic fracture mode with a kind of ductile tearing appearance, a certain degree of plasticity and a very closely spaced nucleation"* [53]. TTS had been found to have the tendency to be oriented towards the free surface, but the orientation was less as one moves away from the free surface. This loss of orientation had been attributed to the increase of triaxiality associated with crack growth or to the decrease of hydrogen concentration at larger distances from the boundary.

SCC surfaces were examined in rock bolts failed in service by SCC, LIST samples and the reported literature. All were quite similar. Hence it could be concluded that LIST testing was a reliable method of simulating field SCC in the laboratory. A laboratory test has been achieved that causes a tensile sample to fail in a manner similar to the failure mode observed from service failures, namely slow SCC followed by fast brittle fracture. The laboratory tests involved subjecting a tensile sample to a linearly increasing stress at a slow applied stress rate whilst the specimen is exposed at the free corrosion potential to a dilute sulphate solution of pH 2.1. Detailed fractography of SCC fracture features from the laboratory test has shown that these fracture surfaces have the same features as fracture surfaces of service failures.

6.12 FIGURES

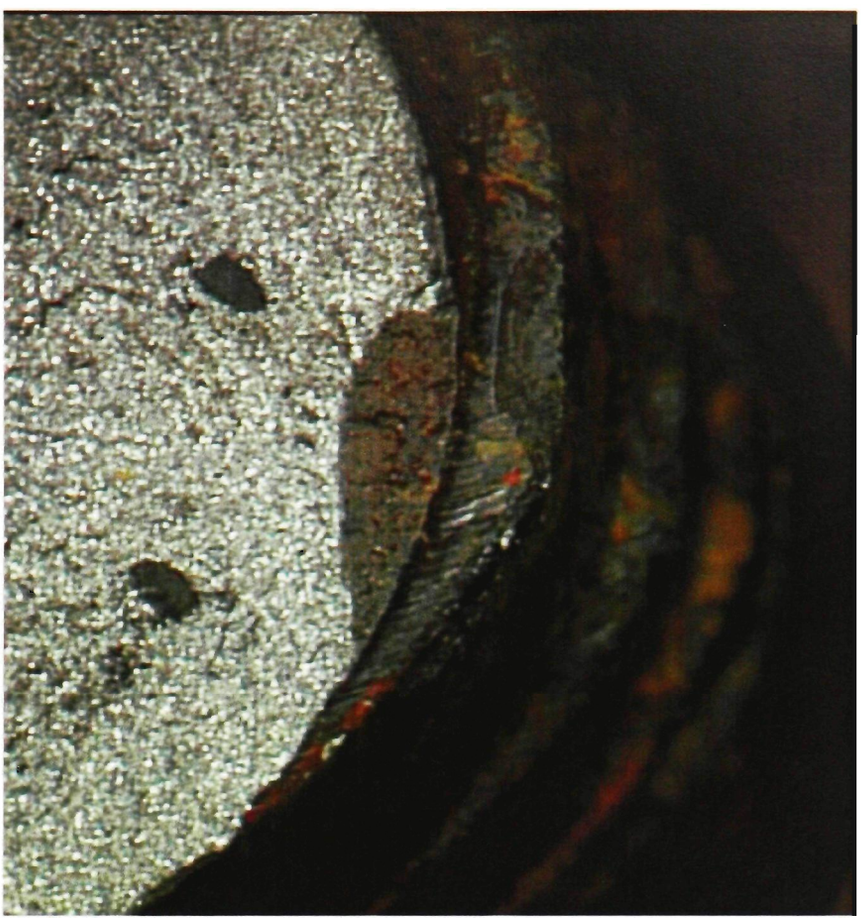

FIGURE 6.1: Overview of the dark thumbnail area on the rock bolt fracture surface.

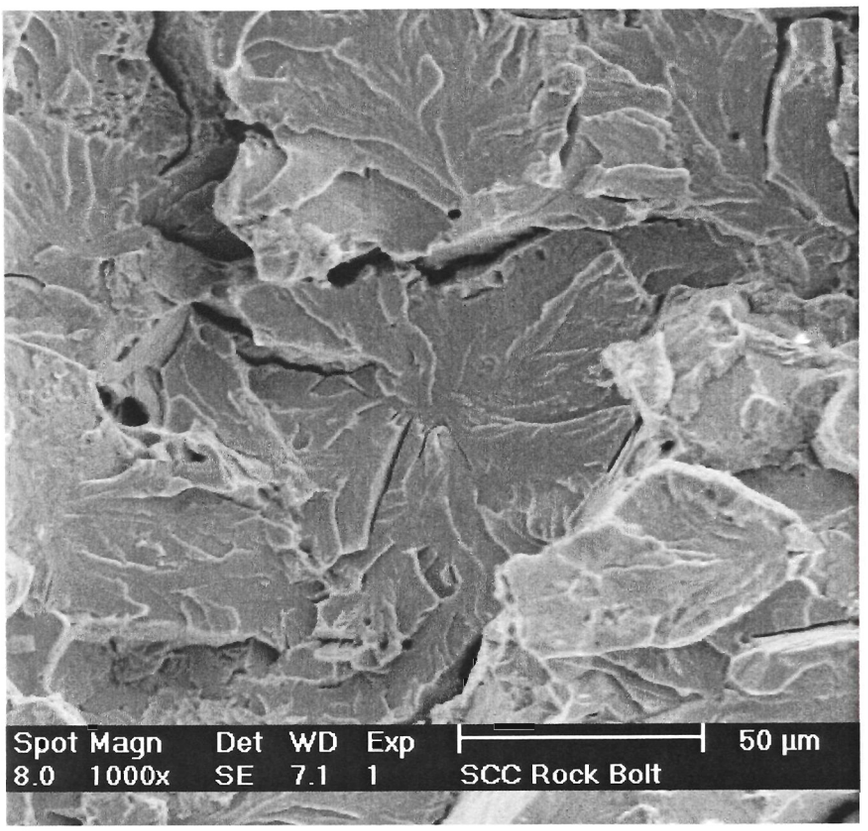

FIGURE 6.2: Detail of FFS at x1000 magnification.

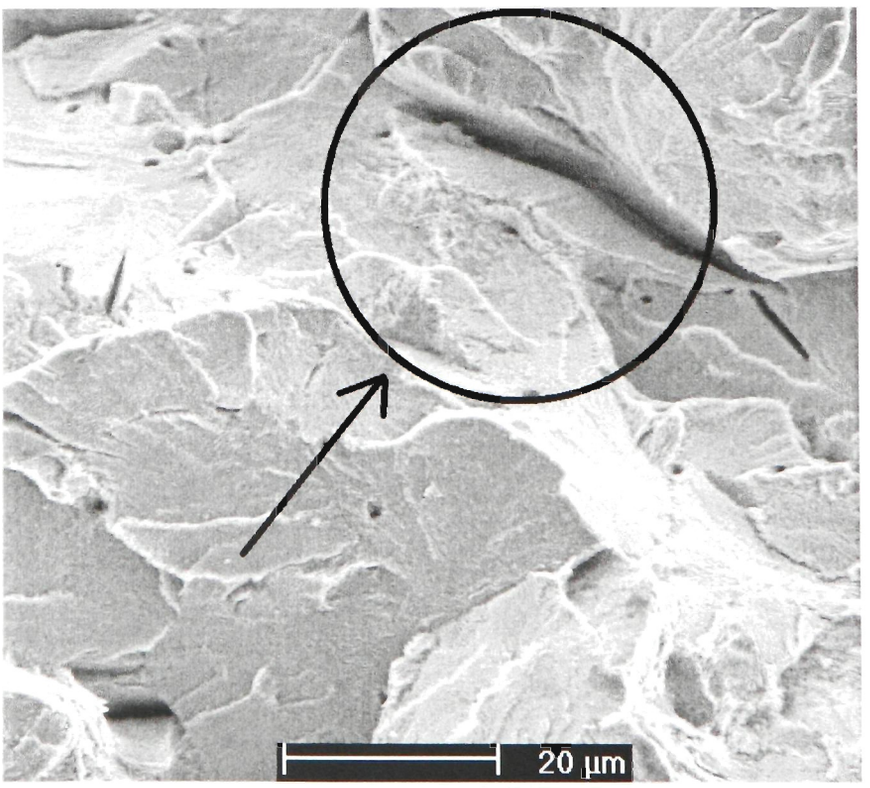

FIGURE 6.3: Detail of a chasm in FFS.

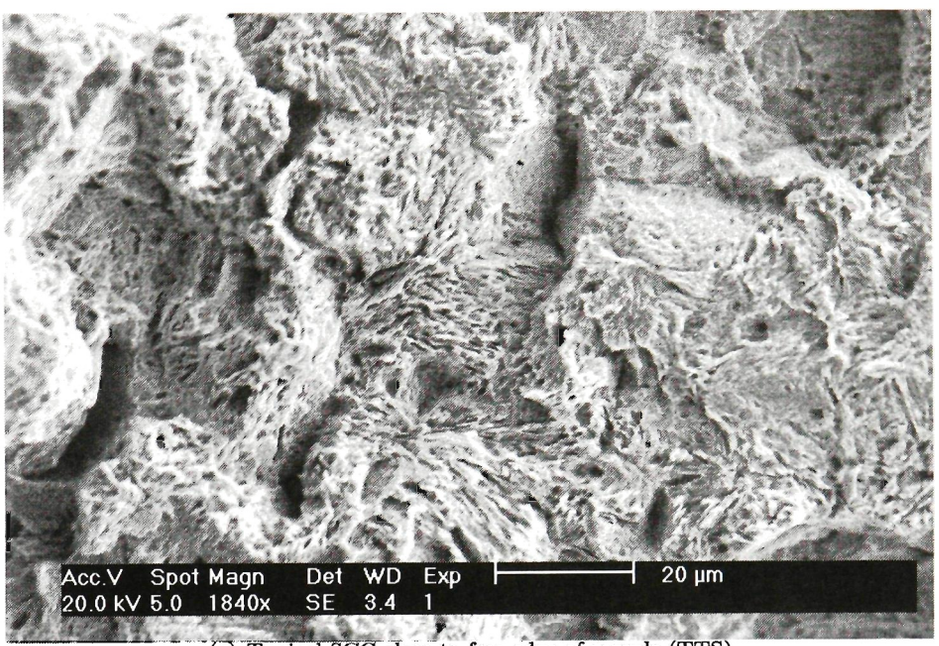

(a) Typical SCC close to free edge of sample (TTS)

(b) Schematic view showing TTS. A: Flat region (bounded by dashed line) B: Chasm or secondary crack

FIGURE 6.4: Typical TTS

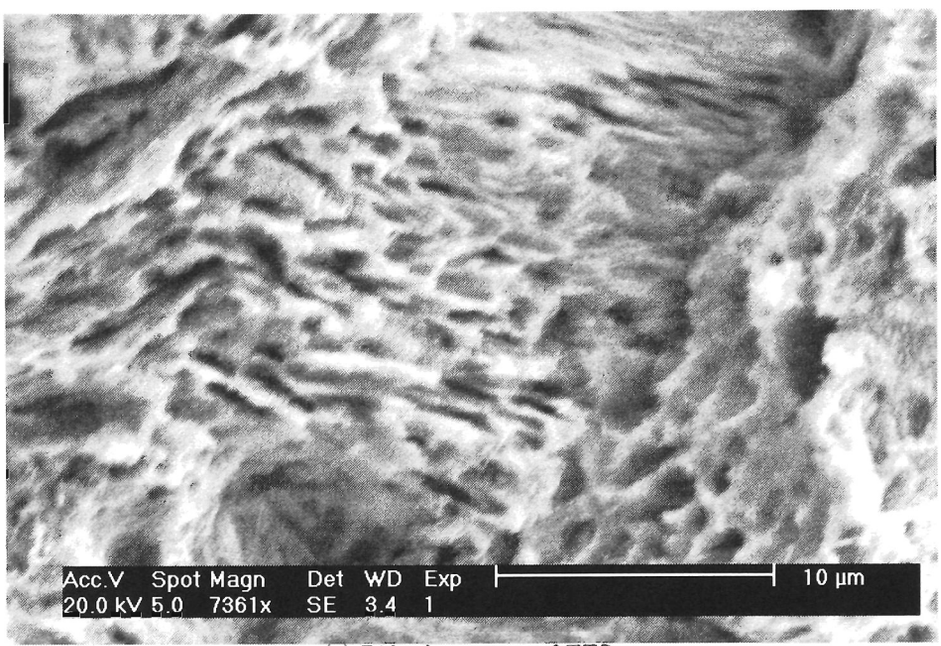

(a) Ridged structure of TTS

(b) Schematic view showing the ridge direction and pearlite colony orientation indicated by the fine parallel lines indicative of the direction of the plates of ferrite and carbide that make up the pearlite.

FIGURE 6.5: Higher magnification of Figure 6.4

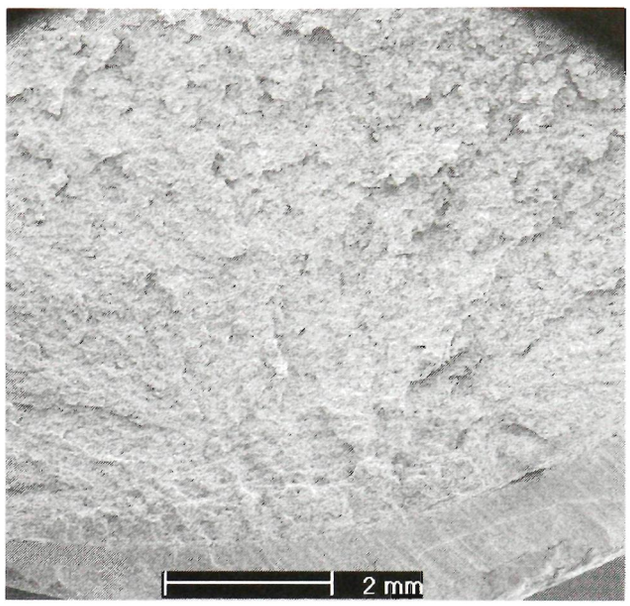

FIGURE 6.6: Overview of a typical SCC region in a rock bolt.

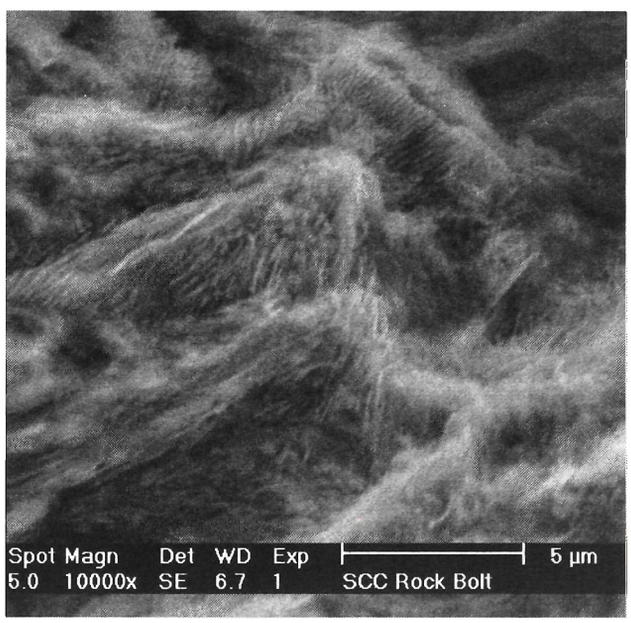

FIGURE 6.7: Fine ridges found on slopes in the SCC region.

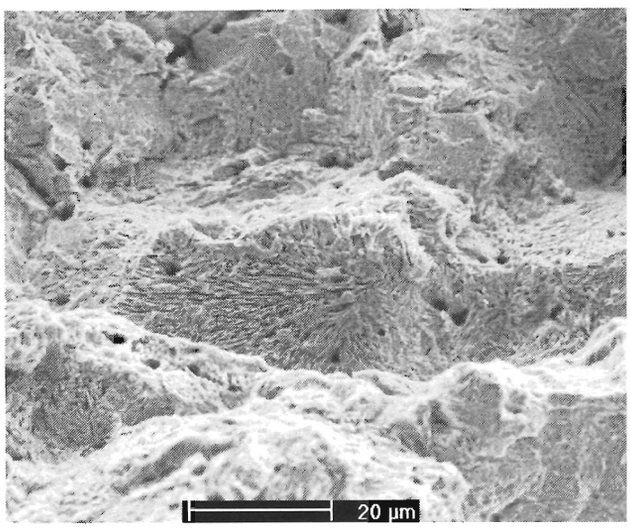

FIGURE 6.8: Flat ridged area.

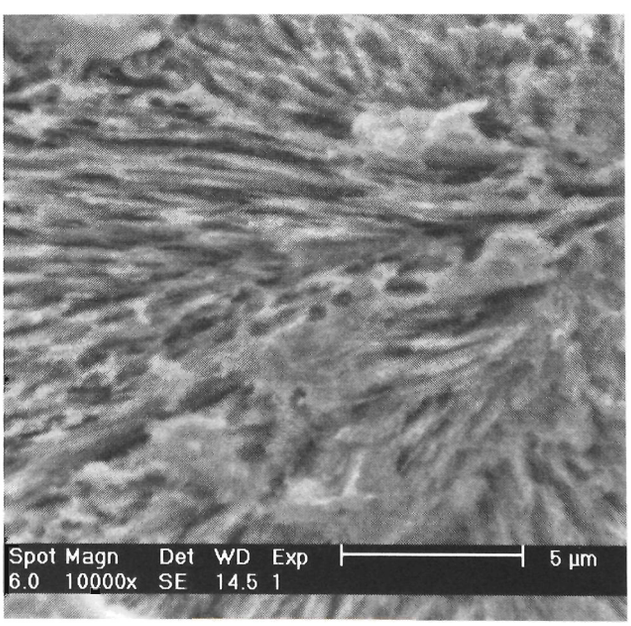

FIGURE 6.9: Detail of Figure 6.8.

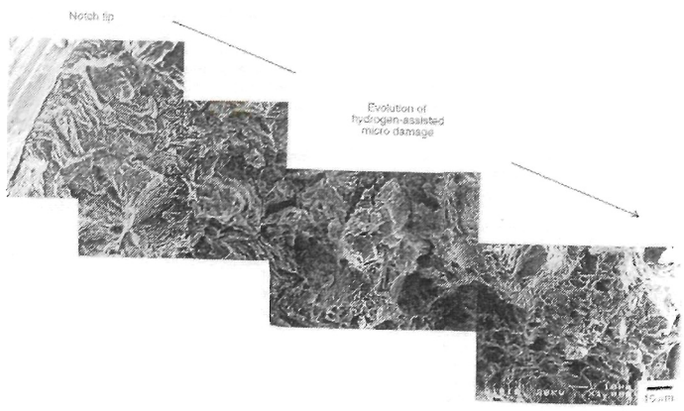

FIGURE 6.10: Picture taken by Toribio and Vasseur of evolution of hydrogen assisted micro damage. [53]

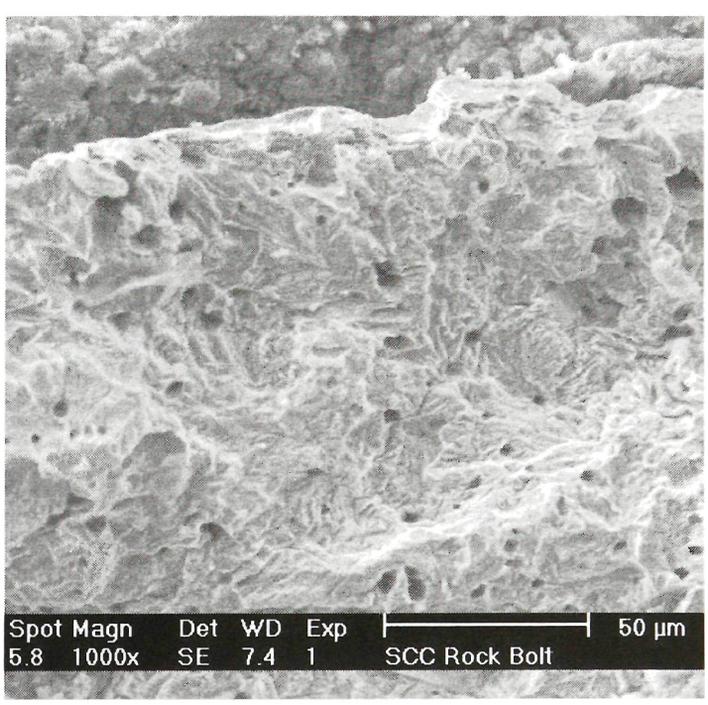

FIGURE 6.11: TTS in a rock bolt sample.

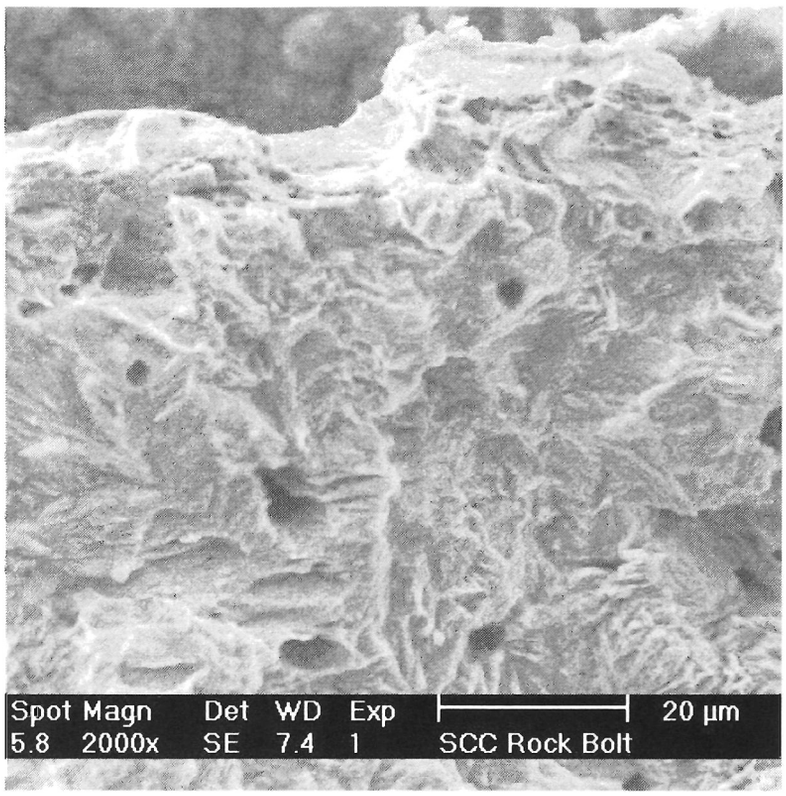

FIGURE 6.12: TTS in a rock bolt sample.

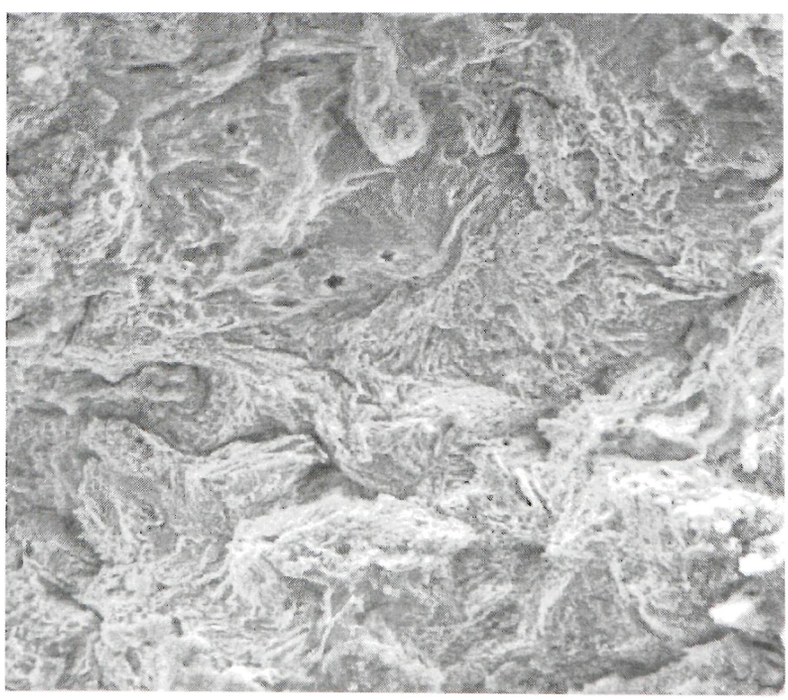

FIGURE 6.13: TTS in a rock bolt sample.

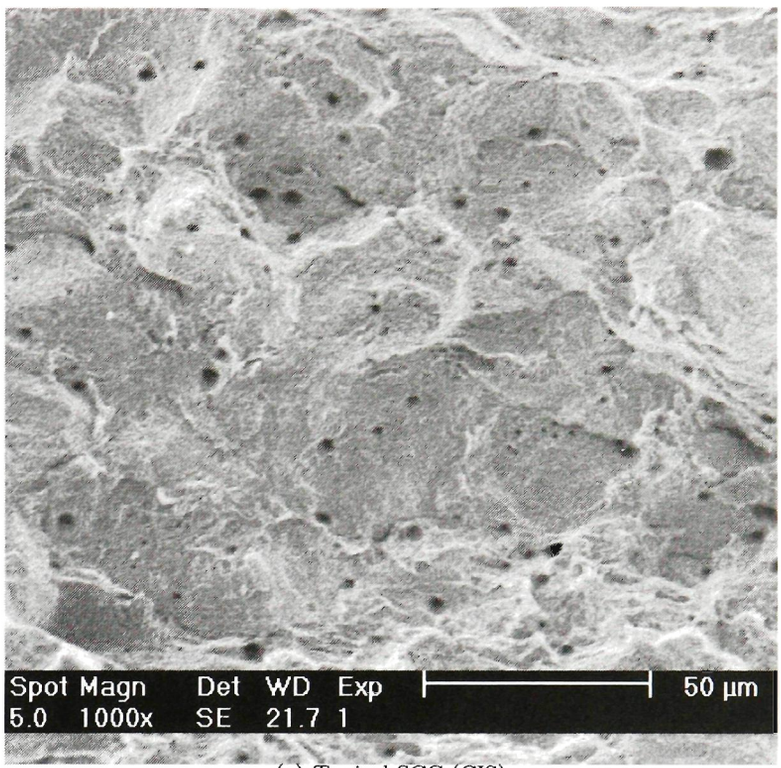

(a) Typical SCC (CIS)

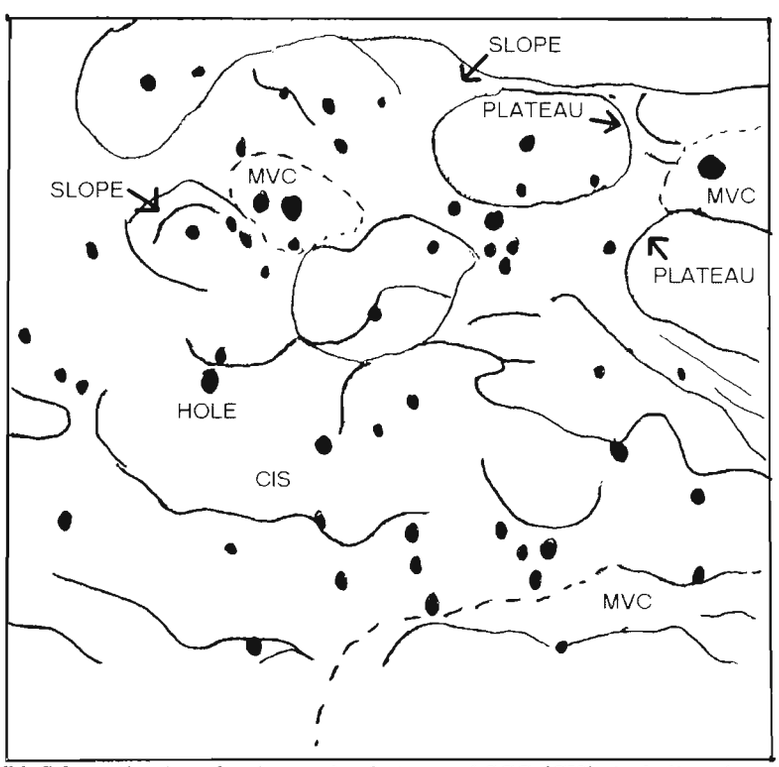

(b) Schematic view showing major features of SCC (CIS), including slopes and plateaus

FIGURE 6.14: Typical SCC (CIS)

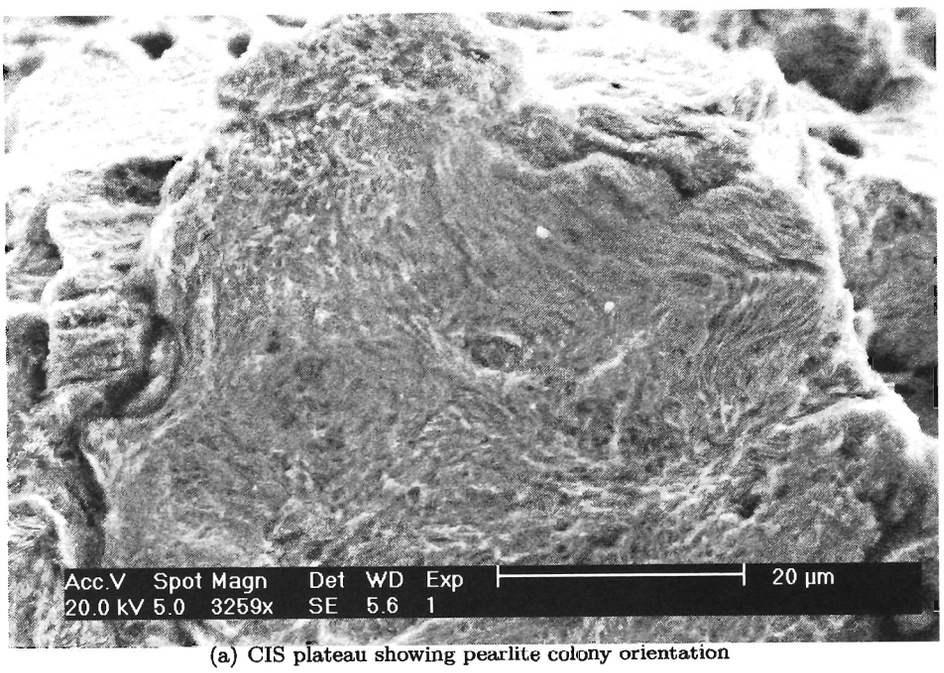

(a) CIS plateau showing pearlite colony orientation

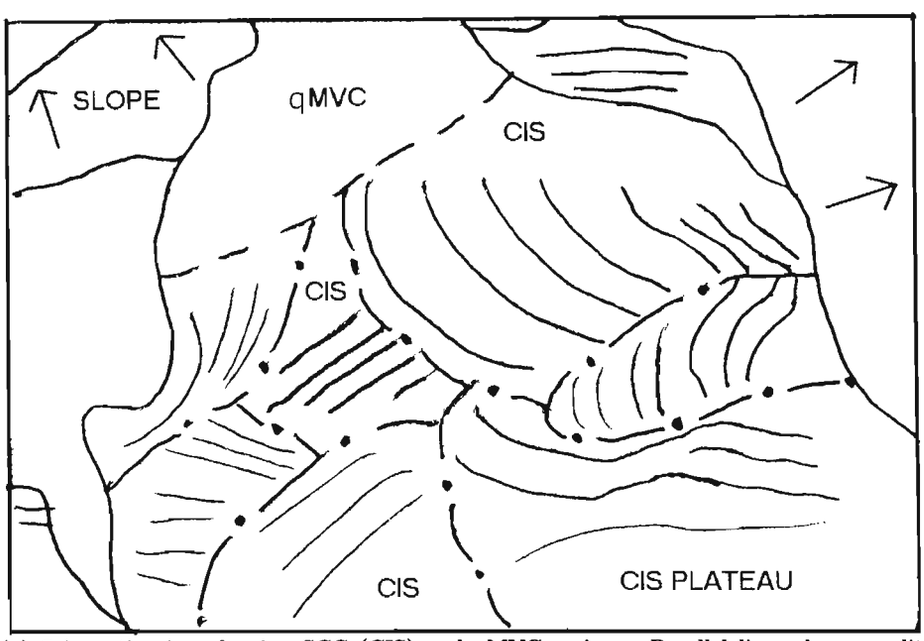

(b) Schematic view showing SCC (CIS) and qMVC regions. Parallel lines show pearlite colony orientation. Arrows show down slopes.

FIGURE 6.15: High magnification view of a plateau within CIS

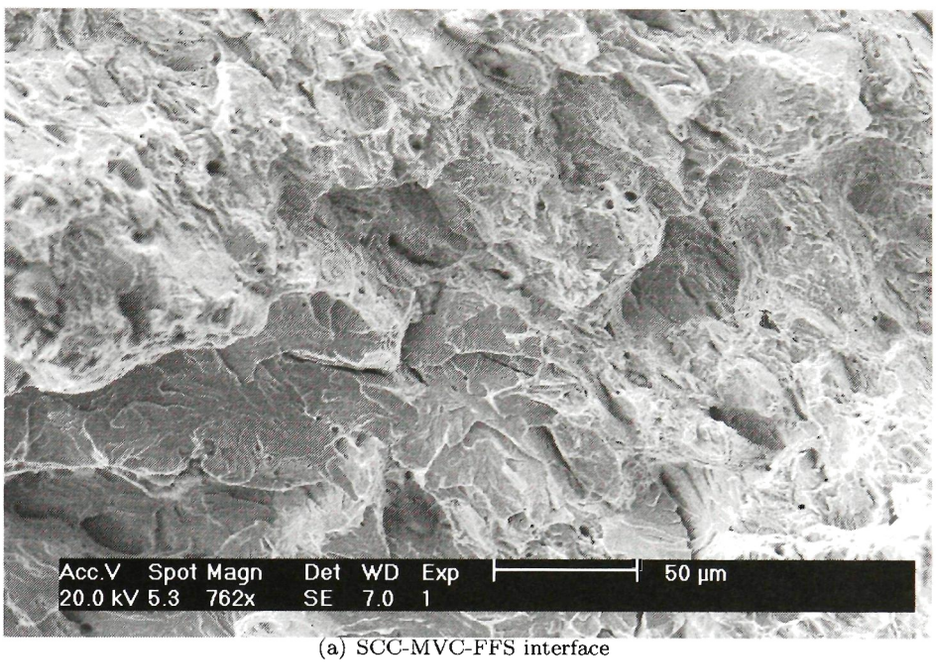

(a) SCC-MVC-FFS interface

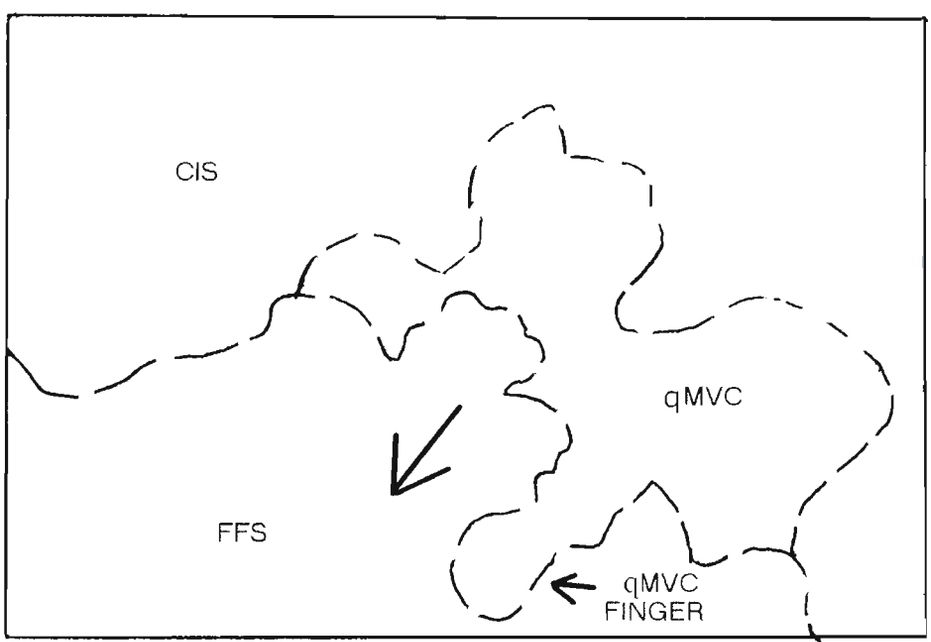

(b) Schematic view showing a qMVC "finger" extending into the FFS. Large arrow shows crack growth direction.

FIGURE 6.16: Typical SCC-MVC-FFS interface

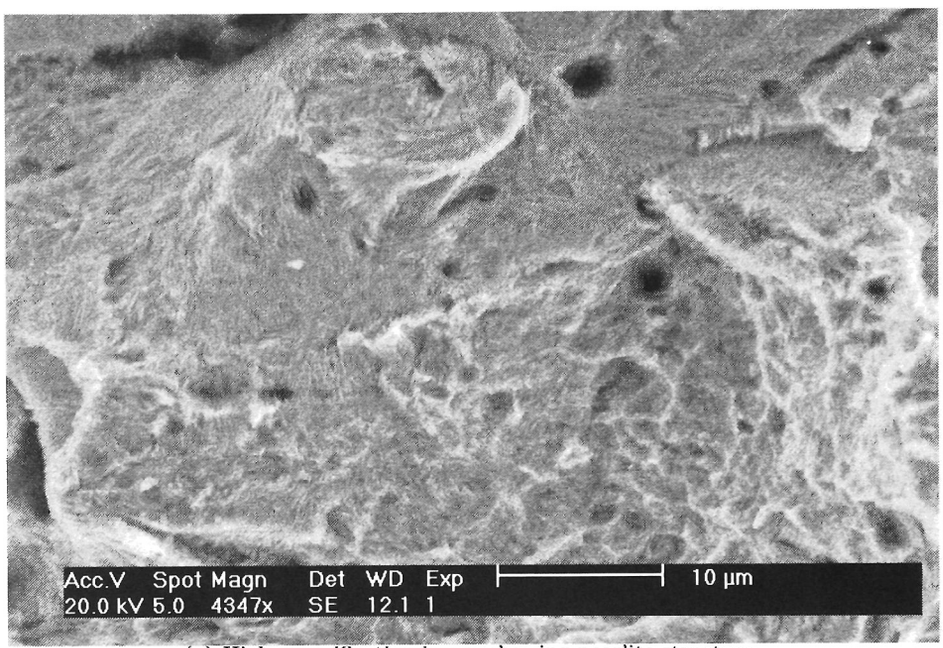

(a) High magnification image showing pearlite structure

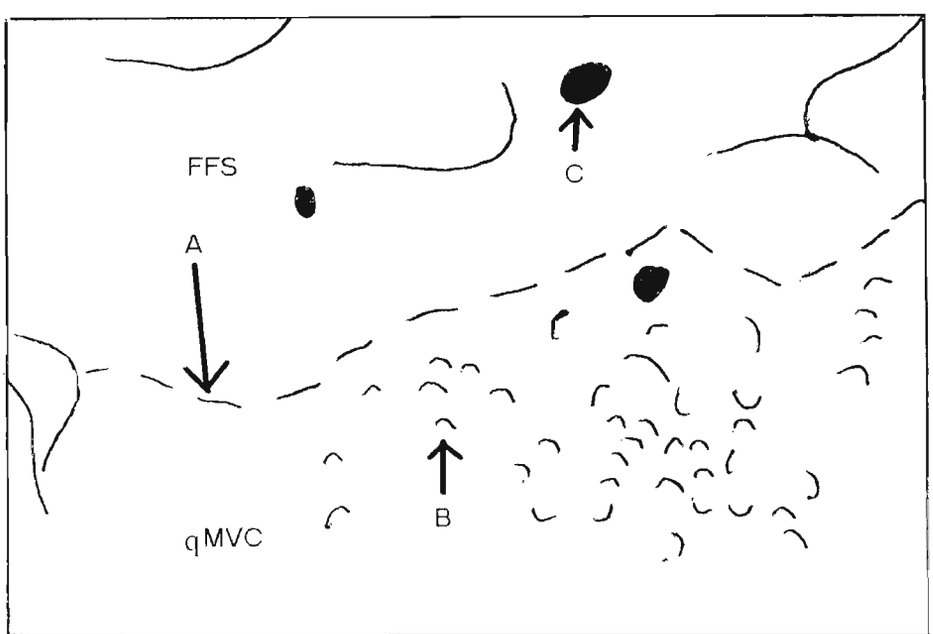

(b) A: Dashed line showing qMVC-FFS interface, B: qMVC dimples, C: Holes

FIGURE 6.17: Flat region within the SCC-FFS interface (x4347)

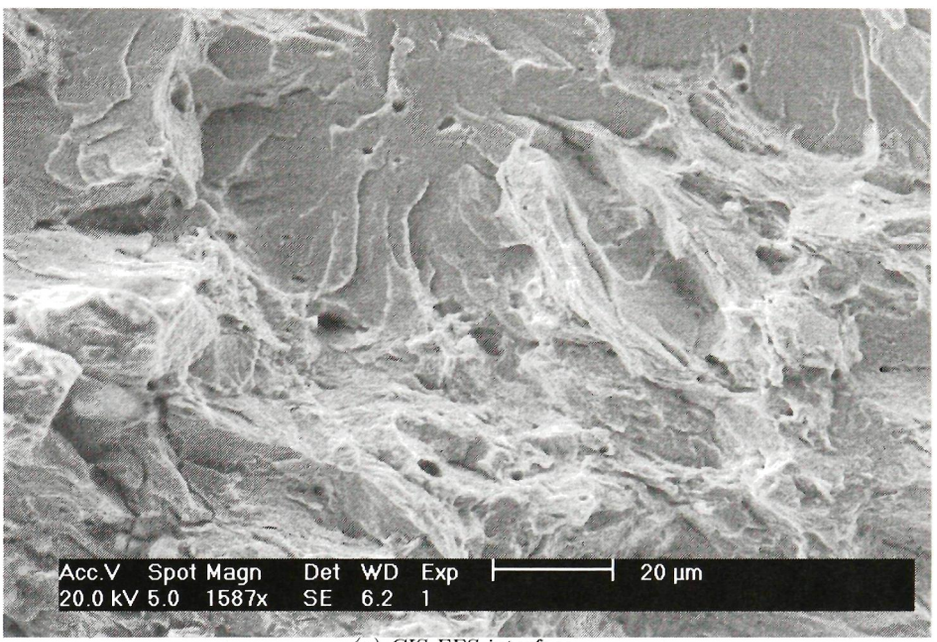

(a) CIS-FFS interface

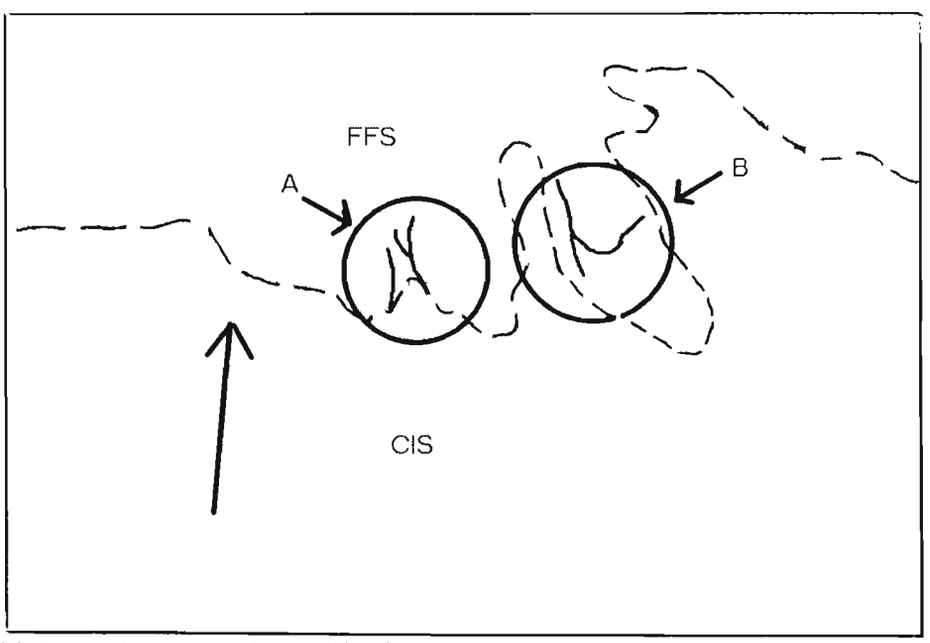

(b) Schematic view showing SCC(CIS) and FFS regions. Large arrow shows crack growth direction. A: Figure 6.19, B: Figure 6.20

FIGURE 6.18: Typical SCC(CIS)-FFS interface (x1587)

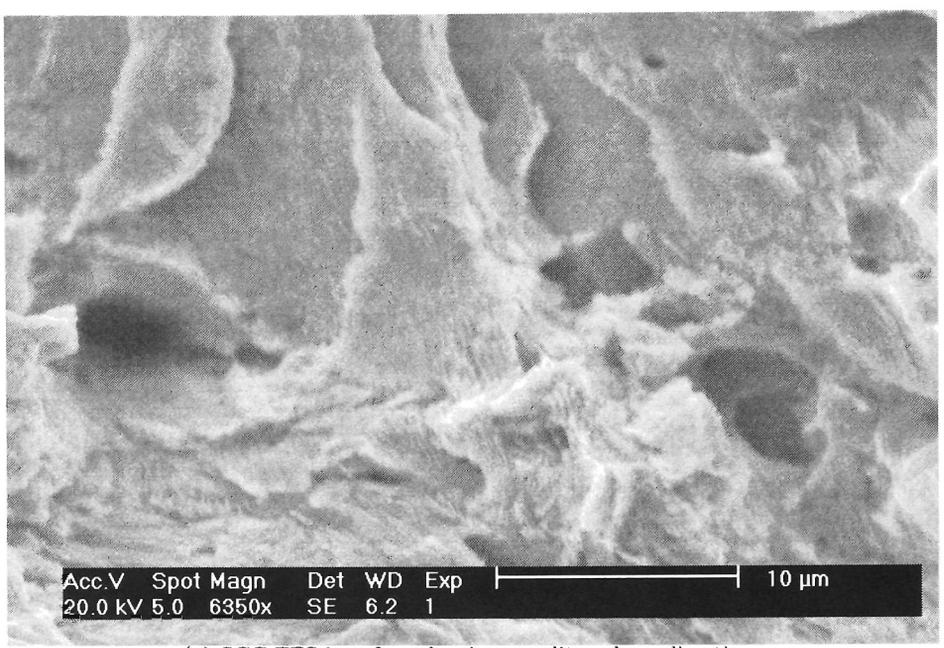

(a) SCC-FFS interface showing pearlite colony direction

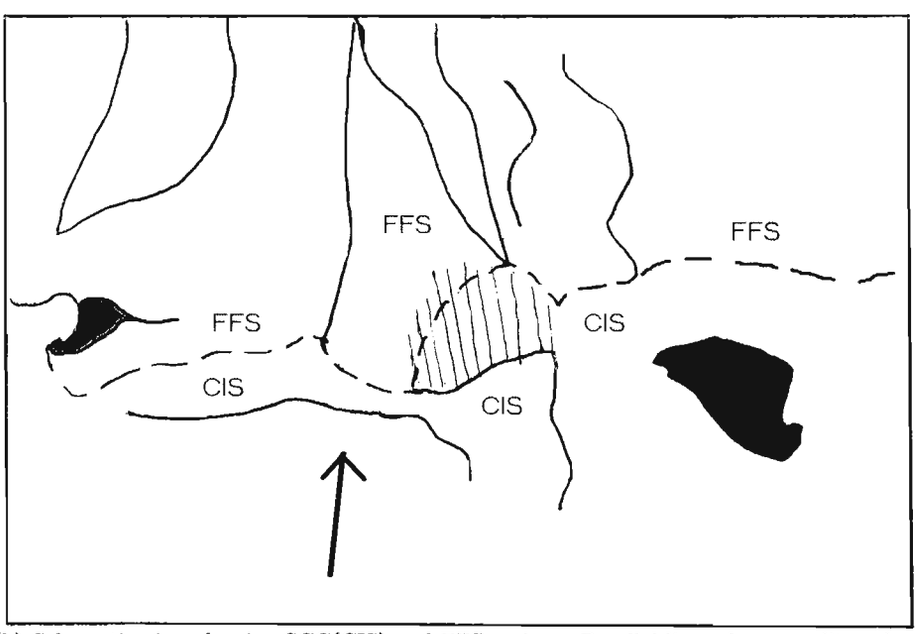

(b) Schematic view showing SCC(CIS) and FFS regions. Parallel lines show pearlite colony orientation. Large arrow shows crack growth direction.

FIGURE 6.19: Higher magnification view of region A of Figure 6.18 (x6350)

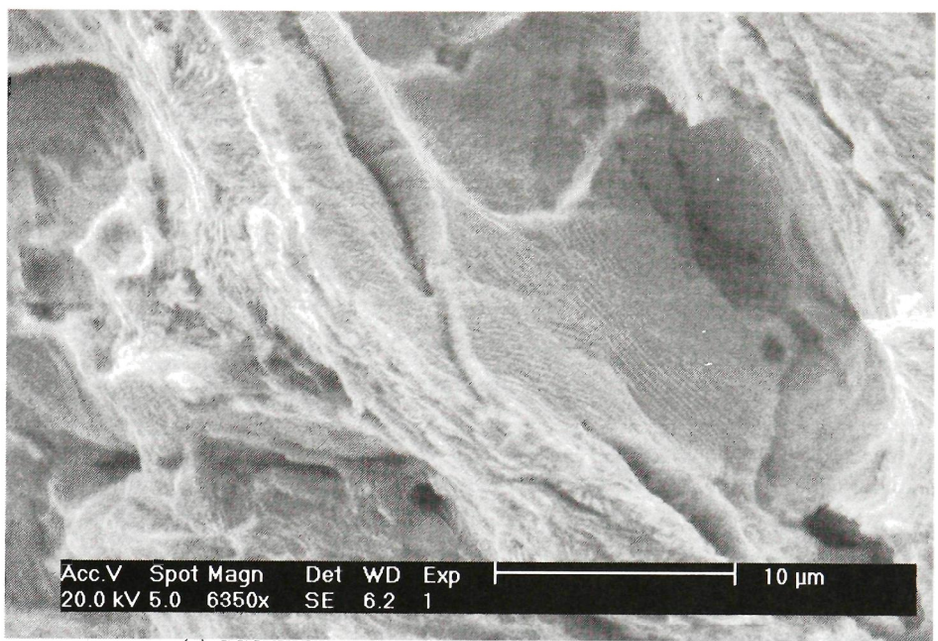

(a) SCC-FFS interface showing pearlite colony direction

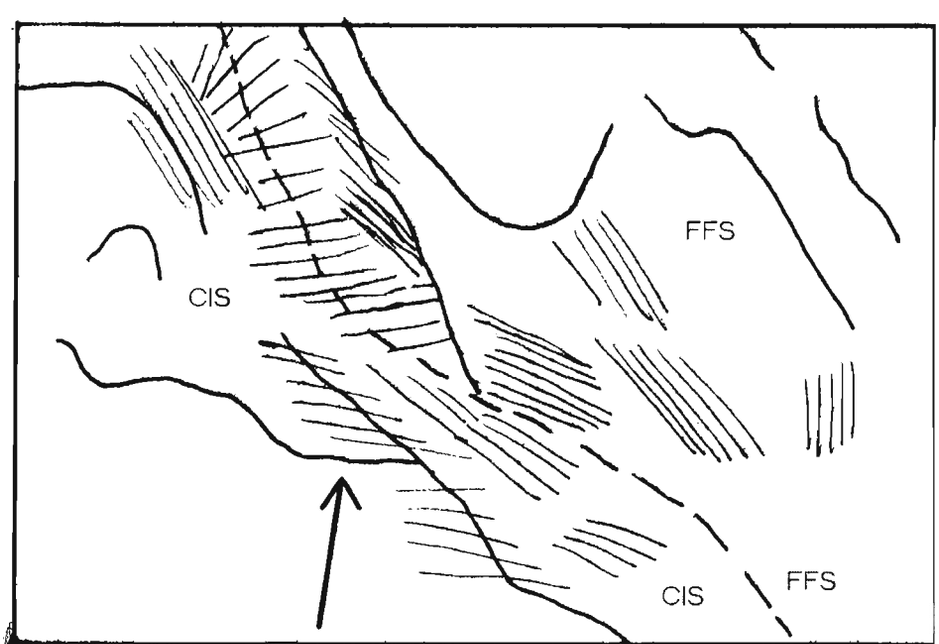

(b) Schematic view showing SCC(CIS) and qMVC regions. Dashed line shows interface. Parallel lines show pearlite colony orientation.

FIGURE 6.20: Higher magnification view of region B of Figure 6.18(x6350)

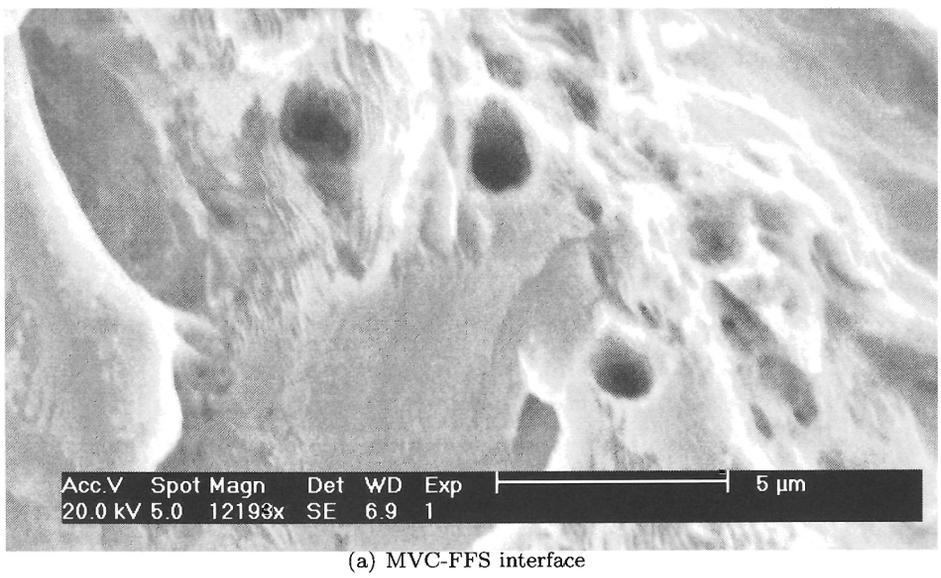

(a) MVC-FFS interface

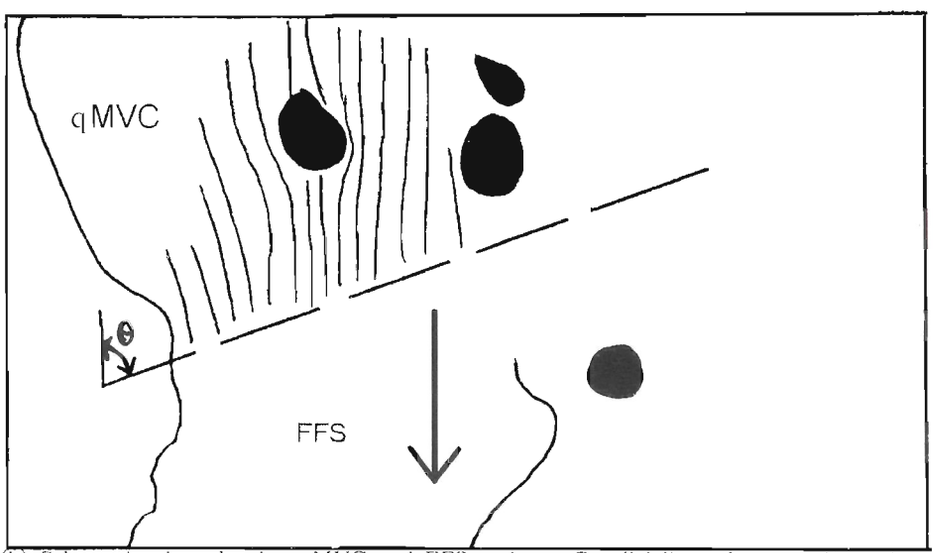

(b) Schematic view showing qMVC and FFS regions. Parallel lines show pearlite colony orientation. Large arrow shows crack growth direction.

FIGURE 6.21: Typical MVC-FFS interface (x12193)

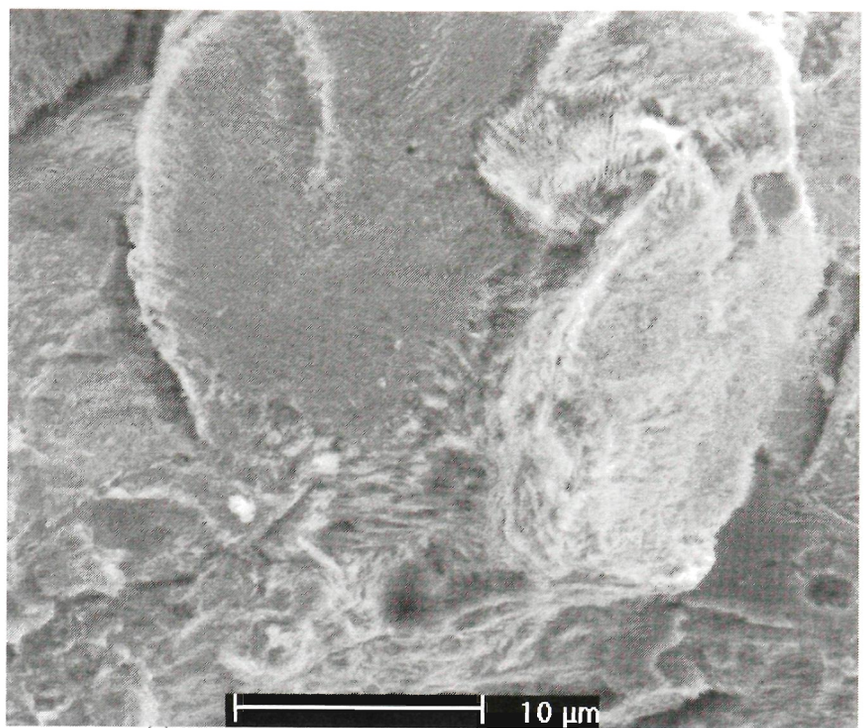

(a) High magnification image showing pearlite structure

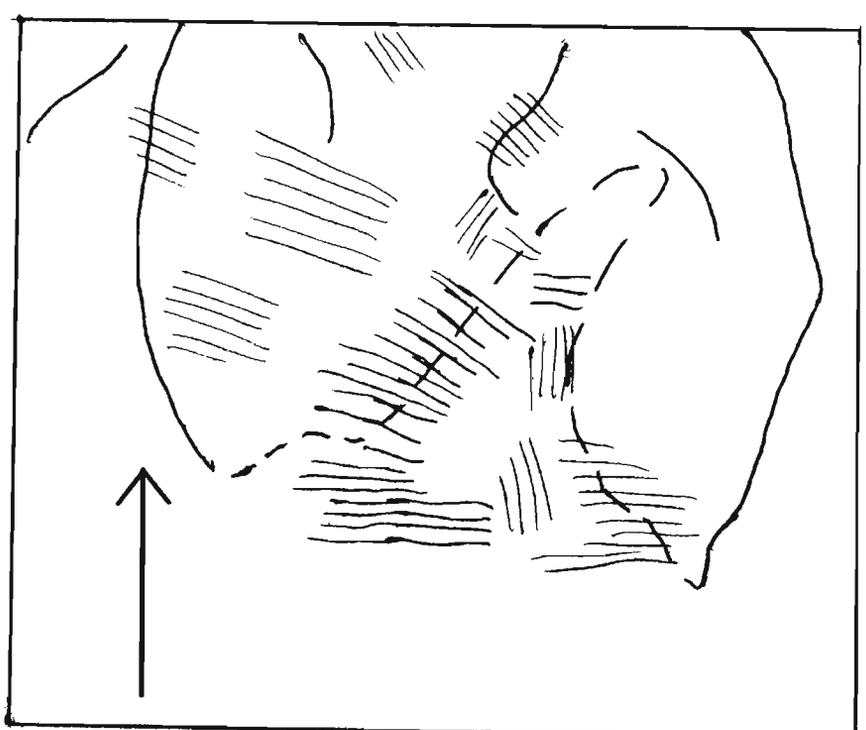

(b) Dotted line is the SCC-FFS interface. Parallel lines are pearlite colony orientations. Large arrow is crack growth direction.

FIGURE 6.22: SCC - fast fracture interface

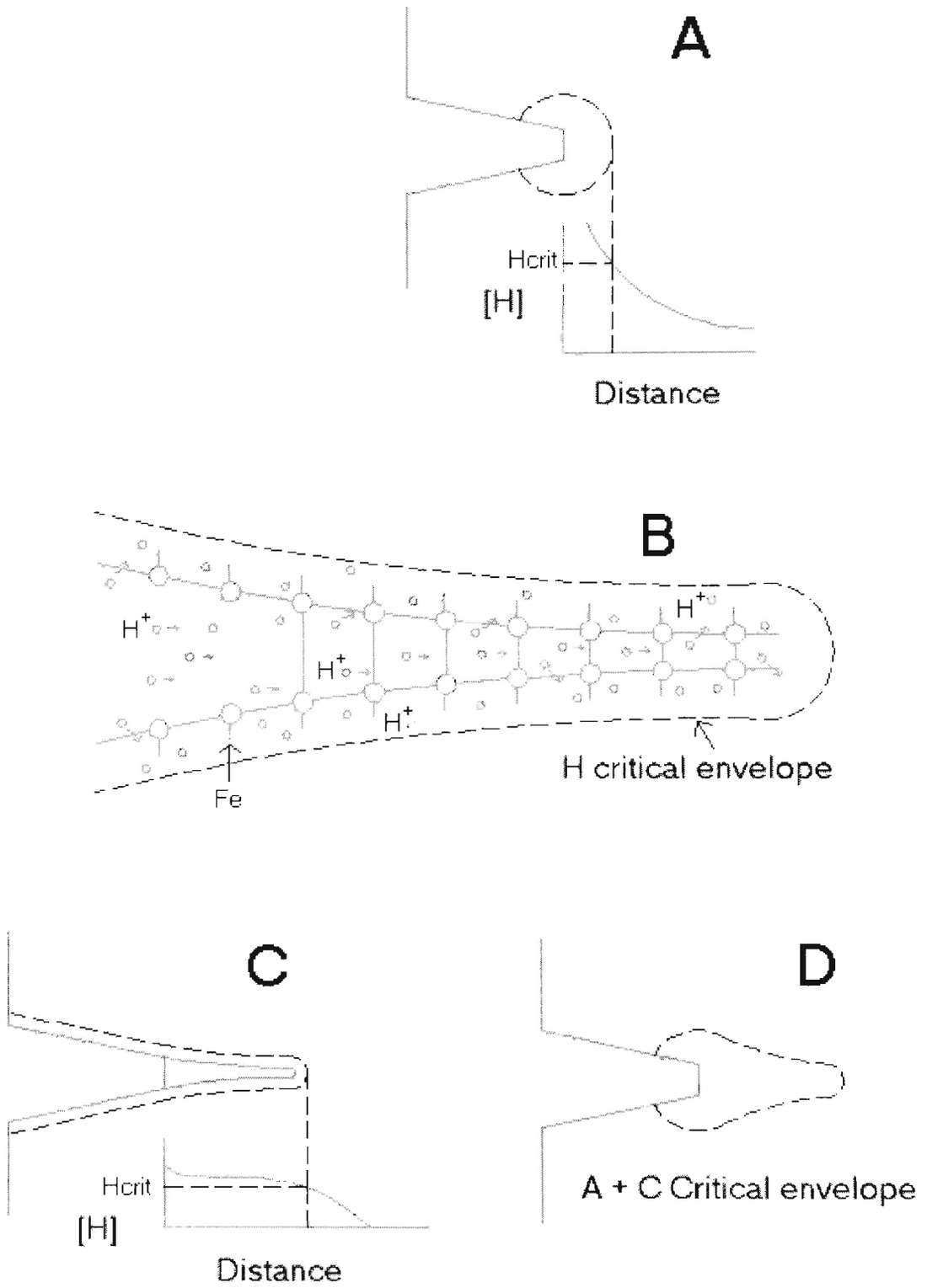

FIGURE 6.23: Critical hydrogen envelope

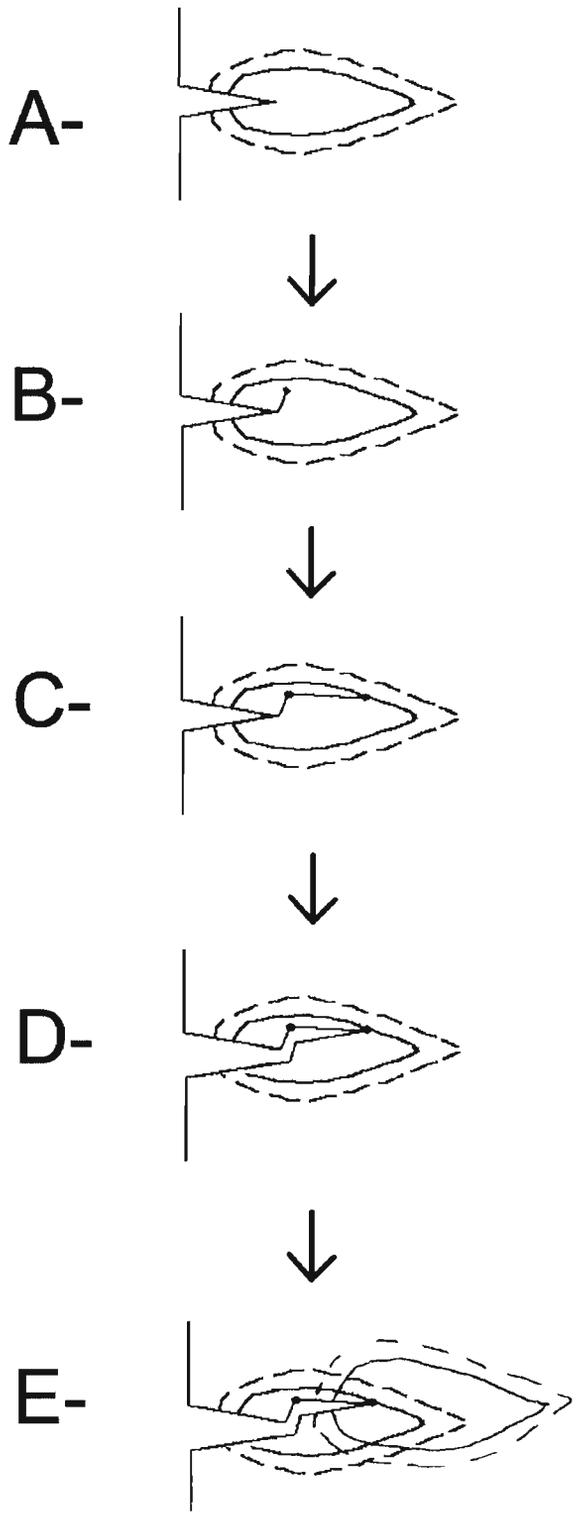

FIGURE 6.24: Slow crack growth propagation

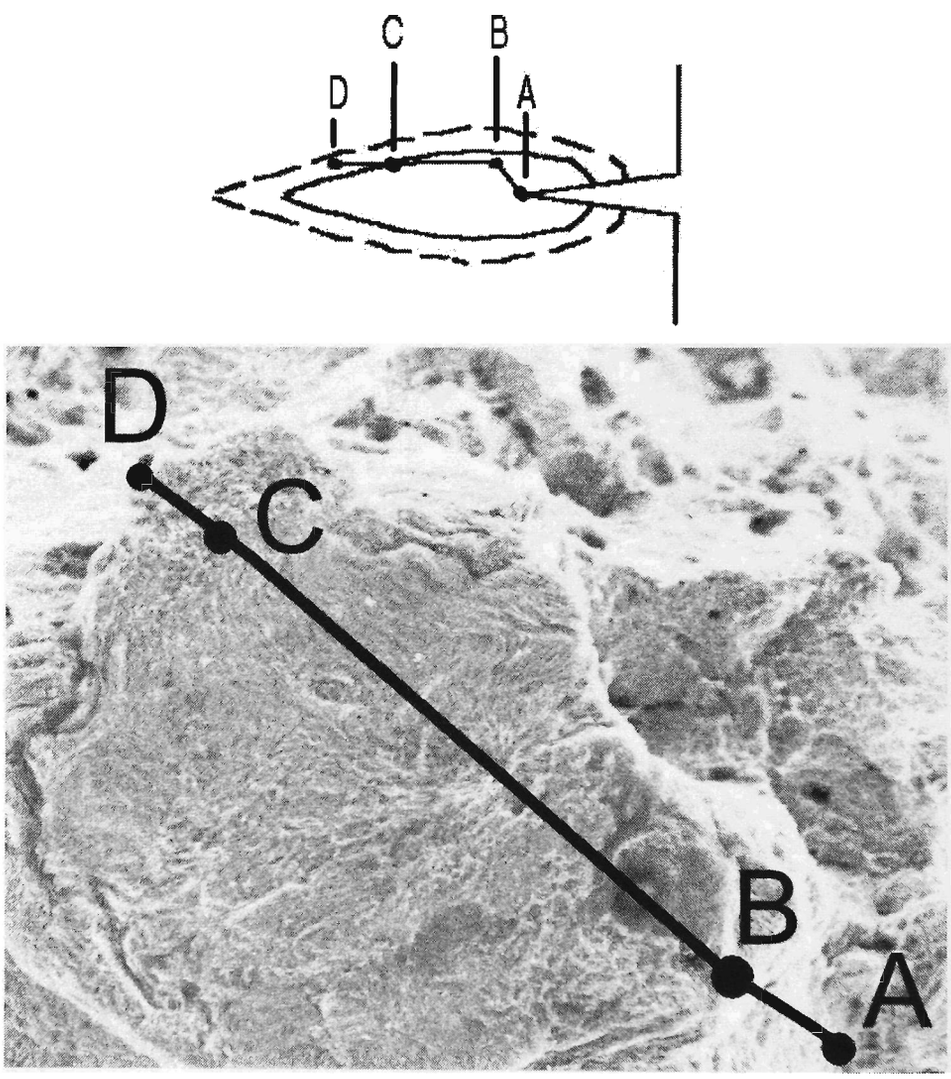

FIGURE 6.25: Crack path related to microstructure

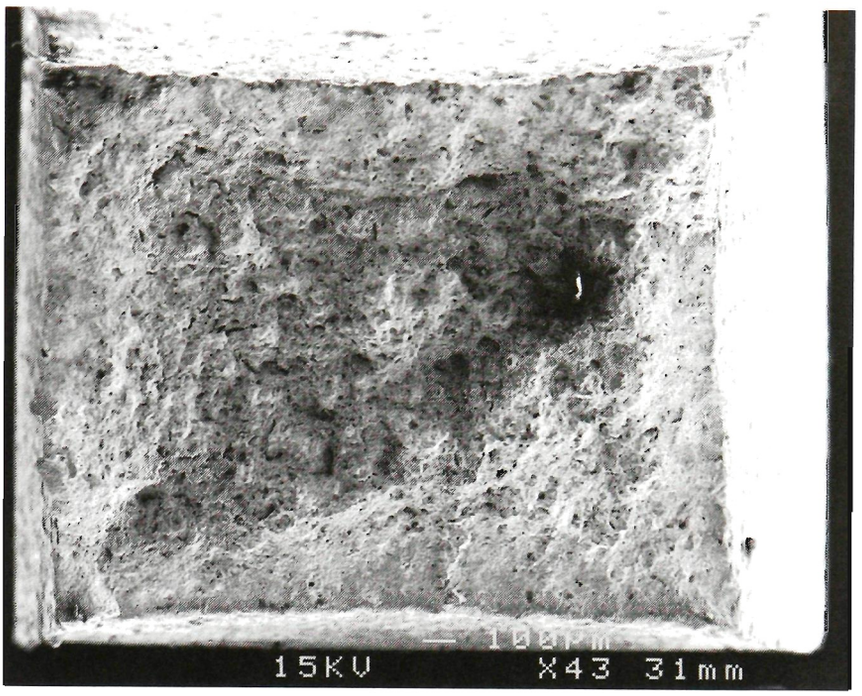

FIGURE 6.26: Overview of EG01 sample

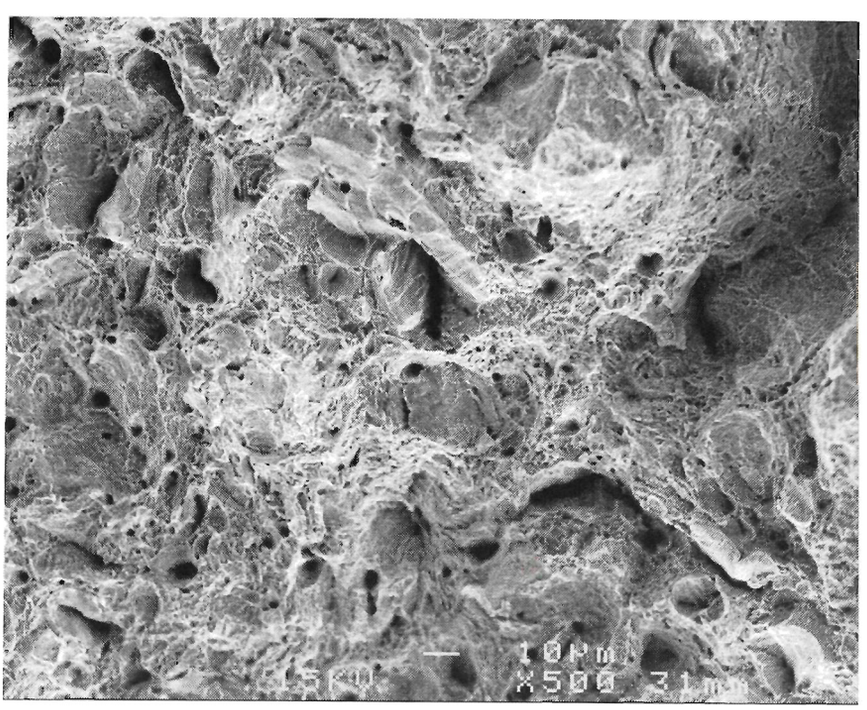

FIGURE 6.27: Detail of EG01 from centre of sample

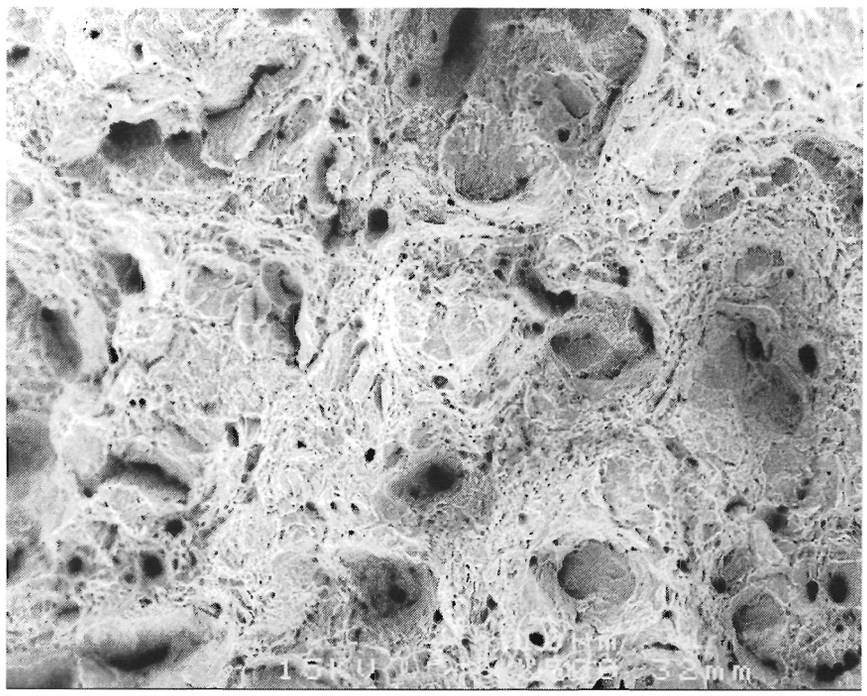

FIGURE 6.28: Another detail of EG01 from centre of sample

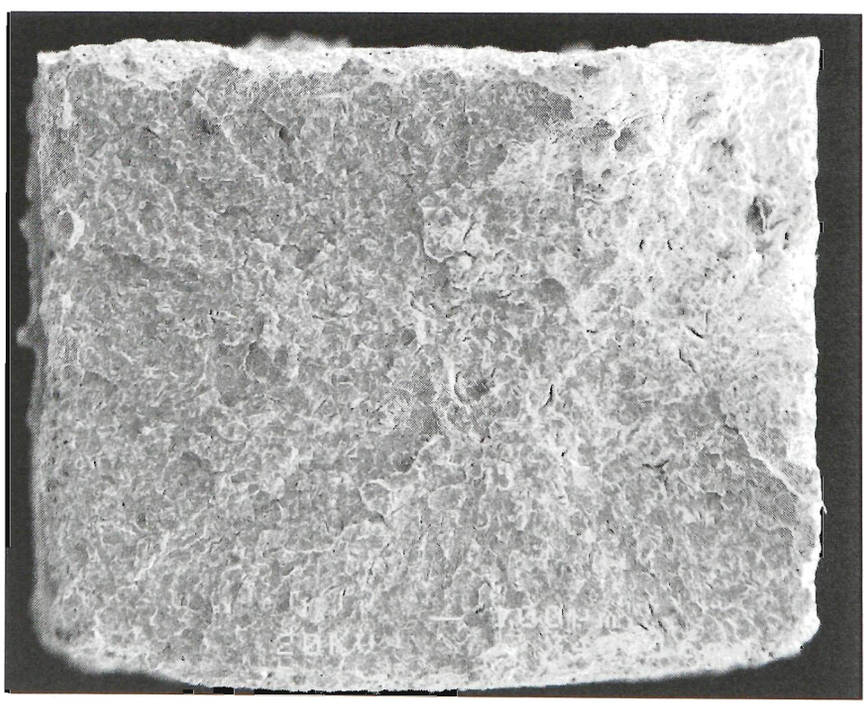

FIGURE 6.29: Overview of SCC in a LIST sample

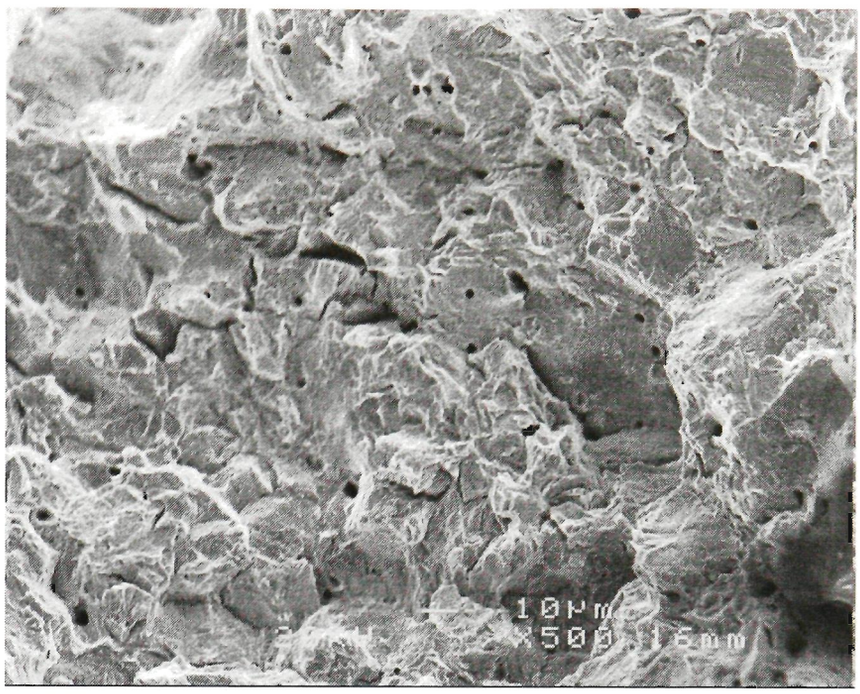

FIGURE 6.30: Detail of LIST SCC

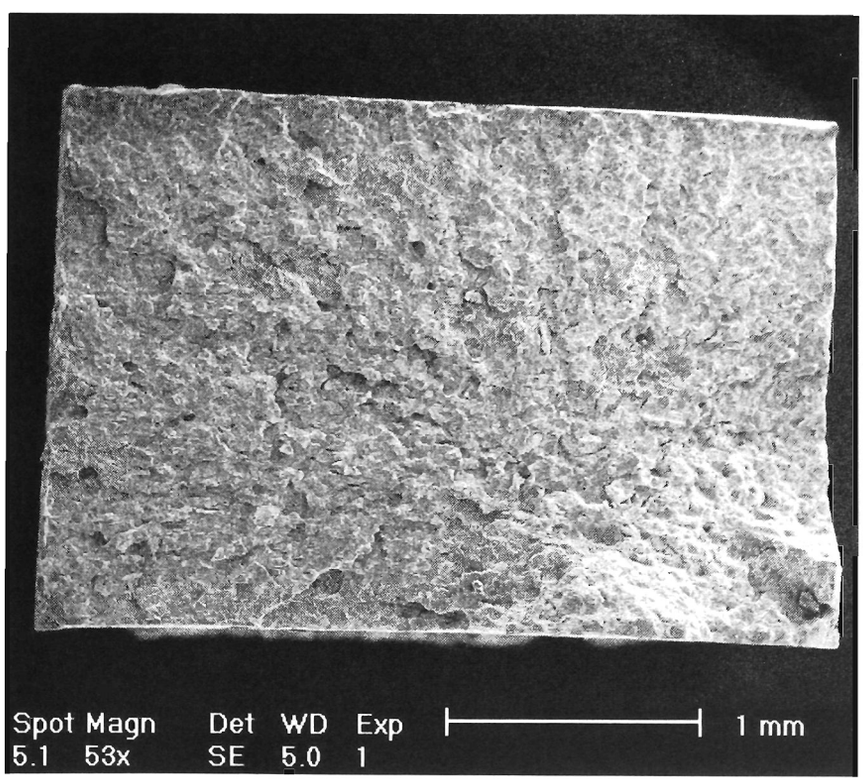

FIGURE 6.31: Overview of LIST sample 24.

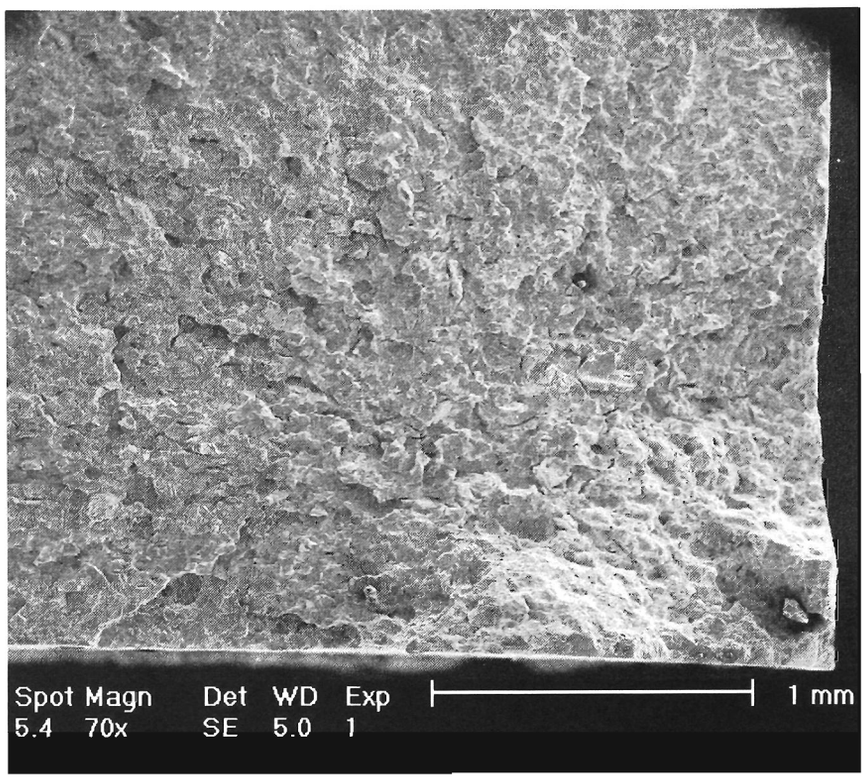

FIGURE 6.32: Detail from Figure 6.31 showing SCC area.

FIGURE 6.33: Overview of LIST sample 41.

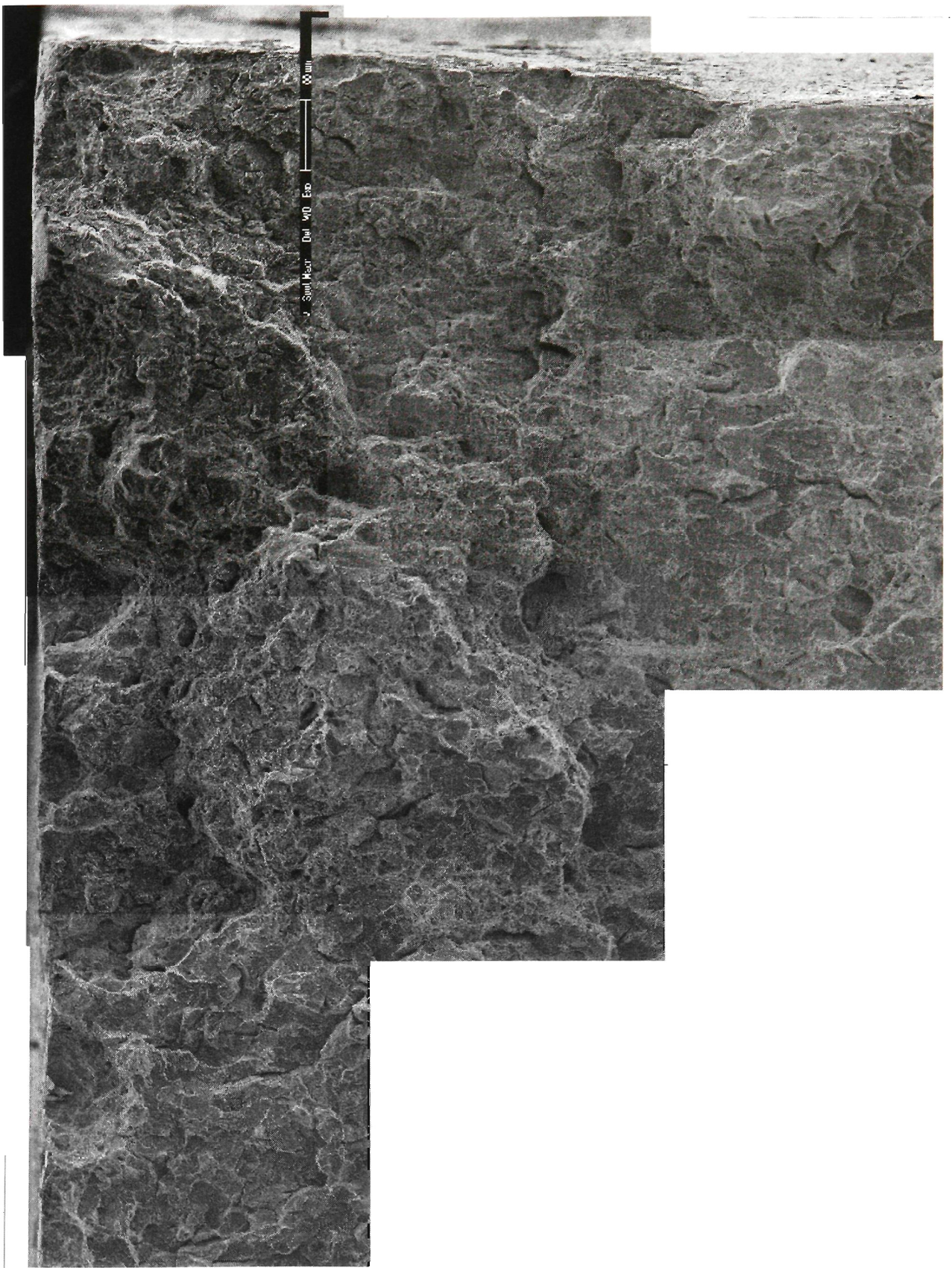

(a) SCC region from Figure 6.33.

FIGURE 6.34: LIST SCC Overview

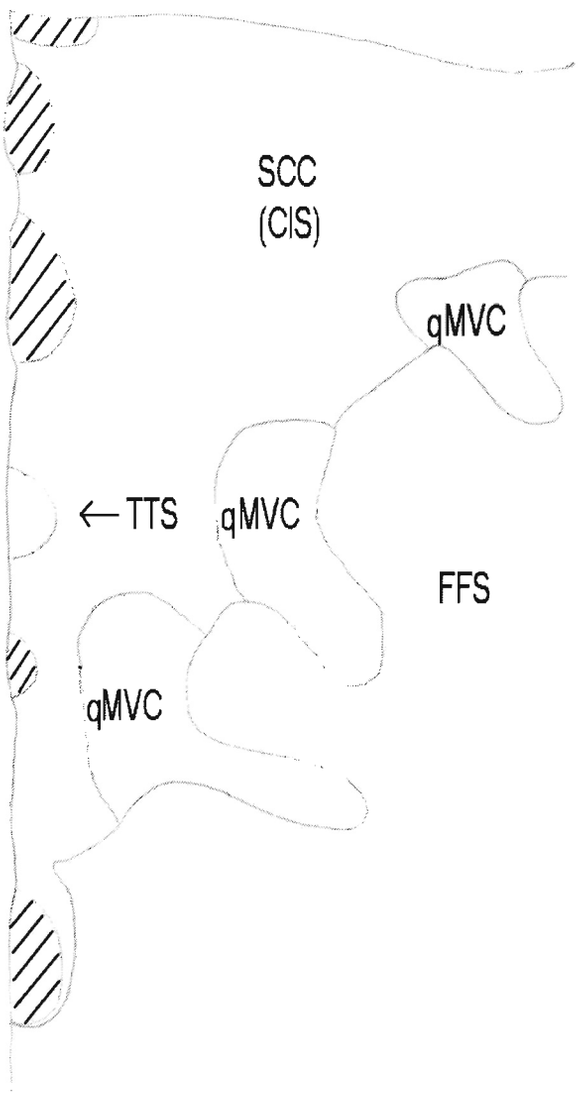

(b) Fracture regions in Figure 6.34(a). Shadowed regions are initiation pits.

FIGURE 6.34: LIST SCC overview

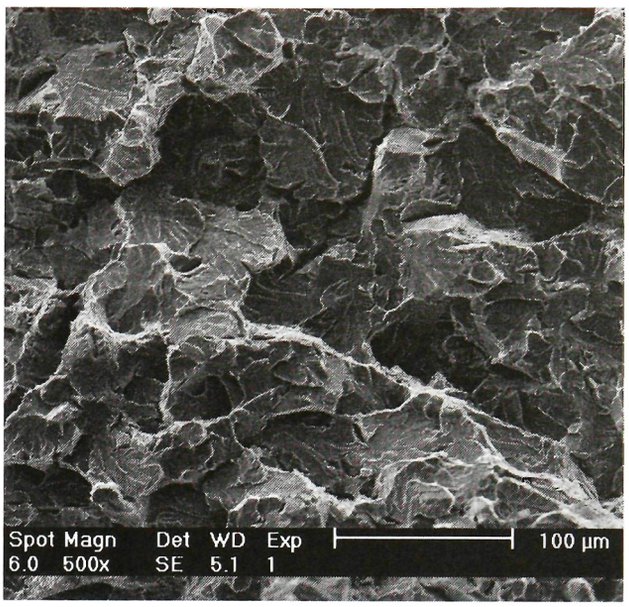

FIGURE 6.35: FFS in LIST sample at x500 magnification.

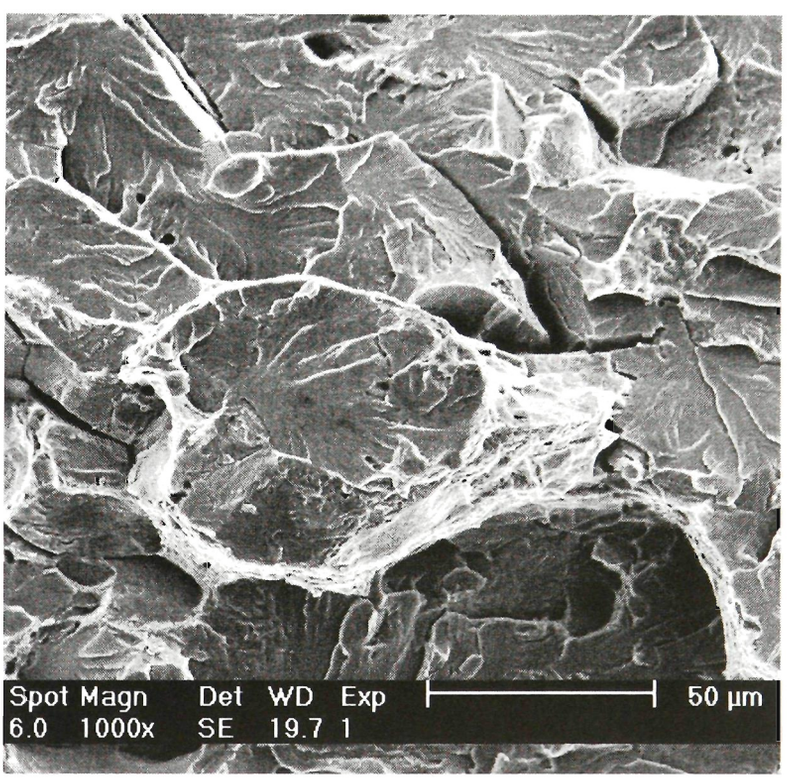

FIGURE 6.36: FFS in LIST sample at x1000 magnification.

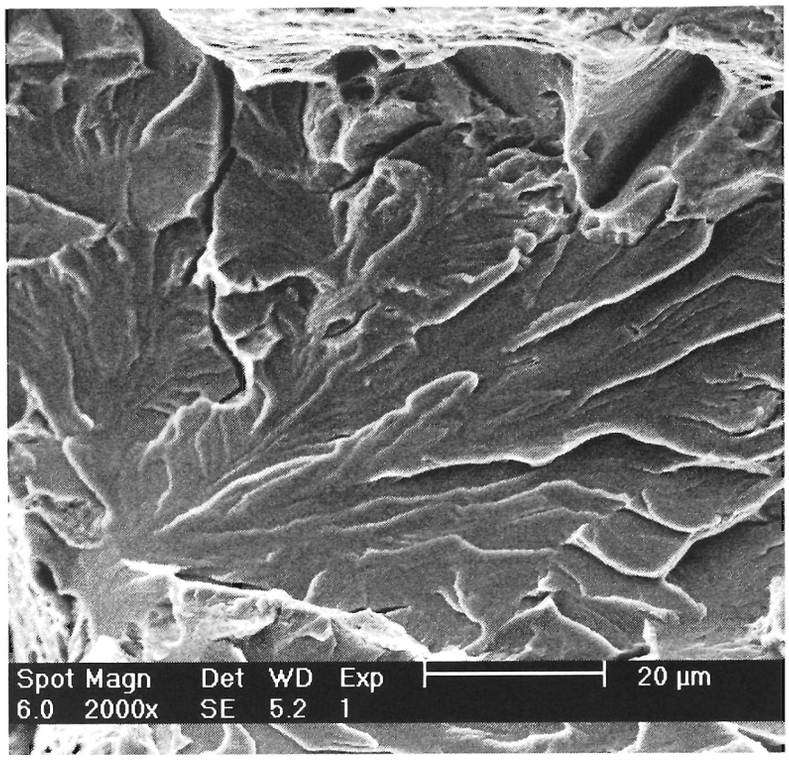

FIGURE 6.37: FFS in LIST sample at x2000 magnification.

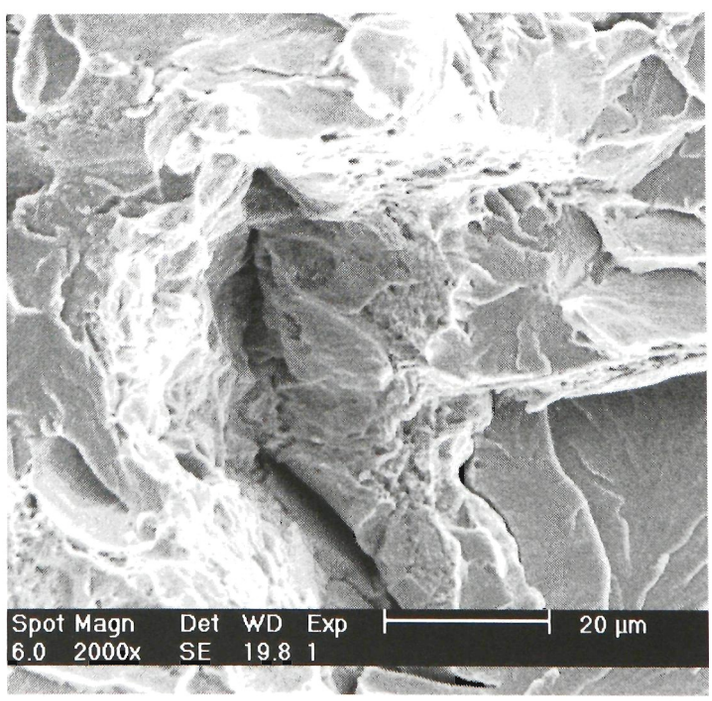

FIGURE 6.38: Chasm surrounded by ductile tearing topography amongst FFS maple leaves.

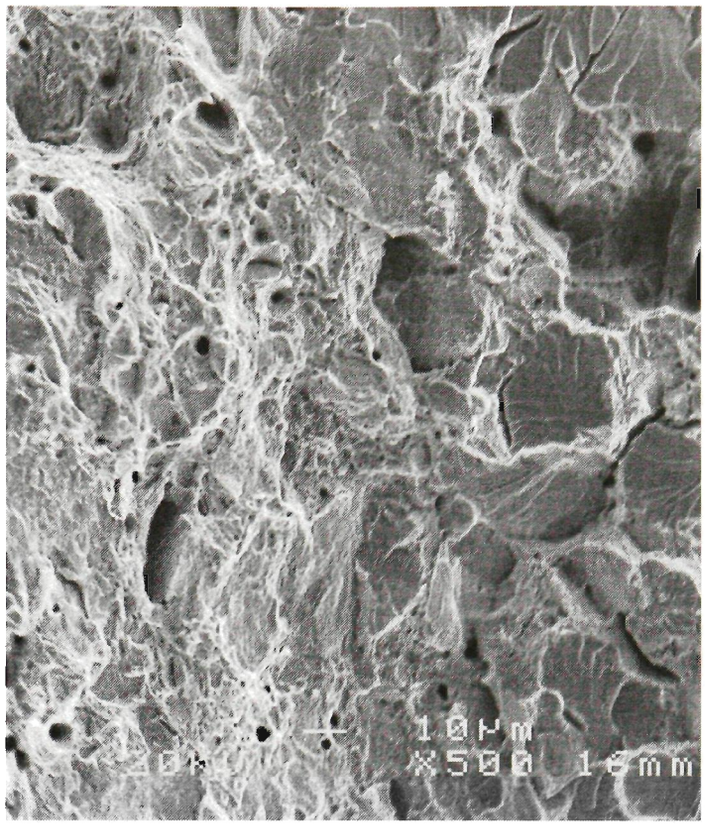

FIGURE 6.39: SCC to FFS transition from sample LIST07.

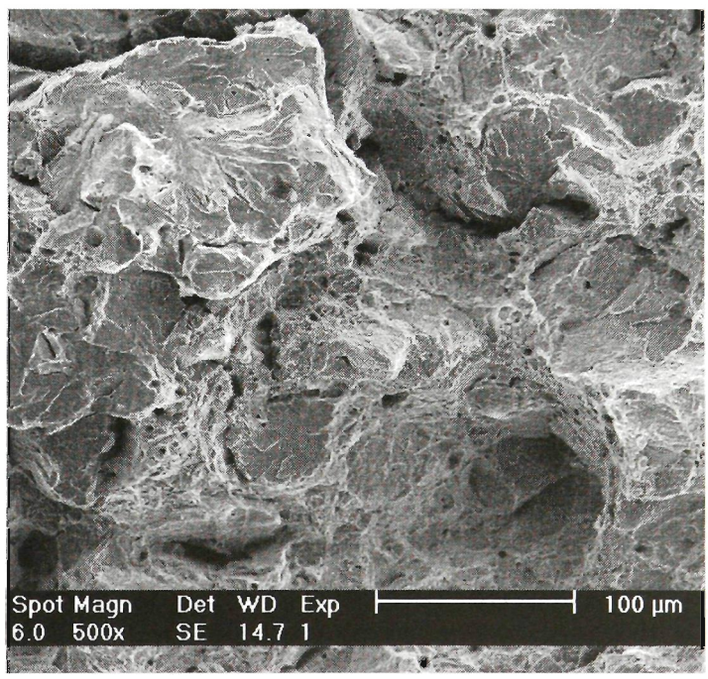

FIGURE 6.40: SCC to FFS transition from sample LIST40.

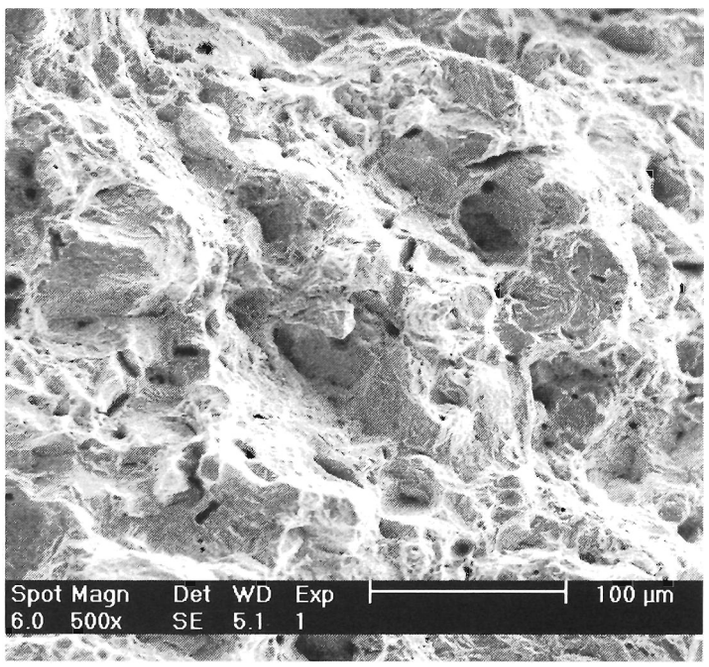

FIGURE 6.41: Typical CIS SCC fracture surface (LIST24). Several slopes with few flat areas.

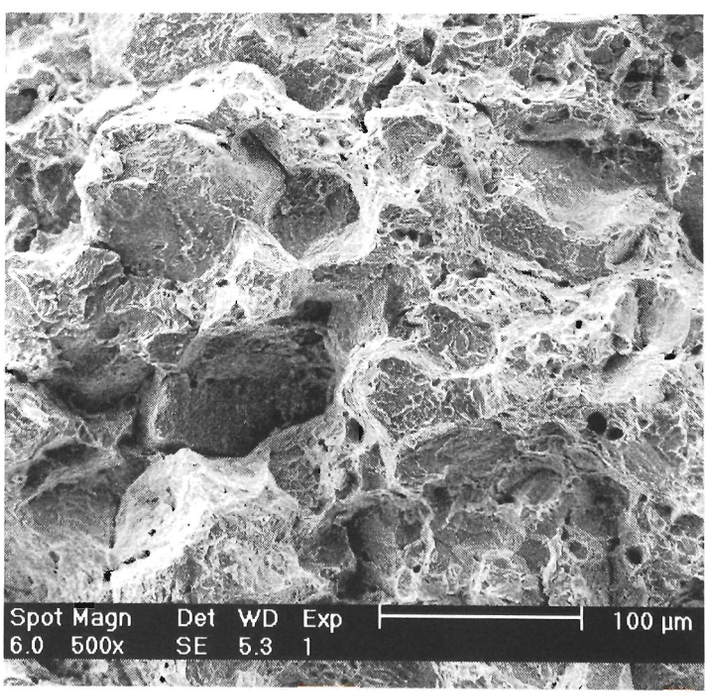

FIGURE 6.42: Typical CIS SCC fracture surface (LIST38).

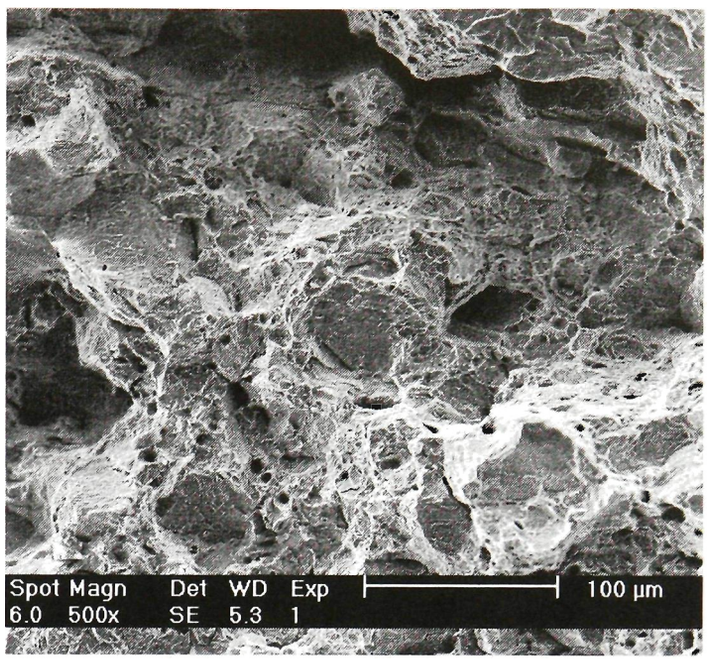

FIGURE 6.43: Typical CIS SCC fracture surface (LIST38).

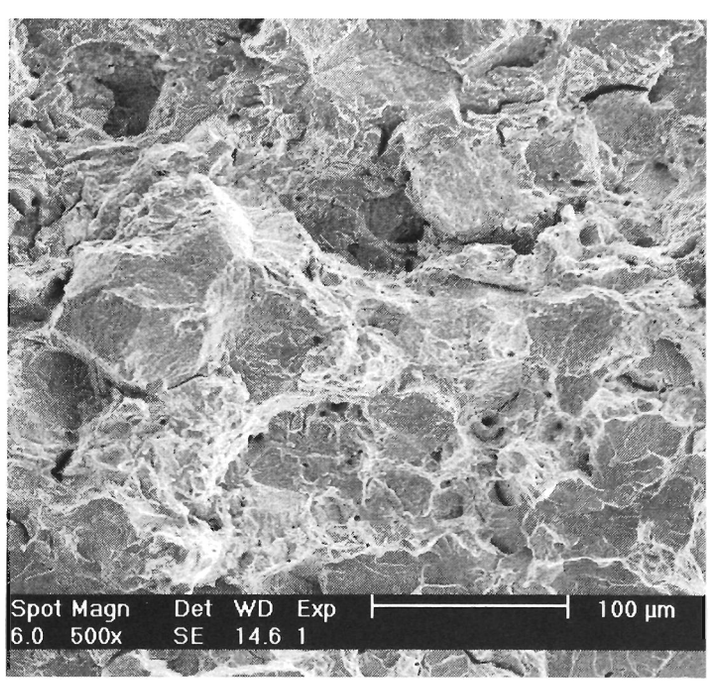

FIGURE 6.44: Typical CIS SCC fracture surface (LIST39).

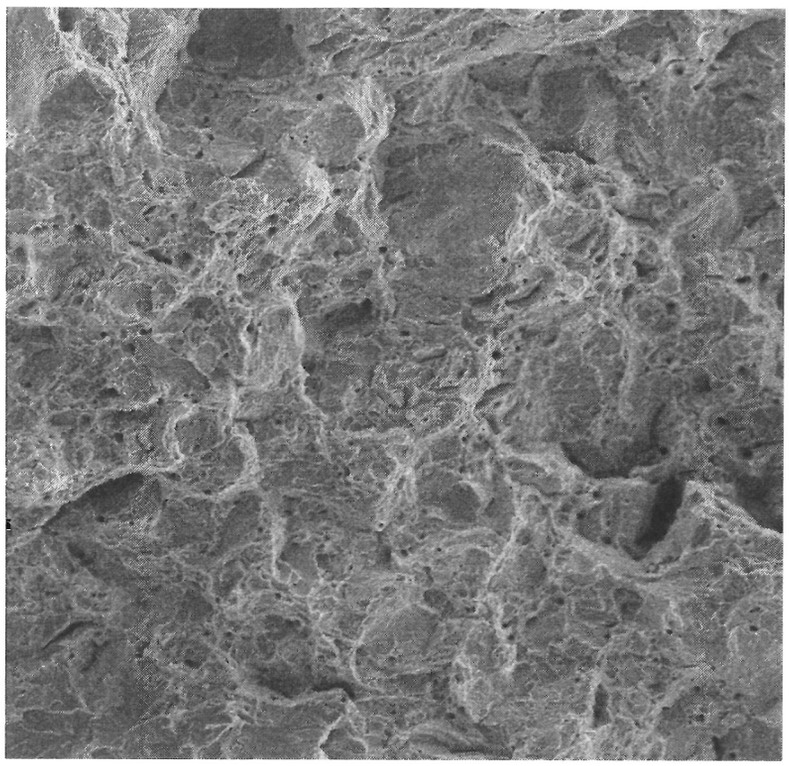

FIGURE 6.45: Typical CIS SCC fracture surface (LIST41).

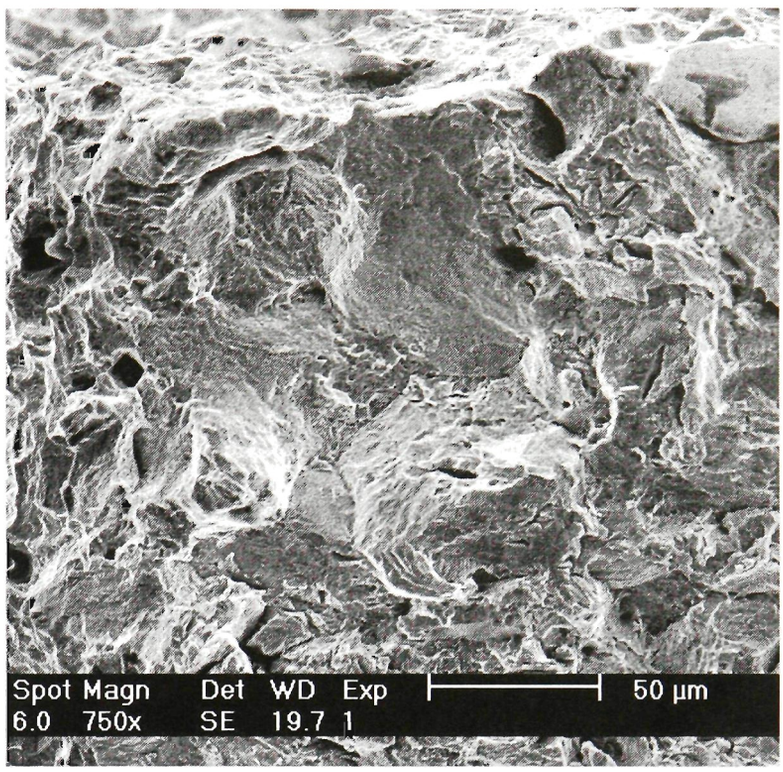

FIGURE 6.46: Typical CIS SCC fracture surface (LIST38).

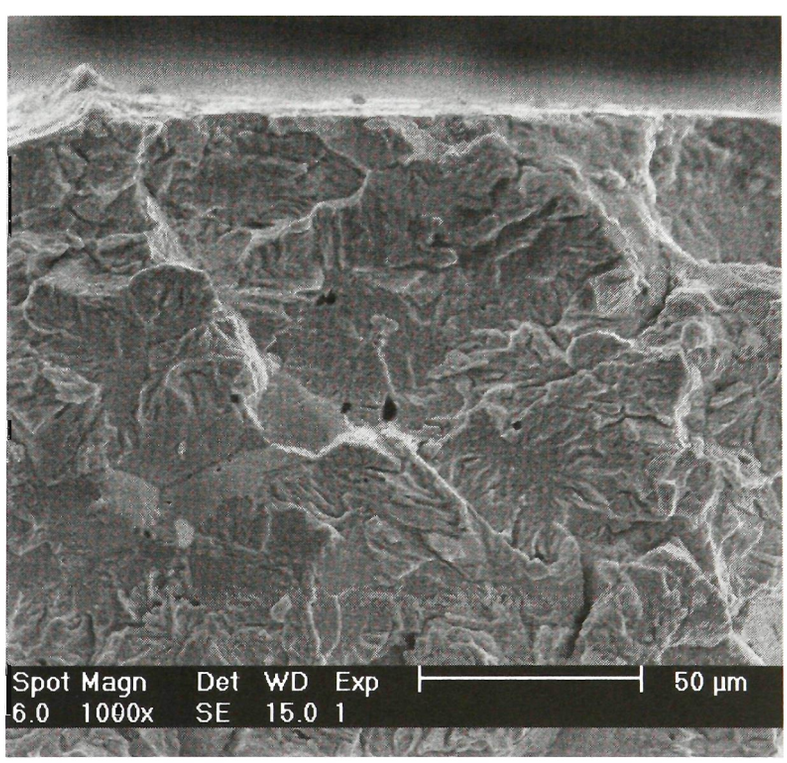

FIGURE 6.47: TTS on a LIST sample.

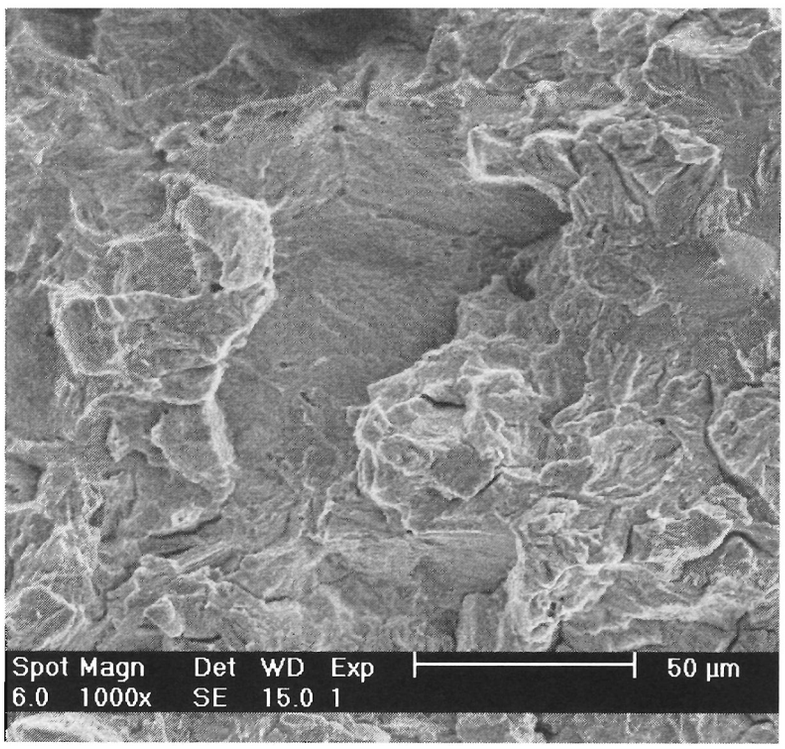

FIGURE 6.48: TTS further away from the free surface.

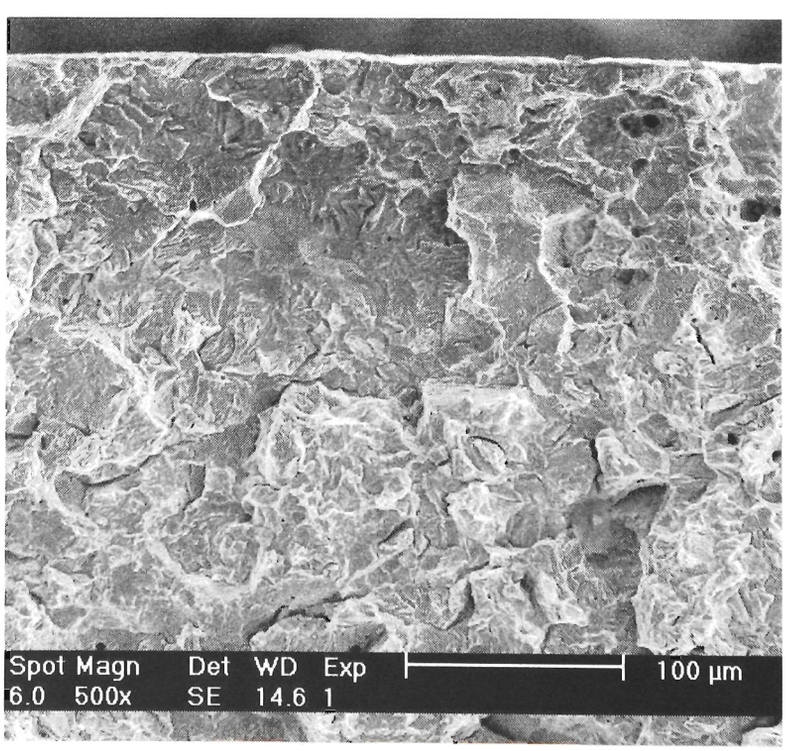

FIGURE 6.49: TTS at a different site within sample LIST39.

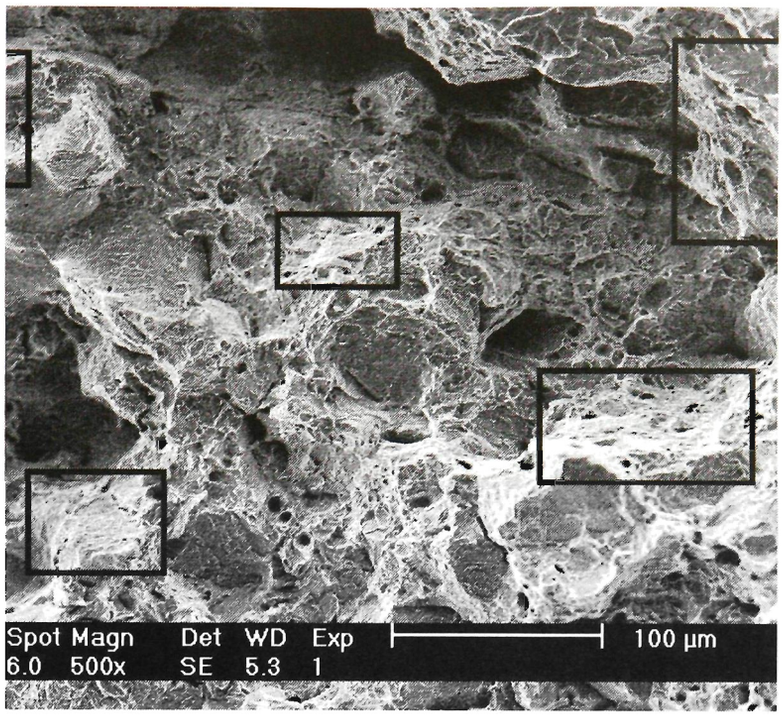

FIGURE 6.50: Corrugated relatively even slope within SCC region.

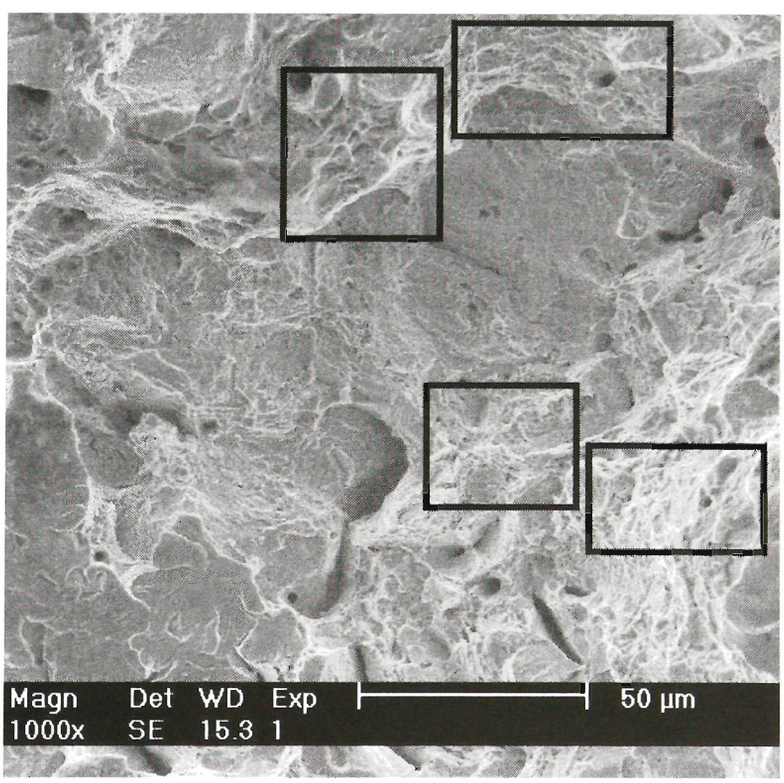

FIGURE 6.51: Dimpled irregular surface within SCC region.

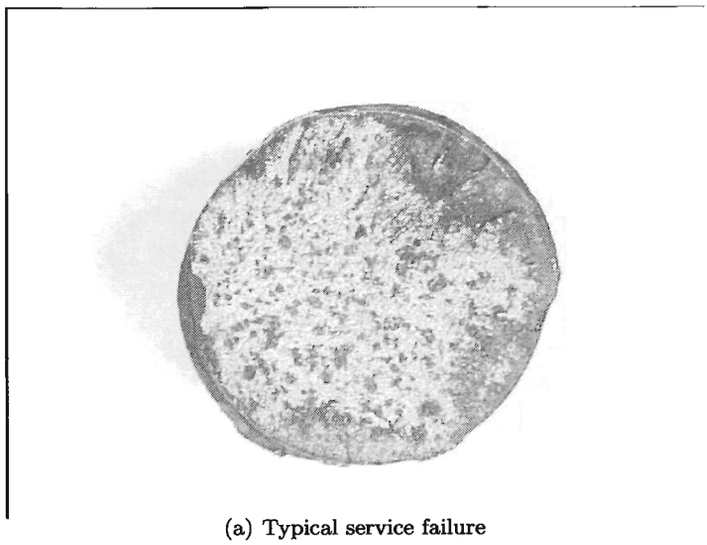

(a) Typical service failure

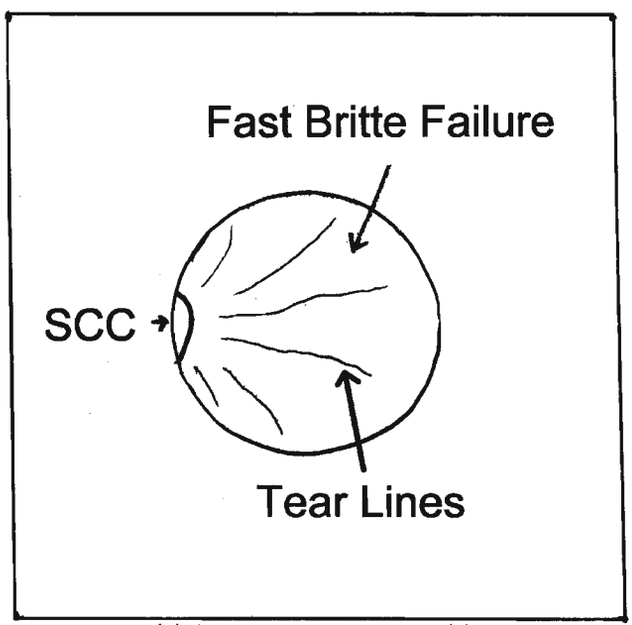

(b) Schematic of Figure 6.52(a)

FIGURE 6.52: SCC overview comparison

(c) LIST sample with SCC

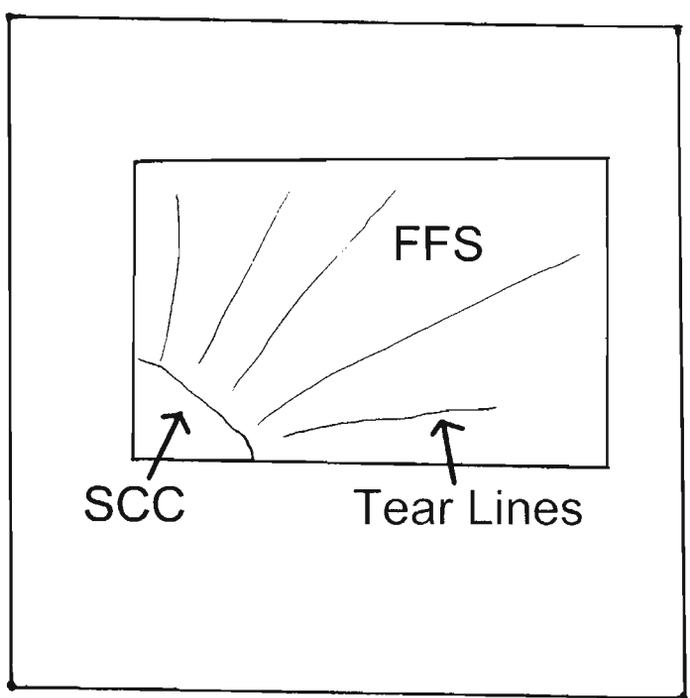

(d) Schematic of Figure 6.52(c)

FIGURE 6.52: SCC overview comparison

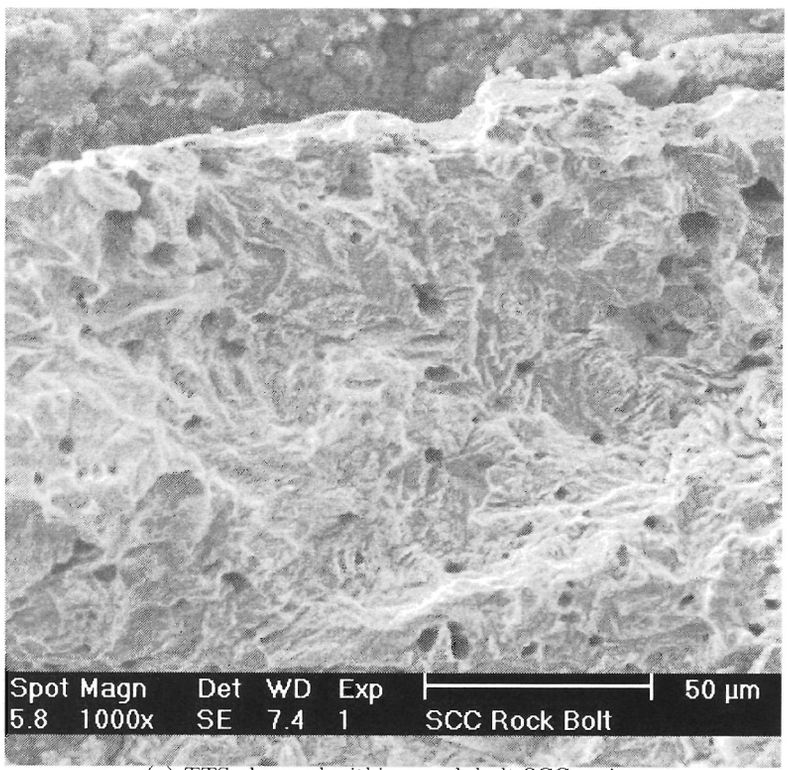

(a) TTS observed within a rock bolt SCC region

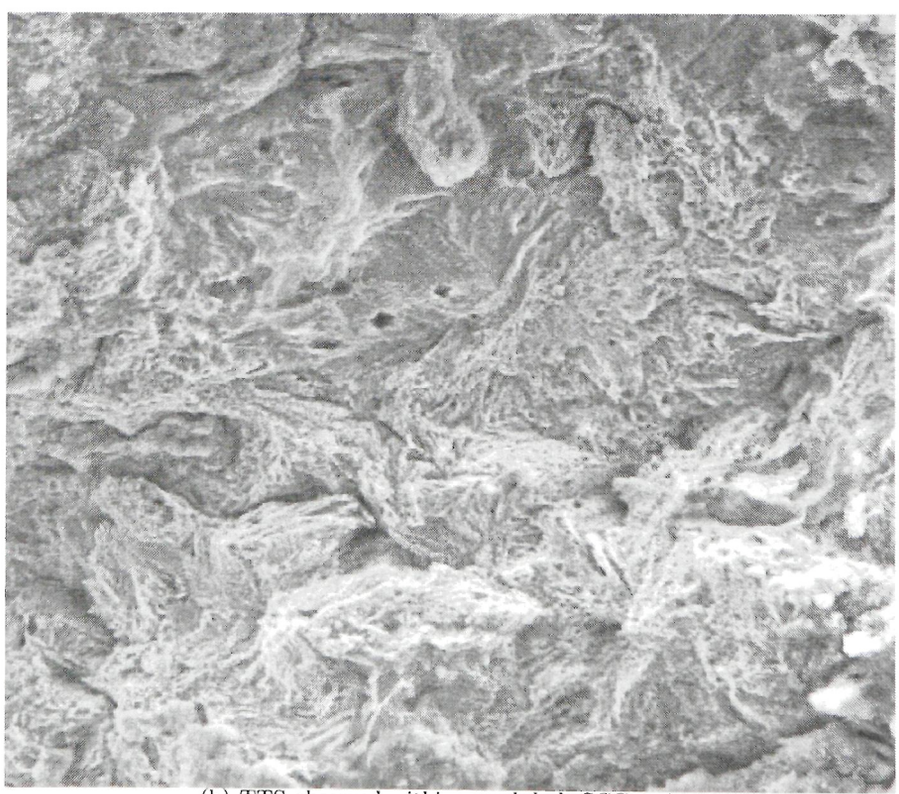

(b) TTS observed within a rock bolt SCC region

FIGURE 6.53: TTS comparison

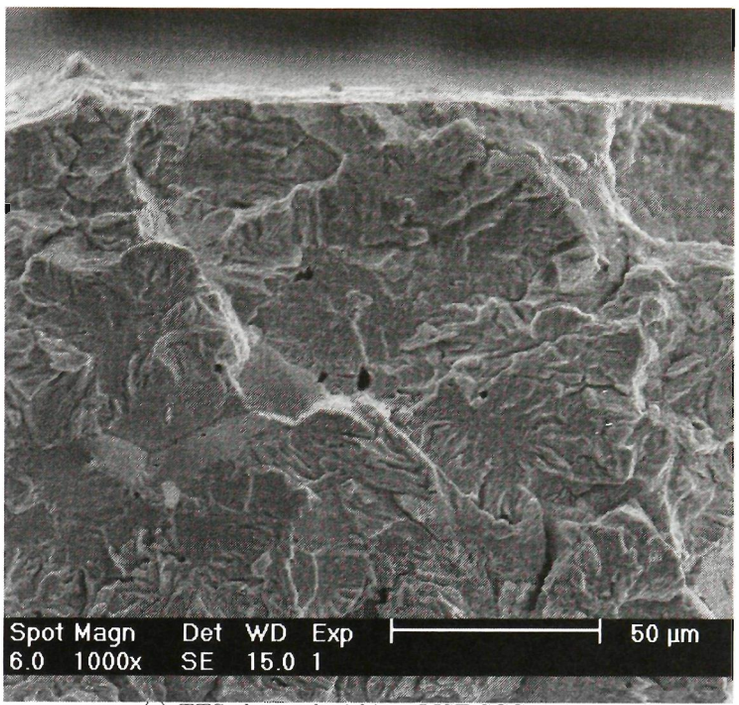

(c) TTS observed within a LIST SCC region

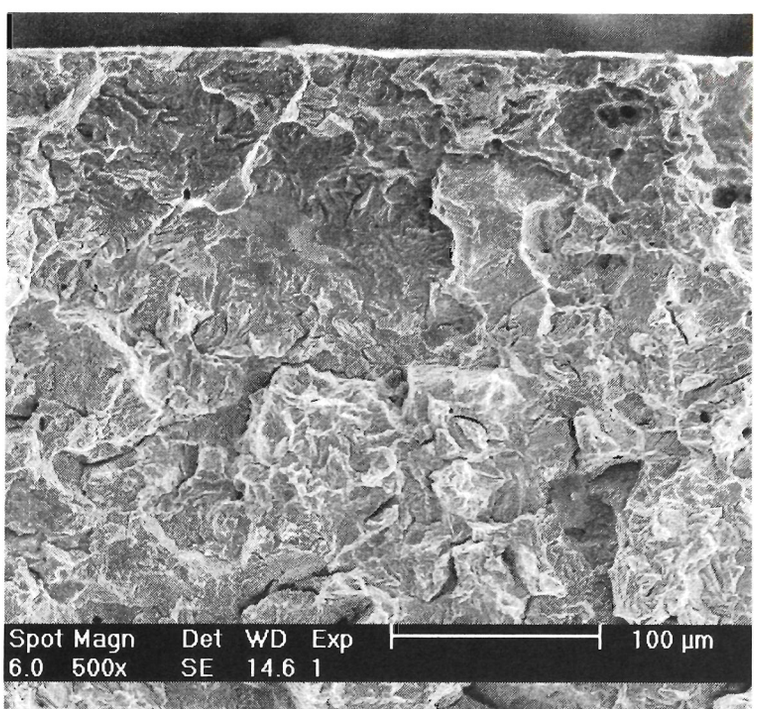

(d) TTS observed within a LIST SCC region

FIGURE 6.53: TTS comparison

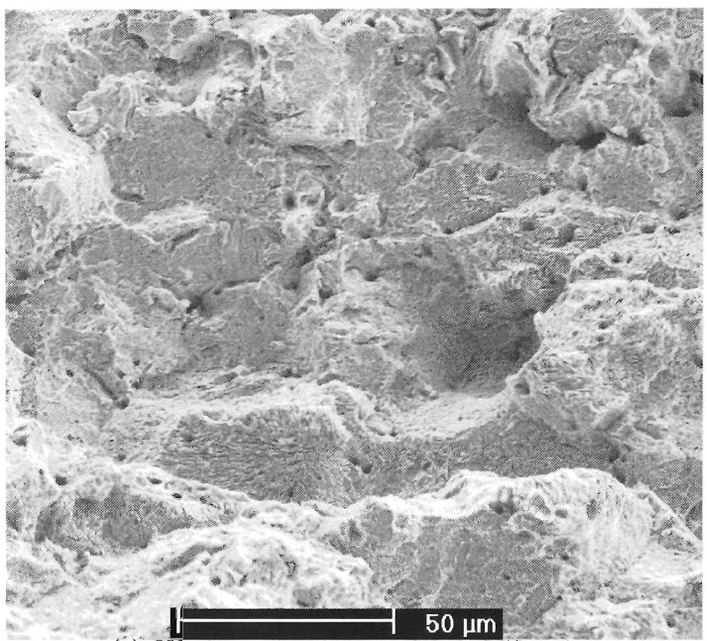

(a) CIS observed within a rock bolt SCC region

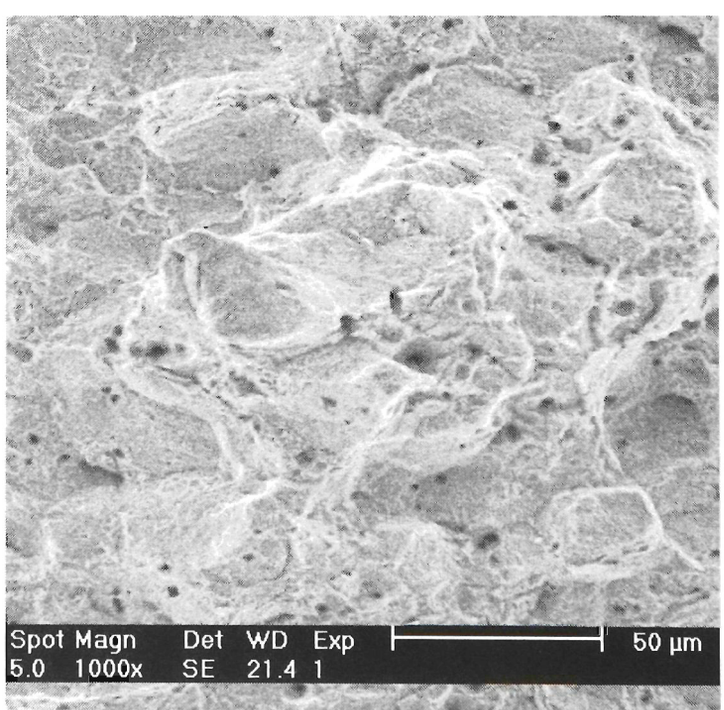

(b) CIS observed within a rock bolt SCC region

FIGURE 6.54: CIS comparison

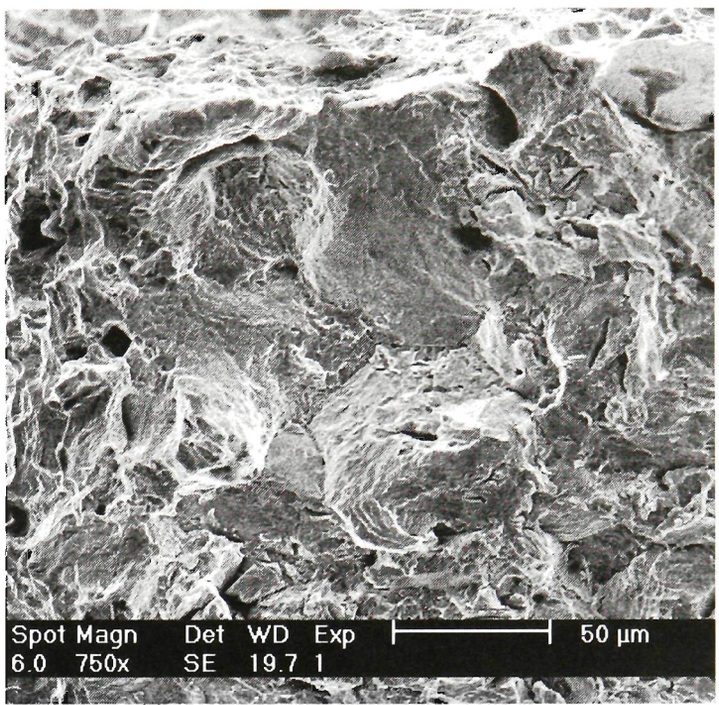

(c) CIS observed within a LIST SCC region

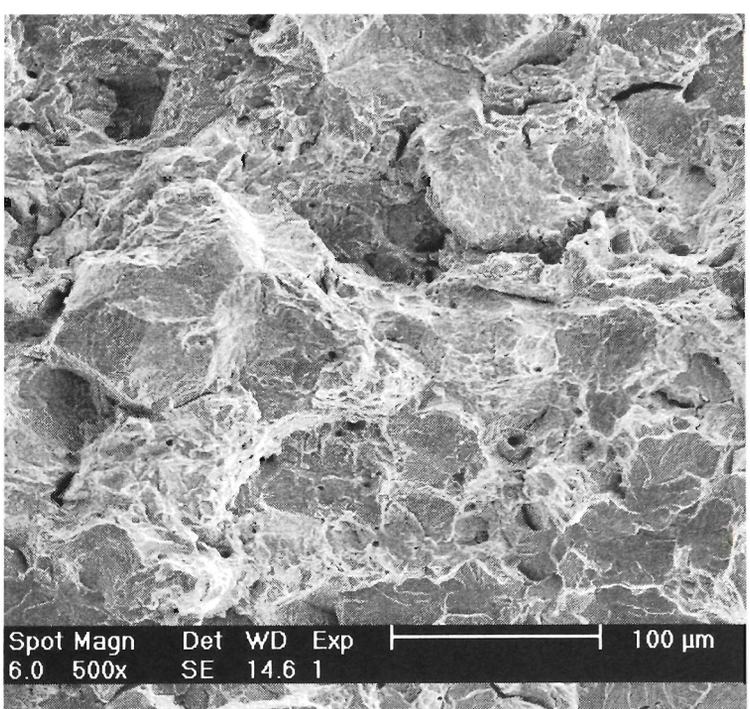

(d) CIS observed within a LIST SCC region

FIGURE 6.54: CIS comparison

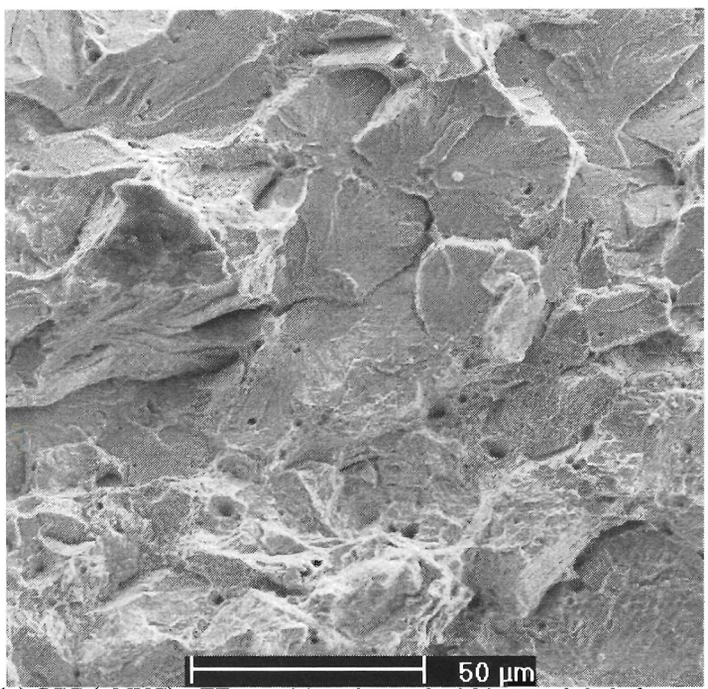

(a) SCC (qMVC) - FF transition observed within a rock bolt fracture surface

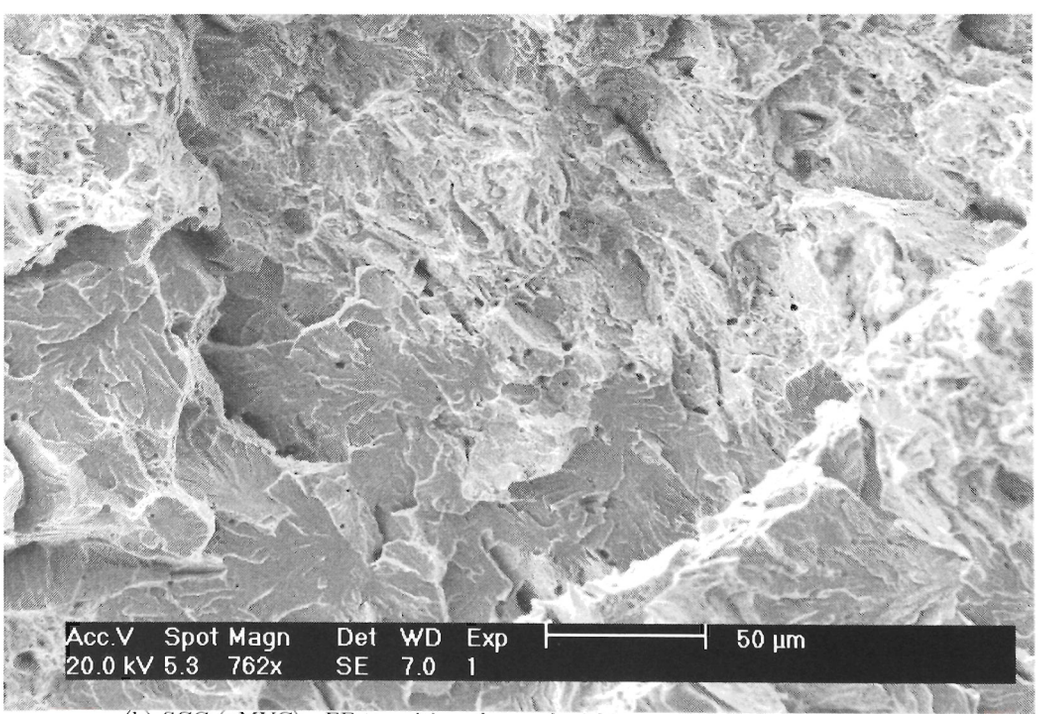

(b) SCC (qMVC) - FF transition observed within a rock bolt fracture surface

FIGURE 6.55: qMVC-FF transition comparison

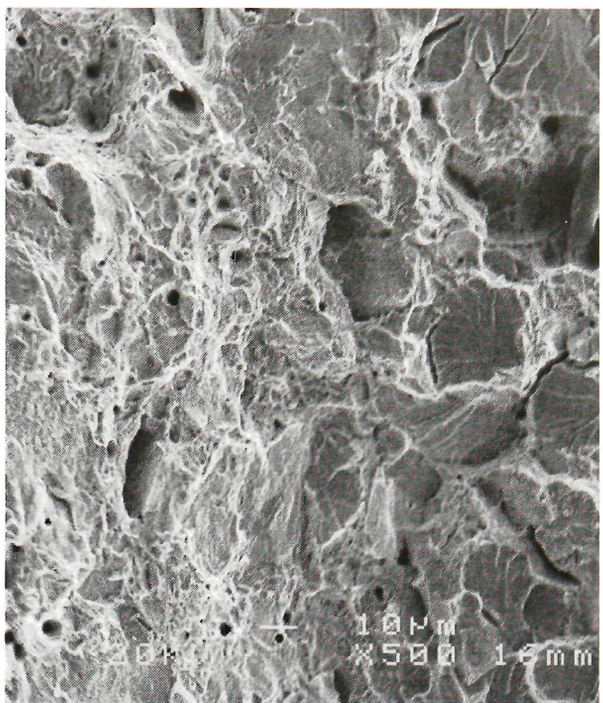

(c) SCC (qMVC) - FF transition observed within a LIST fracture surface

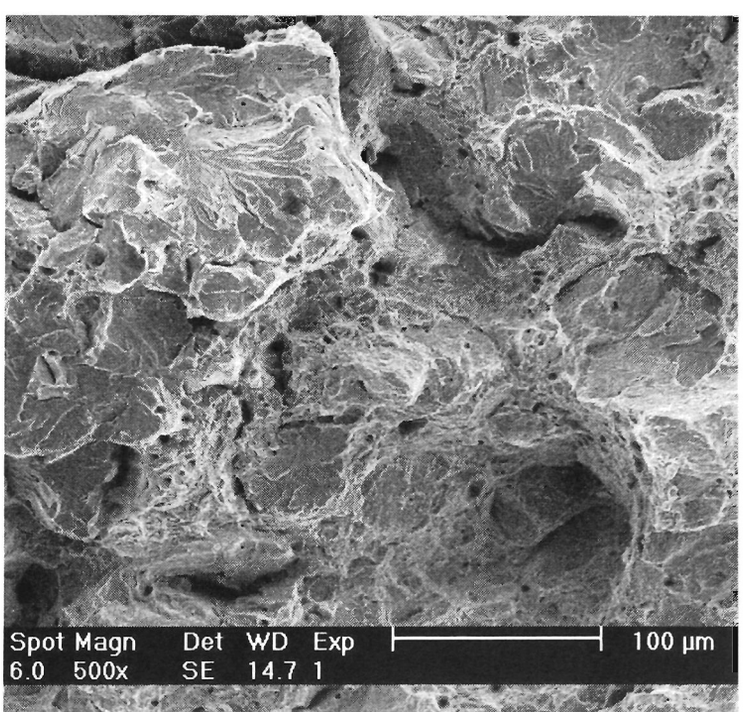

(d) SCC (qMVC) FF transition observed within a LIST fracture surface

FIGURE 6.55: qMVC-FF transition comparison

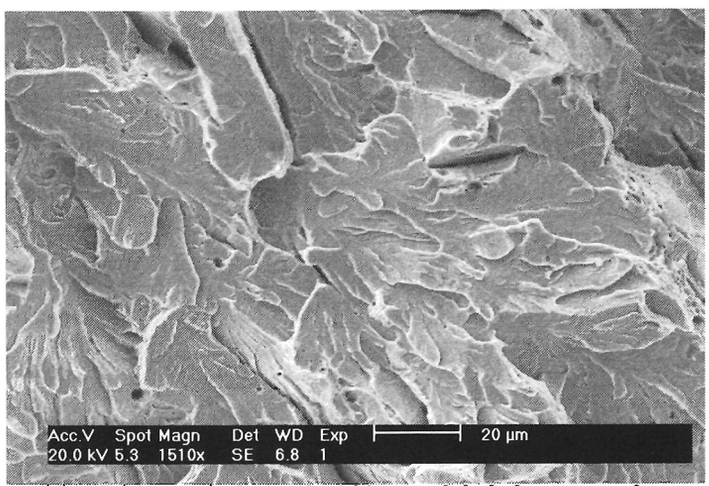

(a) FF (cleavage) observed within a rock bolt fracture surface

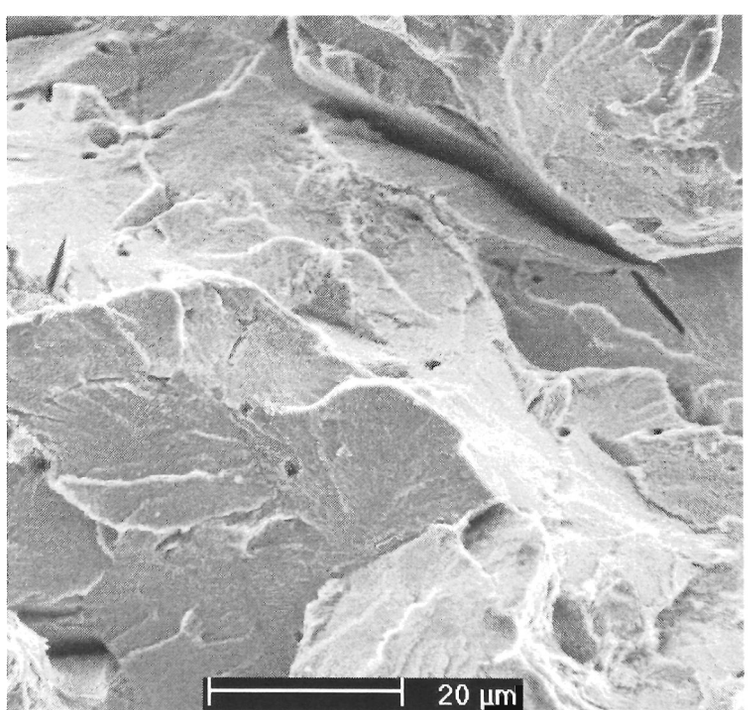

(b) FF (cleavage) observed within a rock bolt fracture surface

FIGURE 6.56: FF comparison

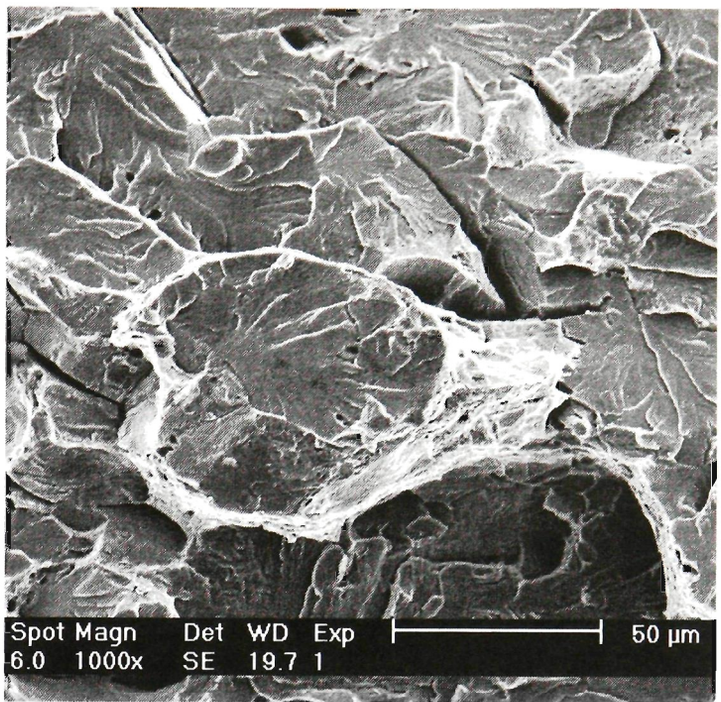

(c) FF (cleavage) observed within a LIST fracture surface

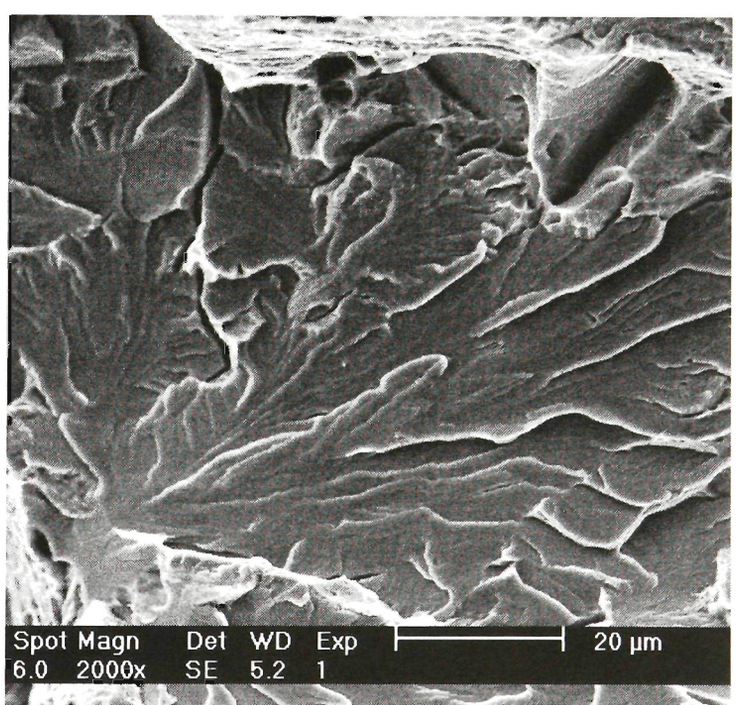

(d) FF (cleavage) observed within a LIST fracture surface

FIGURE 6.56: FF comparison

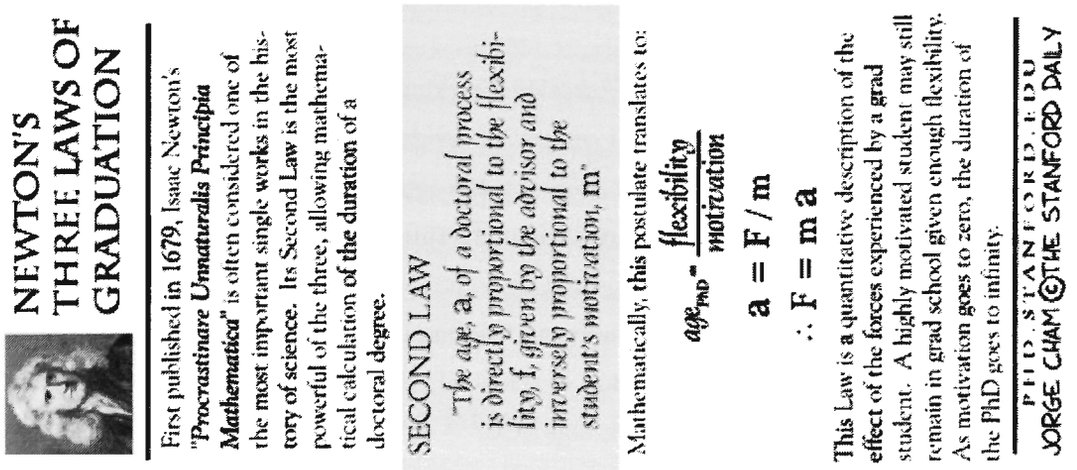

7

ENVIRONMENTAL INFLUENCES

In order to understand rock bolt Stress Corrosion Cracking (SCC), a series of experiments have been performed using the Linearly Increasing Stress Test (LIST). One series of experiments determined the threshold stress of various bolt metallurgies (900 MPa for 1355AXRC, and 800 MPa for MAC and MA840B steels). The high values of threshold stress suggest that SCC begins in rock bolts when they are sheared by moving rock strata. Typical crack velocity values have been measured to be 2.5 x 10^{-8}m s^{-1}, indicating that there is not much benefit for rock bolt steel of higher fracture toughness. Another series of experiments were performed to understand the environmental conditions causing SCC of 1355AXRC and galvanised 1355AXRC rock bolt steel. SCC only occurred for environmental conditions which produce hydrogen on the sample surface, leading to hydrogen embrittlement and SCC. Fracture surfaces of LIST samples failed by SCC were found to display the same fracture regions as fracture surfaces of rock bolts failed in service by SCC: Tearing Topography Surface (TTS), Corrugated Irregular Surface (CIS), quasi Micro Void Coalescence (qMVC) and Fast Fracture Surface (FFS). Water chemistry analysis were carried out on samples collected from various Australian mines in order to compare laboratory electrolyte conditions to those found in underground mines.

7.1 INTRODUCTION

Any failure of a rock bolt is a potential concern. Stress Corrosion Cracking (SCC) failures of rock bolts have been reported at a number of Australian mines. A recent review is provided by Crosky et al [7]. They found that SCC is a substantial issue although it was difficult to assess the total incidence. It has occurred in a number of mines, for rock bolts from various manufacturers, manufactured from a whole range of different steel metallurgies from a range of steel suppliers. It appeared to be associated with clay bands in the rock strata intersecting the rock bolt, shearing in the strata inducing bending in the rock bolts, high tensile steel bolts, some ground water presence and bacterial corrosion of the steel. However, Crosky et al [7], [8] were not able to provide an estimate of the magnitude of rock bolt SCC.

Atrens and Wang [2] provide a review of SCC. SCC may occur whenever a highly-stressed steel is in the presence of an aggressive environment. The stress corrosion cracks initiate and grow slowly. During this phase which may last months or years there may be no indication of any danger. Fast fracture occurs when the stress corrosion crack reaches a critical length, as determined by the applied stress and the fracture toughness of the steel. Reports indicate that the critical crack length can be of the order of only a few millimeters for rock bolts. The fast fracture is sudden and catastrophic.

The fracture surfaces of 1355AXRC rock bolts failed during service by Stress Corrosion Cracking (SCC) have been described in Chapters 5 and 6. The microstructure of these rock bolts was pearlitic. Laboratory research (Chapter 6) on rock bolts with the same fine pearlitic microstructure has shown that service failures can be duplicated in the laboratory using the Linearly Increasing Stress Test (LIST) [10] using specific conditions. These conditions have been defined as the preferred LIST test to be as follows: LIST testing of a tensile sample exposed to a sulphate pH 2.1 solution at a rate of 0.019 MPa s^{-1} [1] The preferred LIST test was shown to provide a good foundation for a test to reproduce service SCC. The resulting fractography of LIST samples were similar to those from service SCC . Rock bolts failed by SCC were subjected to a detailed examination of the fracture surfaces in an attempt to understand the SCC fracture mechanism. The SCC fracture surfaces contained the following different surfaces: Tearing Topography Surface (TTS), Corrugated Irregular Surface (CIS) and Micro Void Coalescence (MVC). TTS was characterised by a ridge pattern independent of the pearlite microstructure, but having a spacing only slightly coarser than the pearlite spacing. CIS was characterised as porous irregular corrugated surfaces joined by rough slopes. MVC found in the studied rock bolts was different to that found in samples failed in a pure ductile manner. The MVC observed in rock bolts was more flat and regular than the pure MVC, being attributed to hydrogen embrittling the ductile material near the crack tip. The interface between the different fracture surfaces revealed no evidence of a third mechanism involved in the transition between fracture mechanisms. The microstructure had no effect on the diffusion of hydrogen nor on the fracture mechanisms.

[1] These conditions caused some metallurgies to fail by SCC. Other metallurgies displayed SCC in these conditions, but with an applied overpotential.

The following SCC mechanism is consistent with the fracture surfaces. Hydrogen diffuses into the material, reaching a critical concentration level. The thus embrittled material allows a crack to propagate through the brittle region. The crack is arrested once it propagates outside the brittle region. Once the new crack is formed, corrosion reactions start producing hydrogen that diffuses into the material once again. The prior work was all carried out on 1355AXRC grade bolt steel.

Chapter 6 proved that the preferred LIST test was a valid and reliable method of simulating field SCC in the laboratory. The present Chapter was aimed to use the LIST test to study the SCC of rock bolts. This Chapter explores:

- Environments causing rock bolt SCC
- Measures SCC threshold stresses for steels currently used in the manufacture of rock bolts
- Explores galvanising as a possible countermeasure and
- Studies crack velocities and their implications on rock bolt SCC.

7.2 ENVIRONMENTS CAUSING SCC

7.2.1 Laboratory Electrolyte

Table 7.1 summarises the results of the SCC tests in the various experiments. "S" indicates sulphate solutions and "C" indicates chloride solutions. In the first tests only one environmental factor was changed (either the pH, the concentration or the corrosion potential), whereas in subsequent tests two factors were modified in order to study interactions, for example the pH and the corrosion potential. This data indicates that SCC was controlled by a combination of the applied potential and the pH. Furthermore, this data indicates that the solution concentration was not an important issue. When the sulphate solution pH was modified to 1.4 and 12.5, the values of E_{corr} changed to -260 and -120 mV vs SHE respectively. Between the pH values of 2.1 and 10.0, the potential remained at -350 mV vs SHE. The free corrosion potential of the chloride solution has not been measured for various pH values, but has been assumed to be of similar value to those of the Sulphur solution.

The results have been displayed on a Pourbaix diagram in Figure 7.1. Sulphate solutions are represented by circles and chloride solutions are represented by squares. A full symbol indicates failure by SCC, whereas an empty circle or square means no SCC was detected. Symbols with a dash represent experiments performed with an applied potential.

SCC occurred in the laboratory for a restricted range of conditions for acid conditions or with negative applied potentials. The restricted conditions were such that copious amounts of hydrogen were produced on the surface of the steel. This suggests that there is a Hydrogen Embrittlement mechanism for the SCC.

Table 7.1: **Environments Giving SCC**

Sample	Environment	Potential mV vs SHE	SCC
LIST 24	S pH 2.1	-350	Yes
LIST 41	S pH 2.1 and CO_2		Yes
LIST 38	S pH 2.1 and coal, aerated		Yes
LIST 44	S pH 2.0, x10 conc	-	Yes
LIST 43	S pH 2.0, x100 conc	-	Yes
LIST 42	S pH 2.0, x1000 conc		Yes
LIST 28	S pH 4.2	-350	No
LIST 29	S pH 6.3	-350	No
LIST 34	S pH 9.4	-350	No
LIST 47	S pH 2.1 E_{corr}	-350	Yes
LIST 48	S pH 2.1 E_{corr}+100 mV	-250	No
LIST 50	S pH 2.1 E_{corr}+150 mV	-200	No
LIST 49	S pH 2.1 E_{corr}-100 mV	-450	Yes
LIST 51	S pH 2.1 E_{corr}-300 mV	-650	Yes
LIST 52	S pH 6.2 E_{corr}	-350	No
LIST 53	S pH 7.27 E_{corr}-300 mV	-650	No
LIST 54	S pH 7.46 E_{corr}-570 mV	-920	Yes
LIST 45	S pH 6.16, x100 conc, E_{corr}	-420	No
LIST 64	S pH 6.6, x100 conc, E_{corr}-300 mV	-720	No
LIST 66	S pH 6.6, x100 conc, E_{corr}-500 mV	-1120	Yes
LIST 68	S pH 9.7, E_{corr}-900 mV	-1350	Yes
LIST 85	S pH 1.2, E_{corr}-150 mV	-350	Yes
LIST 87	S pH 1.2, E_{corr}+100 mV	-150	Yes
LIST 88	S pH 11.8, $E_{corr}-1000$ mV	-1300	Yes
LIST 89	S pH 11.8, $E_{corr}-650$ mV	-950	Yes
LIST 26	C pH 1.8	-350	Yes
LIST 39	C pH 1.8 and CO_2	-	Yes
LIST 40	C pH 1.8 and coal, aerated		Yes
LIST 46	C pH 1.8, x100 conc	-	Yes
LIST 31	C pH 3.1	-350	No
LIST 37	C pH 7.7	-350	No
LIST 36	C pH 10.7	-350	No

The data points on Figure 7.1 indicate that it is possible to draw a straight line that separates the conditions at which SCC occurs from those that do not for 1355AXRC. This SCC line can be drawn parallel to the hydrogen evolution line, and with an overpotential of approximately -350 mV:

$$E(V) = -0.320V - 0.063 * pH \tag{7.1}$$

This relationship is valid down to a pH of pH $\cong$ 2.0. At lower pH values, SCC occurs for lower values of hydrogen overpotential. This is attributed to the ease of hydrogen evolution. At low pH levels there is an abundance of hydrogen evolution, it is possible that this quantity of hydrogen is enough to cause SCC. At higher pH levels, where hydrogen was not as abundant, an increased overpotential was required to cause SCC.

Conditions below the line caused SCC whereas there was no SCC above the line.

7.2.2 Mine Water Chemistry

Important characterisation of the mine water includes the concentration of ions like chloride (Cl^-), sulfate (SO_4), carbonate (CO_3), bicarbonate (HCO_3), Na^+, Ca^{2+}, Mg^{2+}, the pH, the concentration of the dissolved gasses CO_2 and H_2S, total dissolved solids (TDS) and alkalinity. However there is very little actual data from mines with no actual data from situations related to SCC.

Mine water sampling is not a trivial issue, and a "hole in roof water sampling" procedure was suggested. Water samples of most interest relate to water percolating through the roof rocks. These samples might change once out of the roof, so it is advisable to adhere to a strict sampling protocol and to note the actual sampling procedure adopted in each case. One possibility for sampling is to drill a hole in the roof and seal with a suitable stopper containing a "tap". This allows water to collect in the hole, and for the water to be periodically sampled. It also allows evaluation of time changes of water chemistry.

The mine water composition depends on the mine geology and hydrology. Factors which vary with mine "geology and hydrology" are

a. rock species and strata through which water flows,

b. amount of water flow and time the water has been flowing,

c. intersection of aquifers and their composition,

d. rain fall and

e. sulfate reducing bacteria.

The way by which these factors vary are as follows:

a. *Rock species and strata through which water flows.* Water flowing through rock strata picks up soluble species. Chlorides may be associated with old marine sedimentary rocks. Chlorides tend to be soluble

and are easily dissolved, giving neutral solutions. Carbonates are dissolved from limestone and similar rocks, giving "hard" water with pH values in range 8-9. Sulfates seem to be associated with pyrites, particularly through the oxidation of pyrites which is associated with low pH values in range 4-5 but can be as low as pH 2. Dissolved CO_2 gives a mildly acidic solution, pH 6.

b. *Amount of water flow and time water has been flowing.* Chlorides would be expected to be washed completely out of the water path with time, so that with a constant water path, the chloride concentration would be expected to decrease with time. If the water is flowing over limestone or similar, the amount of carbonate pick up would depend on time water is in contact with the limestone. Since carbonate has a low solubility, it is unlikely that all limestone would be dissolved, so the carbonate concentration in the water would not be expected to change with time.

c. *Intersection of aquifers and their composition.* An important consideration is the intersection of mine workings or the water flow to them with aquifers. Aquifers may have pH values up to pH 10.

d. *Rain fall.* The predominance of alkaline mine waters in Australia (in contrast to acid mine waters in Canada and the USA) has been attributed [59] to (1) the lower rainfall in Australia, (2) the intersection of mine workings with alkaline aquifers and (3) the low level of pyrites.

e. *Sulfate reducing bacteria.* Sulfate reducing bacteria are apparently endemic, being present from when the coal was formed [59]. For active metabolism, the bacteria need all of following: (1) an aqueous environment, (2) no oxygen, (3) food, eg methane or H_2, (4) pH not too acid, and (5) sulphate. They ingest the sulfate, expel H_2S and produce acid conditions. These bacteria are associated with acid conditions, pH values down to 2 and high sulphate concentrations. When a new section is opened up, air and oxygen stops bacteria activity. Occlude air and the activity restarts, eg maybe in a crevice next to the rock bolt or in the coal dump.

Changes of mine water chemistry with time can be caused by a number of mechanisms. Active bacteria are associated with decreasing pH down to 2, and higher sulfate levels, SO_4. High CO_2 concentrations (with no dissolved "carbonate/bicarbonate") are expected to be associated with mildly acidic conditions, pH values may be as low as 4-5. The pH increases to more neutral values as the CO_2 comes out of solution. Carbonate solutions, pH 8-9, are expected to be associated with high CO_2 concentrations, (higher CO_2 concentrations than in equilibrium at atmospheric pressure). As the CO_2 comes out of solution, some carbonate may precipitate (the solubility limit being exceeded) and the pH may decrease. Local drying conditions can concentrate the solution at the rock bolt to saturation.

In order to compare the laboratory electrolyte solutions to service conditions, samples were taken from various Australian underground mines by the author in 2002. Table 7.2 shows the composition of the various mine water samples.

Table 7.2: **Mine Water Analysis Results**

Sample	pH	EC mS	Ca mg/L	K mg/L	Mg mg/L	Na mg/L	S mg/L	Cu mg/L	TDS mg/L	Cl mg/L	NO_3 mg/L	Alkalinity mg/L $CaCO_3$
EC1	7.61	50.5	835	99	1188	14839	2090	0.015	47221	23600	2.12	312
EC2	7.23	48.8	809	98	1092	13382	1925	0.014	42161	22600	0.05	347
EC3	8.13	1.88	155	13	109	117	157	0.017	1508	1082	1.24	396
EC4	8.32	1.42	91	17	108	96	132	0.018	1183	636	7.95	334
EC5	6.84	15.3	488	164	4100	831	5854	0.024	30436	83	1.45	211
EC6	7.12	15.4	489	165	4100	831	5760	0.029	31215	57	7.3	209
EC7	7.74	16.4	489	189	4420	938	6148	0.004	30480	84	3.09	176
EC8	7.89	4.39	113	9	165	750	179	0.018	3006	1736	0.99	968
EC9	7.69	4.05	423	9	56	546	464	0.035	3322	1434	0.14	182
EC10	7.11	18.41	376	194	617	2809	975	0.01	7	5374	0.025	447
EC11	7.59	4.62	163	36.8	25.6	617	164	0.074	355	1227	10.7	64
S 2.1	2.1	-	nil	nil	nil	388	540	nil	-	1400	-	100
C 1.8	1.8	-	nil	nil	nil	1942	540	nil	-	1400	-	50

All of these samples were taken from metalliferous mines, except for sample EC8 which was taken from a colliery.

By examining the composition of water samples from underground Australian mines it can be seen that the composition of sample EC8 was not that different to that of the others samples. A comparison of the field samples and the preferred sulphate pH 2.1 and the chloride pH 1.8 solutions indicated that the chemical composition of the laboratory solutions had similarities to those in the field, particularly to samples EC4, EC8 and EC9. Some of the field samples had much higher concentration of sodium, sulphate and chlorides than the laboratory preferred solutions. EC1 and EC2 had more than 4 times the concentration of Na, S and Cl than the laboratory preferred solutions. Even though the field samples had higher element concentrations, none of the mines sampled have reported problems of rock bolt SCC. This was consistent with the observation from the present research that indicated composition was not an important factor. Laboratory testing indicated that no SCC occurred at the free corrosion potentials for neutral pH values. The main difference between the field samples and the laboratory preferred solutions was that the laboratory solutions had a much lower pH (1.8 and 2.1) compared to those from the field (6.84 to 8.32). If the pH value of the water in the coal mine (EC8), as well as in the other metalliferous mines (EC1, EC2, EC5, EC6, EC7) were to drop significantly, it was estimated that they would start suffering SCC failures.

The difference of pH values is attributed to microorganisms changing the pH of the electrolyte to such values. It is suggested that if such microorganisms were introduced in those regions that the samples were taken from, the local pH conditions could also drop into a SCC propense region. This is consistent with reports from the USA reporting rock bolt failures due to the presence of H_2S in the mine atmosphere.

7.3 THRESHOLD STRESS FOR VARIOUS METALLURGIES

Table 7.3 summarises the results of the testing program to determine the SCC thresholds. Some samples did not fail by SCC but failed by pits decreasing the cross section sufficiently to cause ductile overload. Samples that failed this way have been classified as failing by pitting. A "P" indicates pitting causing ductile failure after the specified period of load application. "NP" indicates no pitting. A "P*" indicates a sample failed by pitting but some stress corrosion cracks were found in the pits. For all tests of the 1355AXRC samples, the samples did not fail during the 3 day exposure period to the specified stress. The 5152CW10D material showed ductile failure for a LIST test completed to fracture in the preferred sulphate pH 2.1 solution.

Table 7.3: **Tests to Determine the SCC Threshold Stress in Sulphate pH 2.1**

Metallurgy	Stress not causing SCC	Stress causing SCC	Threshold Stress
1355AXRC	770(NP), 861(NP), 885(NP)	922	900
MAC	700(P after 1.3h), 800(P* after 50h)	830	815
MA840B	700(P after 27h), 800(P after 30h)	850	850
5152CW10D	-	-	>960

1355AXRC samples did not show any evidence of stress corrosion cracks at 770, 861 or 885 MPa. The sample held at 922 MPa fractured by SCC causing brittle overload, after 8 hours at 922 MPa. The SCC fracture surface had the same features as those on the surfaces of preferred LIST tests, as shown by Figure 7.2. Furthermore surface corrosion damage of these 1355AXRC samples was limited. There were wide shallow pits throughout the surface but there was no evidence of secondary stress corrosion cracks opened up elsewhere in the sample. The stress corrosion crack causing the final failure usually grew from one of these wide shallow pits.

The MAC sample held at 830 MPa failed after 50 hours. The sample surface displayed extensive surface corrosion and many secondary stress corrosion cracks. Figure 7.3 shows an overview of this sample that failed by SCC after 50 hours. The diagram shows the different fracture surfaces; the shaded regions shown represent the subcritical stress corrosion cracks, whereas the fracture mechanism for the bulk of the surface was ductile tearing. The SCC regions consisted of CIS close to the surface, with qMVC separating the ductile tearing region from the SCC region. The subcritical cracks penetrated perpendicularly into the sample. As the side view shows, these cracks were at varying heights along the sample. The ductile tearing surface was at an incline, connecting the various subcritical crack regions.

The MA840B sample held at 850 MPa failed after 71 hours. The fracture surface displayed both ductile fracture (shown by the lip formed by plastic flow) and also displayed SCC. Surface damage was extensive, with many pits and secondary cracks present. Figure 7.4 shows the overview of this sample failed after 71 hours. Similarly to the MAC samples, the fracture surface was made up of perpendicular subcritical stress

corrosion cracks joined up by a sloped ductile tearing region joining the subcritical regions.

5152CW10D bolts did not show SCC in the laboratory LIST test at the free corrosion potential in the sulphate pH 2.1 solution (Figure 7.5). Service failures have shown that 5152CW10D can fail due to SCC. This implies that the conditions for 5152CW10D to fail due to SCC are more severe than those for 1355AXRC.

10M30 samples did not show SCC in the laboratory LIST test at the free corrosion potential in the sulphate pH 2.1 solution. Feedback from industry indicated that it was perceived that this metallurgy did not suffer from SCC at all. Subsequent work showed that this perception was incorrect and this work is presented in Section 7.5.

The overload region in MAC, MA840B and 5152CW10D steels have been ductile. The overload region of the 1355AXRC samples has been brittle. This difference is believed to be due to the ductile to brittle transition temperature being different between the various steels. From the results, the transition temperature is lower for the 1355AXRC samples as their overload is brittle, whereas other steels have a ductile overload at the same temperature.

7.3.1 External Tensile Stresses

Failure analysis have indicated that rock bolts have failed whilst subjected to a nominal tensile stress of about 200 MPa due to the tension on the bolt. However, the data of Table 7.3 indicate that the SCC threshold stress was $\approxeq$ 900 MPa. This indicated that the stresses in service of failed bolts have been increased significantly over the nominal tensile stresses due to installation. The most likely cause of the increase in service stress was due to the rock shear causing plastic bending of the rock bolt. Rock bolts failed in service were often bent, indicating a permanent plastic deformation to a stress of a magnitude greater than the yield stress.

The following calculation provides an estimate of the amount of bending required to increase the service stress to above the SCC threshold stress. It is assumed that a typical bolt was installed with a load of 15 tonnes.

A typical 1355AXRC bolt is assumed to be installed with a 8-10 tonne load (by tightening the nut). Bolt can be loaded further by the displacing strata. Due to the rock bolt geometry introducing stress raisers (ribs of 1 mm critical radius give a conservative stress raiser value of 1.25), the load at the foot of the ribs can be as high as 184 kN (for an applied 15 tonne load (147 kN)). With a cross sectional bolt area of 3.7 x 10^{-4} m^2 this corresponds to a stress of $\approxeq$ 500 MPa. This would give a margin of 400 MPa before the stress on the rock bolt would reach the SCC threshold stress. The normal stress σ_x at the surface of the material under a bending load is given by [60],

$$\sigma_x = \frac{My}{I_{xx}} \tag{7.2}$$

where M is the bending moment, y is the distance away from the centroid (0.0107 m in the case of the bolt) and I_{xx} is the second moment of area of the bolt (9.01 x 10^{-9} m^4). Substituting typical values into

Equation 7.2 gives

$$400 * 10^6 = \frac{M * 0.0107}{9.01 * 10^{-9}} \qquad \Rightarrow M = 337Nm. \tag{7.3}$$

Therefore a bending stress of 337 Nm is needed to cause SCC on such a rock bolt. This bending stress can be related to a radius of curvature ρ by means of:

$$\frac{1}{\rho} = \frac{M}{EI_{xx}} \tag{7.4}$$

where E is the Young's modulus (200 GPa for steels). Substituting in the values gives,

$$\frac{1}{\rho} = \frac{337}{200 * 10^9 * 9.01^{-9}} \qquad \Rightarrow \rho = 5.35m. \tag{7.5}$$

Therefore a conservative value of a radius of curvature that would produce SCC in an 1355AXRC rock bolt would be 5.35 m. If a lower initial value of installation stress of 200 MPa is used, the corresponding radius of curvature needed to cause SCC would be approximately 3 meters.

7.4 GALVANISED SAMPLES

Galvanised samples subjected to a preferred LIST test displayed surface cracking of the galvanised surface zinc layer and ductile overload, failing at 856 MPa. The surface appeared cracked and the zinc layer flaked. However the core of the LIST sample (free of zinc) failed in a ductile manner. Ungalvanised samples failed at 950 MPa, indicating that galvanising LIST samples lowered their strength. This was attributed to the heating of the steel to the temperature of the molten zinc causing a coarsening of the steel microstructure.

Figure 7.6 shows the fracture surface of the galvanised sample and a magnified view of the fracture of the zinc layer. Figure 7.6(a) depicts a cracked zinc layer around the perimeter, whilst at the center there was ductile failure. Figure 7.6(b) presents a higher magnification view of the zinc rich layer that cracked and separated as the LIST sample deformed during failure. The zinc layer did not only crack, but it also separated from the non zinc layer of the sample.

The galvanised samples were tested under varied environments and the SCC results are presented in Table 7.4.

These results are presented in a Pourbaix diagram in Figure 7.7. The black circles represent conditions causing SCC, while blank circles represent conditions that did not cause SCC.

Galvanised 1355AXRC samples did not show SCC in the laboratory at the free corrosion potential in the sulphate pH 2.1 solution. SCC was produced by applying a more negative potential to the samples. This suggested that galvanising steel samples could be a countermeasure against SCC. Galvanising has the disadvantages of lowering the UTS of the material. Furthermore the galvanised layer has a short lifetime before the galvanised layer is eaten away, due to the high corrosion rate of zinc in highly acidic conditions.

Table 7.4: **Environments Giving SCC in Galvanised LIST Samples**

Sample	Environment	Potential mV vs SHE	SCC
LIST 67	S pH 2.1	-800	No
LIST 73	S pH 2.1 E_{corr}+300 mV	-500	No
LIST 79	S pH 1.1 E_{corr}	-800	No
LIST 82	S pH 2.1 E_{corr}-500 mV	-1300	Yes
LIST 93	S pH 2.1 E_{corr}-600 mV	-1400	Yes

A test showed that the zinc coating would be corroded away within a week in the sulphate pH 2.1 solution. This short lifetime in acidic conditions suggested that galvanising bolts would not be a good countermeasure if the local mine conditions are highly acidic.

Figure 7.7 shows that galvanised samples could be made to show SCC when a very negative potential was applied. This observation reinforced the identification of hydrogen embrittlement (HE) as the SCC mechanism.

7.5 10M30 SAMPLES

Feedback from industry indicated that 10M30 rock bolts were perceived not to suffer from SCC. 10M30 bolts have been found that had failed (so it was thought) due to ductile tearing.

LIST samples in the preferred sulphate pH 2.1 solution indicated that 10M30 steel does not fail by SCC when loaded at 0.019 MPa s^{-1}, but by ductile tearing. To test an extreme, an 10M30 sample (LIST 102) was tested in the preferred sulphate pH 2.1 solution with an imposed overpotential of -1100 mV vs SHE. This sample showed SCC as shown by Figure 7.8. Figure 7.8(a) shows an overview of LIST 102. Figure 7.8(b) is a diagram of figure 7.8(a) showing the SCC (TTS) and ductile overload regions. Figure 7.8(c) shows a region of TTS within LIST 102. There were no CIS or qMVC regions. This was attributed to a low effective diffusion velocity of hydrogen through the material. Even though prior to fracture there was a considerable amount of hydrogen being evolved on the surface, very little of that hydrogen was able to enter the material, embrittling it in the process.

One main difference between the 10M30 steel and others was that the overload region for the 10M30 steel was ductile, not brittle. The ductile region was formed by the cracks and pits reducing the cross sectional area. The cracks and pits formed were quite small, and careful examination was needed to determine the cause of failure, as the macroscopic appearance was that of ductile tearing. It is suggested that industry believes that 10M30 steels do not suffer from SCC. Based on these results, it is suggested that service failures need to be examined in detail to determine if SCC contributes to the service failures, even if they appear to have failed due to ductile tearing.

Since those extreme conditions showed that 10M30 steels can fail by SCC, an experimental program was carried out to determine the conditions that lead to SCC in 10M30 steels. Table 7.5 shows the varying conditions, whilst Figure 7.9 shows the results from Table 7.5 in a Pourbaix diagram.

Table 7.5: **Environments Giving SCC in 10M30 steel LIST Samples**

Sample	Environment	Potential mV vs SHE	SCC
LIST 94	S pH 2.1	-330	No
LIST 95	S pH 2.1 E_{corr}-200 mV	-530	No
LIST 96	S pH 6.4	-350	No
LIST 98	S pH 2.1 E_{corr}-320 mV	-650	No
LIST 99	S pH 3.0 E_{corr}-470 mV	-800	No
LIST 102	S pH 2.1 E_{corr}-770 mV	-1100	Yes
LIST 106	S pH 2.1 E_{corr}-470 mV	-800	Yes
LIST 110	S pH 1.5	-230	Yes
LIST 112	S pH 12.3	-150	No
LIST 114	S pH 6.5	-350	No
LIST 116	S pH 6.5 E_{corr}-850 mV	-1200	Yes
LIST 117	S pH 6.3 E_{corr}-650 mV	-1000	Yes

Figure 7.10 shows an overview of LIST 106. The macroscopic appearance was that of ductile tearing. Figure 7.11 shows a higher magnification of the right side of sample LIST 106. TTS can be seen on the edge, with CIS further in. Due to the lack of SCC of samples LIST 98 and 99, the evidence of SCC being displayed in LIST 102 and both kinds of fracture surfaces (ductile tearing and SCC) appearing on LIST 106 point to the fact that the environmental conditions of LIST 106 have reached the necessary pH and potential values for SCC to develop.

7.6 5152CW10D SAMPLES

5152CW10D samples did not show SCC in the preferred sulphate pH 2.1 solution. Industry, nevertheless, has reported 5152CW10D bolts to have failed by SCC. Table 7.6 shows the environmental conditions applied to 5152CW10D steel. Figure 7.13 shows the results of Table 7.6 in a Pourbaix diagram.

Figure 7.12 shows an 5152CW10D LIST sample failed by SCC. Figure 7.12(a) shows an overview of the LIST sample, and Figure 7.12(c) shows the TTS of one of the initiation sites. Figure 7.12(c) shows in detail the pearlite colonies, and how the crack advanced through the material irrespective of the microstructure (shown by the varied orientation of pearlite lamella). There were no CIS or qMVC regions on the fracture surface. This was postulated to be due to a low diffusion velocity of hydrogen through the material. Even though prior to fracture there was a considerable amount of hydrogen being evolved on the surface, very little of that hydrogen was able to enter the material, embrittling it in the process.

Figure 7.13 shows that the environmental conditions that lead to SCC in 5152CW10D steel are more

Table 7.6: **Environments Giving SCC in 5152CW10D steel LIST Samples**

Sample	Environment	Potential mV vs SHE	SCC
LIST 57	S pH 2.1	-320	No
LIST 97	S pH 6.4	-360	No
LIST 103	S pH 2.1 E_{corr}-480	-800	No
LIST 104	S pH 2.1 E_{corr}-880 mV	-1200	Yes
LIST 105	S pH 2.1 E_{corr}-680 mV	-1000	No
LIST 109	S pH 1.5	-220	No
LIST 111	S pH 12.3	-270	No
LIST 113	S pH 6.5	-360	No
LIST 115	S pH 6.5 E_{corr}-840 mV	-1200	No
LIST 118	S pH 6.3 E_{corr}-640 mV	-1000	No
LIST 119	S pH 11.5 E_{corr}-1130 mV	-1400	Yes
LIST 120	S pH 7.0 E_{corr}-940 mV	-1300	No
LIST 131	S pH 11.3 E_{corr}-930 mV	-1200	No
LIST 132	S pH 6.9 E_{corr}-1140 mV	-1500	No

severe than those of other steels. The Pourbaix diagram suggests that those bolts that have failed due to SCC during service experienced conditions in service representative of high hydrogen availability.

7.7 304 STAINLESS STEEL SAMPLES

Using stainless steel rock bolts might be a possible solution to rock bolt SCC.

Table 7.7 shows the environmental conditions applied to 304 stainless steel. The 304 steel failed in a ductile manner at sulphate pH 2.1 conditions. Figure 7.14 shows the results of Table 7.7 in a Pourbaix diagram.

Table 7.7: **Environments Giving SCC in 304 stainless steel LIST Samples**

Sample	Environment	Potential mV vs SHE	SCC
LIST 123	S pH 2.1	+310	No
LIST 138	S pH 2.1	-1200	Yes
LIST 140	S pH 2.1	-1000	Yes
LIST 141	S pH 2.1	-800	Yes
LIST 151	S pH 2.1	-200	Yes
LIST 152	S pH 2.1	+140	No
LIST 153	S pH 2.1	-30	No
LIST 156	S pH 6.8	-500	No
LIST 157	S pH 6.8	-700	Yes

The overall macroscopic fracture surface of the 304 steel failed by SCC resembled that of the 10M30,

MA840B and MAC samples. There were several secondary cracks along the sample, whilst the fracture surface was made up of small cracks and pits joined by a ductile overload.

The threshold potential for 304 steel at the preferred sulphate pH 2.1 solution is approximately -100 mV vs SHE. This point coincided with the hydrogen evolution line, suggesting that 304 stainless steel has poor SCC resistance properties, as it failed by SCC as soon as hydrogen started to be evolved on its surface.

7.8 5152 STEEL SAMPLES

5152 steel has the same metallurgy as that of 5152CW10D bolts and 5152CW55 samples, as 5152CW10D bolts are made by cold working 5152 steel by 10% and 5152CW55 by 55%. 5152 steel failed in a ductile manner at sulphate pH 2.1 conditions. Figure 7.15 shows the results of Table 7.8 in a Pourbaix diagram.

Table 7.8: **Environments Giving SCC in 5152 steel LIST Samples**

Sample	Environment	Potential mV vs SHE	SCC
LIST 124	S pH 2.1	-330	No
LIST 136	S pH 2.1	-1000	Yes
LIST 139	S pH 2.1	-800	No
LIST 142	S pH 6.5	-1200	Yes
LIST 143	S pH 6.5	-1000	Yes
LIST 144	S pH 6.5	-800	No
LIST 145	S pH 12.1	-1200	Yes
LIST 146	S pH 12.1	-1000	Yes
LIST 148	S pH 12.1	-800	No

5152 samples failed by SCC in the sulphate pH 2.1 solution with an overpotential of -1000 mV vs SHE, whereas 5152CW10D samples failed by ductile failure at these same conditions. These results showed that cold work increased the SCC resistance of steel.

7.9 THRESHOLD POTENTIALS SUMMARY

Table 7.9 summarises the threshold potentials of the steels studied (mV vs SHE) at various approximate pH levels.

7.10 SCC CRACK VELOCITY

In order to estimate the subcritical stress corrosion crack velocity through the various metallurgies, data was used from the fracture surfaces and from experimental records. The stress corrosion crack velocity was

Table 7.9: **Threshold Potentials**

	pH 1.5		pH 2.1		pH 7		pH 12	
	SCC	no SCC	SCC	no SCC	SCC	no SCC	SCC	no SCC
1355AXRC	-150	-	-350	-250	-920	-720	-950	-
Galvanised	-	-800	-1300	-500	-	-	-	-
10M30	-230	-	-800	-650	-1000	-350	-	-150
304	-	-	-200	-30	-	-	-	-
5152	-	-	-1000	-800	-1000	-800	-1000	-800
5152CW10D	-	-220	-1200	-1000	-	-1500	-1400	-1220

estimated from

$$v_{SCC} = \frac{d}{t} \tag{7.6}$$

where d = stress corrosion crack size at the onset of fast fracture, and t = time for stress corrosion crack propagation.

In the case of the constant load LIST test, the largest crack was measured, and divided by the time for which the sample was held at a constant stress. In the case of the preferred LIST tests, the time used was the complete experiment time, assuming a worst case scenario of a crack initiating and propagating as soon as the material was under any stress.

Figure 7.2 shows the slow crack region to have penetrated 0.5 mm into the sample LIST 63. LIST 63 was a 1355AXRC sample that was stressed at 0.019 MPa s^{-1} up to 922 MPa, then held until it fractured 19140 seconds later (5.3 hrs). For the crack velocity calculation it was assumed that the crack initiated when the stress on the sample reached 922 MPa and grew steadily until it reached a critical size (0.5 mm). SCC velocities v_1 and v_2 were calculated from LIST 63 and LIST 24 using Equation 7.6 to give:

$$v_1 = \frac{500 * 10^{-6} m}{19,140 s} = 2.6 * 10^{-8} m s^{-1}$$

and

$$v_2 = \frac{1,200 * 10^{-6} m}{50,400 s} = 2.3 * 10^{-8} m s^{-1}$$

v_1 and v_2 give an average value of

$$v_{av} = 2.5 * 10^{-8} m s^{-1}$$

This crack velocity can be used to evaluate benefit provided by a material with a higher toughness. There would be an increased lifetime between SCC onset and fast brittle fracture. If the fracture toughness was increased by a factor of two, the critical crack size in service would be increased by a factor of $(\text{two})^2 = 4$, e.g. from say 2 x 10^{-3} m to 8 x 10^{-3} m. The increased life time would be:

$$t = \frac{d}{v} = \frac{6 * 10^{-3}}{2.5 * 10^{-8}} = 240000 s$$

or simply 2.7 days. This increase in life time of a bolt does not seem to provide substantial benefits. It would be more beneficial to change the susceptibility of the bolt to SCC at certain conditions rather than making it more resistant to overload brittle crack growth.

Crack velocities in the order of 2.5 x 10^{-8} m s^{-1} suggest that a rock bolt would fracture within hours of it reaching the threshold stress provided that the local environment is conducive to SCC. This suggests that if a rock bolt failed by SCC, the surrounding rock had sheared within the prior three days. That is, the rock had moved until it touched the bolt and subsequently deformed it. This fact can greatly aid industry. By recording which rock bolt failed at a particular time, a map can be drawn that shows the movement of rock strata with respect to time. This information can aid geologists in better understanding the rock mechanics in the mine, leading to a safer and better mine design.

Tables 7.10 and 7.11 present the results of various constant load LIST tests, and the preferred LIST tests respectively.

Table 7.10: **Determination of SCC velocity for constant load tests**

Metallurgy	Sample	Time at constant stress (s)	SCC crack size (mm)	Velocity m s^{-1}
1355AXRC	LIST 63	19140	0.5	2.6 x 10^{-8}
MAC	LIST 72	180000	1.0	5.5 x 10^{-9}
MA840B	LIST 71	255000	0.5	2.0 x 10^{-9}

Table 7.11: **Determination of SCC velocity for preferred tests**

Metallurgy	Sample	LIST test duration (s)	SCC crack size (mm)	Velocity m s^{-1}
1355AXRC	LIST 24	53398	1.3	2.4 x 10^{-8}
1355AXRC	LIST 23	54000	1.1	2.1 x 10^{-8}
MAC	LIST 70	44280	1.0	2.2 x 10^{-8}
MA840B	LIST 69	50400	1.0	1.9 x 10^{-8}

The velocities presented in Tables 7.10 and 7.11 agree with typical values reported in literature [3]. Similar SCC velocities were evaluated for the three steels for these test conditions.

Table 7.10 indicates that the MAC and MA840B steels had a SCC velocity up to an order of magnitude smaller in the constant load test than in the LIST test. All steels had a similar SCC velocity in the LIST test. The calculations of velocities for the two tables assumed a worst case scenario of zero crack initiation time in order to provide a velocity estimate that could be used to provide an upper bound estimate of rock bolt lifetime. The difference in SCC velocities could be interpreted as to suggest that the MAC and MA840B steels have a longer crack initiation time than the 1355AXRC steel close to their threshold stress. Furthermore, above their threshold stress, but below their ultimate yield stress, the MAC and MA840B

steels seemed to have a reduced crack initiation time. Further testing could study the crack initiation time for the various steels.

The differences in crack velocity in Table 7.10 are of little practical significance. A rock bolt with a crack velocity an order of magnitude (2 x 10^{-9} m s^{-1}) smaller than that of 1355AXRC (2 x 10^{-8} m s^{-1}) would fail within 27 days rather than the estimated 2.7 days for 1355AXRC. This increased lifetime does not offer a viable solution to the problem of rock bolt SCC.

These estimations of the SCC velocity for the constant load tests were based on the assumption that the crack initiated instantaneously as soon as the outer fibres of the bolt reached the threshold stress. This broad assumption is useful for the purpose of estimating the maximum rock bolt lifetime. If the assumption is inaccurate, i.e. if crack initiation time is indeed a sizeable portion of the total time to failure, the implications are that the stress corrosion crack will travel at much greater speeds than those estimated. The conclusions on bolt lifetimes would remain the same, provided the environment was not transitory. The increased crack initiation time would require for the bolt to be immersed in the determined environment for a longer period of time. If the environment in the rock changed quickly, the implication would be that fewer bolts would be observed to fail by SCC. Since the rock strata conditions tend to change slowly, the deductions would remain the same. Crack initiation time hence has no practical effect on the rock bolt lifetime as mine environmental conditions remain quasistatic for longer times than that required to cause a rock bolt to fail by SCC, hence the estimations remain valid.

7.11 CONCLUSIONS

The sulphate pH 2.1 solution produced SCC in the LIST test at an applied stress rate of 0.019 MPa s^{-1} The fractures were macroscopically brittle in contrast to the ductile overload fracture measured in air and also in the distilled water. Detailed SEM examination of the LIST samples tested in the sulphate pH 2.1 solution indicated a fractography similar to that of the service failures. There was a small region of SCC followed by fast brittle fracture. The SCC details were also similar to those of the service failures.

Environmental conditions causing rock bolt SCC in the laboratory were exposure at the free corrosion potential (-350 mV vs SHE) in the acid solution and hydrogen production. SCC conditions (pH and mV vs SHE) have been determined for 1355AXRC. A hydrogen embrittlement mechanism for the SCC was indicated by the particular restricted range of conditions for which SCC occurred in the laboratory. In particular, SCC only occurred in the laboratory for the restricted range of environmental conditions corresponding to acid conditions at the open circuit potential ($\approxeq$ pH 2.1 or more acid) or at negative applied electrochemical potentials corresponding to copious hydrogen evolution at the steel surface. This was consistent with reports from the USA indicating rock bolt failure due to the presence of H_2S in the mine atmosphere and with bacterial corrosion on the rock bolt surface during service producing acid conditions leading to SCC.

A successful method of testing for a material's threshold stress using the LIST apparatus was developed.

A sample was loaded in the apparatus, and the applied load was increased linearly up to a designated level. After reaching the stress level the sample was held at that stress whilst submerged in the desired electrolyte. If the sample did not fracture it was submerged in liquid nitrogen and fractured. The fracture surface was then analysed to determine if subcritical cracks were present.

By using this interrupted method, the threshold stress was measured for 1355AXRC ($\approxeq$ 900 MPa), MAC ($\approxeq$ 830 MPa) and MA840B Steel ($\approxeq$ 850 MPa), indicating that the loading causing SCC in service is due to a combination of the tensile load plus the bending load due to rock shear. This is consistent with the observation that rock bolts are typically bent after failure in service. This bending indicates a stress above the yield stress having been applied to cause the permanent deformation in bending, ie to cause permanent plastic deformation. The bending of the bolt has been attributed to shear in the rock strata. This leads to the issue of whether SCC could be prevented by a rock bolting strata design that prevented shear in the rock strata and thereby maintained the stress in the rock bolt below the threshold stress for SCC initiation.

The threshold stress for MA840B steel was about 850 MPa and for MAC steel 830 MPa. These values were similar to that for the 1355AXRC samples, but nevertheless lower in value.

MA840B and MAC have poorer SCC properties than 1355AXRC, as shown by extensive surface pits and secondary cracks. Although MA840B and MAC have failed by SCC the overall macroscopic appearance was very similar to that of ductile overload. Only careful observation could distinguish the failure mode. For this reason, industry might perceive these bolts to be immune from SCC, believing that these bolts fail in a ductile manner. In reality, these test showed that these metallurgies fare worse than the 1355AXRC metallurgy.

10M30 bolts were not believed to fail due to SCC in service, but laboratory tests show that fails can fail due to SCC but appear to have failed by ductile tearing. Environmental conditions required to cause SCC in 10M30 bolts are more acidic and/or at a more negative potential than for 1355AXRC, MA840B and MAC steels, but not as severe as those causing SCC in 5152CW10D material.

5152CW10D bolts can suffer from SCC (as shown by service failures), but conditions causing SCC in the laboratory were more severe than the free corrosion potential in sulphate pH 2.1. 5152CW10D bolts required the harshest environmental conditions out of all studied metallurgies for them to fail due to SCC. 5152CW10D's high strength further enhances the performance of this steel.

5152 steels suffered from SCC at conditions with less hydrogen production than those required to show SCC in 5152CW10D steels. This confirms that cold work helps increase the resistance to SCC of a steel.

Galvanised samples did not show SCC in the laboratory test at the free corrosion potential in the preferred sulphate solution at pH 2.1, but SCC could be induced in the pH 2.1 solution at a more negative potential. A galvanised coating has a short life due to general corrosion in the pH 2.1 solution.

A hydrogen embrittlement (HE) mechanism for the SCC was indicated by the particular restricted range of conditions for which SCC occurred in the laboratory. In particular, SCC only occurred in the laboratory for the restricted range of environmental conditions corresponding to (1) acid conditions at the open circuit

potential (pH 2.1 or more acid) or (2) at very negative applied electrochemical potentials corresponding to copious hydrogen evolution at the steel surface. This was consistent with reports from the USA indicating rock bolt failure due to the presence of H_2S in the mine atmosphere. Similarly, this was consistent with bacterial corrosion on the rock bolt surface during service producing acid conditions leading to SCC.

Water chemistry analyses has been carried out for a number of Australian mines (including one coal mine). The water in all cases was neutral, with the pH ranging from 6.8 to 8.3. Similarly, the pH = 7.1 for the one analysis of mine water chemistry in the ACARP C8008 [7]. Laboratory testing indicated that SCC would not occur in any of these neutral mine waters. This does indeed suggest that SCC in a coal mine would be caused by bacterial corrosion locally decreasing the mine water pH down to a pH $\approxeq$ 2.1.

Crack velocities of SCC in 1355AXRC samples have been measured to be 2.5 x 10^{-8}m s^{-1} With such a high value a rock bolt would fail due to SCC if the stress reaches about 900 MPa in less than 6 hours if the environment was conducive to SCC. With such small time to failures there is little benefit in increasing the material fracture toughness. From this crack velocity, if a rock bolt fails during surface it suggests rock shearing within the last 3 days.

Steels with slightly lower SCC velocities (i.e. with SCC velocities within an order of magnitude of those measured in this work) would provide little benefit to resolving the issue of rock bolt SCC fracture.

7.12 FIGURES

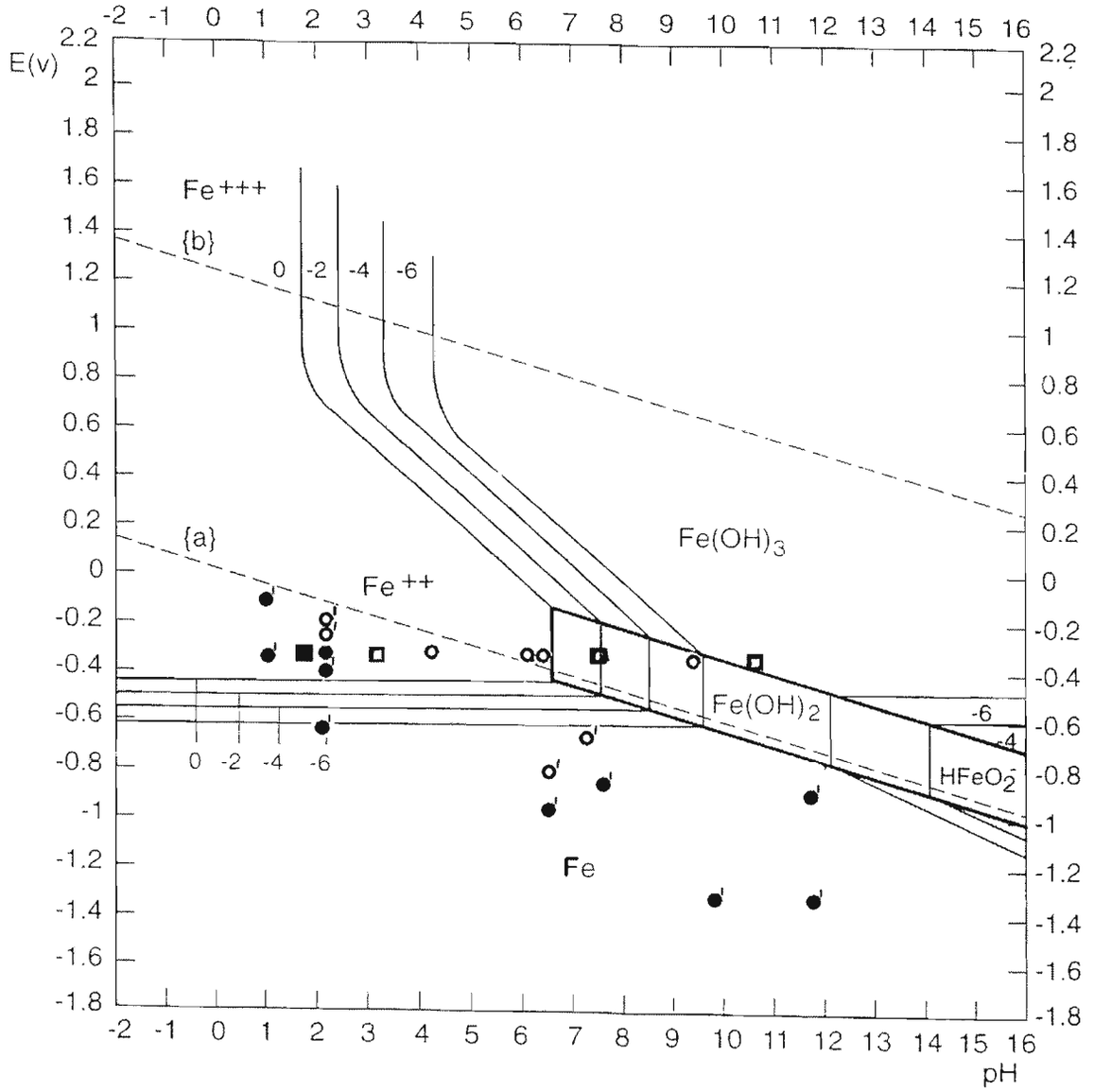

FIGURE 7.1: Pourbaix diagram for iron showing 1355AXRC LIST results. Sulphate solutions are represented by circles and chloride solutions are represented by squares. A full symbol means it failed by SCC, whereas an empty circle or square means no SCC was detected. Symbols with a dash represent experiments performed with an applied potential.

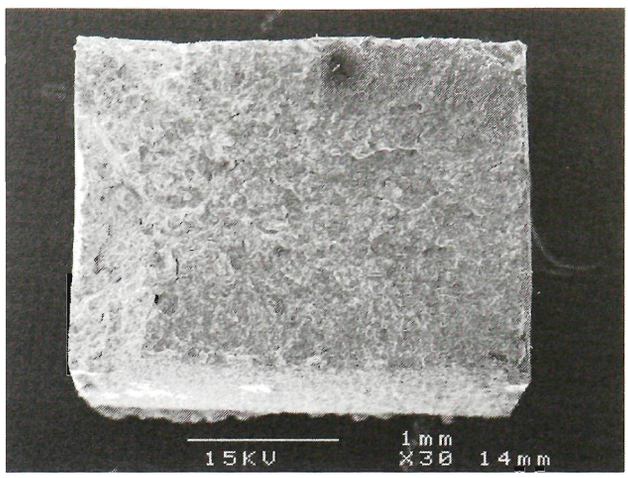

FIGURE 7.2: LIST63 (922MPa) overview

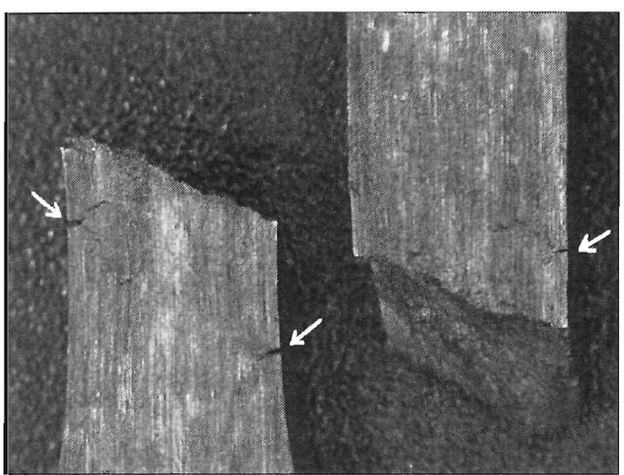

(a) LIST70 showing surface damage. Arrows point to secondary cracks

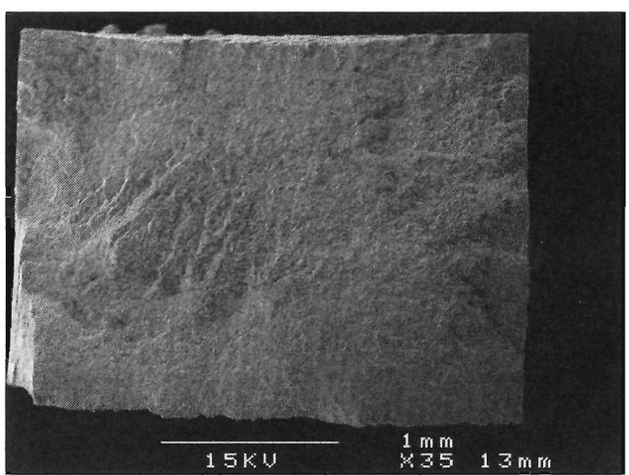

(b) LIST70 (830 MPa)

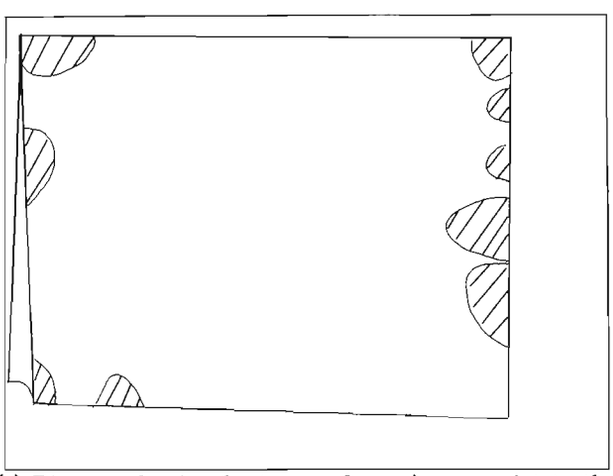

(c) Diagram showing fracture surface. Arrows point to the shaded areas representing SCC, the remaining surface shows ductile failure.

FIGURE 7.3: MAC samples failed at 830 MPa

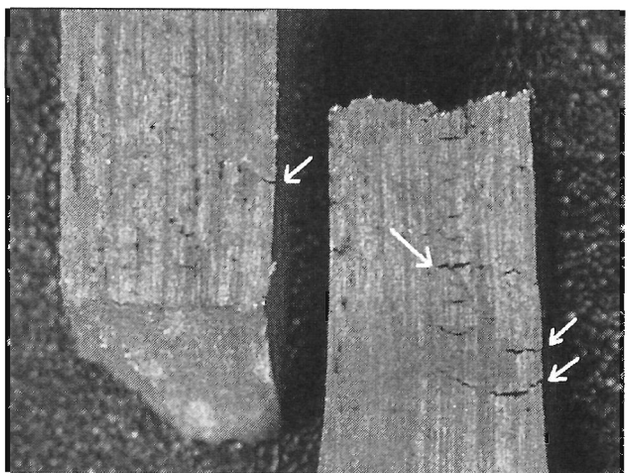

(a) LIST69 showing surface damage. Arrows point to secondary cracks

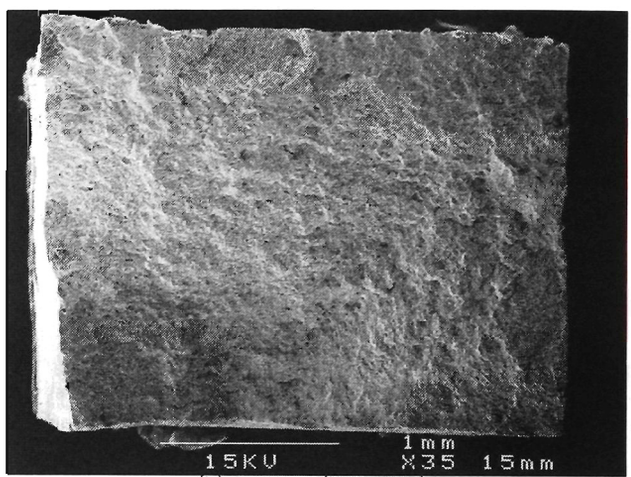

(b) LIST69 (850 MPa)

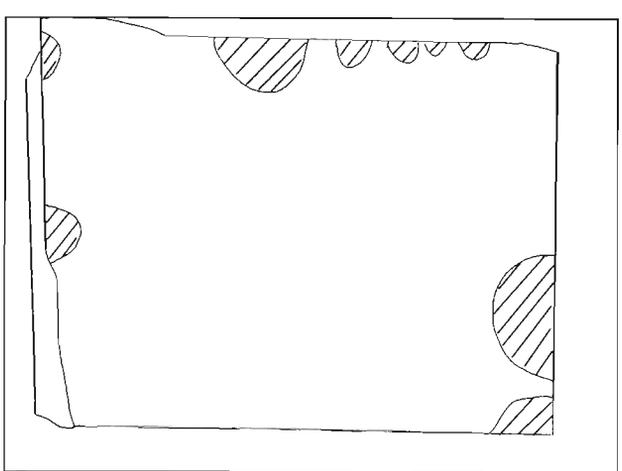

(c) Diagram showing fracture surface. Shaded regions represent subcritical SCC, the renaining surface showed ductile failure.

FIGURE 7.4: MA840B samples failed at 850 MPa

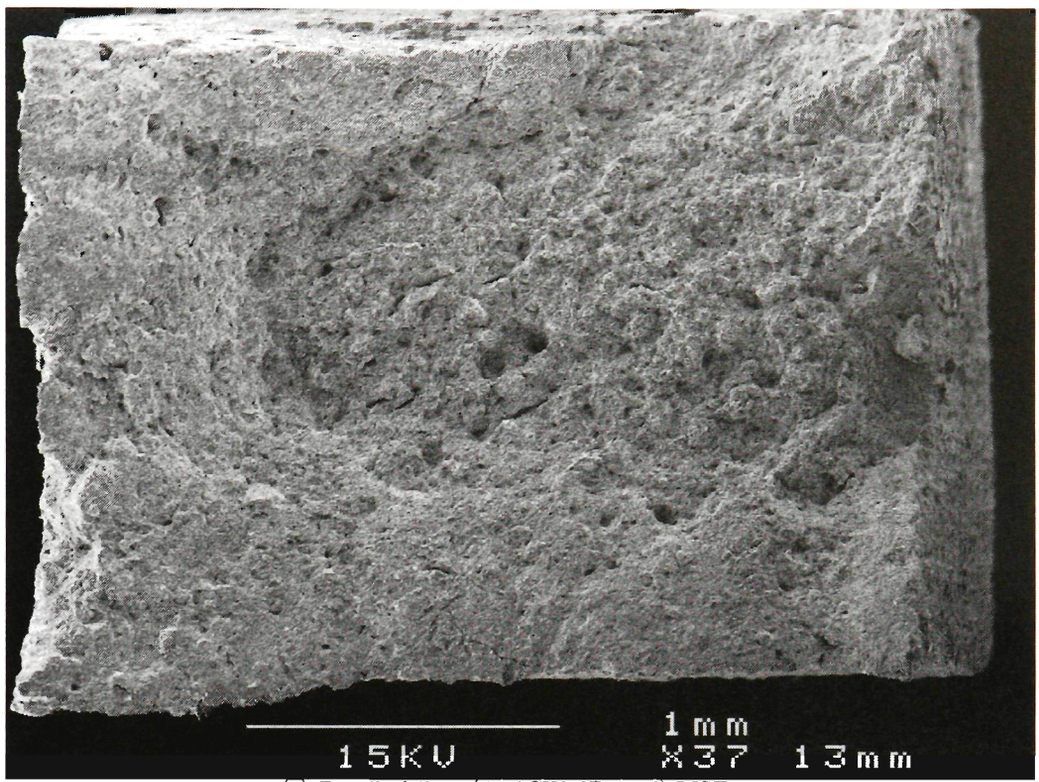

(a) Ductile failure (5152CW10D steel) LIST58

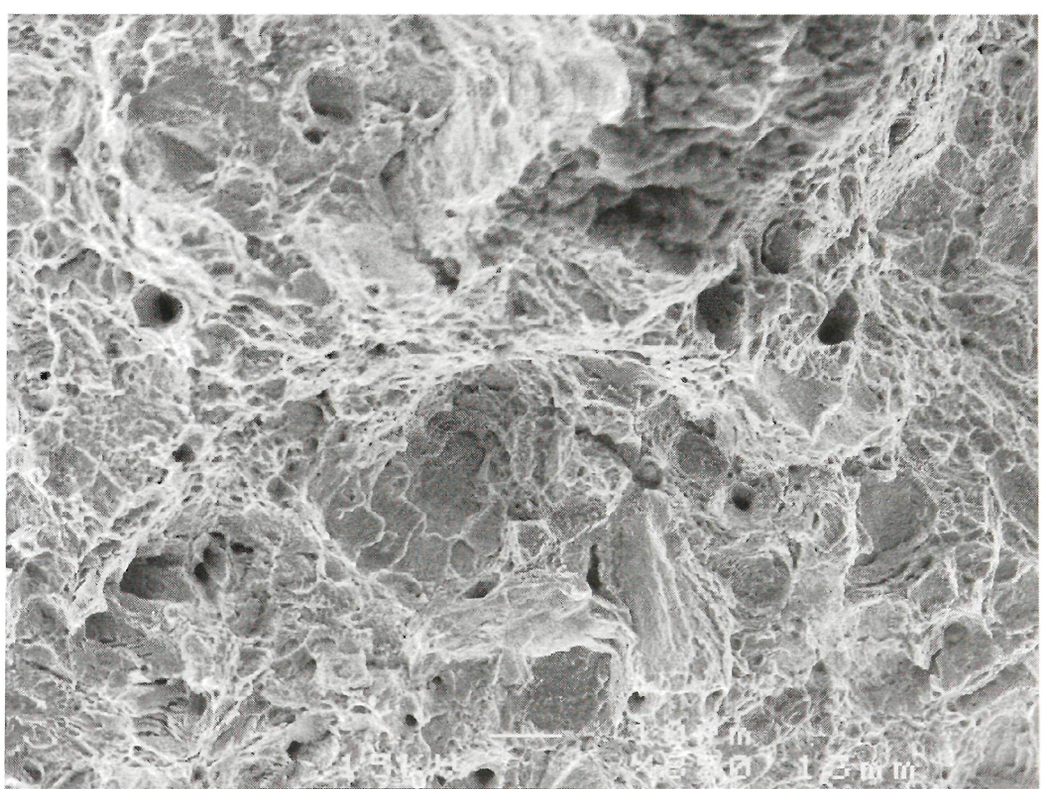

(b) Ductile failure in LIST58

FIGURE 7.5: Ductile failure (5152CW10D steel)

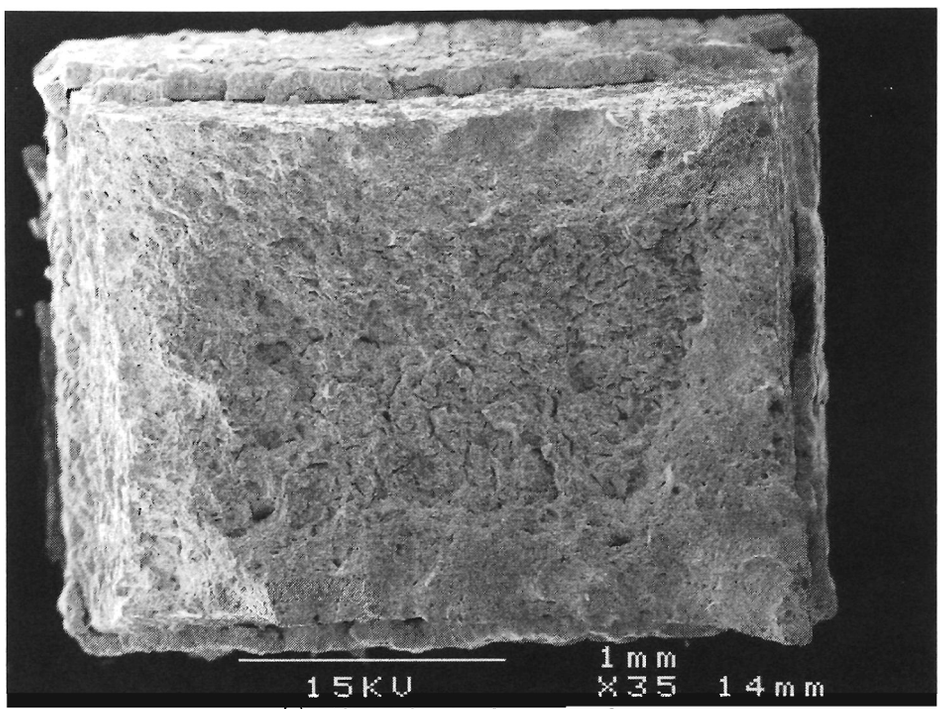

(a) LIST67 showing fracture surface

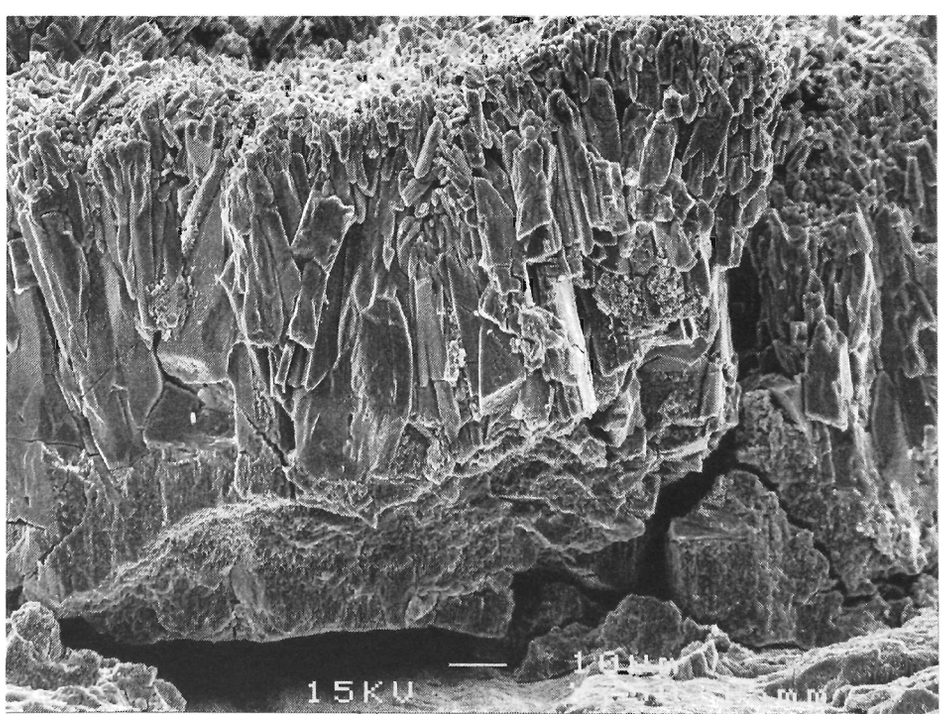

(b) LIST67 zinc layer

FIGURE 7.6: Galvanised LIST 1355AXRC sample

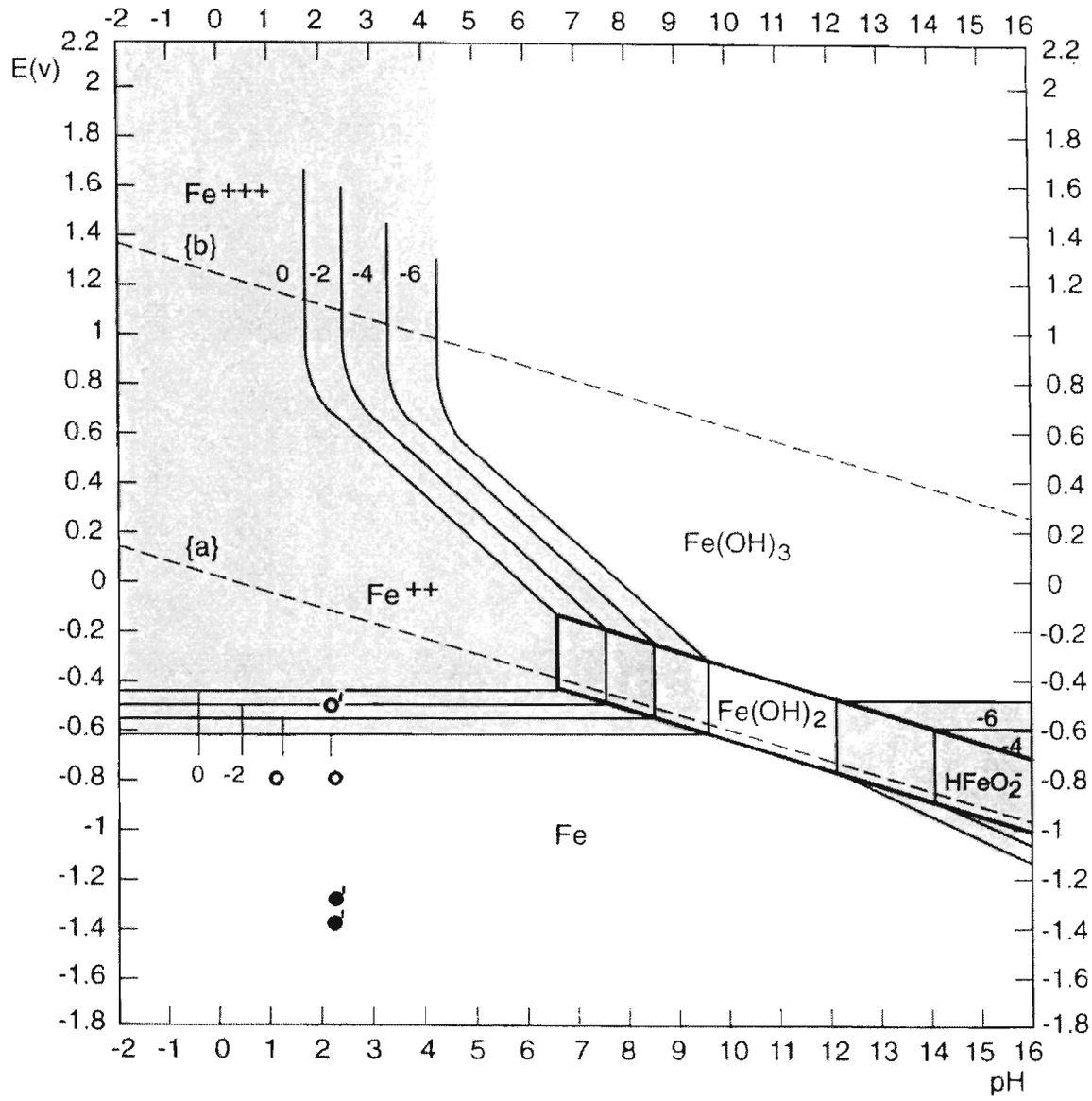

FIGURE 7.7: Pourbaix diagram for iron showing galvanised LIST results. A full symbol means it failed by SCC, whereas an empty circle or square means no SCC was detected. Symbols with a dash represent experiments performed with an applied potential.

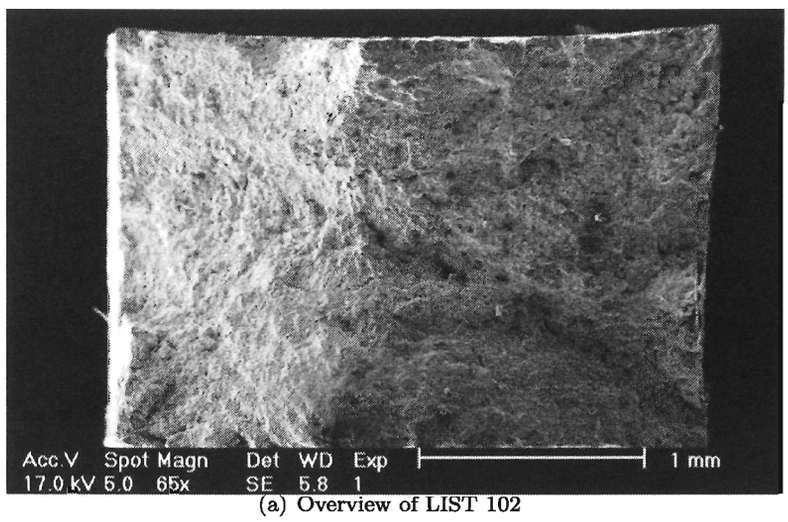

(a) Overview of LIST 102

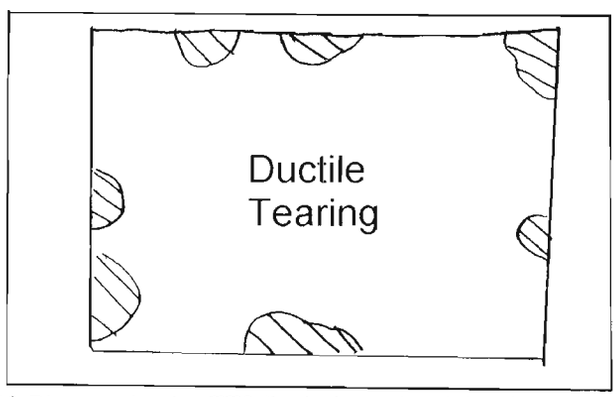

(b) Diagram showing TTS (hashed areas) and ductile overload regions

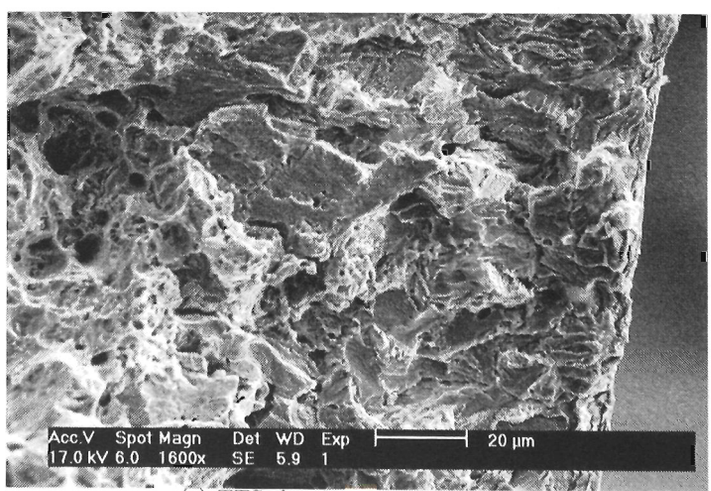

(c) TTS showing pearlite colonies

FIGURE 7.8: 10M30 LIST sample failed by SCC

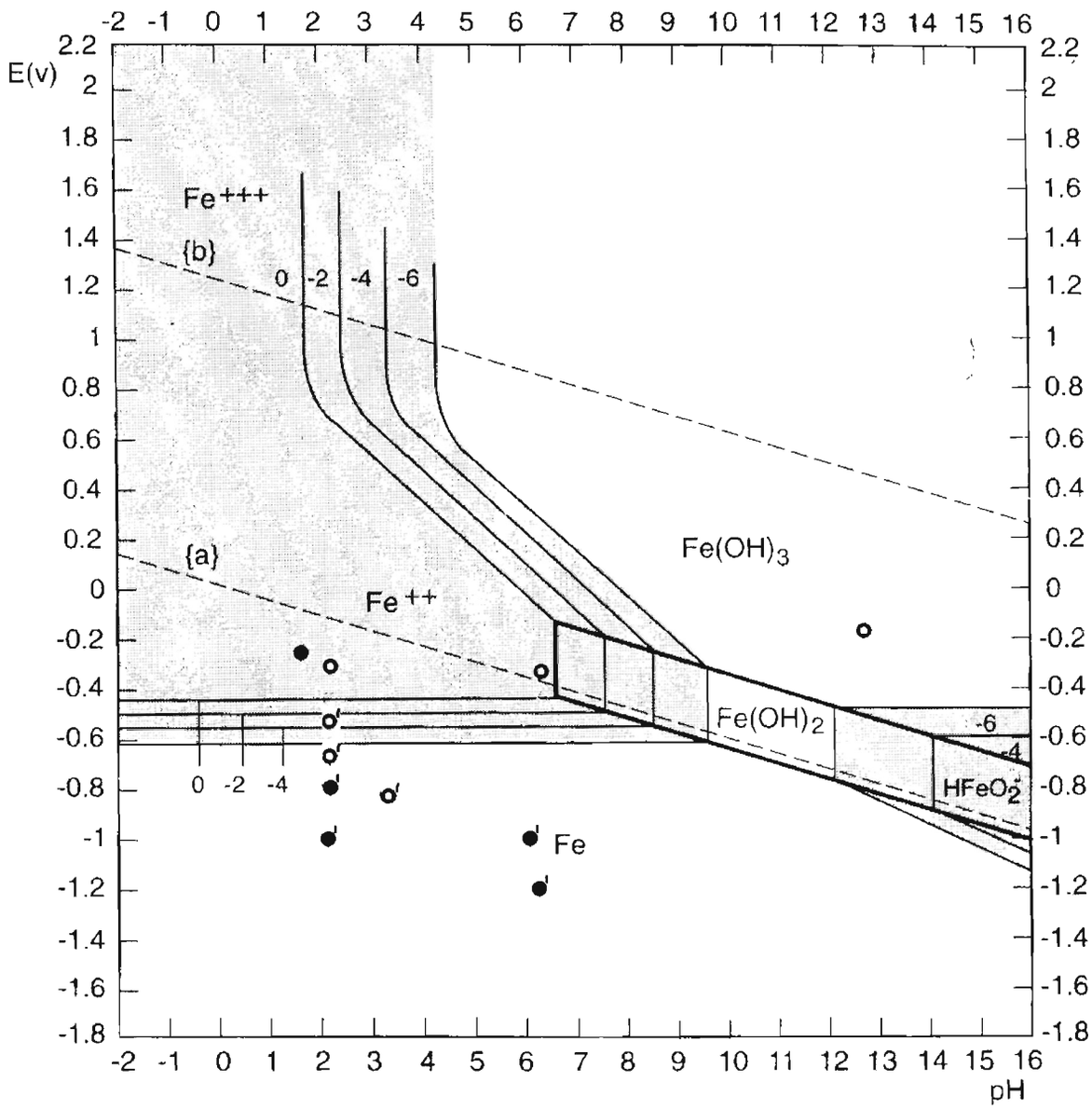

FIGURE 7.9: Pourbaix diagram for iron showing 10M30 LIST results. A full symbol means it failed by SCC, whereas an empty circle means no SCC was detected. Symbols with a dash represent experiments performed with an applied potential.

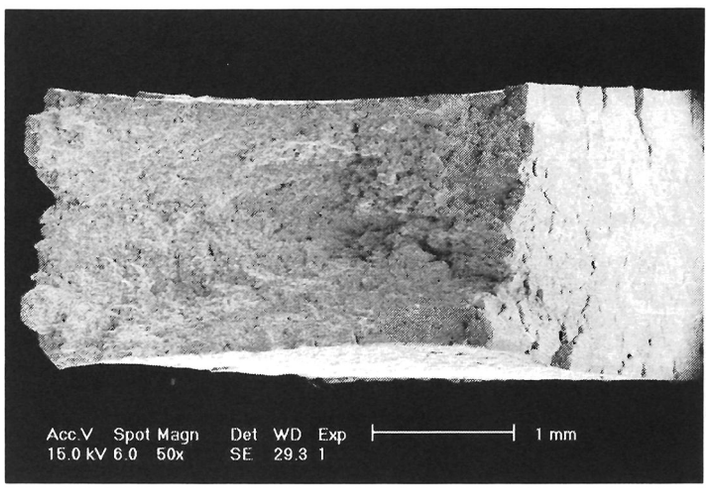

FIGURE 7.10: Overview of LIST 106

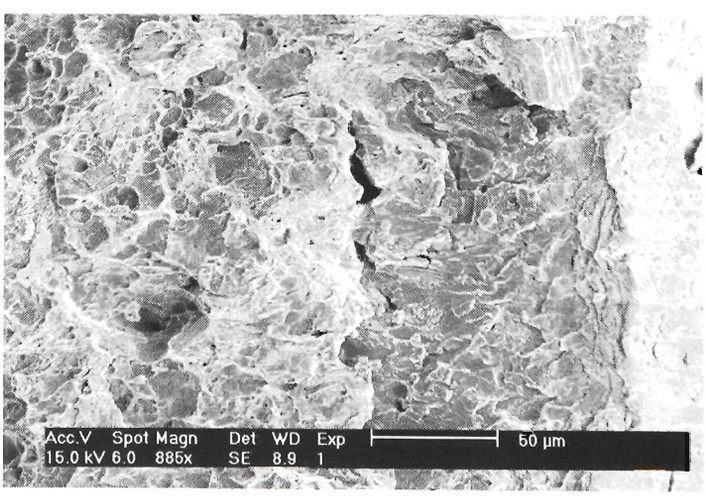

FIGURE 7.11: TTS and CIS within LIST 106

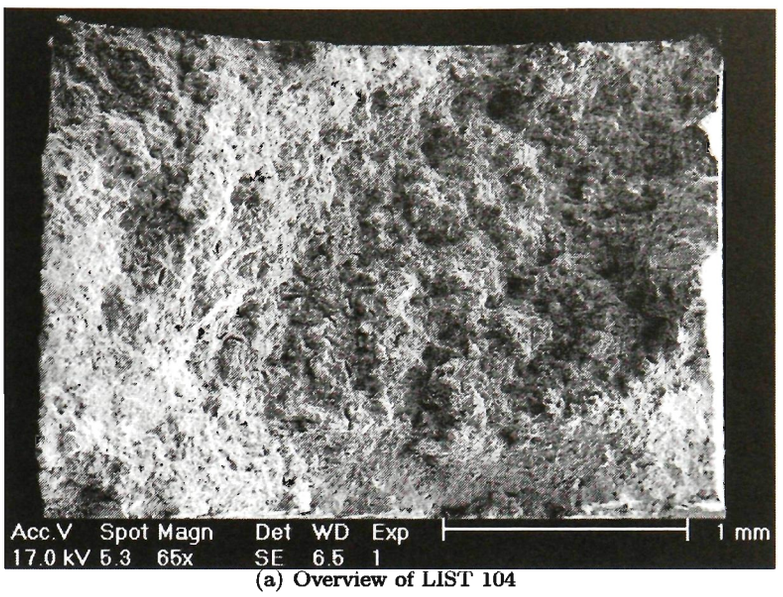

(a) Overview of LIST 104

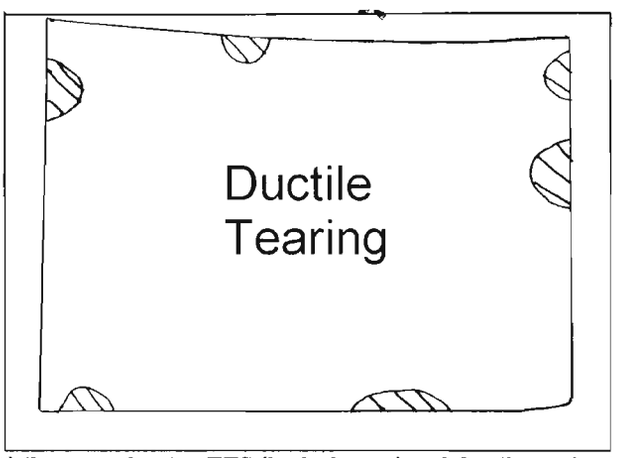

(b) Diagram showing TTS (hashed areas) and ductile overload regions

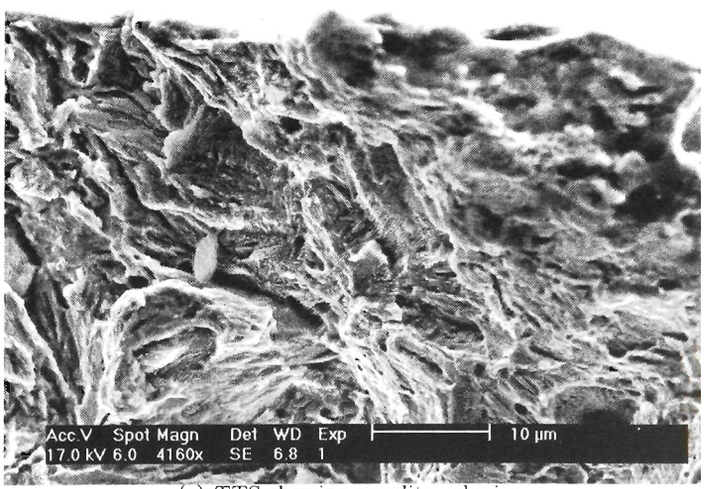

(c) TTS showing pearlite colonies

FIGURE 7.12: 5152CW10D LIST sample failed by SCC

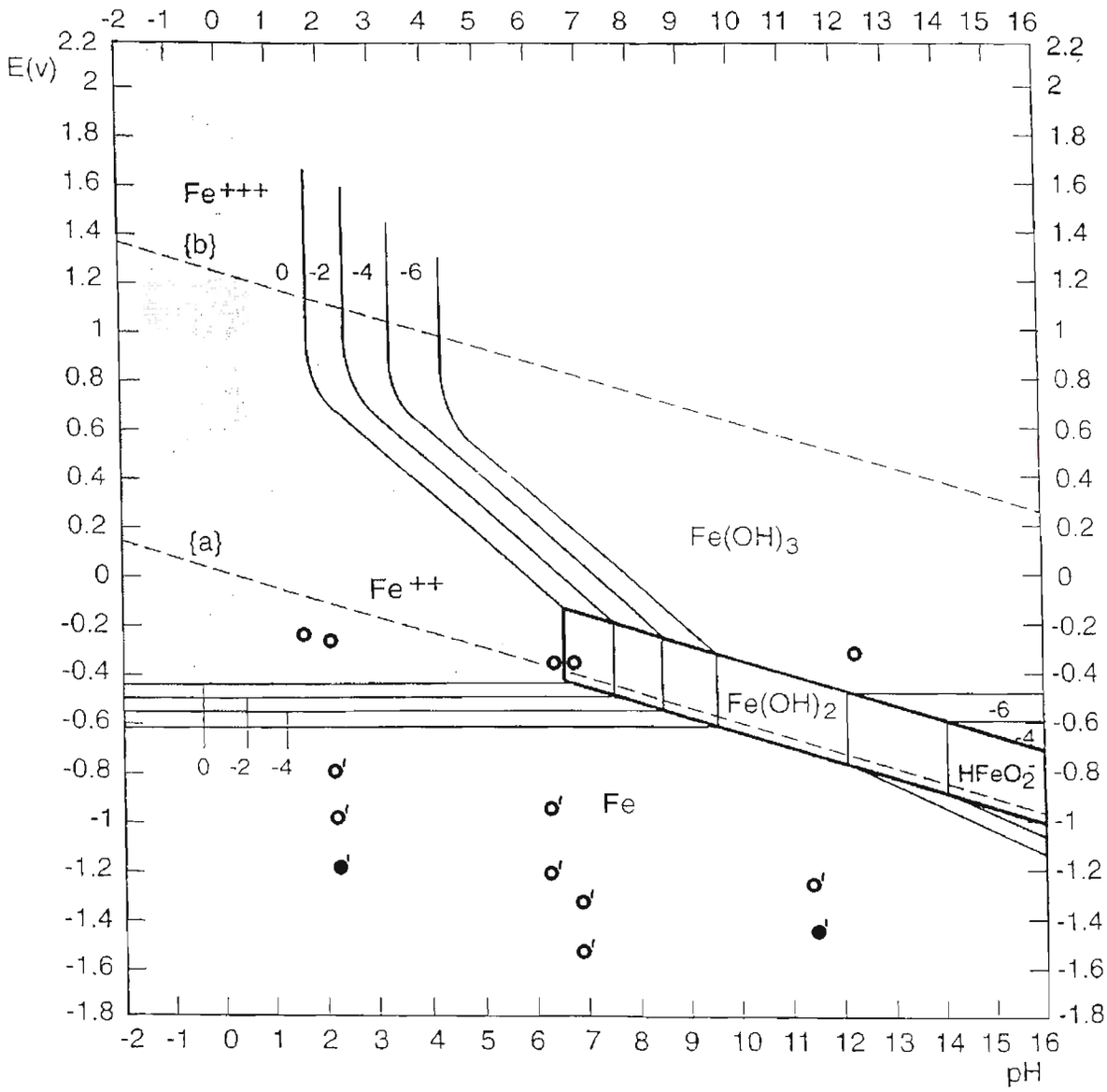

FIGURE 7.13: Pourbaix diagram for iron showing 5152CW10D LIST results. A full symbol means it failed by SCC, whereas an empty circle means no SCC was detected. Symbols with a dash represent experiments performed with an applied potential.

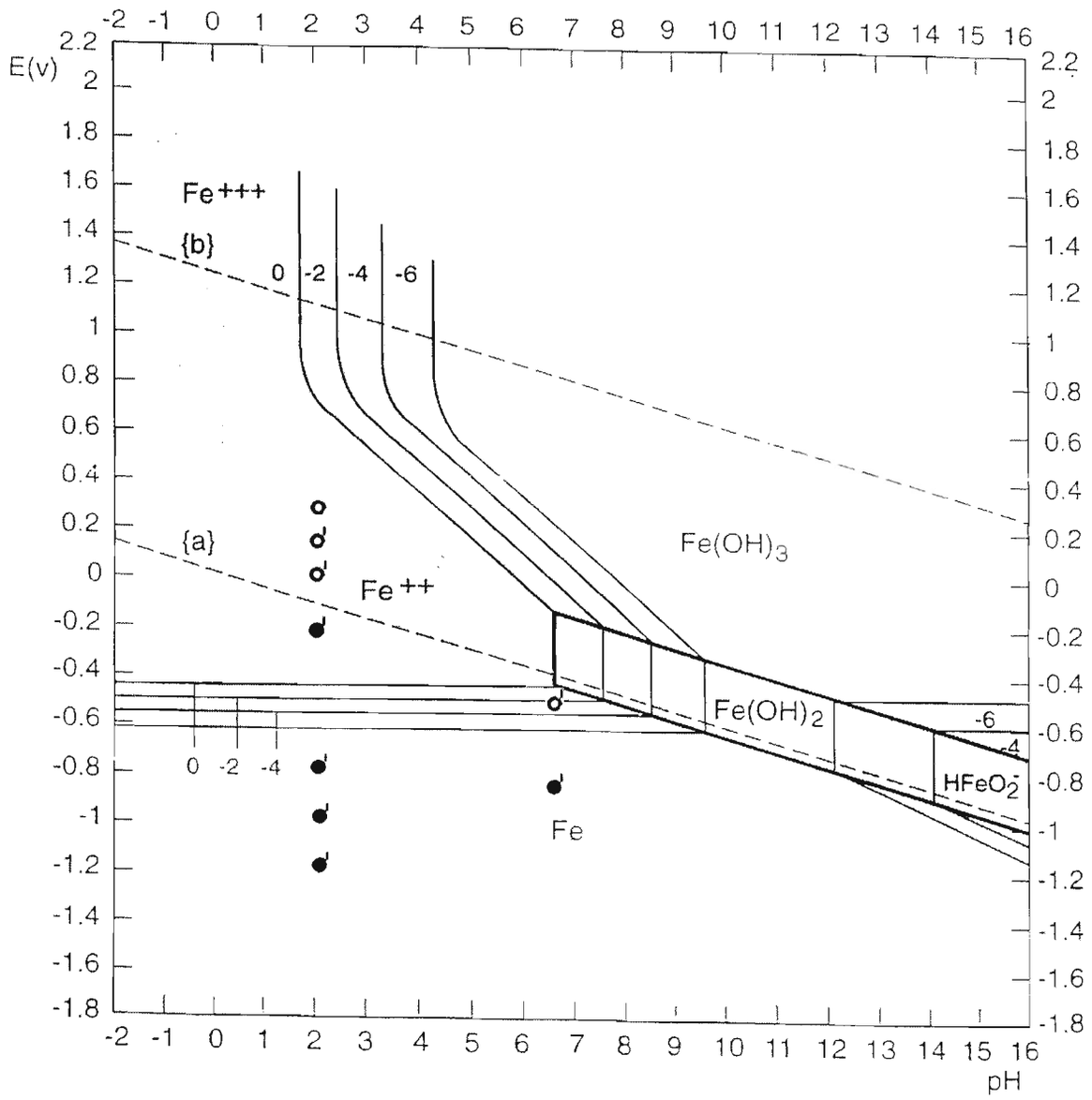

FIGURE 7.14: Pourbaix diagram for iron showing 304 stainless steel LIST results. A full symbol means it failed by SCC, whereas an empty circle means no SCC was detected. Symbols with a dash represent experiments performed with an applied potential.

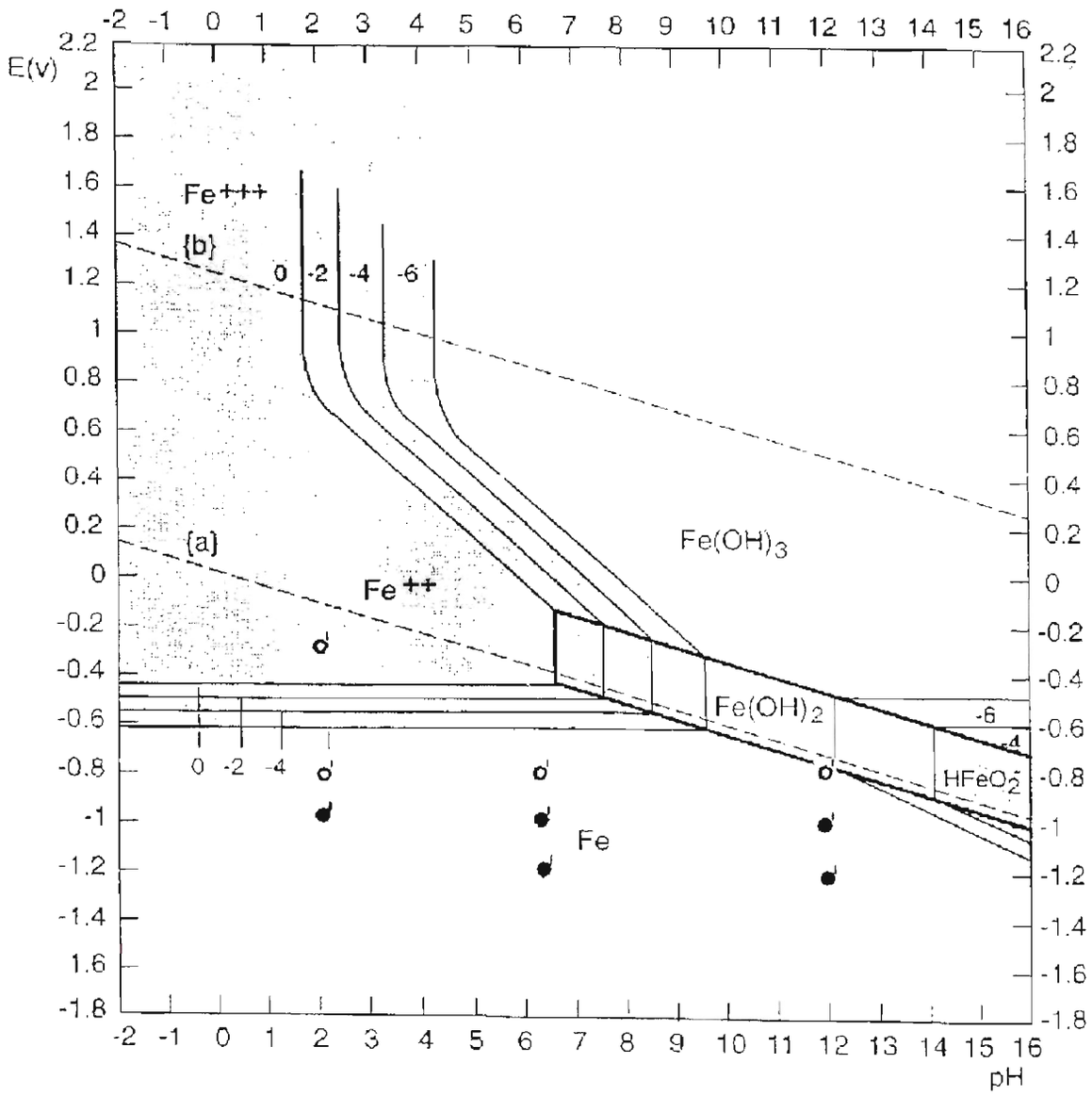

FIGURE 7.15: Pourbaix diagram for iron showing 5152 LIST results. A full symbol means it failed by SCC, whereas an empty circle means no SCC was detected. Symbols with a dash represent experiments performed with an applied potential.

8

METALLURGICAL INFLUENCES

This Chapter presents measurements of the fracture toughness (K_{Ic}) and an investigation into the influence of Cold Work (CW) on SCC.

The first section of this Chapter presents the work done to measure the fracture toughness of the 1355AXRC steel by various methods. Efforts to measure the fracture toughness was made difficult due to the small size of the samples available. In each case, an approximate value was obtained. These values should be used with care, as they only gave an indication of the true value. These measurements indicate that the fracture toughness of 1355AXRC is $K_{Ic} = 51 \pm 8$ MPa$\sqrt{m}$ and that 5152CW10D has a similar value and that the MA840B has a value of $K_{Ic} = 116$ MPa$\sqrt{m}$.

The second section of the Chapter describes how LIST was used to assess the SCC susceptibility of the 1355AXRC rock bolt metallurgy to CW

8.1 FRACTURE TOUGHNESS K_{Ic}

8.1.1 Fast Fracture of LIST Samples

The first estimate for a value of K_{Ic} could be obtained from the formula

$$K_{Ic} = Y * \sigma\sqrt{\pi a} \tag{8.1}$$

where Y is the geometry factor (assumed to be 1 for a simple case), σ is the nominal tensile stress at fracture and a is the crack size. The thumbnail SCC area had typically a crack depth a of 1-1.2 mm in depth. The fracture toughness K_{Ic} could be evaluated as

$$K_I = \sigma\sqrt{\pi a} \approx 50MPa\sqrt{m} \tag{8.2}$$

Using the typical threshold stress (σ_f or σ_{TH}) of 900 MPa from Chapter 7 Table 7.3 and a typical crack size a of 1 mm, this first estimate gave a value of K_{Ic} = 50 MPa$\sqrt{m}$.

Anderson [61] provides a better estimate to K_{Ic} that takes into account the quarter elliptical crack shape. This provides an approximation of the geometry factor Y. Figure 8.1 presents the geometry considerations. Samples LIST 24 (Figure 8.2) and LIST 41 (Figure 8.3) gave the values listed in Table 8.1.

Table 8.1: **Stress Intensity Solutions for LIST 24 and LIST 41**

Measured Value	**LIST 24**	**LIST 41**
σ_m	930 MPa	902 MPa
a	0.00122 m	0.00085 m
w	0.00328 m	0.00324 m
c	0.001265 m	0.00132 m
t	0.00254 m	0.00248 m
Calculated Value		
f_w	≈ 1	≈ 1
f_ϕ	0.99115	0.91708
g_2	1.00288	1.002453
g_1	1.004329	1.00319
M_3	-0.741106	-0.661
M_2	0.39832	0.683
M_1	1.05106	1.06068
Q	2.37907	1.70817
F	1.10161	1.0438
Y	0.7142	0.7986
K_{Ic}	41	37

These results gave a value of 41 MPa$\sqrt{m}$ for LIST 24 and 37 MPa$\sqrt{m}$ for LIST 41. This gives lower values for K_{Ic}. These samples however do not satisfy the ASTM plain strain requirements, which require a specimen size of at least 10.3 mm.

Another method of assessing the fracture toughness is to relate the Charpy V Notch (CVN) values to K_{Ic}. Charpy V notch values were measured by the steel manufacturer, and reported to be 6 J. Rolfe et al [31] relates CVN values to K_{Ic} values for materials in the lower shelf region according to the empirical formula

$$K_{Ic} = \sqrt{0.64 * CVN * E} \tag{8.3}$$

where CVN is in Joules and E is in kPa. The resulting K_{Ic} value was 27 MPa$\sqrt{m}$ for 1355AXRC samples, 48 MPa$\sqrt{m}$ for MA840B samples and 61 MPa$\sqrt{m}$ for MAC samples.

8.1.2 Fast Fracture of Rock Bolts

Murakami [62] provides an approximation to K_{Ic} that takes into account the semi elliptical crack shape by calculating a value of the geometry factor Y Figure 8.4 presents the considerations; in this calculation $F_I = Y$ Table 8.2 presents the K_{Ic} values calculated for the service failures assuming fracture occurred at a fracture stress σ_f= 900 MPa. Poisson's ratio ν for steel is 0.3.

Table 8.2: **Stress Intensity Solutions for Service Failures**

Measured Value	Bolt F 1355AXRC	Bolt G 1355AXRC	Bolt H 5152CW10D	Bolt J MA810	Bolt K 1355AXRC
a	3.3 mm	1.59 mm	3.22 mm	7.5 mm	2.47 mm
b	1.9 mm	1.27 mm	3.11 mm	8 mm	1.07 mm
r	10.75 mm	10.75 mm	10.75 mm	10.75 mm	10.75 mm
Calculated Value					
$\frac{b}{a}$	0.576	0.805	0.966	1.066	0.434
$\frac{b}{r}$	0.177	0.118	0.289	0.744	0.100
$\frac{a}{r}$	0.307	0.148	0.300	0.700	0.230
F_I	0.9	0.75	0.69	0.81	1
K_I	63	43	61	116	52

These results give a maximum value of 116 MPa$\sqrt{m}$ for Bolt J and a minimum value of 43 MPa$\sqrt{m}$. The values calculated for the 1355AXRC metallurgy (63, 43 and 52 MPa$\sqrt{m}$) agree with the values estimated from the LIST samples. The higher value of 116 MPa$\sqrt{m}$ indicates a higher toughness for MA840B, as can be seen by the larger thumbnail area on Bolt J compared to other bolts.

Another method of calculating a K_{Ic} value is to add the fracture toughness values obtained from tension and bending stresses acting on the bolt. As mentioned previously, the tensile stress is applied when the bolt is installed, while the bending stress can be applied by shearing rock strata. In this case, the fracture

toughness K_{Ic} is estimated by:

$$K_{Ic} = Y_b * \sigma_b \sqrt{\pi a} + Y_t * \sigma_t \sqrt{\pi a} \tag{8.4}$$

where Y_b is the geometry factor for sample under bending stress, σ_b is the applied bending stress, Y_t is the geometry factor for sample under tensile stress and σ_t is the applied tensile stress. The critical flaw size a is the same for both cases (1mm). Since the rock bolts are installed at a stress of 145 MPa, the bending stress needs to be 755 MPa in order to achieve the threshold stress of 900 MPa. Geometry factor Y_t can be taken as 0.83 (the average of F_I from Table 8.2), and Y_b can be taken as 0.58, based on work done by da Fonte and de Freitas [63].

Equation 8.4 becomes

$$K_{Ic} = 0.58 * 755\sqrt{\pi 0.001} + 0.83 * 145\sqrt{\pi 0.001} \approx 31 MPa\sqrt{m} \tag{8.5}$$

This value is close to that calculated from LIST 41.

This method was applied to bolts F, G and K. The individual bolt Y_t values were the F_I values from Table 8.2. The Y_b values were identical for all bolts (0.58). The tensile stress for bolts G and K were the estimated installation stress (145 MPa). The tensile stress applied to bolt F during installation was known to be 400 MPa, implying that the bending stress was 500 MPa.

Equation 8.4 gave a result of 50 MPa$\sqrt{m}$ for bolt F, 28 MPa$\sqrt{m}$ for bolt G and 34 MPa$\sqrt{m}$ for bolt K. These values are different to those based upon Murakami's [62] work of 63, 43 and 52 MPa$\sqrt{m}$ respectively. Although different, these values were between those estimated by the CVN method and by Murakami's method.

8.1.3 Experimental Measurement

Results and Discussion

Figure 8.5(a) shows the fractured sample reassembled as it looked like before failure. After fracture, it was observed that the fatigue crack front had not grown in an even manner in either of the samples. Figure 8.5(b) shows the shiny brittle fracture surface on the left and the bolt rib pattern on the right. Figure 8.5(c) shows a higher magnification of the fracture surface. The uneven fatigue pre crack can be seen on the surface, being thinner on the bottom than on the top. This was attributed to the samples rocking sideways while the load applied was fluctuating. This small rocking motion was attributed to the remaining bolt rib pattern causing the load to be distributed unevenly.

In this approach, the pre-fatigued sample was then loaded monotonically until a load drop was reached that defined P_Q as shown in Figure 8.6 taken from the Standard. From P_Q, a K_Q was calculated using

Equation A3.5.3 as defined in the Standard. That Equation is repeated here:

$$K_Q = \left(\frac{P_Q * S}{B * W^{\frac{3}{2}}}\right) * f\left(\frac{a}{W}\right) \tag{8.6}$$

where S is the span (8 cm), B is specimen thickness (1 cm), W is specimen width (2.1 cm), a is crack depth (1.03 cm) and $f\left(\frac{a}{W}\right)$ is obtained from the Standard:

$$f\left(\frac{a}{W}\right) = \frac{3\left(\frac{a}{W}\right)^{\frac{1}{2}}\left(1.99 - \frac{a}{W}\left(1 - \frac{a}{W}\right) * \left(2.15 - 3.93\frac{a}{W} + 2.7\left(\frac{a}{W}\right)^2\right)\right)}{2\left(1 + 2\frac{a}{W}\right)\left(1 - \frac{a}{W}\right)^{\frac{3}{2}}} \tag{8.7}$$

The second validity requirement was that the specimen needed to satisfy plain strain conditions given by

$$a, B \geq 2.5 * \left(\frac{K_{Ic}}{\sigma_y}\right)^2 \tag{8.8}$$

If the plain strain conditions were satisfied using the value of K_Q calculated using Equation 8.6 and provided that P_Q satisfied the condition given in the Standard[1], then the value of K_Q could be considered a valid K_{Ic} value.

The load vs displacement graphs produced from both samples are shown in Figure 8.7. The results of these tests are summarised in Table 8.3.

Table 8.3: K_Q **Values**

Sample	P_Q **MPa**$\sqrt{m}$	a **cm**	W **cm**	$2.5 * \left(\frac{K_{Ic}}{\sigma_y}\right)^2$ **cm**	**Valid** K_Q**?**
1	46	1.03	21	1.25	No
3	51	1.03	21	1.53	No

In both cases K_Q did not yield a valid measurement of K_{Ic}, as both samples failed the plane strain condition (1.25>1.03 for sample 1 and 1.53>1.03 for sample 2), and furthermore, sample 1 also failed the criterion $\frac{P_{max}}{P_Q} < 1.10$.

Nevertheless, the K_Q values can be taken as providing an indication of the value of K_{Ic}, particularly because both samples were close to providing a valid test and because it is well known that the ASTM K_{Ic} is highly conservative.

Table 8.4 presents the varied methods and results for measuring K_{Ic}.

Closest to validity according to ASTM criteria are the evaluations from service and the bend samples. These give values in reasonable agreement to give an average value of $K_{Ic} = 51 \pm 8$ MPa$\sqrt{m}$.

[1]Calculate the ratio $\frac{P_{max}}{P_Q}$, where P_{max} is the maximum load the specimen was able to sustain ... If $\frac{P_{max}}{P_Q}$ does exceed 1.10, then the test is not a valid K_{Ic} test [4].

Table 8.4: K_{Ic} Comparisons

Method	K_{Ic} MPa$\sqrt{m}$	Comments on Validity
Service rock bolts measured a_{crit} lab measured σ_{TH}	43 52 63	Provides good estimate of true value
LIST	41 37	Not valid because outside plane strain conditions
Bend	46 51	Good approximation. Close to providing valid results
CVN	27	Rough approximation
Combined K_{Ic}	31 50 28 34	Bolt average, rough approximation Bolt F Bolt G Bolt K

8.1.4 Applicability of LEFM

It was valid to use Linear Elastic Failure Mechanics to analyse the fracture of rock bolts in service because the plastic deformation was confined to a small part of the cross-section, and was also small compared to the size of the crack. Rock bolts that failed by SCC in service were under a relatively small tensile stress and a bending stress. The yield (and threshold) stress was exceeded only in the outer fibres of the bolt whilst the inner fibres remained lightly stressed, with only low stresses in the elastic region. The stress corrosion crack initiated in the small region of plastically deformed outer fibres, whereas conditions leading to final brittle fracture were reached further into the bolt.

8.1.5 Fracture Toughness Implications

Sections 6.10 and 7.10 calculated an average crack velocity of 2.5 x 10^{-8} m s^{-1}

By applying this to a 1355AXRC bolt with a low fracture toughness (Bolt K with toughness of 43 MPa$\sqrt{m}$ with a crack depth of 1.07 mm), the estimated time to failure for bolt K would be 42800 seconds, or approximately 12 hours.

For design purposes we can use a worst case scenario to study the effects of changing the fracture toughness. If we apply this velocity (2.5 x 10^{-8} m s^{-1}), together with the largest crack geometry from bolt J (8 mm crack depth and estimated fracture toughness of 116 MPa$\sqrt{m}$), the time to failure from initiation for this hypothetical bolt would be 320000 seconds, or approximately 89 hours.

This shows that by doubling the fracture toughness, the bolt lifetime is extended by barely 77 hours (just over 3 days).

It can be seen that to solve the problem of rock bolt stress corrosion cracking it is not a good option to increase the fracture toughness. A better option would be to change the susceptibility of the metallurgy to

SCC, or to choose a rock bolt metallurgy that does not suffer from SCC at the local conditions.

8.2 FRACTURE TOUGHNESS CONCLUSIONS

Fracture toughness values evaluated for a 1355AXRC rock bolt was about 50 MPa$\sqrt{m}$. There is certainly scope for producing steels with higher values of fracture toughness, but the benefits in terms of increased SCC lifetimes seem to be small.

8.3 COLD WORK

304 stainless steel and 5152 steel samples were cold worked (%66 and %55 respectively) in order to study the changes of mechanical and SCC properties.

The 5152CW10D steel was made from 5152 steel and cold worked by 10%. This small amount of cold work modified its yield strength from 560 MPa to 745 MPa, and its UTS from 915 MPa to 890 MPa. Cold working by 10% modified the SCC resistance properties of that metallurgy as shown by Figures 7.13 and 7.15. 5152CW10D steel did not fail by SCC even at a potential above -1600 mV vs SHE at neutral pH, whilst 5152 failed at -1000 mV vs SHE. At abundant hydrogen levels (pH 2.1), 5152 failed by SCC at 200 mV more positive than 5152CW10D (-1000 instead of -1200 mV vs SHE). This increased SCC resistance of the 5152CW10D was also observed in alkaline conditions (pH 11 - 12).

The 5152 steel increased its σ_Y marginally from 560 MPa to 600 MPa, but its UTS dropped considerably from 915 MPa to 740 MPa when it was cold worked by 55%. Samples of the %55 cold worked samples (5152CW55) were tested at -1000 mV and -1200 mV vs SHE in the preferred sulphate pH 2.1 solution. Both samples failed in a ductile manner, showing a higher resistance to SCC than both the 5152 samples (failed by SCC at -1000 mV vs SHE) and the 5152CW10D samples (failed by SCC at -1200 mV vs SHE) in the preferred sulphate pH 2.1 solution. Figure 8.8 presents the results in a Pourbaix diagram.

The 304 steel increased its yield strength σ_Y from 335 MPa to 650 MPa, and its UTS from 780 MPa to 820 MPa when it was cold worked by 66%. Samples of the cold worked 304 steel (named 304CW66) were tested at -200 and -400 mV vs SHE in the sulphate pH 2.1 solution. The sample tested at -200 mV vs SHE failed in a ductile manner while the sample tested at -400 mV vs SHE failed by SCC. Samples that have not been cold worked have failed by SCC when exposed to the same conditions. Figure 8.9 presents the results in a Pourbaix diagram.

The increase in SCC resistance of the various metallurgies is believed to be due to the effect of hydrogen trapping. As a metal is deformed and cold worked, crystalline dislocations are introduced in the material. Hydrogen entering the metal will become trapped in these dislocations, unable to further penetrate the material. As the hydrogen diffusion is hindered, the region embrittled by the hydrogen gets smaller, providing a smaller region able to be affected by SCC. As a result a greater negative overpotential is required to allow

enough hydrogen to enter the material and diffuse ahead of the crack tip to allow the material to fail by SCC.

8.4 COLD WORK CONCLUSIONS

Cold work of the 5152 steel by 10% and 55% showed an increasing resistance of the steel to SCC. Cold working the material by 10% increased the SCC resistance by -200 mV vs SHE in the preferred sulphate pH 2.1 solution. Cold working the material to 55% increased the SCC resistance by -400 mV vs SHE.

Cold work of the 304 stainless steel also displayed an increase in the SCC resistance of the material. Cold working the 304 steel by 66% increased the resistance by at least -200 mV vs SHE in the sulphate pH 2.1 solution. Cold work improved the SCC resistance of rock bolts.

8.5 FIGURES

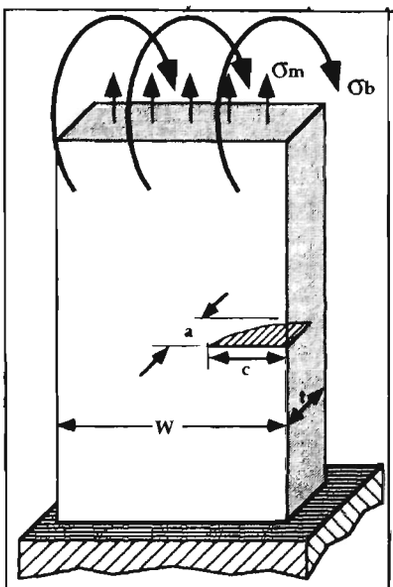

σ_m - Membrane (tensile) stress.
σ_b - Bending stress

$$\sigma_b = \frac{Mt}{2I}$$

where

$$I = \frac{Wt^3}{12}$$

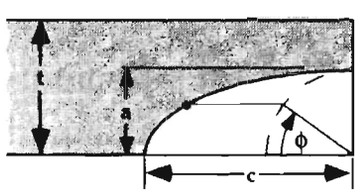

$$K_I = (\sigma_m + H\sigma_b)F\sqrt{\frac{\pi a}{Q}}$$

$$F = \left[M_1 + M_2\left(\frac{a}{t}\right)^2 + M_3\left(\frac{a}{t}\right)^4\right] g_1 g_2 f_\phi f_w$$

$$H = H_1 + (H_2 - H_1)(\sin\phi)^p$$

$$Q = 1 + 1.464\left(\frac{a}{c}\right)^{1.65}$$

$$M_1 = 1.08 - 0.03\left(\frac{a}{c}\right)$$

$$M_2 = -0.44 + \frac{1.06}{0.3 + \frac{a}{c}}$$

$$M_3 = -0.5 - 0.25\left(\frac{a}{c}\right) + 14.8\left(1 - \frac{a}{c}\right)^{15}$$

$$g_1 = 1 + \left[0.08 + 0.4\left(\frac{a}{t}\right)^2\right](1 - \sin\phi)^3$$

$$g_2 = 1 + \left[0.08 + 0.15\left(\frac{a}{t}\right)^2\right](1 - \cos\phi)^3$$

$$f_\phi = \left[\left(\frac{a}{c}\right)^2 \cos^2\phi + \sin^2\phi\right]^{1/4}$$

$$f_w = \left[\sec\left(\frac{\pi c}{2W}\sqrt{\frac{a}{t}}\right)\right]^{1/2}$$

$$g = 1 + \left[0.1 + 0.35\left(\frac{a}{t}\right)^2\right](1 - \sin\phi)^2$$

$$H = H_1 + (H_2 - H_1)(\sin\phi)^p$$

$$p = 0.2 + \frac{a}{c} + 0.6\left(\frac{a}{t}\right)$$

$$H_1 = 1 - 0.34\frac{a}{t} - 0.11\frac{a}{c}\left(\frac{a}{t}\right)$$

$$H_2 = 1 + G_1\left(\frac{a}{t}\right) + G_2\left(\frac{a}{t}\right)^2$$

$$G_1 = -1.22 - 0.12\left(\frac{a}{c}\right)$$

$$G_2 = 0.64 - 1.05\left(\frac{a}{c}\right)^{0.75} + 0.47\left(\frac{a}{c}\right)^{1.5}$$

FIGURE 8.1: Stress intensity solution for a quarter elliptical corner crack in a flat plate for $a < c$ [61]

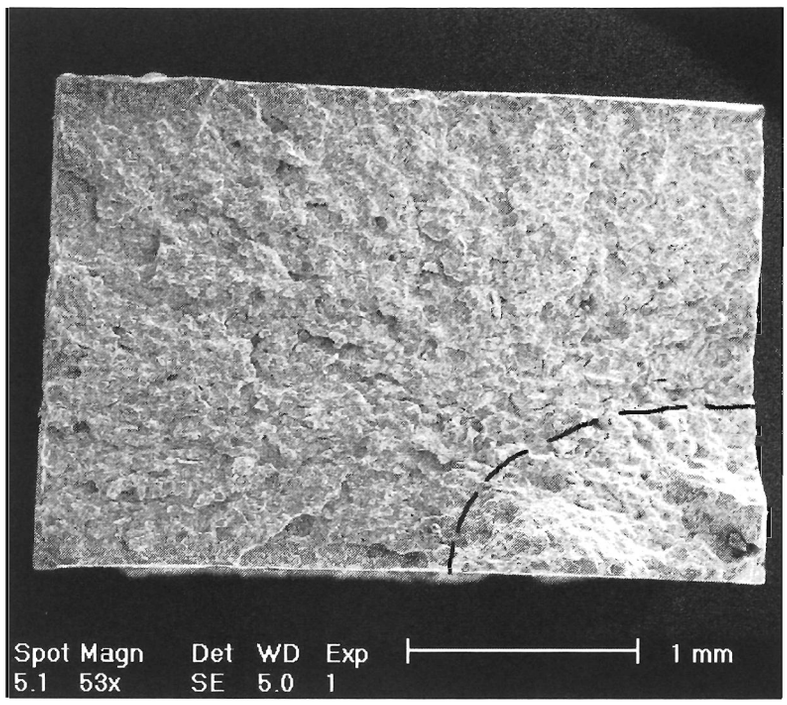

FIGURE 8.2: Overview of LIST 24

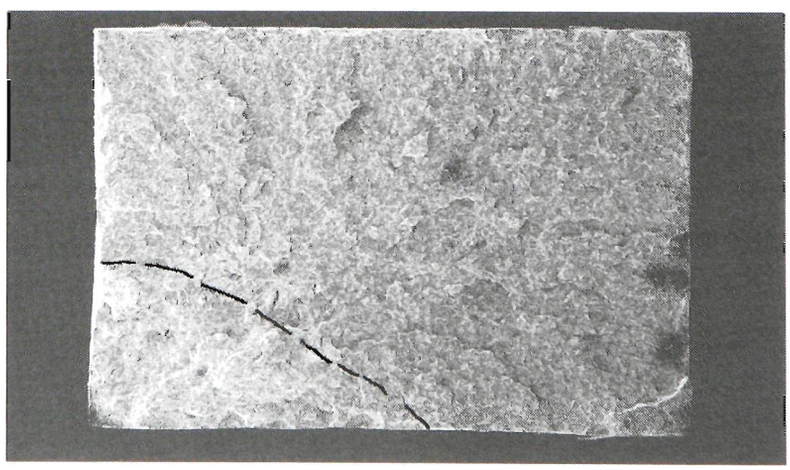

FIGURE 8.3: Overview of LIST 41

9.5 A SEMI-ELLIPTICAL SURFACE CRACK IN A LONG SHAFT UNDER TENSION

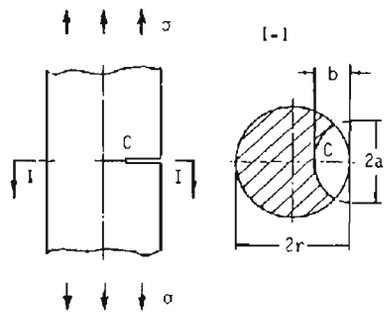

[Reference] H.Nisitani and D.H.Chen [1]
[Method] Body Force Method
[Accuracy] Less than 1%

K_I : Stress intensity factors at the deepest point C of a semi-elliptical crack front

$$F_I = \frac{K_I}{\sigma\sqrt{\pi b}}$$

$K_I|_{r\to\infty}$: K_I for a semi-elliptical surface crack in a semi-infinite body

Table Values of F_I

	b/r	0	0.125	0.250	0.375	0.500
b/a=1	0.0	0.636	0.641	0.656	0.683	0.723
	0.3	0.660	0.665	0.683	0.714	0.756
b/a=0.5	0.3	0.884	0.890	0.920	0.976	1.064

Table Values of F_I

a/r \ b/a	0.25	0.50	0.75	1.00
0	1.022	0.884	0.759	0.660
0.25	1.003	0.890	0.780	0.683
0.50	0.996	0.920	0.840	0.758

FIGURE 8.4: Stress intensity solution for a semi elliptical crack on a round long bar [62].

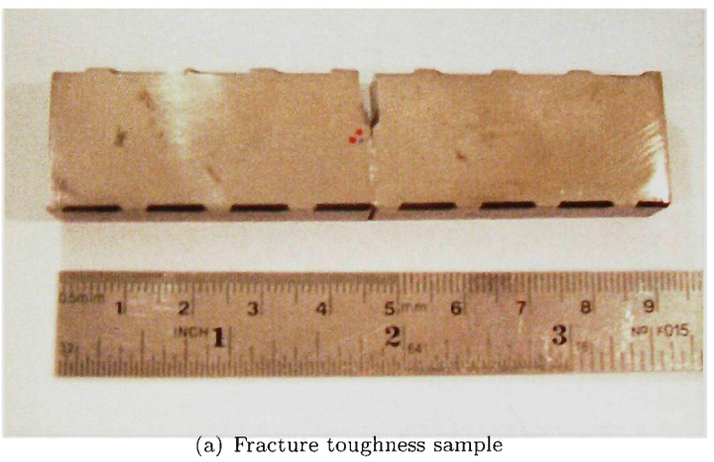

(a) Fracture toughness sample

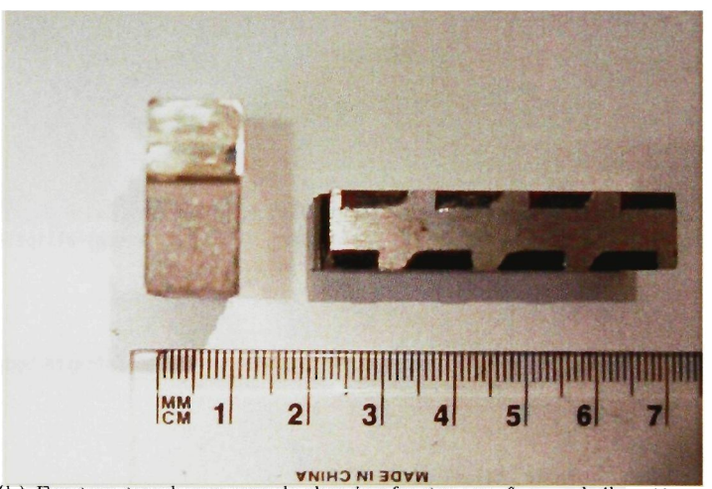

(b) Fracture toughness sample showing fracture surface and rib pattern

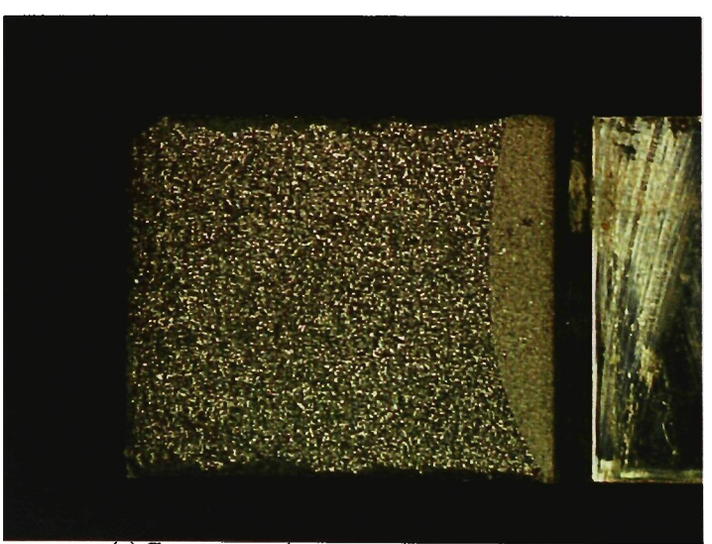

(c) Fracture toughness sample fracture surface

FIGURE 8.5: Fracture toughness sample

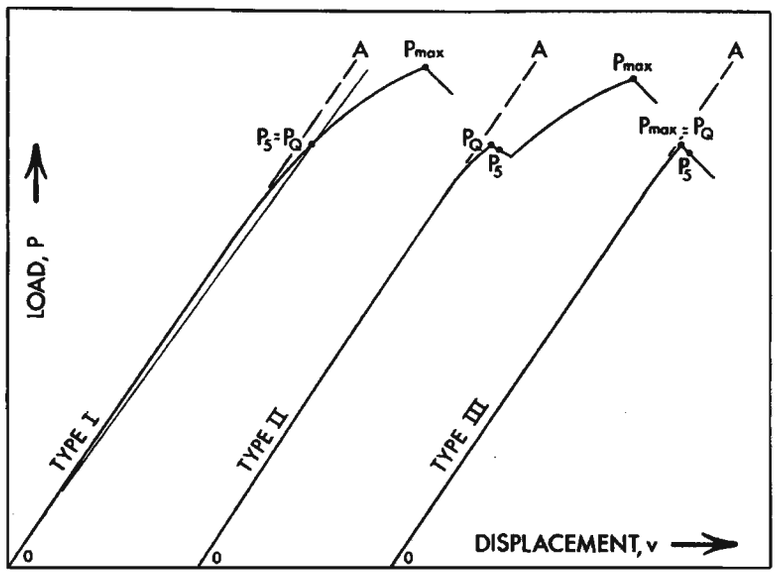

FIGURE 8.6: Principal types of Load-Displacement records [4]

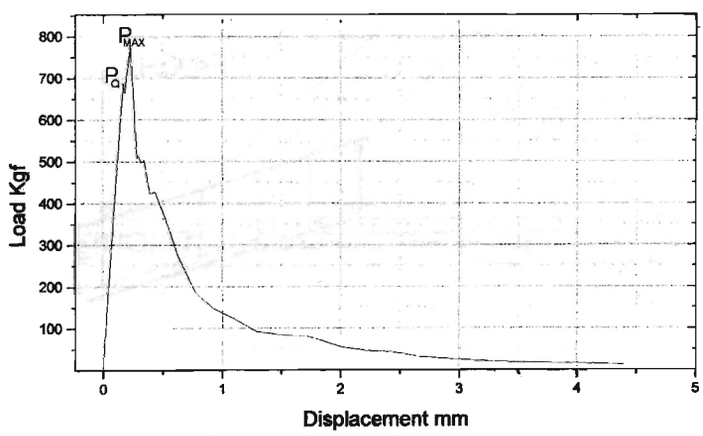

(a) Sample 1 Load vs Displacement

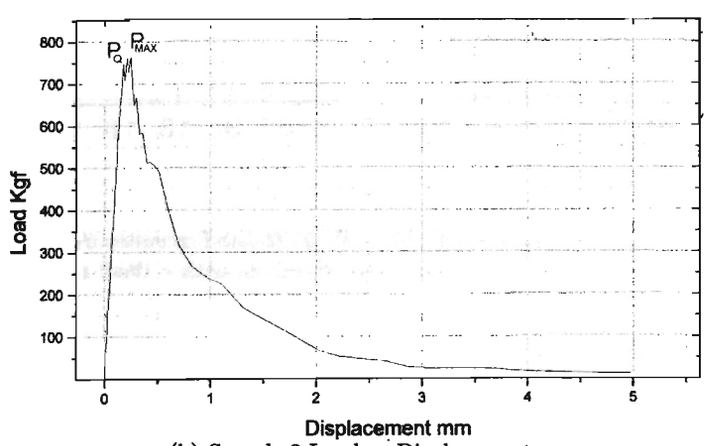

(b) Sample 2 Load vs Displacement

FIGURE 8.7: Load vs displacement graphs

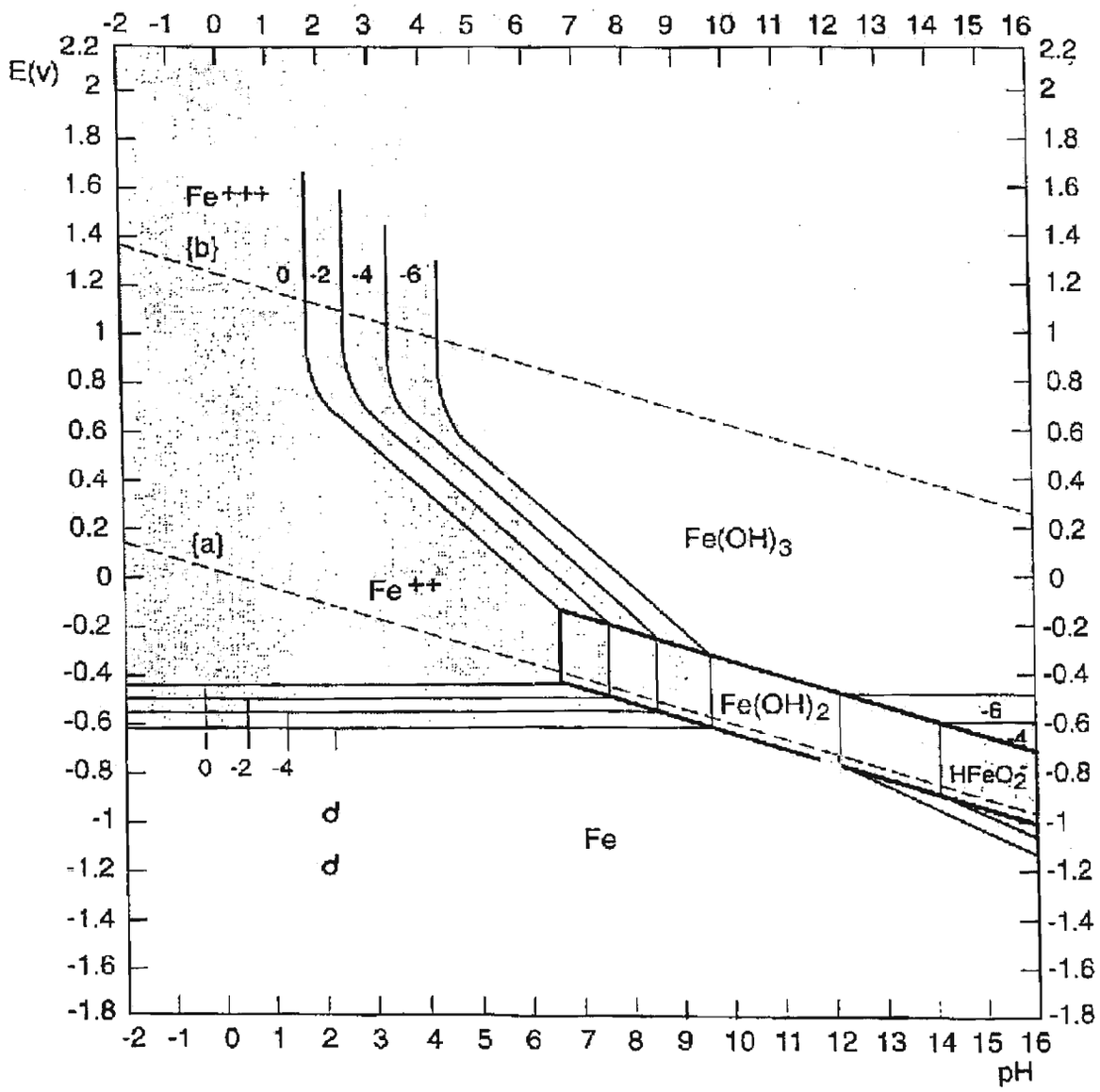

FIGURE 8.8: Pourbaix diagram for iron showing 55% CW 5152 LIST results. A full symbol means it failed by SCC, whereas an empty circle means no SCC was detected. Symbols with a dash represent experiments performed with an applied potential.

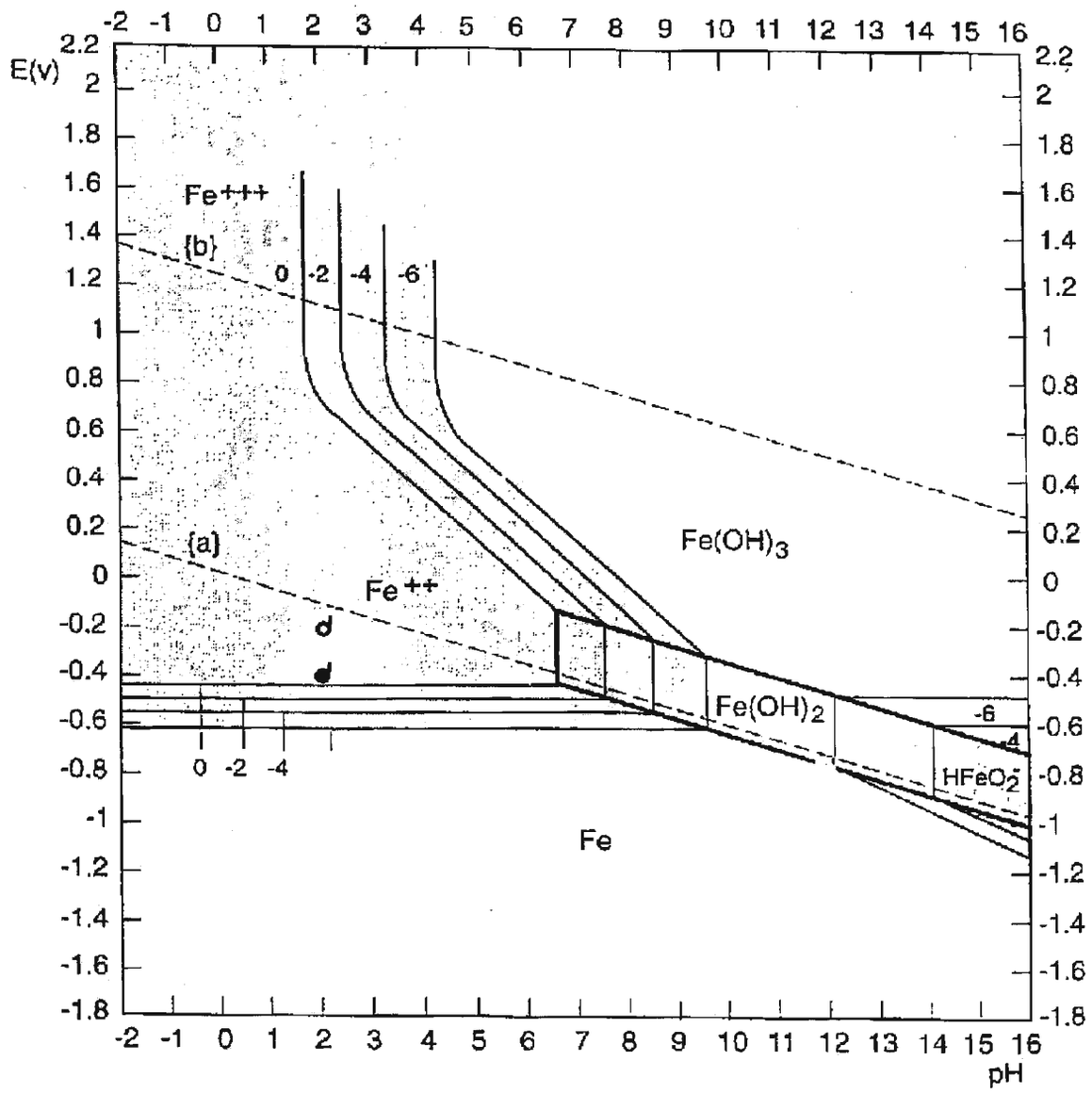

FIGURE 8.9: Pourbaix diagram for iron showing 66% CW 304 LIST results. A full symbol means it failed by SCC, whereas an empty circle means no SCC was detected. Symbols with a dash represent experiments performed with an applied potential.

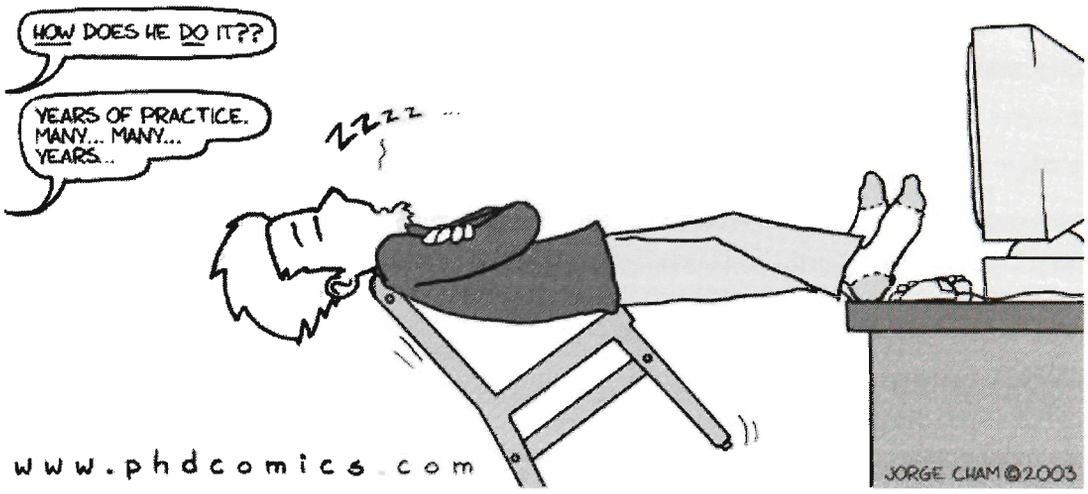

9

ROCK BOLT RIB GEOMETRY

Previous studies have shown that rock bolts failed by SCC display that the stress corrosion crack initiated at the foot of a rib [7], [8]. This observation has been confirmed in Chapter 5.

This Chapter presents the results of a study in the effect of rock bolt rib geometry on the initiation of SCC. Three rock bolts with similar metallurgy have been studied. Two of the bolts had a raised rib (1355AXRO and 1355AXRC), while the third bolt had a smaller rib profile (1355AX).

All bolt profiles studied showed the most hydrogen production at the foot of the ribs.

9.1 RESULTS

Figure 9.1 shows a typical overview of a geometry sample after being immersed in the sulphate pH 2.1 solution for a time at a stress close to the threshold stress. Figure 9.1(a) shows an overview, with the rib running vertically, with the smooth side (larger radius of curvature) on the right. Figure 9.1(b) shows a higher magnification view of the sharp foot of the rib. Figure 9.1(c) shows a higher magnification view of the smoother side of the rib. The Figures show that the smoother side of the rib displays greater corrosion damage. Any of the multiple pits seen can be an initiation site for a stress corrosion crack if the stress goes above the threshold stress.

9.1.1 1355AXRC Samples

1355AXRC geometry samples without a side rib were found to have cracked completely by SCC initiated failure, or to have stress corrosion cracks, after 70.5 hrs and 52 hrs at 908 MPa. Samples failed on the smooth side of the rib.

One sample was tested that had a side rib (LIST 101). That sample cracked at 108.5 hours at a stress of 533 MPa. Figure 9.2 shows CIS fracture surface on that sample.

9.1.2 1355AXRO Samples

One 1355AXRO geometry sample without a side rib cracked at 1150 MPa after 16 hours on the smooth side of the rib.

A ribbed sample cracked at 908 MPa after 192 hours. This extended period of time is believed to have been aided by the fact that the geometry sample had a light coat of paint along the surface.

9.1.3 1355AX Sample

One 1355AX sample without a side rib was held for 192 hours at a stress of 850 MPa in the preferred sulphate pH 2.1 solution. After the 192 hours the sample was taken out of the solution and was found to have no cracks.

9.1.4 Bolt Comparison

Figure 9.3 shows a plot of applied stress versus time to failure for the various rock bolts. A full symbol represents a sample failing due to SCC. An empty symbol represents a sample that did not fail by SCC after being held at the determined stress after 192 hours.

The results in Figure 9.3 show that 1355AXRC bolts can fail when stressed at around 750 MPa. This smaller value than the established threshold stress of 900 MPa for the 1355AXRC suggests that there could have been a residual stress in the rib pattern helping to initiate SCC at a lower applied stress. The magnitude of the residual stress is suggested to be between 150 MPa and 300 MPa, as a sample of the same metallurgy did not fail by SCC after 192 hours at a direct applied stress of 600 MPa.

A comparison of bolts 1355AXRC and 1355AXRO showed that there was no significant advantage of one geometry over the other. The 1355AXRO sample that lasted 190 hours at 900 MPa was covered by paint over most of its surface. The increased lifetime suggests that the paint provided protection in the sulphate pH 2.1 solution for a limited time.

The sample with the smallest rib profile (1355AX) suggests that it does not have a residual stress greater than 50 MPa, as the sample did not fail by SCC at a direct applied stress of 850 MPa.

9.2 CONCLUSIONS

Rock bolt rib geometry does not have a direct impact on the SCC resistance properties of the bolt.

The process by which the ribs are introduced in the bolt can have a negative impact on its SCC properties. If bolt ribs are introduced by rolling, residual tensile stresses remain, lowering the direct stress that they are able to sustain before SCC initiates. On the other hand, cold work may increase the resistance to SCC by introducing dislocations able to trap hydrogen (Chapter 8). Further study is recommended to study the optimum levels of cold/hot rolling of the ribs for SCC resistance.

9.3 FIGURES

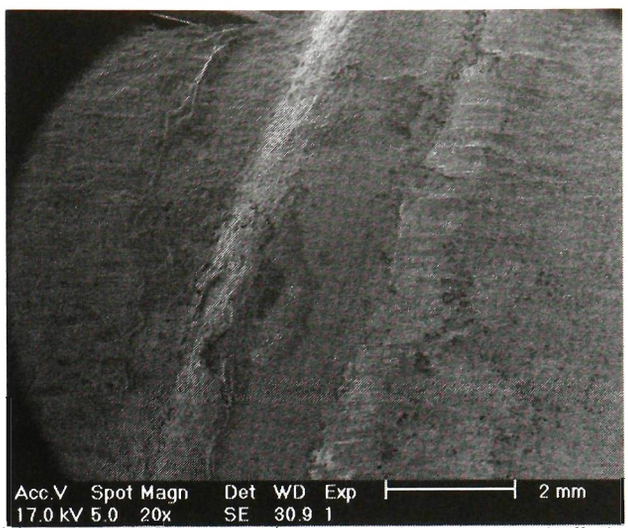

(a) Rock bolt rib overview (raised section running vertically in centre)

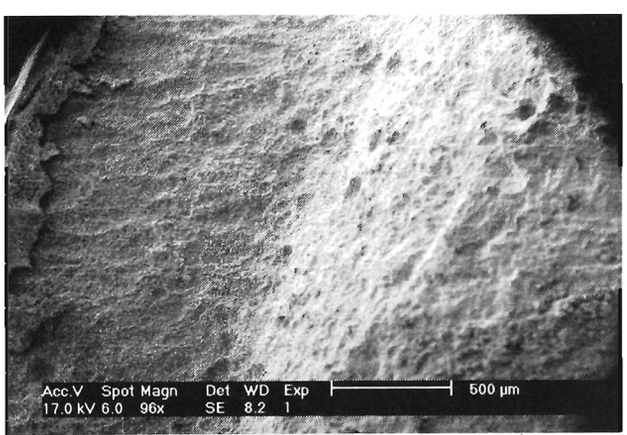

(b) Overview of rib side with the sharper radius

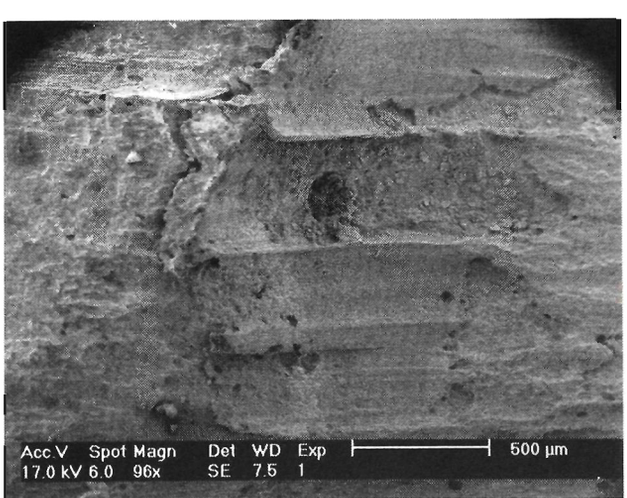

(c) Overview rib side with smoother radius

FIGURE 9.1: Typical rock bolt rib for an AXR rock bolt

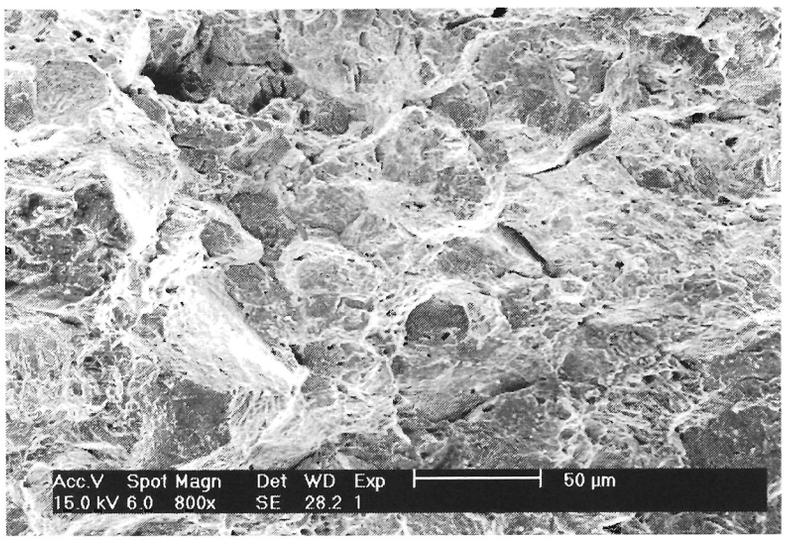

FIGURE 9.2: CIS on a 1355AXRC geometry sample

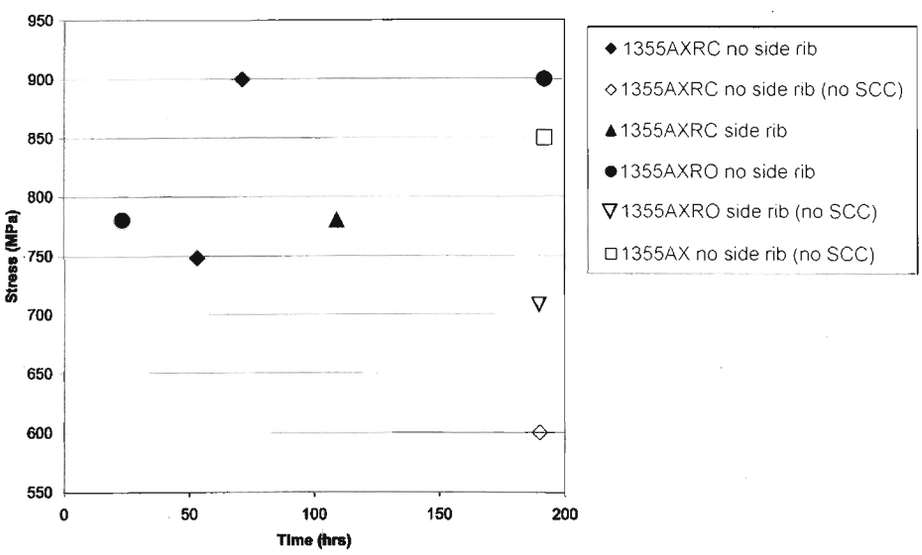

FIGURE 9.3: Applied stress vs time to failure for different rock bolts

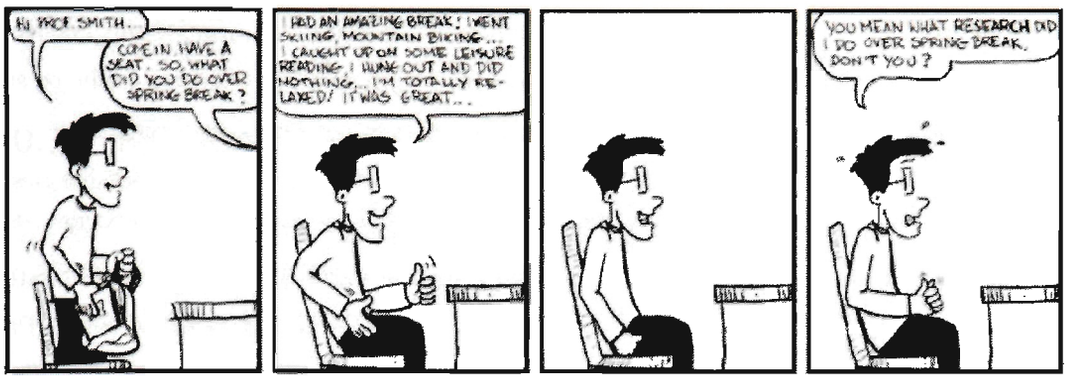

10

CONCLUSIONS

Rock bolts failed in service were analysed in Chapter 5 and found to have failed by Stress Corrosion Cracking (SCC). Their fracture surfaces were documented and found to be characterised by a thumbnail region of slow crack growth (SCC) and a brittle overload region. All fractures were found to have initiated at the smooth side of the rock bolt rib.

The fracture surfaces within the SCC region were characterised and documented in Chapter 6 as Tearing Topography Surface (TTS) [53], Corrugated Irregular Surface (CIS) and quasi Micro Void Coalescence (qMVC).

A fracture mechanism was proposed for rock bolt SCC. The crack propagated as a front outwardly from the crack initiation site, perpendicular to the free surface of the material. Hydrogen formed due to corrosion reactions diffused into the metal along the direction of the greatest triaxial stress; directly into the material perpendicular to the applied axial stress. Subcritical crack growth propagated once the material ahead of the crack tip had reached a critical hydrogen concentration. Once a critical crack size had been reached, the rest of the material failed by fast brittle failure.

The microstructure of the metal did not affect hydrogen diffusion, crack propagation nor the fracture mechanism transition (slow subcritical crack growth to fast brittle failure).

Laboratory work presented in Chapter 7 produced the same SCC fractography as the service failures,

confirming the Linearly Increasing Stress Test (LIST) in the preferred sulphate pH 2.1 solution provided a reliable laboratory test for SCC.

Conditions leading to SCC were found to correspond to copious hydrogen evolution (ie very acidic or at very negative potentials), confirming Hydrogen Embrittlement (HE) as a likely responsible mechanism.

Conditions needed to produce SCC were found to be very specific for different rock bolt metallurgies. No metallurgy displayed SCC when loaded in distilled water, nor at loading rates at or below 0.19 MPa s^{-1} 1355AXRC, MAC and MA840B metallurgies displayed SCC when loaded at 0.019 MPa s^{-1} in the sulphate pH 2.1 solution. 1355AXRC had a threshold stress of 900 MPa, MAC 815 MPa and MA840B 850 MPa in the sulphate pH 2.1 solution at the free corrosion potential. MAC and MA840B steels had worse SCC properties than the 1355AXRC steel.

Galvanised 1355AXRC, 10M30, 304 stainless steel, 5152 and 5152CW10D metallurgies did not fail due to SCC when loaded at 0.019 MPa s^{-1} in the sulphate pH 2.1 solution, but did fail when a negative overpotential was applied or the conditions were more acidic than pH 2.1. Galvanised 1355AXRC samples were found to have the zinc layer stripped within days when submerged in the sulphate pH 2.1 solution, and their strength lowered compared to the plain 1355AXRC metallurgy.

10M30 rock bolts had been thought not to suffer from SCC, but detailed study of the fracture surfaces showed that 10M30 bolts do suffer from SCC, but the macroscopic appearance is that of ductile overload.

5152CW10D rock bolts were found to have the best SCC resistance properties (requiring the most negative overpotential (-1200 mV vs SHE) to produce SCC).

An analysis carried out of various Australian mines showed that some mines had a greater concentration of chlorides and sulphates in their water than the laboratory solution, but all had a neutral pH. These mines could start encountering problems with rock bolt SCC if sulphate reducing microbiology developed in the rock strata close to the bolts and the microbiology would change the neutral pH to more acidic levels.

SCC crack velocity was estimated in Chapter 7.10 to be an average of 2.5 * 10^{-8} m s^{-1} This high velocity and the high threshold stress implied that if a rock bolt falls out of the rock and displays a SCC fracture surface it is because the rock strata has sheared within the last three days, and that there are acidic conditions in the rock (either naturally occurring or due to microbiological activity).

Chapter 8 explored the effect of increasing the fracture toughness of the steel, and found it to be an ineffective method of countering SCC. A fourfold increase in fracture toughness would delay rock bolt failure by a few days.

Chapter 9 presented the results that crack rib geometry does not have a direct effect on SCC initiation, but the amount of residual stresses can lower the directly applied stress at which SCC initiates.

Cold Work (CW) increased the resistance to SCC. A small amount of CW (10%) increased the required overpotential by -200 mV, but further increases in required overpotential are harder to achieve (55% CW required for a required overpotential of -400 mV in 5152 steel). Stainless steel (304) also seems to receive SCC resistance benefits from cold work.

It can be concluded that the conditions leading to rock bolt SCC are specific, and that using a bolt with a different metallurgy at a specific location can avoid SCC failures.

10.1 RECOMMENDATIONS FOR FUTURE WORK

The work carried out on the effects of residual stresses and CW on SCC properties indicated that it would be beneficial to undertake a larger study than the one carried out in this thesis. By better understanding these effects it may be possible to modify manufacturing processes to further improve on SCC properties of a specific metallurgy, or to determine the optimum levels of CW for increased strength and SCC resistance.

The rock bolts studied had similar metallurgies, but different SCC properties. Undertaking a study of the effects on SCC properties by individual trace alloying elements might be able to provide a better solution to rock bolt SCC.

Studies aimed at improving the fracture toughness of rock bolts are not recommended, as increases in fracture toughness do not provide a viable answer to the problem of rock bolt SCC.

Obtaining a sample of underground water that produces SCC failures would provide a further insight into environmental conditions causing SCC.

Testing of these aspects can be carried out on the LIST equipment.

REFERENCES

[1] R. Baboian. *Corrosion Tests and Standards Application and Interpretation* (ASTM, Fredericksburg, VA, 1995).

[2] A. Atrens and Z. F. Wang. *Stress corrosion cracking.* Materials Forum **19**, 9 (1995).

[3] R. Magdowski and M. O. Speidel. *Parkins Symposium on Fundamental Aspects of Stress Corrosion Cracking*, chap. Stress Corrosion Cracking of High Strength Steels, pp. 341–351 (The Minerals, Metals and Materials Society, 1992).

[4] ASTM. *E399 90 standard test method for plane-strain fracture tougnness of metallic materials.* In *1998 Annual Book of ASTM Standards - Metals Test Methods and Analytical Procedures*, vol. 03.01, pp. 413 – 443 (ASTM, 1998).

[5] R. H. Jones. *Stress-Corrosion Cracking Materials Performance and Evaluation* (ASM International, 1993), second ed.

[6] A. Arnall. *Practical Guide to Rock Bolting* (ANI ARNALL, 25 Pacific Highway Bennets Green, NSW 2290, 1991).

[7] A. Crosky, M. Fabjanczyk, and P. Gray. *Final report premature rock bolt failure, acarp c8008.* Tech. rep., Australian Coal Association Research Program (2002).

[8] A. Crosky, B. Smith, and B. Hebblewhite. *Failure of rockbolts in underground mines in australia.* In *International Conference and Exhibition on Failure Analysis (ICFA), Melbourne, Australia* (20-22 November, 2002).

[9] R. M. Magdowski. *Spannungsrisskorrosion von ferritischen stählen in wasser.* Ergebnisse der Werkstoff-Forschung, Band 1: Moderne Stähle p. 107 (1987).

[10] A. Atrens, C. C. Brosnan, S. Ramamurthy, A. Oehlert, and I. O. Smith. *Linearly increasing stress test (list) for scc research.* Measuring Science Technology **4**, 1281 (1993).

[11] J. A. Beavers and G. H. Koch. *Limitations of the slow strain rate test for stress corrosion cracking testing.* Corrosion **48**(3), 256 (1992).

[12] E. N. Pugh. *Corrosion*, vol. 41 (1985).

[13] J. J. Harwood. *Stress Corrosion Cracking and Embrittlement* (John Wiley and Sons, 1956).

[14] S. Lynch. *Hydrogen Effects in Metals*, p. 863 (The Metallurgical Society, 1981).

[15] H. H. Uhlig. *Physical Metallurgy of Stress Corrosion Fracture* (Interscience, 1959).

[16] E. N. Pugh. *Stress Corrosion Cracking and Hydrogen Embrittlement of Iron Based Alloys* (National Association of Corrosion Engineers, 1977).

[17] A. J. Forty. *Physical Metallurgy of Stress Corrosion Fracture* (Interscience, 1959).

[18] N. K. Mukhopadhyay, G. Sridhar, and N. Parida. *Hydrogen embrittlement failure of hot dip galvanised high tensile wires.* Engineering Failure Analysis **6**, 253 (1998).

[19] J. Toribio. *Hydrogen plasticity interactions in pearlitic steel: a fractorgraphic and numerical study.* Materials Science and Engineering pp. 180–191 (1996).

[20] W. D. Robertson. *Stress Corrosion Cracking and Embrittlement* (John Wiley and Sons, 1956), first ed.

[21] A. R. Troiano. *Hydrogen Embrittlement and Stress Corrosion Cracking* (American Society for Metals, 1984), first ed.

[22] E. C. N. Podesta, J. J. and M. A. Esteso. *Evaluation of the absorption on mild steel of hydrogen evolved in glucose fermentation by pure cultures of clostridium acetobtylicum and enterobacter.* Sensors and Actuators B **32**, 27 (1995).

[23] B. M. Victoria. *The role of hydrogen in microbiologically influenced corrosion and stress corrosion cracking.* International Journal of Hydrogen Energy **26**, 515 (2001).

[24] B. R. H. Mba, D. and G. E. Findlay. *Mechanical redesign of the rotating biological contactor.* Wat. Res. **33**(18), 3679 (1999).

[25] Y. Hirose and T. Mura. *Growth mechanism of stress corrosion cracking in high strength steel.* Engineering Fracture Mechanics **19**(6), 1057 (1984).

[26] Y. Hirose and T. Mura. *Effect of loading history on stress corrosion cracking in high strength steel.* Mechanics of Materials **3**, 95 (1984).

[27] C. S. Kortovich and E. A. Steigerwald. *A comparison of hydrogen embrittlement and stress corrosion cracking in high strength steels.* Engineering Fracture Mechanics **4**, 637 (1972).

[28] M. O. Speidel. *Corrosion in Power Generating Equipment*, chap. Stress Corrosion Cracking and Corrosion Fatigue Fracture Mechanics, pp. 85–130 (Plenum Press, 1984), first ed.

[29] B. G. Pound. *Hydrogen trapping in high strength steels.* Acta Mater. **46**(16), 5733 (1998).

[30] A. Mazur and B. Pawlowski. *The stress corrosion cracking of high strength cr-mn-si-ni and cr-mo steels.* Corrosion Science **26**(1), 7 (1983).

[31] S. Rolfe and J. Barsom. *Fracture and Fatigue control in Structures - Applications of Fracture Mechanics* (Prentice Hall, Englewood Cliffs, NJ, 1987).

[32] A. Oehlert. *Primary Creep and Stress Corrosion Cracking in High Strength Steels.* PhD thesis, The University of Queensland (1994).

[33] H. G. Nelson and D. P. Williams. *Stress Corrosion Cracking and Hydrogen Embrittelment of Iron Based Alloys.*, chap. Quantitative Observations of Hydrogen Induced, Slow Crack Growth in a Low Alloy Steel, pp. 390–404 (NACE, 1977).

[34] S. Glasstone and D. Lewis. *Elements of Physical Chemistry* (McMillan and Company, 1963), 6th ed.

[35] W. W. Gerberich. *Fracture mechanics: Microstructure and micromechanisms.* ASM Materials Science Seminar p. 201 (1987).

[36] R. M. Schroeder and I. L. Muller. *Stress corrosion cracking and hydrogen embrittlement susceptibility of an eutectoid steel employed in prestressed concrete.* Corrosion Science **45**, 1969 (2003).

[37] D. Craig, F. Ellyin, and D. Kujawski. *The behaviour of small corner cracks in a ferritic / pearlitic steel: Experiments and analysis.* Fatigue and Fracture of Engineering Materials and Structures **18**(7/8), 861 (1995).

[38] J. Toribio and E. Ovejero. *Microstructure based modelling of hydrogen assisted cracking in pearlitic steels.* Materials Science and Engineering A **A319-321**, 540 (2001).

[39] L. E. Miller and G. C. Smith. *Tensile fractures in carbon steels.* Journal Iron Steel Inst. **208**, 9981005 (1970).

[40] M. P. J. J. V. S. H. H. Gerberich, W. W. *Corrosion Deformation Interactions*, p. 325 (Les Editions de Physique, Les Ulis, 1993).

[41] K. A. Narayan, R. and K. P. Singh. *The anodic polarisation and stress corrosion cracking of eutectoid steel.* Corrosion Science **25**(6), 449 (1985).

[42] J. Toribio. *Role of crack-tip residual stresses in stress corrosion behaviour of prestressing steel.* Construction and Building Materials **12**, 283 (1998).

[43] J. Toribio and A. M. Lancha. *Overload retardation effects on stress corrosion behaviour of prestressing steel.* Construction and Building Materials **10**(7), 501 (1996).

[44] L. A. Toribio, J. and M. Elices. *Factors influencing stress corrosion cracking of high strength pearlitic steels.* Corrosion Science **35**(1-4), 521 (1993).

[45] J. Toribio and A. M. Lancha. *Effect of cold drawing on environmentally assisted cracking of cold-drawn steel.* Journal of Materials Science **31**, 6015 (1996).

[46] R. W. Staehle. *The Theory of Stress Corrosion Cracking in Alloys* (North Atlantic Treaty Organization, 1971).

[47] R. W Staehle. *Stress Corrosion Cracking and Hydrogen Embrittlement of Iron Based Alloys* (National Association of Corrosion Engineers, 1977).

[48] J. M. Silcock and P. R. Swann. *Environment Sensitive Fracture of Engineering Materials* (The Metallurgical Society, 1979).

[49] S. Ramamurthy and A. Atrens. *The stress corrosion cracking of as-quenched 4340 and 3.5nicrmov steels under stress rate control in distilled water at 90c.* Corrosion Science **34**(9), 1385 (1993).

[50] J. Salmond and A. Atrens. *Scc of copper using the linearly increasing stress test.* Scripta Metallurgica et Materialia **26**, 1447 (1992).

[51] Z. F. Wang and A. Atrens. *Initiation of stress corrosion cracking for pipeline steels in a carbonate bicarbonate solution.* Metallurgical and Materials Transactions **27A**, 2686 (1996).

[52] M. Rataj. *Private communication sept 2000.*

[53] J. Toribio and E. Vasseur. *Hydrogen assisted micro-damage evolution in pearlitic steel.* Journal of Materials Science Letters **16**, 1345 (1997).

[54] M. Rataj. *Private communication 25 january 2002.*

[55] M. Rataj. *Private communication 15 august 2002.*

[56] J. Toribio, A. Lancha, and M. Elices. *Characteristics of the new tearing topography surface.* Scripta Metallurgica et Materialia **25**, 2239 (1991).

[57] J. Toribio, A. Lancha, and M. Elices. *Macroscopic variables governing the microscopic fracture of pearlitic steels.* Materials Science and Engineering A **145**, 167 (1991).

[58] J. Toribio, A. Lancha, and M. Elices. *Hydrogen embrittlement of pearlitic steels: Phenomenological study on notched and precracked specimens.* Corrosion p. 781 (1991).

[59] S. Dobos. *Private communication nov 2002.*

[60] F. Beer and E. Johnston. *Mechanics of Materials* (McGraw Hill, 1992), 2nd ed ed.

[61] T. L. Anderson. *Fracture Mechanics Fundamentals and Applications* (CRC Press, USA, 1995), 2nd ed.

[62] H. Nisitani and D. Chen. *Stress Intensity Factors Handbook*, vol. 2, pp. 654–656 (Pergamon Press, 1990), 3rd ed.

[63] M. da Fonte and M. da Freita. *Stress intensity factors for semi-elliptical surface cracks in round bars under bending and torsion.* International Journal of Fatigue **21**, 457 (1999).